Application de techniques d'opto-acoustique et de calculs de premiers principes à la caractérisation des propriétés élastiques de films minces

Chenhui Li

UNIVERSITÉ PARIS 13, UNIVERSITÉ SORBONNE PARIS CITÉ

N° attribué par la bibliothèque
|__/__/__/__/__/__/__/__/__/__/

THESE

pour obtenir le grade de

DOCTEUR DE L'UNIVERSITÉ PARIS 13

***Discipline:* Physique**

présentée et soutenue publiquement

par

CHENHUI LI

le 11 déc 2019

APPLICATION OF OPTOACOUSTIC TECHNIQUES AND FIRST PRINCIPLES CALCULATIONS TO THIN FILMS ELASTICITY CHARACTERIZATION

Directeur de thèse:

M. Philippe Djemia, Professeur, Université Paris 13

JURY

M. David Holec	Professeur, University of Leoben	Rapporteur
M. Rafael Estevez	Professeur, Université Grenoble Alpes	Rapporteur
M. Grégory Abadias	Professeur, Université de Poitiers	Examinateur
M. Philippe Djemia	Professeur, Université Paris 13	Examinateur
M. Damien Faurie	Professeur, Université Paris 13	Examinateur
M. QingMiao Hu	Professeur, Institute of metal research, Chinese Academy of Science	Examinateur
M. Vincent Ji	Professeur, Université Paris Saclay	Examinateur
M. Bernard Perrin	Professeur, Sorbonne Université	Président
Mme. Danièle Fournier	Professeure, Sorbonne Université	Membre invité

Laboratoire des Sciences des Procédés et des Matériaux, UPR CNRS 3407

SHORT SUMMARY

Elastic properties are of fundamental importance for a material. With the combination of picosecond laser ultrasonic and (PLU) Brillouin light scattering (BLS) techniques, we measured sound velocities in various magnetron-sputtering-deposited thin films including epitaxial binary and ternary transition metal nitrides (*TaN*, *TiN*, *ZrN*, $Ti_xZr_{1-x}N$), polycrystalline high entropy alloys or multicomponent transition metal alloys ($(CoCrCuFeNi)_{1-x}(Al,Nb)_x$), and their nitrogen interstitial alloys ($CoCr(Cu,Mn)FeNiN_x$). The longitudinal and shear sound velocities (V_L and V_T respectively) are correlated to the effective elastic constants through $\langle C_{33} \rangle = \rho V^2_L$ and $\langle C_{44} \rangle = \rho V^2_T$. On the other hand, Density functional theory (DFT) based *ab-initio* calculations were performed to provide single crystal elastic constants w/o considering vacancies.

In the epitaxial case, the as-measured sound velocities and derived elastic constants were directly comparable to the corresponding elastic constants calculated by DFT depending on the probing crystallographic orientation. While in the polycrystalline case, the single crystal elastic constants were further averaged by the Voigt-Reuss-Hill (VRH) method considering different textures or a self-consistent averaging method taking porosity into account.

It was found that for the epitaxial binary and ternary nitrides, vacancies play a huge role on elastic properties especially in the case of *TaN*. While in the case of *TiN*, *ZrN* and $Ti_xZr_{1-x}N$, the influence of vacancies is smaller but still noticeable. In the case of polycrystalline multicomponent alloys and interstitial alloys, the sound velocities and

effective elastic constants were found to be associated to chemical alloying (*Al*, *Nb* and *N*) effetcs, phase transitions (FCC, BCC and amorphous), textures and porosity changes. The elastic modulus agrees to nanoindentation modulus E_{IT}. The overall agreement between our elastic property measurements and DFT calculations were reached. Besides, DFT calculations also provided valuable insights into structural properties and phase stability.

Additionally, we studied structural and mechanical (including elastic) properties of a bulk *CoCrCuFeNi* as a reference to thin film properties. With the *CoCrCuFeNi* films on a flexible Kapton® substrate, we performed tensile tests and studied fracture properties of thin films, as a preliminary work to further link thin film elasticity to plasticity.

Keywords: Thin film, epitaxial, polycrystalline, sound velocity, elastic constant, transition metal nitride, multicomponent alloy, interstitial alloy, point defects, microstructure, porosity, texture, Brillouin light scattering, picosecond laser ultrasonic, nanoindentation, mechanical property, flexible substrate, fracture toughness, crack and buckle, ab-initio, DFT.

RESUME

Les propriétés élastiques sont d'une importance fondamentale pour un matériau. Avec la combinaison des techniques acoustique picoseconde (PLU) et de la diffusion Brillouin (BLS), nous avons mesuré les vitesses du son dans divers films minces déposés par pulvérisation magnétron, y compris des nitrures de métaux de transition, binaires et ternaires épitaxiés (*TaN*, *TiN*, *ZrN*, $Ti_xZr_{1-x}N$), des alliages polycristallins à haute entropie ou des alliages de métaux de transition multicomposants ($(CoCrCuFeNi)_{1-x}(Al, Nb)_x$), et leurs alliages de nitrure interstitiels ($CoCr(Cu, Mn)FeNiN_x$). Les vitesses du son longitudinale et de cisaillement (V_L et V_T respectivement) sont corrélées aux constantes élastiques effectives par $\langle C_{33} \rangle = \rho V^2_L$ et $\langle C_{44} \rangle = \rho V^2_T$. D'autre part, des calculs *ab-initio* basés sur la théorie de la fonctionnelle de la densité (DFT) ont été effectués pour fournir des constantes élastiques monocristallines avec ou sans considérer la présence de lacunes.

Dans le cas des film épitaxiés, les vitesses du son mesurées et les constantes élastiques sont directement comparables aux constantes élastiques calculées par DFT en fonction de l'orientation cristallographique. Alors que dans le cas polycristallin, les constantes élastiques monocristallines ont dû être ensuite moyennées par la méthode de Voigt-Reuss-Hill (VRH) en tenant compte de différentes textures ou par une méthode auto-cohérente de moyenne, prenant en compte la porosité.

Il a été constaté que pour les nitrures binaires et ternaires, les lacunes jouent un rôle énorme sur les propriétés élastiques, en particulier dans le cas de *TaN*. Alors que dans le cas de *TiN, ZrN* et $Ti_xZr_{1-x}N$, l'influence des lacunes est moindre mais reste perceptible.

Dans le cas des alliages polycristallins à plusieurs composants et des alliages interstitiels, les vitesses du son et les constantes élastiques effectives sont associées à des effets de composition chimique (*Al, Nb* et *N*), à des transitions de phase (FCC, BCC et amorphe), et des changements de textures et de porosité. Le module élastique correspond au module de nanoindentation E_{IT}. La concordance globale entre nos mesures de propriétés élastiques et les calculs DFT a été atteinte. En outre, les calculs DFT ont également fourni des informations précieuses sur les propriétés structurelles et la stabilité des phases observées.

De plus, nous avons étudié les propriétés structurelles et mécaniques (y compris élastiques) d'un *CoCrCuFeNi* massif servant de référence pour comparer aux propriétés des films minces. Avec les films *CoCrCuFeNi* sur un substrat Kapton®, nous avons effectué des tests de traction couplés à un microscope confocal, et étudié les propriétés de rupture des films minces, en tant que travail préliminaire pour relier ultérieurement l'élasticité des films minces à la plasticité.

Mots-clés: film mince, épitaxie, polycristallin, vitesse du son, constantes élastiques, nitrure de métal de transition, alliages multicomposants, alliages interstitiel, défauts ponctuels, microstructure, porosité, texture, diffusion Brillouin, acoustique picoseconde, nanoindentation, propriétés mécaniques, substrat flexible, fissure et cloque, ab-initio, DFT.

[To my parents and my wife]

ACKNOWLEDGEMENTS

I would like to express my first gratitude from deep my heart to Prof. Philippe Djemia. He is not only a good science advisor but also a trustworthy man who kindly considers everthing for me as his student. I am also grateful for China Scholarship Council who provide reliable support to my life and research during the last four years.

Obviously, this work can not be done without the efforts from our extrodanary collaborators. I would like to acknowledge Prof. Grégory Abadias from Poitiers University who has beening sharing a lot of samples and data; Prof. Diederik Depla and Robin Dedoncker from Ghent University for sharing their samples, data and welcoming me to visit and work in their lab; Prof. Laurent Belliard, Doc. Bernard Perrin and Eric Charron from Paris 6 who performed many PLU characterizations w/o me; Prof. Danièle Fournier from Paris 6 who is a great scientist and attractive lady to work with on thermoreflectance microscopy; Prof. Qingmiao Hu from IMR for introducing me here and sharing the high entropy alloy targets as well as his skills of DFT calculations; Prof Vincent Ji for the accessment of XRD equipment at Paris Saclay; Prof. Levente Vitos from KTH for my visit in Sweden and usage of EMTO and Doc. Wei LI from his group also for the assitance of EMTO calculations. Many thanks to the administrator of MAGI the cluster, Nicolas Greneche, without him, the theoretical work are not even possible; Also many colleagues from LSPM, Doc. Florent Tétard at Paris 13 who has conducted massive nanoindentation characterizations, Doc. Yves Roussigné for his unlimited assitance on BLS and his wisdom from many aspects, Prof. Damien Faurie for the micro-tensile experiments but not only, Doc. Fatih Zighem and Nabil Challab on magnetism characterization, Garcia Alexis for

the AFM assitance, Doc. Akbar Ghazavizadeh for his work on micromechanical modelling, Prof Andreas Zerr for sharing his high pressure and hard material knowledge, Doc. Fatiha Chalalli, Prof Mohamed Haboussi for daily greetings and fruitful discussions.

I would like to acknowledge Ouafa Rahmani, Sandrine Ouazan for their patience in doing their administrative work and kindness. I appologize to my colleagues in LSPM or outside in France whose name is supposed to be on the list but not. I appreciate the inclusiveness and respect they've been showing during my stay.

Finally, I would like to thank all my committee members. It is my honor to have all of them involed in assessing my work for PhD. They are Pr. Rafael Estevez, Université Grenoble-Alpes, Doc. David Holec, Leoben university, Pr. Grégory Abadias, Université Poitiers, Dr. Bernard Perrin, Sorbonne Université, Pr .Philippe Djemia, Pr. Damien Faurie, Université Paris 13, Pr. Qing-Miao Hu, Institute of Metal Research and Pr .Vincent Ji, Université Paris Saclay.

For sure, I will not forget the efforts from my wife, always being precious as she is also working busy on her own thesis.

VITA

1990 … Born – Jiangsu, China

2013 … B.S, Northeastern University, China

2015 … Master, University of Chinese Academy of Sciences

2015 to Dec. 2019: PhD China Scholarship Council Research Fellow, University Paris 13, Sorbonne Paris Cité, LSPM-CNRS, France

PUBLICATIONS & CONFERENCES

-*Large influence of vacancies on the elastic constants of cubic epitaxial tantalum nitride layers grown by reactive magnetron sputtering*. Grégory Abadias, Chen-Hui Li, Laurent Belliard, Nicolas Greneche, Qing Miao Hu, Philippe Djemia, under review Acta Materiala (2019).

-*Temperature dependent elastic constants of "soft" metal Al from first principles theory*. Zhang Haijun; Li Chenhui; Djemia Philippe; Yang Rui; Hu Qing-Miao, under review Journal of Materials Science & Technology (2019).

-*Defects influence on the structural and elastic properties of epitaxial MgO/TiZrN films.* C. H. Li, P. Djemia, L. Belliard, Q.M. Hu, F. Wang, F. Tasnádi, M. Odén, G. Abadias, To be submitted to Surface and Coatings Technology…. (2019).

TABLE OF CONTENTS

LIST OF TABLES

LIST OF FIGURES

LIST OF SYMBOLS AND ABBREVIATIONS

APW	Augmented plane wave
BLS	Brillouin light scattering
BPW	Back-extrapolated partial wave
CPA	Coherent potential approximation
DFT	Density functional theory
DMA	Dynamical mechanical analysis
DSC	Differential scanning calorimetry
EBSD	Electron backscatter diffraction
EDS	Energy dispersive spectroscopy
EMTO	Exact Muffin-Tin Orbitals method
HEAs	High entropy alloys
HEANs	High entropy alloys nitrides
IMR	Institute of Metal research, Shenyang, China
INSP	Institut des Nanosciences de Paris
LSPM	Laboratoire des Sciences des Procédés et des Matériaux
MCAs	Multicomponent alloys
MC2	Multi-scale computational design of novel hard nanostructured coating
PAW	Projector-augmented-wave method
PLU	Picosecond laser ultrasonic
PP	Pseudopotentials
PW	Partial wave
RUS	Resonant ultrasound spectroscopy
SCCM	Standard cubic centimeters per minute
SEM	Scanning electron microscope
SQS	Special quasirandom structures
SSW	Screened spherical waves
TMN	transition metals nitrides
VASP	Vienna atomistic simulation package
VSM	Vibrating sample magnetometer
WDS	Wavelength dispersive spectroscopy
XRD	X-ray diffraction
XRR	X-ray reflectivity

LONG SUMMARY

Kinetically limited low temperature physical-vapor-deposited thin films usually exhibit 2 issues 1) unavoidable lattice defects such as interstitials or vacancies due to the non-equilibrium process, 2) microstructural characters including varying grain shapes (V-shape columns, spheroids) and sizes, pronounced crystallographic textures, porosity, residual stress depending on deposition parameters and inherent (oxygen) impurities as well as thickness of films. Such structural and microstructural issues can influence many properties of a material, e.g. the formation energy, phase, lattice parameter, mass density, elasticity, hardness, etc. The purpose of this work is to study structural and mechanical (elastic) properties of several kinds of deposited thin films (mainly nitrides) with such issues by various experimental techniques together with computational calculations based on density functional theory (DFT). Well-defined ground state properties (F, a, ρ) and single-crystal elastic constants C_{ij} were calculated accurately from first-principles within DFT. The calculations were done either with the supercell method considering different defects and their concentrations as well as ordering/disordering by VASP, or with coherent potential approximations (CPA) implemented in EMTO, for a systematic comparison to experiments. We used non-conventional but state-of-the-art optoacoustic experiments, namely, the Brillouin light scattering (BLS) and the picosecond laser ultrasonic (PLU) techniques to accurately and selectively measure shear (V_T) and longitudinal (V_L) sound velocities in various single crystalline or polycrystalline thin films, and their vertical shear ($C_{44} = \rho V^2_T$) and longitudinal ($C_{33} = \rho V^2_L$) elastic constants. Complementarily, we performed nanoindentation tests to evaluate hardness and compare the indentation test

elastic modulus E_{IT} to the one deduced from the combination of BLS and PLU. Attempts were also made to link elasticity to plasticity by simple criteria such as the shear modulus ($G = C_{44}$) over bulk modulus (B) Pugh's ratio $k = G/B$ and Cauchy pressure $p = C_{12}$-C_{44}, from which brittleness or ductile behavior and bonds directionality can be assessed.

Metallic and nitride thin films materials were deposited by DC non-reactive and reactive magnetron sputtering in *Ar* and Ar/N_2 plasma discharge, respectively. The crystal structure, lattice parameter, texture, mass density, porosity and film thickness were carefully characterized by x-ray diffraction (XRD) together with x-ray reflectivity (XRR). Mechanical profilometry was also used to measure the thickness. Chemical analysis was done by EDS in combination with WDS which was specifically used to determine contents of the light elements (*N & O*).

First, we considered available epitaxial single crystal early transition metal nitrides *(TiN, ZrN, TiZrN, TaN)* close to stoichiometry elaborated by Pr. G. Abadias (Institut PPRIME, @Poitiers University) on *MgO* susbtrates and polycrystalline multicomponent metallic alloys $(Al_x(CoCrCuFeNi)_{1-x}$ *and* $Nb_x(CoCrCuFeNi)_{1-x}$, $0 \leq x \leq 25$ *at. %*) elaborated by Dr. B. Braeckman and Pr. D. Depla (DRAFT group @Gent University) on silicon substrates. Note in the latter case, FCC→BCC and BCC→amorphous phase transitions were induced by Al and Nb chemical alloying to the base FCC *CoCrCuFeNi* HEA, respectively. Specifically, *Al* addition leads to porous films, which further increased the complexity of the analysis.

Epitaxial films permit a direct comparison of measured elastic properties to the DFT predicted ones. For "simple" epitaxial nitrides films with *Ti* and *Zr* metals from group

IVB (four common valence electrons *[Ar] $3d^3$ 4s*), period IV (first period with *d*-block elements) and period V (same general structure as IV), respectively, metal vacancies defects are energetically favored and showed a moderate influence on the structural and elastic properties when compared to our DFT predictions. In case of ternary alloys $Ti_xZr_{1-x}N$, we introduced a three-dimensional representation of the energies of removing *Ti* and *Zr* atoms as a function of numbers of *Zr* atoms in the first (n_{1st}) and second (n_{2nd}) neighboring shells and predicted the metal atom vacancy formation energy $\Delta E_{Ti}^{vac}(n_{1st}, n_{2nd})$ and $\Delta E_{Ti}^{vac}(n_{1st}, n_{2nd})$ in arbitrary local chemical environments. More stable *Ti* and *Zr* mono-vacancy having lower energy are expected for the rich-*Zr* solid solution at a position where the 1st-shell and the *2nd*-shell are rich in *Zr* and *Ti*, respectively. The lattice parameter decreased more in the presence of metal vacancies than for nitrogen ones. Single crystal C_{44} elastic constant is increasing while C_{11} is decreasing with both metal and nitrogen vacancy concentration increasing, enabling a better comparison to experiments. Similar tendencies were observed in the case of cubic *TaN* from group VB (five common valence electrons, *[Xe] $4f^{14}$ $5d^3$ $6s^2$*) and period VI (first period with f-block elements). Metal and nitrogen vacancies or Schottky defects are energetically favored, inducing a few percent difference for the lattice parameter while *a huge difference* of C_{11} (-27 %) and C_{44} (+180 %) elastic constants between the theoretical defects-free and 10 % defected crystal ones. By comparing, we concluded that our *TaN* (nearly stoichiometric) should contain ~10 % Schottky defects (to ensure stoichiometry) in order to obtain a satisfactory agreement with the measured sound velocities (V_L and V_T) and single crystal elastic constants *(C_{11}, C_{12} and C_{44})*.

Available $(CoCrCuFeNi)_{1-x}(Nb_x, Al_x)$ thin films were deposited by magnetron sputtering at Ghent University using compacted powders targets, in the DRAFT group of Prof. D. Depla during the PhD work of B. Braeckman. By varying the *Al/Nb* concentration, phase transitions were observed as well as crystallographic texture changes. By adding *Al*, an FCC to BCC phase transition took place at ~20 at. % *Al* addition, while for Nb alloying, an FCC to amorphous transition happened at ~15 at. %. Besides the occurrence of phase transitions, in the case of *Al* alloying, films were meanwhile porous which also plays a role in material properties. DFT calculations were not only able to capture all phase transitions from energetics, but also provided good predictions of structural (lattice parameter and mass density) and elastic properties modifications as a function of *Al/Nb* concentration. Single crystal elastic properties were simulated and used as input parameters in a micro-mechanical self-consistent model which takes into account the crystallographic textures and porosity of the films and produces effective elastic constants to compare to our optoacoustic measurements. EMTO-CPA was used due to its superior efficiency (accuracy and computing time) for calculating multicomponent metallic alloys. As a comparison, we performed more accurate VASP calculations combined with SQS to evaluate the influence of local lattice distortion, or atomic relaxation which is absent in EMTO calculations. VASP AIMD calculations were carried out for the amorphous phase at the highest concentration ~20 at. % *Nb* and ~25 at. % *Al*.

Prior to deal with MCA films, we characterized thermal, electrical, structural and mechanical properties at different scales, of *CoCrCuFeNi* bulk HEA elaborated by arc-melting, as a reference for later comparison to films properties. Several samples of 1" and 2" in diameter, and 3 mm thick from the same ingot were synthesized by Pr. L-M Dong

and co-workers at Institute of Metal Research (Shenyang, China). The samples were used as targets for later deposition of our films in order to compare to those previously elaborated films from a composite target made of compacted powders. Ab-initio simulations (EMTO-CPA and VASP-SQS) of structural and elastic properties were conducted on this CoCrCuFeNi base HEA, accounting for FM or PM magnetic state. Note that, experimentally, we identified a PM state from vibrating sample magnetometer measurements (VSM) at room temperature (20°C) for the bulk and films deposited on silicon while a FM state for films deposited on Kapton. Nevertheless, we found only a little influence of the magnetic state on the lattice parameter and elastic constants, while a systematic stiffening of elastic constants is provided by EMTO-CPA in comparison with VASP-SQS.

Secondly, more complex multicomponent metal nitrides *CoCr(Cu,Mn)FeNiN*$_x$ films with nitrogen concentration as high as 40 at. % were also elaborated with R. Dedoncker and Pr. D. Depla (@Gent University) through reactive magnetron sputtering using the solid *CoCrCuFeNi* target and a composite *CoCrMnFeNi*. The depositions were done in a newly designed high vacuum chamber in order to control the influence of oxygen impurities. Films with different nitrogen content were deposited by varying the nitrogen partial pressure $R_N = p_{N2}/(p_{N2}+p_{Ar})$. We investigated the influence of replacing *Cu* by *Mn* on forming high entropy alloy nitrides and their properties, and how nitrogen filled the empty interstitial sites (octahedral or tetrahedral) in the initial FCC lattice, and finally transformed to a rocksalt B1-structure. A modification of texture from (111) to (001) was observed at the early stage of nitrogen insertion. Lattice parameter and mass density were continuously increasing and decreasing, respectively. A deviation between measured and

DFT calculated lattice parameter was observed above ~10 at. % *N* and was correlated with a jump of C_{44}, which is increasing and decreasing as a function of nitrogen content, for *CoCrCuFeNi*-N_x and *CoCrMnFeNi*-N_x, respectively, as measured by BLS.

From DFT calculations, with such techniques as VASP-AIMD, SQS and the EMTO-CPA approach to simulate randomness of chemical elements and point-defects, we were able to evaluate metal vacancy, nitrogen vacancy and interstitials, and *(Al, Nb, N)* alloying effects on formation energy, structural, phase transitions and elastic properties for all materials. A good agreement can be obtained by considering the existence of point defects (vacancy and interstitial) and microstructural parameters (texture and porosity) in our theoretical self-consistent calculations. We emphasis the strong influence of both metal and nitrogen vacancies on the elastic properties of *TaN* films (+180 % for C_{44}) with opposite trend for C_{44} and C_{33}, underlying in this thesis, and also the efficiency of optoacoustic techniques as performant tools to study thin film elasticity and improve the presently scarce data.

A final case of growth of multicomponent metallic alloys, i.e., the FCC *CoCrCuFeNi* polycrystalline films elaborated on a flexible Kapton® substrate was considered at the end of this thesis, taking the opportunity of recent developments of micro-tensile tests coupled to a large view-field Keyence confocal microscope. It enabled us performing tensile tests, observing the surface changes (cracks and buckles on-set appearances, cracks density, morphology of buckles) as a function of the deformation (up to 15 %) and film's thicknesses (20 - 400 nm). We derived their fracture toughness K_{Ic}, increasing from ~5 to 22 MPa.$\sqrt{m}$ with the grain size (20 - 50 nm), from the analysis of

the modification of the crack density *vs.* the film thickness. The model took into account the variation of the measured residual stress *vs.* the film thickness. *CoCrCuFeNi* is found more brittle than its bulk counterpart, suggesting a significant role of its specific nanostructure.

Keywords: First-principles, metallic and nitride thin films, multicomponent alloys, point defects, porosity, Brillouin light scattering, Picosecond laser ultrasonic, nanoindentation, elastic constants, tensile tests, flexible substrate, fracture toughness, buckles, AIMD, VASP-SQS, EMTO-CPA

CHAPTER 1. INTRODUCTION, STATE-OF-THE-ART AND OBJECTIVES

1.1 Introduction and organization of the manuscript

In this thesis, we aimed to study structural and mechanical properties of transition metals nitrides (TMN) films with increasing complexity, both experimentally and theoretically, starting from "simple" *epitaxial* binary early transition metals nitrides (*TiN*, *ZrN* and *TaN*) and their pseudo-binary solid solutions ($Ti_xZr_{1-x}N_y$). *This initial stage* was motivated by a running Material-Eranet project between France (Pr. G. Abadias, PPRIME Institute and Pr. Ph. Djemia, LSPM), Luxemburg (Dr. D. Dudday, LIST) and Sweden (Pr. M. Oden, Dr. F. Tasnadi, Linköping university and Dr. M. Johansson, Seco Tools company), named MC2 (Multi-scale computational design of novel hard nanostructured coatings). The goal of the MC2 (2013-2017) project was a systematic development of new fundamental (basic) and technological (applied) concepts for the design of novel hard multi-component nitride coatings. It suggested a research strategy that goes beyond the standard combinatorial investigation by implementing a property (elasticity, hardness, toughness, wear-resistance) oriented multi-scale data mining and computational driven design of coatings. We were supposed to contribute to the *theoretical ab initio* study of *point-defects* influences on structural and elastic properties (C_{ij}) of nitrides coatings. The initiative also entails C_{ij} data-mining from measurements on many binary epitaxial films (*TiN, ZrN, CrN, VN, NbN, TaN and MoN*) and ternary or quaternary polycrystalline ones (*TiZrN, TaZrN, TiTaN, TiAlN and TiAlZrN*), provided by the picosecond laser ultrasonic

(PLU) and Brillouin light scattering (BLS) techniques [1-4]. Hence, many experimental data belonging to either epitaxial or polycrystalline films were available at the beginning of this thesis (Nov. 2015), but with several issues when they were compared to *ab-initio* computational ones of defects-free structures.

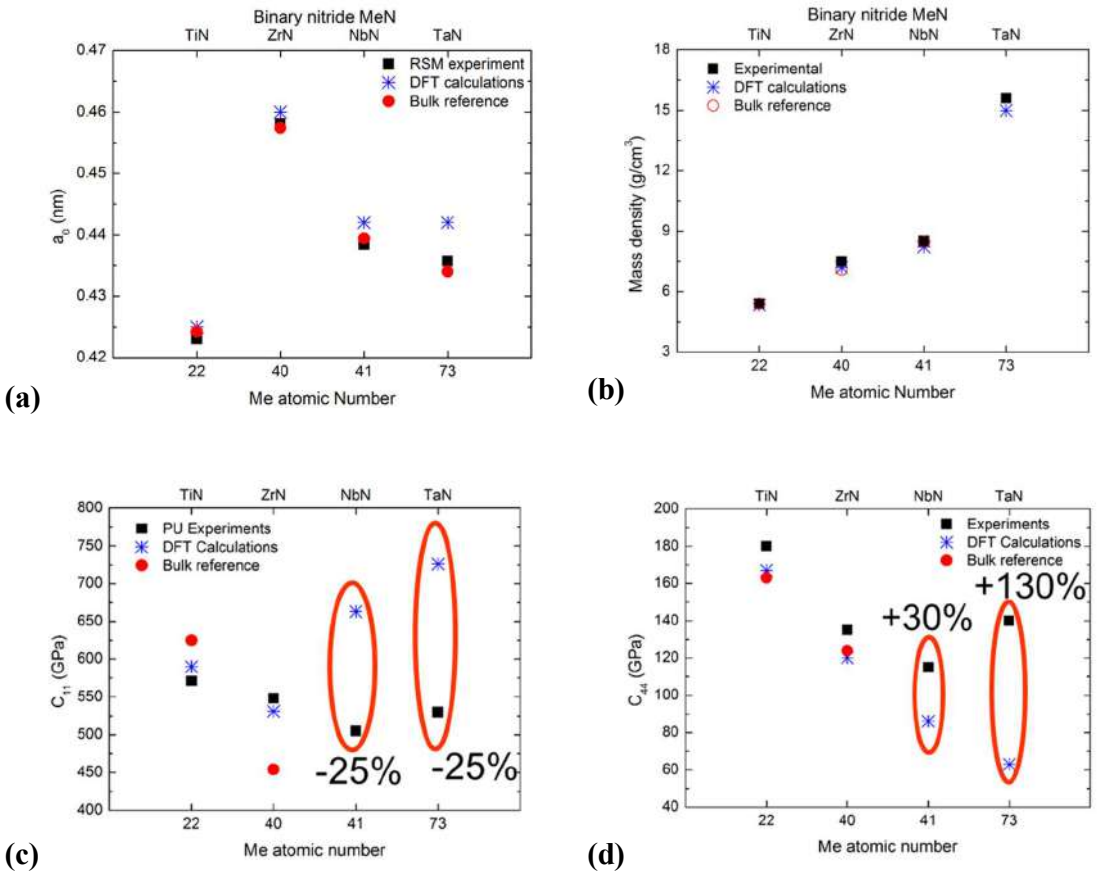

Figure 1.1 – Initial comparison between experimental and computational DFT of defect-free *TiN, ZrN, NbN and TaN* epitaxial films (a) Lattice parameter form XRD, (b) mass density from XRR, (c) c_{11} elastic constant from PLU, (d) c_{44} elastic constant from BLS.

The goal is to provide explanations for the observed differences on the lattice parameter, the mass density and the elastic constants (see **Figure 1.1**), dealing with real lattice having defects.

In the continuity of this project, *the final stage* of the thesis was the investigation of a new class of *polycrystalline* films of materials with a distinct design strategy, made of multicomponent metallic alloys (MCAs) based on the **two** famous metallic high entropy alloys (HEAs): (*i*) ***CoCrCuFeNi*** and (*ii*) ***CoCrMnFeNi***. Different from conventional alloys that are typically designed with one or two principal elements, MCAs are composed of more than five principal elements, with maximum entropy for equiatomic concentration of elements forming HEAs. First, we studied the bulk polycrystalline *CoCrCuFeNi* elaborated by arc-melting by our Chinese colleagues at the Institute of Metals Research (Pr. L-M Dong and Pr. Q-M. Hu, Shenyang) to get some reference bulk properties and later comparing to films properties. Another challenge was to probe mechanical and thermal properties of individual grain that could be directly compared to *ab initio* simulations. This bulk material will be used also as a solid HEA target for thin films deposition in addition to composite powder targets[5]. Influence of the addition of a 6th element on the formation of *(Nb, Al)* substitutional alloys or interstitial alloys films (nitrogen) and their properties, is investigated both experimentally and computationally by first-principles methods. This study was possible thanks to a newly established collaboration with Pr. D. Depla (DRAFT group, Gent University) who is currently designing metallic [5-9], nitrides [10] and oxides [11] HEAs films using DC magnetron sputtering of composite compacted powders targets. Two Belgium PhD students were particularly involved in this story: R. Dedoncker and Dr. B. Braeckman. This common interest was of great support to this thesis, sharing elaboration of samples and many results on their structural and physical properties.

Thin film materials obtained from PVD process may grow on different substrates (silicon, *W-C* steel, flexible polymers, sapphire, magnesium oxide, silicon oxide, ..)

depending on the applications, and usually exhibit imperfections due to limited kinetics, i.e., most commonly, large amount of point defects like interstitials or vacancies with deviation from stoichiometry, varying grain shapes (V-shape column or spheroid) and size (nm-µm) or amorphous (no grains), pronounced crystallographic textures as well as porosity and some inherent oxygen impurities. The applications range from tribological thick coatings for wear and cutting tools industry (Sandvik & Seco Tools), to thinner optical films for glass windows industry (St Gobain), ophthalmic optics (Essilor), flexible microelectronic (Samsung). In all cases, the goal is a homogeneous coating with defined stoichiometry, controlled microstructure and internal stresses. For such applications, knowledge of effective elastic properties of poly(nano)crystalline or amorphous materials is mandatory but most of time only partially identified.

Lattice defects and microstructures can influence many material properties including the ground state energy F (phase stability), structural (lattice parameter a, mass density ρ), mechanical (hardness, strength, fracture toughness, dislocation mobility, residual stresses, elasticity, etc.), but also functional properties (electrical and thermal conductivity, magnetism, etc.) by very different amounts. Specifically, we focus on ground state properties (F, a, ρ) and single-crystal elastic constants C_{ij} are well defined and can be calculated accurately from first principles within the electronic density functional theory (DFT), using in this thesis work two well-known programs: the Vienna atomistic simulation package (VASP) [12, 13] and the Exact Muffin-Tin Orbitals (EMTO) method [14, 15]. In case of random solid solutions, VASP is used in combination to the special quasi-random structures (SQS) to build supercells [16] while EMTO is employing the coherent potential approximation (CPA) [17, 18] to mimic efficiently the randomness of

atoms and defects positions. In the specific case of amorphous phase, ab initio molecular dynamics (AIMD) can be employed [19-22], but moderately in our case as it is highly computational demanding and our computational resources limited (MAGI cluster with 50 nodes, 2000 CPU). Elasticity can be used to correlate to many other material properties, for example, hardness[23], plasticity, by simple relations such as the shear modulus (G) over bulk modulus (B) Pugh's ratio $k = G/B$, from which brittleness or ductile behavior can be assessed [24]. Cauchy pressure $p = C_{12}$- C_{44} can also help to identify bonds type, covalent if $p < 0$ and metallic if $p > 0$, following Pettifor criterion [25].

Beyond the chemical and structural characterization techniques of our films, we used non-conventional but state-of-the-art optoacoustic experiments [4], namely, the Brillouin light scattering (BLS) and the picosecond laser ultrasonic techniques (PLU) to measure shear (V_T) and longitudinal (V_L) sound velocities in various single crystalline or polycrystalline thin films, and their out-of-plane shear ($C_{44} = \rho V^2_T$) and longitudinal ($C_{33} = \rho V^2_L$) elastic constants. Complementary, we performed more widely employed nanoindentation tests to evaluate hardness and compare the indentation test elastic modulus E_{IT} to the one derived from BLS and PLU.

Our motivations are the study of structural and elastic properties and their simultaneous comparisons to first-principles DFT-based simulations, of "simple" and complex alloys: modifying the shape/size (thin film *vs*. bulk materials), deposition parameters, and solid target vs. powder target. We can compare to existing data of the materials (bulk and films) from the literature, as well as providing some new ones. The

physical trends related to the chemistry, phase stability, electronic structures, atomic size mismatch, defects concentration, and porosity can be captured.

There are very scarce elastic properties of high entropy alloys in the literature, most of them being devoted to the bulk materials. Some are even found to be contradictory with ab initio simulations. Only a few experimental techniques are well adapted to the study of elastic properties of thin films and coatings, offering good enough evaluations for comparison with density functional theory ones for which accuracy better than 10 % is expected. We can more easily deal with the transformation from micro-scale (a single grain) properties to macro-scale (polycrystalline) ones using a pertinent micromechanical model, if intra-granular or single crystal properties of a single phase are known from experiments and/or DFT simulations. This is the case of single crystal elastic constants and effective averages for polycrystalline defect-free and defected materials, taking into account preferential or isotropic crystallographic orientations and porosity. A simple micromechanical model such as Hill approach [26] can be used for non-porous materials, while a more complex one based on effective medium elastic constants averaging [27] is mandatory in the case of porous ones.

The manuscript is organised as follow: in this *chapter 1*, we present the current state-of-the-art of transition metal nitride films and multicomponent alloys.

In *chapter 2*, we begin with an introduction to the methods that will be used for energetics, structural and elastic properties calculations. The methods include density functional theory, ab initio molecular dynamics, design of a supercell that mimics the randomness of atomic positions and a micro-mechanical model to link single crystalline to polycrystalline elastic properties. Then, we recall the fundamentals of the characterization techniques, the chemical and structural properties of the studied samples.

First results and discussion on elastic properties from "simple" binary *(TiN, ZrN and TaN)* and pseudo-ternary *(TiN-ZrN)* epitaxial films are provided in *chapter 3*.

Before the investigation of the complex multicomponent nitrides, we discuss in *chapter 4* and *chapter 5* the results on the mechanical properties of bulk *CoCrCuFeNi* and $(CoCrCuFeNi)_{1-x}(Nb_x, Al_x)$ thin films. A particular effort is done to characterize intra-granular properties of the polycrystalline bulk material to provide equivalent single crystalline information and the influence of magnetic ordering is discussed in case of DFT simulations for the bulk *CoCrCuFeNi.* A first comparison between EMTO-CPA and VASP-SQS methods for high entropy alloys is done for $(CoCrCuFeNi)_{1-x}(Nb_x, Al_x)$, *with the purpose* to evaluate the atomic relaxation effects on energetics and elastic constants.

Chapter 6 is dedicated to the comparison of structural and mechanical properties from DFT (phase stability, structural, sound velocities and elastic properties) and experiments (XRD, XRR, BLS, PLU and nanoindentation) of $CoCr(Cu, Mn)FeNiN_x$ nitride films.

As an illustration of some of the perspectives, in *chapter 7*, we studied the fracture toughness (K_{IC}) of the films with an additional experiment: in-situ coupled confocal microscopy and tensile tests of *CoCrCuFeNi* metallic films deposited on Kapton® substrates with varying thicknesses, hence their brittleness/ductility assessment. This last technique could help us in the future, to correlate the elastic properties of the films to their plastic properties.

The *conclusions* and more perspectives are given in *chapter 8*.

There is one *appendix* that summarized the ordered structures of Ta_xN_y and the design of defected supercells, as a supplement to *chapter 3*.

1.2 Current state-of the-art of nitride coatings and films

1.2.1 From binary to quaternary alloys

Hard TMN coatings define a class of materials where fundamental microscopic understanding combined with operational testing has become a fruitful approach in improving industrial efficiency. Computational simulations [20] could predict general design routes to improve the thermal stability of hard coatings, for example *TiAlN* alloyed with *CrN* [28]. However, a challenging task is to elucidate the stress state [29, 30], toughness [31] and related elastic behaviour of hard ceramic coatings [32], as they are key indicators in wear performance of cutting tools [33, 34]. Many MeN_x thin films, where *Me* is an early transition metal belonging to group 4 to group 6, crystallize in their cubic, B1-rocksalt structure (space group of $Fm\bar{3}m$ symmetry) and exist in a large compositional field, covering both under- and over-stoichiometric compositions. As far as the mechanical properties are concerned, MeN_x thin films of group 5 (*VN, NbN, TaN*) and group 6 (*CrN, MoN and WN*) have recently being the subject of active investigations because they offer improved ductility compared to inherently brittle group 4 *TiN* or *ZrN* coatings, while retaining a high hardness [31, 35-41]. Thus, alloy design strategies based on the formation of metastable, cubic multicomponent *TMN* solid solutions by incorporation of group-5 or group-6 metals, or tailoring of interfaces in superlattices, have been proposed for toughness enhancement [4, 31, 42-50]. Such toughening has been predicted to be originating from an increase in valence electron concentration [31, 36, 51], and was confirmed experimentally in a few systems either from a direct observation of nanoindentation imprints [38, 52],

improvement in the hardness over Young's modulus *(H/E)* ratio [37, 47, 49] or assessment of their elastic constants [4, 31, 45].

Of particular interest is the cubic *δ-TaN* compound, which exhibits the highest hardness (30-33 GPa) among *TMN* binaries [53-55]. However, there exists a large discrepancy in the literature regarding phase stability, lattice parameters and mechanical properties of polycrystalline TaN_x thin films. For instance, published values of the lattice parameter range from 4.33 to 4.42 Å depending certainly on the residual stress and defects concentration. We reported in Ref. [2], shear modulus values ranging from 95 to 257 GPa for sputter-deposited TaN films depending on the Ar working pressure. A large spread in hardness values, from 25 to 42 GPa, is also noticed for polycrystalline TaN_x layers [53]. This is likely related to the fact that the Ta-N system is inherently complex as exhibiting a large variety of stable and metastable phases [56, 57]. Therefore, the mechanical behavior of polycrystalline TaN_x films is anticipated to be extremely sensitive to the growth conditions which affect chemical and phase compositions, as well as microstructures. Besides, the elastic properties are expected to be crystal-orientation and phase dependent, based on *ab initio* calculations of single-crystal elastic constants of *δ–TaN* compound [2, 35, 45, 51] and other non-cubic *TaN* phases [58]. This motivates the need for further investigations of the structure and elastic properties of well-characterized single-phase *TaN* layers.

The *TaN* compound (1:1 stoichiometry) exists in three stable forms, depending on temperature and pressure conditions [56, 59]. The hexagonal *ε*-phase (space group of $P\bar{6}2m$) is found to be most stable at room temperature [60], closely followed by the θ-phase

(space group of $P\bar{6}m2$, *WC-type*) observed at high pressure [61]. The *δ-TaN* compound with cubic symmetry (space group of $Fm\bar{3}m$, *NaCl*-type) is typically stabilized at high temperatures. This cubic phase is highly anisotropic (Zener anisotropy ratio ~0.20 [2, 35]) and can support a large density of vacancies up to 20%. Using DFT Kim *et al*. [59] calculated the electronic and structural properties of these three stoichiometric tantalum mononitride phases. Interestingly, they first reported that the cubic *δ-TaN* phase undergoes a spontaneous distortion into a tetragonal structure (*δ'-TaN*, space group of *P4/nmm*), with a reduced metal interatomic distance, d_{Ta-Ta}, by as much as 0.155 Å in the plane normal to the *c*-axis (*ab-plane*). This was attributed to a Jahn–Teller type distortion that lifts degeneracy at the Fermi level. The electronic structures indicate that the largest carrier density, hence the highest electronic conductivity, is expected for *δ-TaN*. Very recent simulations and experimental studies of binary nitrides have focused on the stability and the influence of point-defects on their structural and mechanical properties resulting to a deviation from stoichiometry. In Ref. [62], the authors did a very detailed DFT investigation focusing on the role of metal and nitrogen vacancies with different level of ordering/disordering, on the modification of the lattice parameter in *TaN* and *MoN* cubic structures. They showed that the ordering/disordering of point-defects has a significant influence in *MoN* but is very limited in case TaN. Furthermore, they found again the new *TaN* tetragonal phase (*P4/nmm, #129*) having lower formation energy than its cubic counterpart and dynamically stable [63]. Balasubramanian *et al*. [64] demonstrated that both under-stoichiometric ($x < 1$) and over-stoichiometric ($x > 1$) TaN_x compositions are due to relatively low vacancy formation energies of ~0 and −3.4 eV/defect for *N* and *Ta*, respectively, indicating that both metal and nitrogen vacancies become thermodynamically

stable at zero temperature. On the other hand, nitrogen and metal interstitials in tetragonal and 111- or 110-split configurations are unstable, as well as all antisite defects which possess high positive formation energies and are unlikely to form for groups 3 to 6 nitrides. Koutná *et al*. [62, 63] also predicted that sub-stoichiometric δ-TaN_x structures are more stable, with $Ta_{0.78}N$ (~11% *Ta* vacancies) having the lowest formation energy of –2.1 eV/(*f.u.*). The formation energy can be considerably decreased even when keeping the 1:1 metal-to-nitrogen stoichiometry, by introducing Schottky (metal + nitrogen vacancy pair) defects. Such a configuration is practically undetectable by conventional tools used for chemical analysis. Structures containing Schottky defects yield smaller lattice constant [62] and hence may contribute to explain the relatively large scatter of experimental data. Additionally, the stability of each defect type in MeN_x compounds is predicted to depend on the thermodynamic conditions (N_2 partial pressure and deposition temperature) [64] as other gas [65] and can be merely neglected for solid elements.

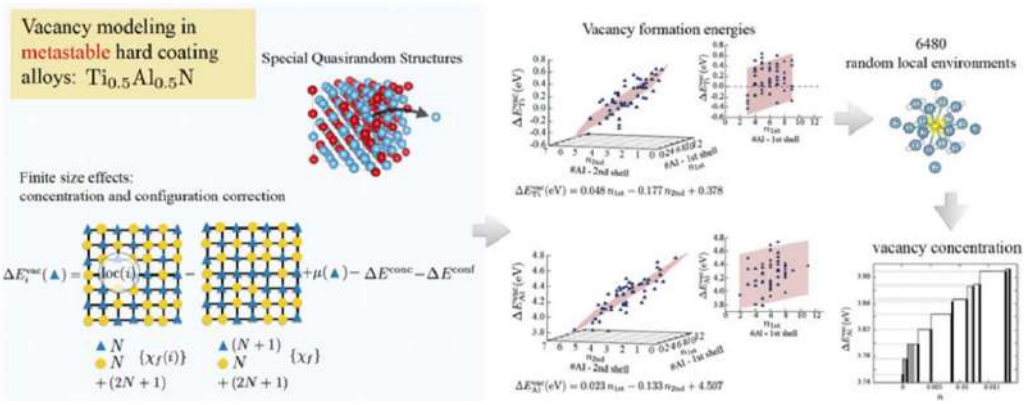

Figure 1.2 – Schematic of the methodology employed in Ref. [66] for modelling of metal vacancy in *$Ti_{0.5}Al_{0.5}N$* ternary alloy.

The situation is more complex in case ternary or higher *TMN* alloys (see **Figure 1.2**). Non-equilibrium vacancy formation energies in ternary solid solution $Ti_{0.5}Al_{0.5}N$ have

been computationally investigated in Ref. [66]. Tasnadi *et al.* proposed a computational technique to study non-equilibrium vacancies in metastable alloys. In contrast to equilibrium materials, calculation of the energy of removing an alloying atom requires a finite size configurational correction and the vacancy formation energy in metastable alloys is defined up to an arbitrary constant. They argue that in non-equilibrium alloys no statistical considerations are required and there is a distribution of the vacancy formation energy with large variation. Using cluster expansion, they demonstrated the major importance of the first two metallic coordination shells. They introduced a three-dimensional representation of the energies of removing *Ti* and *Al* atoms as a function of number of *Al* atoms (n_{1st}, n_{2nd}) in the two first neighboring shells and predicted the metal atom vacancy formation energy in arbitrary local chemical environments. Neglecting the interactions between the vacant sites and assuming their simultaneous occurrence, it was extracted information about the energy cost of a vacancy concentration in metastable alloys. Conclusion was that in metastable disordered alloys, vacancies should occur in local environments that correspond to the lowest formation energies rather than distributed statistically. This interesting methodology will be applied to our *TMN* ternary alloy case for three compositions $Ti_{0.25}Zr_{0.75}N$, $Ti_{0.5}Zr_{0.5}N$ *and* $Ti_{0.75}Zr_{0.25}N$ for discussion of metals and nitrogen vacancy stability and their influence on elastic properties. In our case, due to a limited available computational resources (we are sharing MAGI cluster of the university: ~ 50 nodes, 2000 cores), a lower size of SQS supercell is used (64 atoms) comparing to their supercell (208 atoms) that may induce a non-negligible chemical concentration correction after a monovacancy appearance.

From the literature survey outlined above, it is clear that point defects decisively affect the compositional variations and structural parameters in many B1-rocksalt structure MeN_x and other ternary *TMN* compounds, especially for group 4-6 nitrides. However, their impact on the elastic properties remains to date mostly unexplored in detail. In this work, we contribute to address this issue by combining experimental assessment and DFT-based calculations of the elastic constants of epitaxial cubic binary TaN_x, TiN_x, ZrN_x and ternary $Ti_{1-x}Zr_xN_y$ solid solution layers with different crystallographic orientations. We systematically study the influence of vacancies on the phase stability, the structural, the sound velocities and the elastic properties of various Me_yN_x compounds over a wide range of defect concentration (up to $x,y=0.40$). We specifically discuss the case of Schottky pair as a defect structure consisting of one nitrogen and one metal vacancy in case *TaN*. Its formation or annihilation does not affect the overall composition and should be considered because our produced *TaN* films were found to be nearly stoichiometric but with high electrical resistivity revealing the existence of defects.

Computational treatment of elastic properties of disordered solid solutions for coatings has been developed this last decade [20], with modelling elasticity of disordered alloys with distinct short- and long-range configuration (clustering vs. ordering) [67, 68]. Several binary MeN_x systems *(Me = Ti, Nb, V, W, Mo, Hf)* have been investigated [69-71]. The advanced Brillouin light scattering (BLS) technique has been successfully applied to determine elastic properties of several *TMN* alloys [1, 2, 4, 71-73] with simultaneous DFT simulations. In some of these works as in many others, various numerical averaging methods [26, 27, 68] could be applied to describe the effective elastic properties of the polycrystalline material. Several studies [38, 41, 54, 55, 69, 71, 73-77] were dealing with

epitaxial films avoiding the influence of crystallographic orientations distribution on the resulting averaged elastic properties, being strongly influenced by elastic anisotropy defined by the Zener ratio $A = 2c_{44} / (c_{11} - c_{12})$ for cubic symmetry. Only two similar approach to our, were conducted using PLU and BLS, measuring sound velocities of a longitudinal bulk wave and of the Rayleigh surface acoustic wave on *VN* films grew on *MgO* substrates [55] with (001), (011) and (111) orientations and on $MoN_x(001)/MgO(001)$ films [71]. The set of $(C_{11}, C_{12}$ *and* $C_{44})$ three independent single crystal elastic constants of cubic VN_x was successfully measured and (C_{11}, C_{44}) in case MoN_x.

The complex relationship between microstructure (spinodal decomposition), hardness and wear performance is uncovered and thus not yet utilized. The age hardening and strain evolution of *TiAlN* during spinodal decomposition have been investigated using both advanced electron microscopy [78] and atom probe tomography [79]. In *TiAlN/TiN* multilayers, the beneficial role of interfaces [34] on thermal decomposition and related machining performance has been recently evidenced, driving further studies on microstructural design-based approaches. Complimentary mesoscopic phase-field simulations [80, 81] have underlined the relation between microstructure/hardness and elasticity [82]. This clearly indicates the possibility to improve the wear performance of cutting tools by engineering elasticity. The high cutting temperature (high industrial speed, efficiency, more cutting) is expected to change drastically the elasticity of coatings. Extending the current-state-of-art computational methods with the inclusion of temperature using ab-initio molecular dynamics (AIMD) calculations [83, 84] is an unambiguous challenge for the design of next generation of hard coatings. This out the scope of this thesis.

We first go through the research of elastic properties on simple transition metal nitrides: binary *TaN, TiN, ZrN and TiZrN* ternary and second, on complex metallic alloys and their nitrides, from the literature and our own films' growth, including all the above aspects. In case of bulk cast or sintered *CoCrCuFeNi*, the influence of adding *Al or Nb* has been investigated in Refs. [85, 86] while nitrogen alloying in Ref. [87].

1.3 Increasing the number of elements in the metallic alloys: MCAs and HEAs

This specific work on multicomponent alloys (MCAs) is related to "Physical Metallurgy", which seems important to recall its meanings from Ref. [88, 89] and introducing our objectives. ***What is physical metallurgy***? It is a science focusing on the relationships among composition, processing, crystal structure, and microstructure, and physical and mechanical properties [90, 91]. **Figure 1.3** shows the straightforward correlation. Composition and processing determine the structure and microstructure, which in turn determine the properties. The relationships in the first stage are thermodynamics, kinetics, and deformation theory. The relationships in the second stage are solid-state physics, strengthening, toughening, fatigue, creep, wear mechanisms, etc. Therefore, an understanding of physical metallurgy is very helpful to control and improve materials. The progress of physical metallurgy has occurred over 100 years and the underlying principles were thought to have become mature [91]. However, the progress is based on the observations on conventional alloys. As compositions of MCAs are entirely different from that of conventional alloys, physical metallurgy principles might need to be modified or explored. This work will be a contribution to this issue, in particular for the case of *thin films and coatings*, still not well explored.

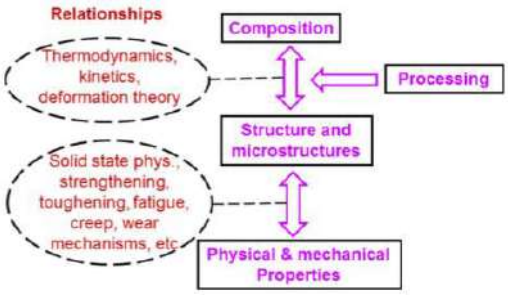

Figure 1.3 – Physical metallurgy scheme in standards metallic alloys, general features.

HEAs (see recent review of Ref. [92] are defined as solid solution alloys containing more than five principal elements in equal or near equal atomic percent. For standard alloys, the solid-solution phase is based on one element, which is called the solvent, and contains other minor elements, which are called the solutes. In HEAs, it is very difficult to differentiate the solvent from the solute because of their equimolar portions. Being different from the conventional alloys, compositions in HEAs are complex due to the near equimolar concentration of each component. Yeh [93] summarized mainly four core effects for HEAs, that are: (***i***) for thermodynamics, they have high-entropy effects; (***ii***) for kinetics, they have sluggish diffusion; (***iii***) for structures, they have severe lattice distortion; and (***iv***) for properties, they have cocktail effects.

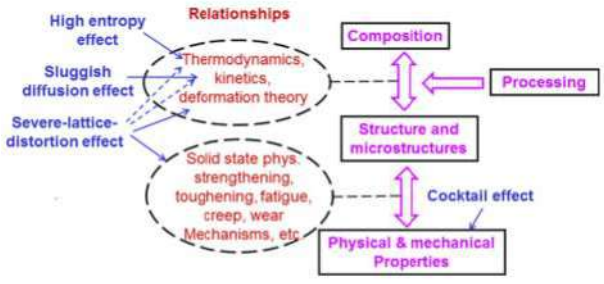

Figure 1.4 – Specific features influenced by four cores effects of HEAs. Figures are from Ref. [89].

Figure 1.4 (from Ref. [89]) shows the influence positions of these four core effects in the scheme of physical metallurgy for HEAs. Then, every aspect of physical metallurgy needs to be

rechecked through the four core effects of HEAs, and the four core effects are helpful in understanding the physical metallurgy of HEAs. It can be expected that when the physical metallurgy from conventional alloys to HEAs is built, the whole understanding of the alloy world becomes realized. We will discuss these four core effects influence separately.

Many researchers reported that the multi-principal-element alloys can only form simple phases of body-centered-cubic (BCC) or face-centered-cubic (FCC) solid solutions, and the number of phases formed is much fewer than the maximum number of phases that the Gibbs phase rule allows [94]. For a systematic discussion of structural stability of simple solid solution HEA, several empirical parameters widely used nowadays have been defined. Most often two or more parameters can be used to build parametric models to better assess their stability. The majority of these parameters are based on the mixing enthalpy (ΔH_{mix}) and atomic size difference *(δ)* concepts [95]. It was originally identified by Yang *et al.* [96] and recently reaffirmed by Gao *et al.* [97] that high entropy solid solution formation is expected for mixing-tendency parameter $\Omega > 1.1$ and atomic size difference $\delta \leq 6\ \%$. Valence electron concentration (*VEC*) concept is also used to evaluate their phase stability type of HEA [97, 98], FCC $(VEC \geq 7.8)$ or BCC $(VEC \leq 6)$. Similarity of the electronic structures of atoms of constitutive elements can also be captured by the Pauling and Allen electronegativity difference [99]. Nonetheless, near-zero mixing enthalpy and small atomic size difference can only be the necessary conditions and not the sufficient ones for a simple HEA solid solution formation, as several incorrect predictions exist and necessitate additional specific phase formation criterions [100]. Another empirical method was recently developed, based on the calculated theoretical elastic-strain energy [101], to predict the phase formation and its stability for complex concentrated

alloys. The "elastic-strain ensergy vs. valence-electron concentration" criterion showed an improved ability to distinguish between single-phase solid solutions, and mixtures of solid solutions and intermetallic phases. Furthermore, Kube *et al.* [102] performed important data mining and revealed that HEAs with increasing atomic size difference prefer BCC structure over FCC. Not suggested by the Hume-Rothery rules [103], this preference originates from the ability of the BCC structure to accommodate a large atomic size difference with lower strain energy penalty which can be practically only realized in High Entropy Alloys.

The superior properties exhibited by HEAs over conventional alloys, along with the huge number of possible compositions that may give new phenomena and functional uses, makes HEAs of great interest not only from a research perspective but also in numerous industrial applications. They exhibit high ultimate tensile strength and reasonable ductility. These excellent properties remain up to 800 K or higher for some refractory HEAs, which makes them ideal candidates for applications at some extreme environmental engineering such as nuclear, turbine, and aerospace industries. They are also potential candidates for high temperature electronic [104], magnetic [105], anticorrosion [106], and wear-resistant [107] applications. Many of these properties arise out of their unique structural feature, a multicomponent solid solution (***cocktail effects, iv core effect***).

For refractories HEAs (*WNbMoTa*, *WNbMoTaV*), microhardness tests show solid-solution strengthening [108]. Their single phase BCC structure remains stable at temperature as high as 1400°C with excellent compression yield strength of 405-477 MPa and good ductility. Senkov also developed notable low density refractory HEAs including *NbTiVZr*, *CrNbTiZr*, and *CrNbTiVZr* having densities 6.3-6.7 g/cm^3. In the temperature

range 298-1273 K, some of the alloys can endure 50% compressive strain without fracturing. In the Cr containing alloys, the ductility at room temperature are somewhat low, while at elevated temperatures the ductility are remarkably high. In addition, the specific strength of *CrNbTiVZr* alloys is far superior to that of superalloys. It is believed that with further modifying the composition and microstructure, this alloy will have better combination of strength and ductility.

Due to ***sluggish diffusion (ii core effect)*** effect and second phase strengthening, HEAs might exhibit high strength at elevated temperatures. For example, $AlCo_{0.1}CrFeMo_{0.5}Ni$ shows a hardness of 347 HV at 1273K, which is higher than that of *Ni*-based superalloys *IN718*/*IN718H* by 220 HV [109]. These alloys also possess a less negative value of softening coefficient at high temperature regime compared to the same superalloys.

In *HfNbTaTiZr* synthesized by arc melting [110, 111], the yield strength was shown to be 929 MPa, with a deformation in compression up to 50% strain without any sign of fracture. Twins and flow lines were observed during deformation. Unlike most BCC alloys and BCC intermetallics phases which are brittle and tend to fracture by cleavage, this alloy provides a good basis for developing ductile high strength BCC alloys by composition tailoring.

Many studies on HEAs are focused on the relationships between microstructure and mechanical properties whereas a few investigations are reported on the ***functional physical properties*** of these alloys. These include behavior of HEAs as diffusion barrier, hydrophobic surface [112], electrical, thermal, magnetic [104], hydrogen storage,

irradiation resistance, and catalytic materials. ***Lattice distortion (iii core effect)*** has effects on the thermal and the electrical properties. The distortion can cause severe scattering of electrons and hence a reduction in electron conductivity. This in turn can decrease the electron contribution of thermal conductivity. The distorted lattice also has an effect on phonon properties, i.e., this distortion scatters more phonons, resulting in a decrease in thermal conductivity. But this kind of transport properties is quite temperature insensitive comparing with conventional alloys. It might be due to the atomic vibration effect that is relatively small comparing to lattice distortion.

Mechanical properties are of the main concern for the HEAs as structural materials. Nevertheless, only a few efforts have been devoted to measure the elastic modulus of HEAs and even less for thin films. The experimental techniques used for bulk materials are resonant ultrasound spectroscopy (RUS) in the case of *CrCoFeMnNi* at cryogenic temperature [113], dynamical mechanical analysis (DMA) as a function of temperature [114], standard pulse echo ultrasound combined with Brillouin light scattering for *TiZrHfTaNb* at room temperature [111]. In recently years, a few *ab initio* calculations based on DFT have been applied to predict the mechanical properties (such as ideal strength and elastic modulus) of HEAs. The main first-principles methods employed was exact muffin-tin orbital (EMTO) [14, 115] in combination with coherent potential approximation (CPA) and the Vienna ab initio simulation package (VASP) in combination with the standard quasirandom structure (SQS) method [16, 116], that facilitates the description of the atomic randomness of the HEAs disordered solid solutions. Niu *et al.* [115] have systematically studied the high entropy alloy *NiFeCrCo* in the range of near-equal atomic concentrations, i.e., 10-40 at.%, by first-principles, finding a good agreement

when comparing both simulations approach. In the *CoCrMnFeNi* case, experimental Young's modulus and shear modulus compared reasonably with estimations based on DFT calculations using EMTO [117] and average elastic properties of the polycrystalline substance. The numerical errors of the bulk modulus, Young's modulus, and shear modulus are no more than 15%. However, such experimental data are still scattered and suffer from large uncertainties if measured from stress-strain slope in the elastic regime of mechanical tests using bulk samples. Indeed, it is particularly surprising that for *CoCrCuFeNi*, simulated Young's modulus of 234 GPa [118] is about four times larger than 55.6 GPa found in compression test experiments [119]. For $CoCrCuFeNiTi_x$ *(x=0.5 and 1.0)* alloys, the Young's modulus is about twice of that from experiment.

The significant scattering of the experimental elastic modulus and the large discrepancy between experimental measurements and simulations indicate that the reliability of either the experimental measurements and/or the theoretical predictions is questionable in some cases. The accuracies of both the experimental measurements and theoretical predictions have to be carefully checked and improved in order to obtain reasonable and reliable elastic modulus. This particular point is important if we aim to relate elastic properties to plastic properties. Also, this can justify studying the same material but *varying the elaboration process* (bulk or films processes), the chemical contents and thus the resulting microstructure.

One core effect for HEAs is that their mechanical properties are adjustable in a wide range upon the changing of compositions and number of constitutive elements (***cocktail effects core iv***). For the conventional one-element principal alloys, the principal element dominates the mechanical properties, e.g., the Young's modulus *E* of *Fe*-based alloys is

about 200 GPa, that of *Ti*-based alloys is approximately 110 GPa, and that of *Al*-based alloys is about 75 GPa. In contrast, for HEAs, the mechanical properties can be very different from any of the constituent elements in the alloys. For example, Wang *et al.* [120] reported that Young's modulus *E* of the $CoCrFeNiCuAl_{0.5}$ HEA is about 24.5 GPa, which is much lower than the modulus of any of the constituent elements in the alloy. Therefore, it is of fundamental interest to explore the relationship between the elastic properties of HEAs and their constituent elements as exampled using the *CALPHAD* model [121, 122]. With such relationship, one may try *to predict* more or less accurately the properties of HEAs according to the known properties of their unary and binary constituent elements. While this methodology is more sophisticated than the simplest widely employed one, that uses the weighted properties, it can suffer from some discrepancy to predict the behavior of specific alloys and has to be checked when it is possible.

Understanding of *deformation mechanism* underlying *mechanical properties* is important if one want to identify the links and the relationships between the *elastic and plastic* properties. For the conventional alloys with regular crystal lattice, the plastic deformation is governed by the slip of dislocations or twinning, whereas for the amorphous alloys without regular crystal lattice, shear-transition-zone [123] was proposed. The lattice structure of HEAs is in between conventional and amorphous alloys, i.e., having regular crystal lattice but with severe lattice distortion. Therefore, it was believed that the plastic mechanism is in between the conventional and amorphous alloys, as well. However, although tremendous efforts have been made to measure their mechanical properties, very less is known about the details of the underlying mechanisms. *Generalized stacking fault energy* (GSFE) is one of the most important quantities relevant to the deformation

mechanisms. GSFE treated within the semi-discrete variational Peierls-Nabarror model provides insights into the dislocation behavior, e.g., critical shear (Peierls) stress, dislocation core energy, dislocation displacement density [124, 125]. These properties dominate the dislocation movement, then the mechanical properties. Nowadays, ab initio calculated GSFE has been widely used to understand the mechanical properties of metals. But, although the stable stacking fault energies of some HEAs (e.g. *CoCrMnFeNi*) have been calculated by using EMTO-CPA [126] or VASP-SQS method [127] showing that SFE decreases with the number of components., GSFEs of HEAs remain untouched.

Many efforts have been devoted to the investigations of *phase stability* of the HEAs as the mechanical properties of HEAs are highly pertinent to the microstructure (i.e. FCC are more ductile than BCC for example). Experiments have demonstrated that the FCC-structured HEAs exhibit low strength and high plasticity, while the BCC-structured HEAs show high strength and low plasticity at room temperature. Therefore, proper phase design is crucial to the control of the mechanical properties of HEAs to satisfy different applications. It has been noticed that the phase stability of HEAs may be roughly judged with the valence electron concentration (*VEC*), i.e., the FCC phase is stable with $VEC > 8$ whereas the BCC one is stable with $VEC < 6$. This empirical rule indicates that the phase stability is physically controlled by the binding between the atoms at electronic structure level. Therefore, a detailed analysis based on the electronic structures of HEAs is highly desirable to provide more insight into the phase stability.

Concerning the *thermodynamics*, it was believed that the *mixing entropy* [128] contributes to the stability of the HEAs as single phase solid solution. However, recent finite-temperature ab initio calculations showed that entropy beyond the configurational

one determines the phase stability of HEAs such as *CoCrMnFeNi*. The electronic, magnetic, and vibrational entropies cause strong effects on the stability difference between different phases [129].

Since HEAs contain 5 or 6 different elements with significant atomic size mismatch, they suffer from severe *lattice distortion*. The lattice distortion, as one of the core effects for HEAs, affects the mechanical properties such as hardness and strength through heavy solid solution hardening. For example, the lattice distortion was believed to contribute to the high strength of BCC HEAs. However, it is still unclear why FCC HEAs, where the severe lattice distortion is present as well, have low strength, in contrast to that of BCC HEAs. Room temperature XRD measurements demonstrated that, pure *Ni*, low entropy binary *CoNi*, medium entropy ternary *CoFeNi*, quaternary *CoCrFeNi*, and HEA *CoCrMnFeNi*, remains FCC solid solutions. The XRD peak intensities lowered with increasing number of elements due to the increasing diffuse scattering induced by the lattice distortion. Yeh [89] suggested that the lattice distortion is ascribed not only to the atomic size mismatch but also the crystal structure difference and bonding strength difference. Obviously, a full understanding of the severe lattice distortion requires fundamental knowledge at electronic structure level which can be obtained through ab initio calculations.

EMTO-CPA method as one of main tools has been employed to investigate the phase stability, elastic modulus, and ideal strength of HEAs as random solid solutions. However, since the site-site approximation is adopted in EMTO-CPA, this method fails to take into account the lattice distortion, as relaxation of atoms is not allowed. Another technique to treat the random solid solution is the special quasi-random structure (SQS)

method that has been widely employed in the firstly discussed hard coatings TMN alloys. The idea of SQS is to construct a special supercell of which the atomic correlation functions mimic those of the physically most relevant ones of the perfectly random alloys. Within the supercell, the atomic positions may be relaxed through minimizing the interatomic Hellmann–Feynman forces [116] during the ab initio calculations such that the local lattice distortion effect induced by alloying atoms is taken into account. This is the main advantage of SQS over CPA [115]. However, the size of the supercells needed for multi-components alloys such as HEAs might eventually become of limiting factor for the SQS approach. When using SQS to model HEAs, the supercell size must be carefully checked in order to ensure reasonable outputs.

1.4 High entropy alloys nitrides (HEANs)

In comparison to metals and alloys, nitrides can have higher wear, corrosion and oxidation resistance, higher strength, melting point, hardness, which still holds true for HEAs. In case of *N*-free HEAs, high hardness was only reported for refractory high entropy alloys [130]. Although *CoCrNi*-based series of alloys exhibit exceptional mechanical properties, for instance, Gludovatz *et al.* [113] reported *CoCrMnFeNi* has plane-strain fracture toughness exceeding 200 MPa/m^2 and a tensile strength larger than 1 GPa, the reported yield strength is relatively low, which is below 200 MPa at RT [131](grain size 50-155 μm). Besides, *CoCrMnFeNi* and related FCC based HEA suffer from low hardness and low wear resistance [132, 133], which certainly prohibits its tribological applications. The average micro-hardness of *CoCrMnFeNi* coating prepared by laser cladding [134] is 360 $HV_{0.2}$. With the application of plasma nitriding, Nishimoto [135] succeeded to produce

a 50 μm-thick nitride layer onto a bulk *CoCrMnFeNi* with a hardness of 1300 HV. The nitride layer has a single B1 phase at low nitriding temperatures and the N concentration reached 30 - 40 at. %.

On the other hand, small amount of nitrogen addition leads to interstitial hardening, which has been used to strengthen many conventional materials [136]. Strengthening examples on HEAs are very limited in this case with *N* alloying. Only Moravcik and co-workers [137] have reported on N strengthening of *CoCrMnFeNi* and no significant strengthening effects was found except a slight increase of hardness. However, significant strengthening effect has been found in *TiZrHfNb* doped with 2 at. % of oxygen [138] which exhibits an increased tensile strength of 48 % and the ductility was substantially improved by 95%. The enhanced strength is due to the formation of ordered interstitial oxygen complexes changing the dislocation shear mode from planar to wavy slip and promote double cross-slip and thus dislocation multiplication through the formation of Frank-Read source during deformation. Besides, there are other interstitial strengthening examples with metalloid elements which show enhanced mechanical properties by alloying of boron [139] and carbon [140-142].

Further interstitial alloying beyond the solubility limit promotes the formation of interstitial compounds phase. For example, nitrides will be formed at high nitrogen concentrations. In contrast to the binary and ternary transition metal nitrides, which has been widely used as hard coating materials in industry and intensively studied in academy, less is known about such HEA nitrides.

For HEANs, many works have convinced the formation of an FCC single solution phase. In the systematic work [10, 143] dealing with progressively increased *N/O* concentrations, the XRD patterns show gradually increase of the lattice constant, while the structure maintains cubic from FCC metal to B1 nitride. No abrupt change of lattice parameter as a function of *N* content was observed. This finding suggests the high solubility of *N/O* in *CoCrCuFeNi* HEA. Besides, no formation of a second phase was reported. The nitrides were stable as a single-phase solid solution in the whole *N/O* concentration range. The stability of the single phase HEAN is due to entropy stabilization in analogy to HEAO. Roster *et al.* [144] found that single-phase solid solution oxide can be formed from non-isostructural oxides *(MgO, CoO, NiO, CuO and ZnO)* even with a positive mixing enthalpy (0.1 eV/atom). Many other works reported the formation of the single phase B1 HEAN, e.g., RF magnetron sputtered *AlCrNbSiTiV-N* [145], *AlCrTaTiZr-N* [146], *AlMoNbSiTaTiVZr-N* [147], *AlCrNbSiTi-N* [148], DC magnetron sputtered *FeCoNiCrCuAlMn-N* and *FeCoNiCrCuAl$_{0.5}$-N* (41 at. % *N* maximum solubility) [149], *AlCrMnMoNiZrB-N* [150], *CoCrCuFeNi-N* [10], as well as cathodic arc deposited *AlTiVNbCr-N* [151]. Regarding the structure of high entropy carbides, *TiZrNbHfTa-C* solid solution [152] prepared by DC magnetron sputtering were also found to have FCC phase.

Table 1.1- Hardness of various HEAN found from available literatures.

Materials	H (GPa)	Ref.
AlCrTaTiZrN	32	[146]
TiHfZrVNbN	44	[153]
	66	[154]
TiZrNbHfTaN	32	[152]
TiZrNbHfTa	5	

AlCrNbSiTiN	36	[148]
TiAlCrSiVN	30	[155]
AlCrMoSiTiN	35	[156]
AlMoNbSiTaTiVZrN	35	[147]
AlCrNbSiTiVN	41	[157]
CrTaTiVZrN	36	[158]
TiVCrZrHfN	48	[159]
AlCrMnMoNiZrBN	10-15	[150]
AlCrFeNiTiN	21	[160]
CoCrCuFeNiN	10-15	[149]
CoCrCuFeNiN	15	[10]

Hardness is the most commonly studied mechanical properties for HEAN because high hardness can be easily achieved. We provide in **Table 1.1**, a list of the published work on HEAN and their reported hardness. Elements forming HEANs can be divided into nitride-forming elements (such as *Al, Cr, V, Ti, Ta, Zr, Nb, Mo and Hf*) and non-nitride forming elements (such as *Mn, Co, Ni, Fe and Cu*) as summarized in [161]. It can be seen from the **Table 1.1** that high hardness can be obtained for HEAN without non-nitride forming elements. The two prototypes under study in this thesis, i.e., *CoCrCuFeNi* and *CoCrMnFeNi*, belong to the type where high hardness should not be anticipated form their nitrides. Hardness close to ~15 GPa is expected, higher than that of hardened steel ~10 GPa, but lower than for ceramics ~20 - 30 GPa and superhard materials > 40 GPa. However, there is not enough research on these materials yet, from both theoretical and experimental parts.

Computational research is rare in the case of high entropy nitrides due to very limited knowledge on HEAN. Yalamanchili [151] calculated the formation energy of the stoichiometric *AlTiVNbCrN* by DFT, they found a positive enthalpy relative to their parent

binaries. Experimentally, it decomposed to wurtzite-*AlN* and cubic-*TiVNbCrN*, suggesting the *AlTiVNbCr-N* is a metastable HEAN. Apart from this, no more literature of theoretical investigations on HEAN can be found, making this type of material quite mysterious. In this context, we aim to provide systematic studies on HEAN with the support of atomic scale modelling. *CoCrCuFeNi* and *CoCrMnFeNi* were chosen because they are the HEA prototypes which have been widely studied although not true for their nitrides. Moreover, there is already one published work [10] on *CoCrCuFeNi-N* which has provided many preliminary details on structures, sound velocities, effective elastic constants and hardness as a function of *N* alloying. We did the same depositions again of *CoCrCuFeNiN*, varying the thickness, to cross check the results and diminish the influence of oxygen impurities by using a solid target and a high-vacuum chamber with DRAFT group in Gent University (R. Dedoncker & Pr. D. Depla). New *CoCrMnFeNiN* films were deposited and studied following the same procedure to study the effect of *Mn* by replacing *Cu*. Note, nitrogen has very small solubility in *Cu* system as shown in the *Cu-N* phase diagram and electronegativity of *Mn* (1.55, close to *Ti* 1.54) is lower than *Cu* (1.90), which might affect the nitrides formation as well as mechanical properties.

In the work of *CoCrCuFeNi-N* [10], the evolution of mechanical properties (elastic constants, Young's modulus and nanohardness) are coupled with microstructural (crystallographic orientations and grain size) changes and the variation of *N* content simultaneously. Hence it is absolutely necessary to perform DFT calculations in order to separate the chemical contribution from the contribution of microstructural part, namely the orientation and porosity, to the change of mechanical property.

In doing theoretical calculations, we started with the assumption that *N* as a small atom will fill the interstitial holes of the initial FCC metallic lattice. *N* contents were progressively added until the formation of stoichiometric nitride. For non-stoichiometric compounds, the *N* atoms were considered to be randomly distributed in the interstitial area. Both types of interstitial holes namely, octahedral and tetrahedral ones, were studied under DFT. In order to have a picture where the nitrogen prefers to sit, the formation energy criteria was utilized to distinguish whether it is octahedral or tetrahedral. Besides, the calculated lattice parameters and mass density were compared to XRD and XRR respectively. Single crystal elastic constants vs. *N* concentration were calculated and compared to the ones measured by optoacoustic methods and nanoindentation.

1.5 Objectives

In this thesis, the structural and mechanical properties of "simples" binary, ternary films, and of prototype HEAs and their nitrides will be measured by well adapted techniques. It will be at different scale size, in the specific case of the base alloy *CoCrCuFeNi*, thanks to the synthesis of bulk and films, with different microstructure (grain size) and film thickness. Different chemical alloying (number of elements and concentration) will be compared and differences will be discussed in regard to DFT simulations. Influence of defects (metal and nitrogen vacancy) and different structures (FCC and BCC or amorphous by alloying with *Nb, Al or N* element) will be investigated.

Several experimental techniques in combination with computational methods will be used for exploring the influence of defects, the different scale size and core HEAs

effects, from which, measured mechanical properties will be voluntary, complementary or to be compared:

(*i*) The non-conventional Brillouin light scattering (BLS) and picosecond laser ultrasonic (PLU), for accurate local raw measurements of sound velocities (V_L and V_T) from which Debye temperature (θ_D), heat capacity (C_v) in the Debye model approximation and isotropic elastic properties (C_{ij}) or single crystalline elastic constants (c_{11}, c_{12}, c_{44}) are calculated. New insight on the elastic and plastic relationship should be provided. This is a unique combination for studying opaque thin films.

(*ii*) Nanoindentation for Young's modulus (E_{IT}) and hardness (H), and direct comparison to the existing data in literature as to our BLS and PLU results.

(*iii*) Tensile tests on films deposited on flexible Kapton substrate, for plastic properties (stress-strain curves), using a DEBEN-micro tensile device for displacement control and force gage measurements, in-situ with a KEYENCE confocal microscope for cracks and buckle observations and later pictures analysis. Unfortunately, film's strength (σ_y) of the coating could not be determined by "subtraction" of the substrate contribution in this case [162], our substrate being too thick (120 µm).

(*iv*) Additional functional/physical properties: thermal and electrical conductivity and magnetic were investigated, respectively, by thermoreflectance, four probes tests, vibrating sample magnetometer and ferromagnetic resonance. It should provide further insights on the influence of core HEAs effects [163] but will not be fully discussed in this manuscript.

(*v*) We check the reliability of DFT calculations on metallic HEAs (*CoCr(Cu,Mn)FeNi*, $(CoCrCuFeNi)_{1-x}(Nb_x, Al_x)$ by performing both EMTO-CPA and VASP-SQS calculations. The atomic position relaxation effect on elastic properties which is missing in EMTO-CPA calculations is particularly evaluated using VASP-SQS. As atomic position of nitrogen can be modified a lot during the relaxation, DFT calculations on "simple" nitrides (TaN_x, TiN_x, ZrN_x, $Ti_{1-x}Zr_xN_y$) and complex HEANs ($CoCr(Cu,Mn)FeNiN_x$ are performed exclusively with VASP-SQS.

By increasing the complexity of alloys, we want to study both experimentally and by computational simulations, the relationship between the microstructure, the chemical composition, the grains size and the mechanical properties of bulk and films multicomponent alloys (MCAs), in particular, equimolar high entropy alloys (HEAs), either crystalline or amorphous. So far, the literatures of modeling and simulations on the HEA films and coatings are limited. More investigations on the predictive computational modeling of the HEA films and coatings need to be explored, which will help illuminate the relationship among the preparation processes, microstructures, and properties [161]. Relationships between structural and thermo-mechanical properties remain not enough documented for new materials such as high entropy alloys with an amorphous or a crystalline state, even more for thin films and coatings materials and particularly for elastic properties in comparison to plastic properties. Furthermore, nearly no data are provided for this class of materials concerning physical properties such as thermal and electrical conductivity, for design of thermal barrier and thermoelectric materials.

Prototype bulk and films HEAs starting with a single FCC crystalline phase solid solution are selected: (i) starting from the base HEA alloys *CoCr(Cu, Mn)FeNi* (bulk and film shape); and (ii) adding a 6th element (*Nb, Al, N*), two metals and one metalloid.

The role of key parameters such as chemical alloying (number of elements and concentrations), crystalline or amorphous phase and size effects (grain size and film's thickness) is investigated thanks to their distinct influence on the different measured properties. The influence of chemical composition on the structural stability and phase transition is investigated and correlated to the change of lattice parameter, mass density, sound velocities (V_L *and* V_T) and elastic properties (C_{33}, C_{44}, *H and* E_{IT}). A database dedicated to the structural and all measured properties of binary and ternary nitrides, HEAs and HEANs is established both experimentally and theoretically by ab initio density functional theory calculations well suited for disordered solid solutions. We plan to compare experimental results to simulations and to identify a mean for each selected HEAs to correlate the influence of defects and the plastic behaviour to the elastic properties.

LSPM (CNRS - Université Paris 13) and INSP (CNRS - Sorbonne Université), DRAFT (Ghent University, Be) and the Institute of Metal Research (IMR, Chinese Academy of Science), share their competences on synthesis, characterizations and theoretical studies. IMR (Pr. L. Dong) elaborated several bulk *CoCrCuFeNi* by vacuum arc melting that are used as consolidated targets for the deposit of coatings by DRAFT (R. Dedoncker, C. H. Li and Pr. D. Depla). Collaborating with INSP, we characterized single grains of bulk *CoCrCuFeNi* HEA and single crystalline or averaged elastic properties of epitaxial or polycrystalline films by optoacoustic techniques (Pr. L. Belliard, B. Perrin, Pr. D. Fournier, C. H. Li and E. Charron) while we did ab initio calculations for comparison

to experiments. Elastic properties characterization of single grain and average properties are obtained thanks to original optoacoustic techniques at LSPM and INSP: the Brillouin light scattering and the picosecond laser ultrasonic techniques. Both surface and bulk acoustic waves can be measured in opaque materials by these local probe techniques that are also well suited for thin films characterizations. Complementary tests by nanoindentation (Dr. F. Tétard, LSPM) are also provided, as a comparison to a more widely used technique in R&D Labs. Most of experiments are performed on films deposited on silicon while tensile tests coupled to a confocal microscope are conducted on flexible Kapton substrates (Pr. Faurie and C. H. Li, LSPM) in order to extract fracture toughness and brittleness/ductility of the HEA films, to compare to their bulk counterparts whose microstructures and defects are necessarily different but with close chemical composition, further evaluating the influence of scaling size on mechanical properties. Uniaxial tension tests have the advantage of applying uniform stress and strain fields to the specimen [164]. Such a feature makes it easy to employ and is the reason why it is so widely used to determine mechanical properties at larger scale. However, performing tension tests at micro/nanoscale or Lab-on-chip [165] is challenging because of the difficulties in preparing free-standing and stress-free specimens. Furthermore, the requirements for sample alignment, deflection and load measurements are stringent, and in the case of brittle materials, fracture induced by specimen gripping may be an additional problem.

Not discussed in this manuscript, thermal conductivity was measured by photoreflectance at INSP (C. H. Li and Pr. D. Fournier), while electrical conductivity of MCAs was measured at LSPM, by the four probes technique (C. H. Li). Collaborating with our colleague (Dr. F. Zighem, C. H. Li, LSPM), magnetic properties (magnetic anisotropy,

magnetostriction and magnetization) of magnetic MCAs were also investigated by ferromagnetic resonance (FMR) and vibrating sample magnetometer (VSM).

DRAFT group (Pr. Diederik Depla, GHENT university) started to elaborate thin films of metallic and nitrides HEA a few years ago [5-10, 143], with compacted powders as a target for PVD, providing all the starting HEA films samples. Additional films of *CoCr(Cu, Mn)FeNiN* were elaborated during a visit of C. H. Li in Gent during one month. As in the case of "simple nitrides", chemical analysis of nitrogen light element was conducted by WDS and EDS at PPRIME Institute by Pr. G. Abadias.

The main objectives of the thesis are as follows:

1. Obtain reliable structural and elastic properties of the "simple" binary and ternary nitrides, HEAs and HEANs alloys through both experimental measurements and ab initio simulations; correlate the elastic and plastic properties of HEAs films. Identify their relationship to address the cocktail effect and sluggish diffusion.

2. Determining the phase stability and thermodynamics of HEAs alloys by comparing the experimental determined structural and ab initio predictions; find the relationship between the phase stability and microstructure of the HEAs to that of the constituent elements; build the connection between the microstructure and the mechanical properties of HEAs (to address the high entropy effect).

3. Thermal and electrical functional properties in connection with the severe lattice distortion effect, *but not reported in this manuscript*.

4. Explore the severe lattice distortion effects on the phase stability and elastic properties through ab initio calculations; reveal how the lattice distortion affects the mechanical properties of HEAs (Severe lattice distortion effect).

CHAPTER 2. METHODS AND MATERIALS

This chapter describes the theoretical methods we used for prediction of energetics of crystals and amorphous phases, structural and elastic properties, sound velocities of the materials under study in this work, and the synthesis and characterization techniques of thin films and of the bulk. The bulk (*CoCrCuFeNi*) is serving as reference material for several structural and physical properties and a solid HEA target for further metallic and nitrides film's growth. The structural and chemical properties of our samples are presented in this chapter and will be discussed later in more details with numerical simulations and optoacoustic or nanoindentation experimental results.

2.1 Theoretical and numerical background

2.1.1 Density functional theory

An exact description of a system containing ions and interacting electrons is inherently determined by quantum mechanics, and is simply based on the many body Schrödinger equation:

$$\hat{H}\Psi = E\Psi \tag{2.1}$$

$\Psi = \Psi(\mathrm{r}_1, \mathrm{r}_2, \ldots, \mathrm{R}_1, \mathrm{R}_2, \ldots; \mathrm{t})$ is the many body wave function, in which r_i and R_j denotes the coordinates of electrons and nucleus, respectively. The Hamiltonian $\hat{\mathrm{H}}$ contains the kinetic energy of electrons, nucleus, and the Coulomb interaction energy among them.

$$\hat{H} = \underbrace{-\sum_{n} \frac{\hbar^2}{2M} \nabla_n^2}_{\hat{T}_N} \underbrace{-\sum_{n} \frac{\hbar^2}{2m_e} \nabla_i^2}_{\hat{T}_e} + \underbrace{\frac{1}{4\pi\epsilon_0} \frac{1}{2} \sum_{n \neq m} \frac{Z_n Z_m e^2}{R_n - R_m}}_{\hat{V}_{NN}} + \underbrace{\frac{1}{4\pi\epsilon_0} \frac{1}{2} \sum_{i \neq j} \frac{e^2}{|r_i - r_j|}}_{\hat{V}_{ee}} \underbrace{- \frac{1}{4\pi\epsilon_0} \sum_{i,n} \frac{Z_n e^2}{|r_i - R_n|}}_{\hat{V}_{eN}} \quad (2.2)$$

To simplify this situation with many kinds of interaction terms, we assume that the electron which has much less mass than the nuclei, moves much faster than the nuclei in space. This leads to the well-known Born-Oppenheimer approximation[166] which states electrons stay in the ground state at any instant time of a given nucleus configuration. Electronic structure calculations are generally done in the context of the Born-Oppenheimer Approximation. For a given atomic configuration, where the ions are at rest, we can further write down the Hamiltonian of the electrons neglecting the ionic part,

$$\hat{H} = \underbrace{-\sum_{n} \frac{\hbar^2}{2m_e} \nabla_i^2}_{\hat{T}_e} + \underbrace{\frac{1}{4\pi\epsilon_0} \frac{1}{2} \sum_{i \neq j} \frac{e^2}{|r_i - r_j|}}_{\hat{V}_{ee}} \underbrace{- \frac{1}{4\pi\epsilon_0} \sum_{i,n} \frac{Z_n e^2}{|r_i - R_n|}}_{\hat{V}_{eN}} \quad (2.3)$$

For systems with more electrons, the many body electron wave function cannot be solved exactly due to the many body electron- electron interaction. Assumptions need be used in order to solve the Schrödinger equation. The first is the Hartree approximation, which assumes that the electrons were non-interacting particles. The Hartree approximation indeed simplifies the many-body electron system into a single-particle picture. However, in the Hartree equation, the potential term contains only the Coulomb repulsion between electrons which is not adequate to describe the many-body effects. The

fermion nature of electrons in the many body wavefunction was further considered later in the Hartree-Fock approximation by introducing the exchange term.

Instead of dealing with the many-body Schrodinger equation directly, Hohenberg, Kohn and Sham [167, 168] reformulate the Schrodinger equation to a density-based equation, which has been called the density functional theory (DFT).

As the basis of DFT, the Hohenberg-Kohn theorems state that,

Theorem 1: the external potential, and hence the total energy is a unique functional of the electron density.

Theorem 2: the ground-state can be solved variationally by minimizing the total energy as a function of the electron density.

The Kohn-Sham ansatz replaces the interacting electrons in real potentials with non-interacting auxiliary particles in an effective potential, assuming the ground state density of interacting system is equal to that of some non-interacting soluble system. In the Hamiltonian of the Kohn-Sham equation, the kinetic and potential part are all represented as a functional of electron density. The exchange and correlation terms, included in the effective potential of the Kohn-Sham equation, contains the effects of the many-body character of the true electron system. This simplifies the many-body physics to a one-particle picture. The solution to the Kohn-Sham equation is named Kohn-Sham orbitals, can be solved iteratively.

$$\left(-\frac{1}{2}\nabla^2 + v_{ext}(r) + v_H(r) + v_{xc}(r)\right)\phi_i(r) = \epsilon_i\phi_i(r) \tag{2.4}$$

Depending on the different choice of basis sets of the Kohn-Sham orbitals and different forms of external potential, there are many methods or programs to electronic structures. A short introduction will be given to two widely used packages, i.e. VASP and EMTO, which are based on the augmented plane wave (APW) and muffin-tin orbitals (MTO) respectively.

2.1.2 Exact Muffin-Tin Orbitals Method and coherent potential approximation

2.1.2.1 Exact-Muffin-Tin Orbital method (EMTO)

EMTO [169, 170] uses atomic spheres approximation for solids, i.e., by partitioning the cell into two regions basically, namely, the atomic spheres and the interstitials between them. Inside the atomic sphere or hard sphere, where the potential is strongly varying and similar to a free atom, the partial wave (PW) is chosen as the basis of electron wave function as shown in **Figure 2.1**. Between the hard sphere and potential sphere, where the potential is relatively smooth, screened spherical waves (SSW) is chosen as the basis sets in the EMTO package. Additionally, a back-extrapolated partial wave (BPW) is used to connect the PW and SSW between the hard sphere boundary and potential sphere boundary, make the overall wave function continuous and derivable.

Kohn-Sham orbital can be written in the context of Muffin-Tin approximation as

$$\bar{\Psi}^{a}_{RL}(\epsilon.r_R) = \underbrace{N^{a}_{Rl}(\epsilon)\phi_{Rl}(\epsilon,r_R)Y_L(\hat{r}_R)}_{PW} + \underbrace{\psi^{a}_{RL}(\kappa,r_R)}_{SSW} + \underbrace{\varphi^{a}_{Rl}(\epsilon,r_R)Y_L(\hat{r}_R)}_{BPW} \quad (2.5)$$

Unlike pseudopotential-based methods which will be introduced in the next section, in EMTO method, the core and semicore electrons can be included in the calculations. This can be important in high pressure physics where the core states may be involved.

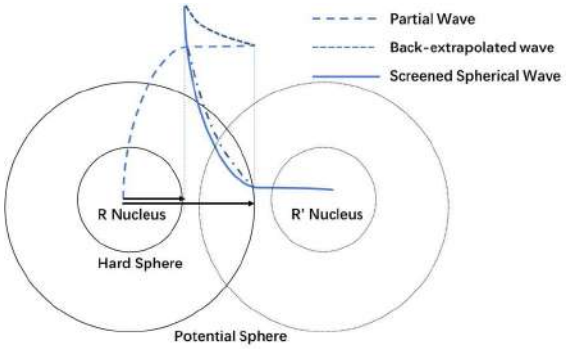

Figure 2.1 – Schematic illustration of the construction of Muffin-Tin orbitals

One of the advantages using the EMTO package, is its ability to deal with random alloys with the application of coherent potential approximation (CPA) [171, 172] based on Green's function method.

2.1.2.2 Coherent potential approximation (CPA)

In disordered alloys where translational invariance is missing, coherent potential approximation (CPA) replaces the actual environment seen by an electron, which is site dependent in disordered systems, by an effective or site-independent coherent potential as illustrated in **Figure 2.2**. Details can be found in several papers. This approximation method makes it very efficient to calculate random alloy system. To use CPA, the precondition requires that the elements need to have nearly the same bandwidth [173], which is satisfied in *CoCrCuFeNi(Al,Nb)*. Besides, CPA is also capable of modeling the magnetic disorder within the disordered local magnetic moment (DLM) model [174].

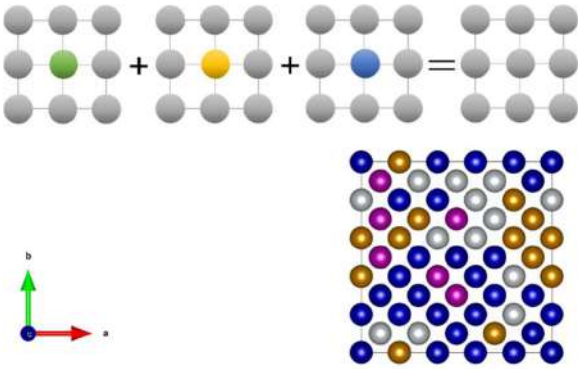

Figure 2.2 - Schematic illustration of the coherent potential approximation (above), below is a supercell used to calculate random materials.

CPA assumes that atoms of the same type have the same effective potential, whatever the chemical environment. Although CPA is effective in modelling alloys, it neglects the local chemical environment of an atom. Consequently, CPA ignores the local lattice distortion, which can lead to certain shortcomings especially when the atomic radii mismatch is significant as will be discussed in chapter 5.

Apart from the one-site approximation, another choice is to use supercells as shown in **Figure 2.2**, to treat the impurity problem. One can model paramagnetic (PM) structure with randomly oriented magnetic moment on atoms, by building a supercell in which random magnetic moment (orientation) is assigned for each atom. More importantly, the supercell method can be used to model alloys composed of different elements with the local chemical environment clearly defined unlike in CPA. The calculation becomes expensive when a large cell is needed.

2.1.3 Vienna Ab initio Simulation Package and Special Quasi-random Structures

2.1.3.1 Projector-augmented-wave method (PAW)

In VASP [12, 175, 176], the Kohn-Sham orbitals and electron density are expressed in plane wave basis sets. So do the kinetic energy and the effective potential. The interactions between the electrons and ions are described using norm-conserving or ultra-soft pseudopotentials (PP) [177], or the projector-augmented-wave method (PAW) [178]. PP can greatly increase the computational efficiency by neglecting the core/semicore change. Inside the ion core region where all states are non-zero, the fast oscillations of valence electron wave-functions due to the requirement of orthogonality to core states rapidly increase the computational cost because a very large basis sets of plane waves is required. PP arises from the fact that the core electrons do not participate in bonding when forming molecules or solids so that the collective system of core and core electrons can be replaced by a smooth potential (PP) which provides the same scattering property to the valence electrons. However, the core states cannot be described correctly within PP. Unlike PP, PAW is an all-electron wave-functions method. The oscillatory core wave-functions are mapped with smooth auxiliary functions through transformation by projector functions. The PAW methods can provide the same accuracy as other full potential methods meanwhile maintaining relatively high efficiency.

2.1.3.2 Special Quasi-random Structures (SQS)

Instead of modelling an infinite random alloy which is not possible for DFT, one seeks a small periodic supercell which shares the same radial correlation functions as true random structures, namely special quasi-random structures (SQS) [179, 180]. SQS can provide satisfactory material properties since they are determined by atoms and correlations functions. SQS were generated using the Alloy Theoretic Automated Toolkit

(ATAT) [181-183]in this work. The algorithm [181] is based on a Monte Carlo simulation of an objective function that seeks to perfectly match the maximum number of correlation functions.

In this work, SQS is used to model random distribution of elements as well as vacancies. In chapter 3, SQS is used to model *TaN* and *TiN-ZrN* structures with random distribution of metallic and nitrogen vacancies. For both systems we employed a cubic-shape SQS supercell containing 64 lattice sites (32 cation sites + 32 anion sites) in total. In the case of *TaN*, we have considered Ta vacancies or N vacancies or both at the same time, namely Schottky vacancies. In the case of *TiZrN*, SQS was used not only to model the random vacancies but also to mimic the random distribution of *Ti* and *Zr* at cation sites. The convergence test of this size was done by comparing the total energy and output elastic constants to a larger cell with 96 lattice sites.

Later in chapter 4 and 5, we used SQS to model high entropy alloys, i.e., *CoCrCuFeNi* and $(CoCrCuFeNi)_{1-x}(Nb_x, Al_x)$. Comparing to EMTO calculations with CPA approximations, the atomic relaxations can be considered in the SQS calculations, giving opportunity to evaluate relaxation energy [184] and lattice distortion [185] as a function of chemical content and to compare to a more simple approach which can evaluate the elastic-strain energy [101] of MCAs. The SQS cell contains 64 atomic sites for the $(CoCrCuFeNi)_{1-x}(Nb_x, Al_x)$ with various *(Al, Nb)* concentrations, while for the pure *CoCrCuFeNi*, we've used a slightly larger cell with 80 atomic sites. The convergence test was done by comparing the output total energy and magnetic moments to SQS supercells with 125 atoms. For elastic constants calculations, Niu [186] has demonstrated that the size of the SQS supercells has minor influence on determining elastic constants of quaternary

CoCrFeNi HEA by showing that supercells containing only 24 atoms can provide comparable values to supercells containing 108 atoms. The elastic constants are in fact more sensitive to the chemical induced anisotropy from the limited size of the supercell, which can be further resolved by averaging relevant elastic constants from different crystallographic orientations. We applied this strategy to provide more reliable elastic constants at a limited computational cost.

In chapter 6 where we deal with *CoCr(Cu,Mn)FeNi*N_x of various *N* concentrations, we consider random distributions of metal atoms in a FCC lattice, and interstitial *N* atoms in an octahedral or tetrahedral interstice by designing different SQS supercells. The cell contains 80 metallic as well as 80 octahedral/tetrahedral interstitial sites. Different SQSs were generated representing various *N* concentrations (0-50 at. %). The convergence test was done by comparing the output total energy and magnetic moment to larger SQS cells with 250 atoms.

2.1.3.3 Local lattice distortion (*LLD*) and relaxation energy (ΔE_{nr}) in MCAs from DFT

For MCAs, although all constitutional elements form together a uniform (FCC, BCC or HCP) lattice macroscopically, at atomic scale, the crystals do not preserve strictly the translational symmetry due to different atomic sizes and interatomic bonding characters between different elements, leading to the lattice distortion effect (see Figure 2.3). As a feature of MCAs, local lattice distortion (*LLD*) is important as it relates to the phase stability, structural and mechanical properties. It is defined as the average distance between the ideal lattice sites and relaxed atomic positions:

$$LLD = \frac{1}{N}\sum_{i}\sqrt{(x_i - x_i')^2 + (y_i - y_i')^2 + (z_i - z_i')^2} \quad (2.6)$$

with (x_i, y_i, z_i) and (x_i', y_i', z_i') being the unrelaxed and relaxed positions of atoms *i* in the cell-coordinates and *N* is the total number of atoms in the supercell.

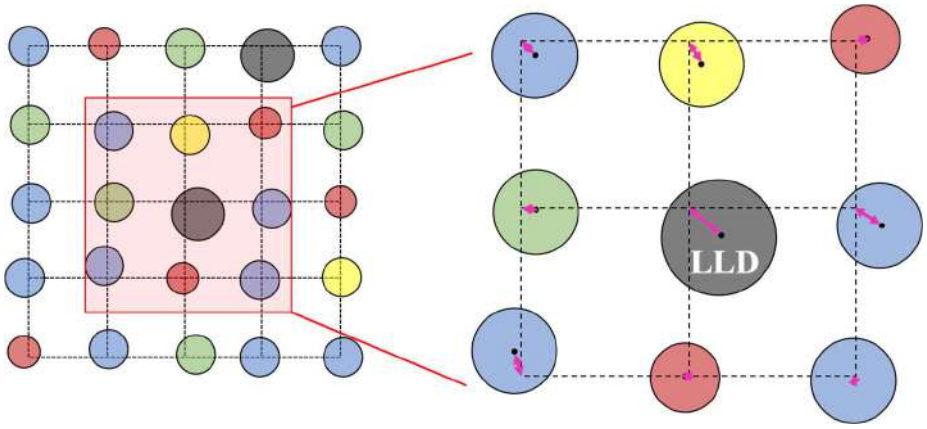

Figure 2.3- Schematic illustration of the local lattice distortion (*LLD*) for MCAs. The

Relaxation energy (ΔE_r) is the energy difference between the total energy of the partially relaxed supercell, i.e., only the shape and size of the cell can relax, not the atomic positions, and the fully relaxed supercell. It is a positive number and becomes larger when the *LLD* is more severe.

$$\Delta E_r = E_{nr} - E_r > 0 \quad (2.7)$$

where E_{nr} denotes the partially relaxed total energy and E_r the totally relaxed energy. Note that the relaxation energy term is not included in the method of EMTO-CPA calculations. This will certainly cause errors in describing HEAs especially those containing elements with large size mismatch which leads to more severe *LLD*, e.g. *CoCrCuFeNi* with the addition of *Al* or *Nb*, of which *Al* or *Nb* has a significantly larger atomic size.

2.1.4 Ab initio molecular dynamics (AIMD) for amorphous $(CoCrCuFeNi)_{1-x}(Nb_x,Al_x)$

The adiabatic approximation states that electrons stay in the ground state at any instant time of a given nucleus configuration. Nucleus move on the ground state Born-Oppenheimer potential energy surface. In this way, electrons and nucleus can be treated together simultaneously. This is the idea of Born-Oppenheimer molecular dynamics, which is implemented in VASP for AIMD calculations [176].

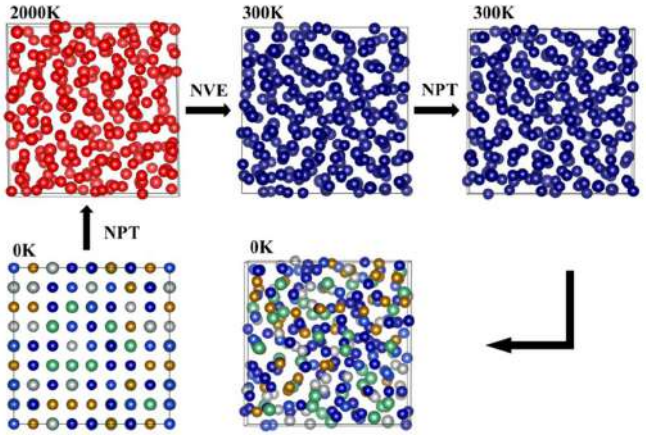

Figure 2.4 – The process to obtain the amorphous high entropy alloy.

Amorphous structures do not have translational symmetry as crystals. In chapter 5, amorphous phase is formed when *CoCrCuFeNi* is heavily alloyed with *Nb*. To calculate properties of amorphous materials, an amorphous structure is necessary as an initial input. However, it is not straightforward to obtain an amorphous structure since it does not have a well-defined unit cell as crystalline materials. The amorphous structure is usually generated from MD/AIMD simulations. The idea is to play a fast quench from high temperature liquid phase to a temperature well below glass transition temperature. The procedure to get an amorphous $(CoCrCuFeNi)_{1-x}(Nb_x, Al_x)$ is depicted in **Figure 2.4**.

Additionally, in order to discuss the structural properties of the amorphous phases, ab initio molecular dynamics (AIMD) simulations were performed using the plane-wave pseudo-potential as-implemented in VASP. The plane-wave cu-toff energy was set to 296 eV. The simulations were performed at the Γ point only and magnetism was not considered during these AIMD simulations. We build three cubic supercells of 256 atoms corresponding to the compositions of $(CoCrCuFeNi)_{0.899}Nb_{0.101}$ (10.1 at. % *Nb*), $(CoCrCuFeNi)_{0.84}Nb_{0.16}$ (16.0 at. % *Nb*) and $(CoCrCuFeNi)_{0.742}Nb_{0.258}$ (25.8 at. % *Nb*) and others for *Al* alloying at higher concentration. AIMD simulations are performed initially above the melting temperature, at 2000 K, using a Langevin thermostat in a canonical ensemble (NPT). The duration of this simulation is 9 ps with a time step of 3 fs. Then, it is followed by a cooling process where the temperature smoothly went down to 300 K within 3000 simulations steps in analogy to the real cooling process, but much faster than in reality. A micro-canonical ensemble (NVE) is utilized for cooling. Finally, we use again the NPT ensemble to equilibrate the final structures for 9 ps at 300 K that allows the volume to change. Since the elastic properties vary slightly with temperature within the interval 0-300 K, we calculate only the 0K elastic constants of the amorphous structures for the sake of saving computational costs. As for force calculations when accuracy is needed, we consider magnetism (FM configuration) and employ a higher cut-off energy of 500 eV. The formation energy is calculated also at 0 K for a better comparison to other calculated crystalline structures.

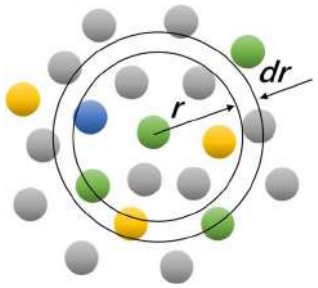

Figure 2.5 - Schematic illustration of the definition of the radial distribution function (rdf) with the reference atom in the centre.

Radial distribution function (rdf) as illustrated in **Figure 2.5** describes how density varies as a function of distance (r) from a reference particle (i), with this definition:

$$g(r[i]) = \frac{n_{pair}[i]}{v[i]} \cdot \frac{V}{N_{pair}} \tag{2.8}$$

where $n_{pair}[i]$ is number of pairs in bin from $r[i]$ to $r[i+1]$, $v[i]$ is the volume of the bin, N_{pair} is number of pairs, and V is the volume of simulation cell. RDF is a crucial parameter because it reflects the interaction between different elements, which can be further linked to microstructural and mechanical properties, e.g., the segregation of *Cu* in *CoCrCuFeNi* can be understood from simulated RDF that the *Cu-Cu* pair correlation is larger than pair correlation between *Cu* and other elements. Besides, RDF can provide average interatomic distance, which can be compared directly to XRD.

Experimentally the average interatomic distance (D) of an amorphous phase, or the average atomic radius (r) can be calculated based on the peak position of the broad hump (principal diffraction peak) that appears in the x-ray diffraction pattern, using the Ehrenfest equation [187]:

$$1.23\lambda = 4r\sin(\theta) \quad (2.9)$$

where λ denotes the x-ray beam wavelength and θ is the Bragg-diffraction angle. Then, considering an FCC or a BCC lattice, an equivalent lattice parameter ($a\sqrt{2}=2D$ or $a\sqrt{3} = 2D$) can be calculated from the average interatomic distance ($D = 2r$).

In this work, the atomic volume and mass density are extracted from the last 1000 frames of the trajectories in equilibrium. For elastic constants calculations, the deformation matrix is the same as for the cubic crystalline materials which will be discussed later in this chapter. For amorphous phases, they have only two independent elastic constants, c_{11} and c_{44}.

2.1.5 Point-defects in lattices and formation energy

2.1.5.1 Point-defects

Point defect is a common type of defect in solids, usually referred to vacancies and interstitials. In transition metal nitrides, a lot of attention has been paid to vacancies, because they can be used to improve the performance of hard coatings by the vacancy/interstitials hardening effect [188, 189].

We assume the vacancies and interstitials are randomly distributed in the materials under study in this work. Under this assumption, we use SQS to model the system with defects, e.g. *TaN*, *TiN*, *ZrN*, *TiZrN* with metal and *N* vacancies, and *N* interstitials for *CoCr(Mn,Cu)FeNiN*$_x$ in a *NaCl* (octahedral interstitials sites) or *ZnS* structure (tetrahedral interstitials sites).

2.1.5.2 Formation energy of a crystal

To compare various systems in terms of their thermodynamic stability, the formation energy, E_f, was calculated as

$$E_f = \frac{1}{\sum_s n_s}\left(E_{tot} - \sum_s n_s \mu_s\right) \quad (2.10)$$

where E_{tot} is the total energy of the supercell, n_s and μ_s are the number of atoms and the chemical potential, respectively. Chemical potential was calculated from the most stable bulk phase of the metal element in nature. In case of *N*, N_2 molecular was chosen as the reference state. The reference energies used in this work are listed in **Table 2.1**.

Table 2.1 - DFT reference energies for VASP formation energy calculations in this work

	N	***Al***	***Ti***	***Zr***	***Ta***	***Nb***	***Cr***	***Mn***	***Fe***	***Co***	***Ni***	***Cu***
Reference state	N_2	FCC	HCP	HCP	BCC	BCC	BCC NM	αMn	BCC FM	HCP FM	FCC FM	FCC
Reference energy (eV/atom)	-8.322	-3.738	-7.801	-8.52	-11.804	-10.212	-9.487	-8.986	-8.237	-7.036	-5.468	-3.726

Balasubramaniana *et al.* [64] has recently calculated defect formation energy for various binary transition metal nitride systems, they found the metal and *N* vacancy have lower formation energy than other defects like antisite defects and interstitials in *TiN*, *ZrN*, and *TaN*. For this reason, we restrict ourselves to the possibility of metal or *N* vacancies

and both in studying defects in simple binaries (including also ternary *TiZrN*) and their effects on elastic properties which will be presented later in Chapter 3.

In the case of high entropy alloy nitrides studied in Chapter 6, we start from *N*-free alloy, increasing gradually the *N* content until the forming of stoichiometric nitrides. The *N* atoms prefer to fill in the interstitial region because it has smaller radius comparing to transition metals.

2.1.6 Elastic constants, sound velocities and homogenization methods

2.1.6.1 Elastic, acoustic and other related properties

A crystal with a cubic symmetry has three independent elastic constants *(c_{11}, c_{12} and c_{44})* and the elements of the fourth rank elastic constant tensor (c_{ijkl}) can be conveniently stored in a 6x6 matrix (c_{ij}), below, considering the Voigt notations (*I = i if i = j and J = k if k = l otherwise I = 9-(i+j) and J = 9-(k+l)*). c_{ij} will refer to the single crystal elastic constants while C_{ij} will later be referred to the effective polycrystalline elastic constants.

$$\begin{pmatrix} c_{11} & c_{12} & c_{12} & 0 & 0 & 0 \\ c_{12} & c_{11} & c_{12} & 0 & 0 & 0 \\ c_{12} & c_{12} & c_{11} & 0 & 0 & 0 \\ 0 & 0 & 0 & c_{44} & 0 & 0 \\ 0 & 0 & 0 & 0 & c_{44} & 0 \\ 0 & 0 & 0 & 0 & 0 & c_{44} \end{pmatrix} \quad (2.11)$$

Elastic constants relate the stress tensor (σ_{ij}) to the strain tensor (ε_{kl}) by the Hooke law ($\sigma = c.\varepsilon$) with $\varepsilon_{ij} = \frac{1}{2}\left(\frac{\partial U_i}{\partial x_j} + \frac{\partial U_j}{\partial x_i}\right)$, $\vec{U}(U_1, U_2, U_3)$ being the displacement vector and

(x_1, x_2, x_3) the Cartesian coordinates. Considering the above Voigt notations, it is convenient to express the Hooke's law with vectors (σ_1, σ_2, σ_3, σ_4, σ_5, σ_6) and (ε_1, ε_2, ε_3, ε_4, ε_5, ε_6) and Hooke's law as follows:

$$\begin{pmatrix}\sigma_1\\ \sigma_2\\ \sigma_3\\ \sigma_4\\ \sigma_5\\ \sigma_6\end{pmatrix} = \begin{pmatrix}c_{11} & c_{12} & c_{13} & c_{14} & c_{15} & c_{16}\\ c_{12} & c_{22} & c_{23} & c_{24} & c_{25} & c_{26}\\ c_{13} & c_{23} & c_{33} & c_{34} & c_{35} & c_{36}\\ c_{14} & c_{24} & c_{34} & c_{44} & c_{45} & c_{46}\\ c_{15} & c_{25} & c_{35} & c_{45} & c_{55} & c_{56}\\ c_{16} & c_{26} & c_{36} & c_{46} & c_{56} & c_{66}\end{pmatrix}\begin{pmatrix}\varepsilon_1\\ \varepsilon_2\\ \varepsilon_3\\ \varepsilon_4\\ \varepsilon_5\\ \varepsilon_6\end{pmatrix} \quad (2.12)$$

The stress-strain approach relies on the feature of VASP to directly calculate the stress tensor. Once the stress tensor components can be computed by an ab initio method, the elastic constants matrix can be directly derived from the generalized Hooke's law. For cubic structures, the Hooke's law can be expressed as,

$$\begin{pmatrix}\sigma_1\\ \sigma_2\\ \sigma_3\\ \sigma_4\\ \sigma_5\\ \sigma_6\end{pmatrix} = \begin{pmatrix}c_{11} & c_{12} & c_{13} & 0 & 0 & 0\\ c_{21} & c_{22} & c_{23} & 0 & 0 & 0\\ c_{31} & c_{32} & c_{33} & 0 & 0 & 0\\ 0 & 0 & 0 & c_{44} & 0 & 0\\ 0 & 0 & 0 & 0 & c_{55} & 0\\ 0 & 0 & 0 & 0 & 0 & c_{66}\end{pmatrix}\begin{pmatrix}\varepsilon_1\\ \varepsilon_2\\ \varepsilon_3\\ \varepsilon_4\\ \varepsilon_5\\ \varepsilon_6\end{pmatrix} \quad (2.13)$$

with $c_{11}=c_{22}=c_{33}$, $c_{44}=c_{55}=c_{66}$, $c_{12}=c_{13}=c_{23}=c_{21}=c_{31}=c_{32}$, we define then the strain matrix mostly used in this work for materials with cubic symmetry,

$$\begin{pmatrix}\varepsilon_1 & \varepsilon_6 & \varepsilon_5\\ \varepsilon_6 & \varepsilon_2 & \varepsilon_4\\ \varepsilon_5 & \varepsilon_4 & \varepsilon_3\end{pmatrix} = \begin{pmatrix}\varepsilon & 0 & 0\\ 0 & 0 & \frac{1}{2}\varepsilon\\ 0 & \frac{1}{2}\varepsilon & 0\end{pmatrix}, \begin{pmatrix}0 & 0 & \frac{1}{2}\varepsilon\\ 0 & \varepsilon & 0\\ \frac{1}{2}\varepsilon & 0 & 0\end{pmatrix}, \begin{pmatrix}0 & \frac{1}{2}\varepsilon & 0\\ \frac{1}{2}\varepsilon & 0 & 0\\ 0 & 0 & \varepsilon\end{pmatrix} \quad (2.14)$$

with ε =0, ±0.002 and ±0.004. The elastic constant matrix can be solved thanks to the stress tensor calculated by *ab-initio* codes. Consequently, the 3 independent single crystal elastic constants (c_{11}, c_{12}, c_{44}) for cubic materials are obtained from average on the relevant elastic matrix component by, The 3 independent elastic constants (c_{11}, c_{12} and c_{44}) were obtained from the following averaging process,

$$c_{11} = \frac{1}{3}(c'_{11} + c'_{22} + c'_{33}) \tag{2.15}$$

$$c_{12} = \frac{1}{6}(c'_{12} + c'_{23} + c'_{13} + c'_{21} + c'_{31} + c'_{32}) \tag{2.16}$$

$$c_{44} = \frac{1}{3}(c'_{44} + c'_{55} + c'_{66}) \tag{2.17}$$

where *c'* denotes the element in the full elastic tensor and can be calculated directly using the stress-strain method. For crystals with lower symmetry, we use a different strain set to derive the full elastic tensor, with ε=0.005.

$$\begin{pmatrix} \varepsilon_1 & \varepsilon_6 & \varepsilon_5 \\ \varepsilon_6 & \varepsilon_2 & \varepsilon_4 \\ \varepsilon_5 & \varepsilon_4 & \varepsilon_3 \end{pmatrix} = \begin{pmatrix} \pm\varepsilon & \frac{1}{2}\varepsilon & 0 \\ \frac{1}{2}\varepsilon & 0 & 0 \\ 0 & 0 & 0 \end{pmatrix}, \begin{pmatrix} 0 & \frac{1}{2}\varepsilon & 0 \\ \frac{1}{2}\varepsilon & \pm\varepsilon & 0 \\ 0 & 0 & 0 \end{pmatrix}, \begin{pmatrix} 0 & \frac{1}{2}\varepsilon & 0 \\ \frac{1}{2}\varepsilon & 0 & 0 \\ 0 & 0 & \pm\varepsilon \end{pmatrix}$$

$$\begin{pmatrix} 0 & \frac{1}{2}\varepsilon & \frac{1}{2}\varepsilon \\ \frac{1}{2}\varepsilon & 0 & 0 \\ \frac{1}{2}\varepsilon & 0 & 0 \end{pmatrix}, \begin{pmatrix} 0 & \frac{1}{2}\varepsilon & -\frac{1}{2}\varepsilon \\ \frac{1}{2}\varepsilon & 0 & 0 \\ -\frac{1}{2}\varepsilon & 0 & 0 \end{pmatrix}, \begin{pmatrix} 0 & \frac{1}{2}\varepsilon & 0 \\ \frac{1}{2}\varepsilon & 0 & \frac{1}{2}\varepsilon \\ 0 & \frac{1}{2}\varepsilon & 0 \end{pmatrix} \tag{2.15}$$

$$\begin{pmatrix} 0 & \frac{1}{2}\varepsilon & 0 \\ \frac{1}{2}\varepsilon & 0 & -\frac{1}{2}\varepsilon \\ 0 & -\frac{1}{2}\varepsilon & 0 \end{pmatrix}, \begin{pmatrix} 0 & \varepsilon & 0 \\ \varepsilon & 0 & 0 \\ 0 & 0 & 0 \end{pmatrix}, \begin{pmatrix} 0 & 0 & 0 \\ 0 & 0 & 0 \\ 0 & 0 & 0 \end{pmatrix}$$

In EMTO methods, the elastic constants are calculated by the energy-strain method described as follows. The deformation matrix, is defined by:

$$D(\varepsilon) = \begin{pmatrix} \varepsilon_1 & \frac{1}{2}\varepsilon_6 & \frac{1}{2}\varepsilon_5 \\ \frac{1}{2}\varepsilon_6 & \varepsilon_2 & \frac{1}{2}\varepsilon_4 \\ \frac{1}{2}\varepsilon_5 & \frac{1}{2}\varepsilon_4 & \varepsilon_3 \end{pmatrix} \tag{2.16}$$

with deformation amplitude $\varepsilon = (0 - \pm 0.05)$ typically applied for stress-strain and crystal ground state (free-stress lattice parameter a_0 and volume V_0) calculations,

$$\sigma_\alpha = \left[\frac{1}{V}\frac{\partial E}{\partial \varepsilon_\alpha}\Big|_s\right]_{\varepsilon=0} \tag{2.20}$$

$$c_{\alpha\beta} = \left[\frac{1}{V}\frac{\partial^2 E}{\partial \varepsilon_\alpha \partial \varepsilon_\beta}\Big|_s\right]_{\varepsilon=0} \tag{2.21}$$

$$\mathrm{E}(\mathrm{V}, \varepsilon_\alpha) = E(V_{0,0}) + V_0\left(\sum_{\alpha=1}^{6}\sigma_\alpha\varepsilon_\alpha\right) + \frac{V_0}{2}\left(\sum_{\alpha,\beta=1}^{6} C_{\alpha\beta}\varepsilon_\alpha\varepsilon_\beta\right) + O(\{\varepsilon_\alpha^3\}) \tag{2.22}$$

For a material with cubic symmetry, volume energy of a crystal is:

$$\frac{E}{V} = \frac{1}{2}c_{11}(\varepsilon_{11}^2 + \varepsilon_{22}^2 + \varepsilon_{33}^2) + \frac{1}{2}c_{44}(\varepsilon_{23}^2 + \varepsilon_{31}^2 + \varepsilon_{12}^2) + c_{12}(\varepsilon_{11}\varepsilon_{22} + \varepsilon_{33}\varepsilon_{22} + \varepsilon_{11}\varepsilon_{33}) + O(\varepsilon^3) \quad (2.23)$$

For the two different strain matrices:

$$\begin{pmatrix} 1+\varepsilon_0 & 0 & 0 \\ 0 & 1-\varepsilon_0 & 0 \\ 0 & 0 & \frac{1}{1-\varepsilon_0^2} \end{pmatrix} \& \begin{pmatrix} 1 & \varepsilon_m & 0 \\ \varepsilon_m & 1 & 0 \\ 0 & 0 & \frac{1}{1-\varepsilon_m^2} \end{pmatrix} \quad (2.24)$$

The energy of the strained crystal is:

$$E(\varepsilon_0) = E(0) + 2V_0 c'\varepsilon_0^2 + O(\varepsilon_0^4) \quad (2.25)$$

$$E(\varepsilon_m) = E(0) + 2V_0 c_{44}\varepsilon_m^2 + O(\varepsilon_m^4) \quad (2.26)$$

$$B = \frac{1}{3}(c_{11} + 2c_{12}), c' = \frac{1}{2}(c_{11} - c_{12}) \quad (2.17)$$

$$B(V) = -V\left(\frac{\partial P}{\partial V}\right) = V\frac{\partial^2 E(V)}{\partial V^2} \quad (2.18)$$

Bulk modulus can be fitted by the Morse equation from the calculated energies of different volumes.

2.1.6.2 Homogenization methods

In the case of polycrystalline films with many small grains (10 nm-µm), we can only measure effective elastic properties within the small surface/volume probed by the nanoindentation or opto-acoustic techniques (~µm). To evaluate these average properties,

two methods were used: (*i*) the well-known Voigt-Reuss-Hill [26] averaging of elastic constants (*C*) or elastic compliances (*S*) over all crystallographic orientation distribution for isotropic or textured materials having cubic symmetry with (111), (011) and (001) preferential growth axis that works well for non-porous materials, and offering analytical formula [190]; (*ii*) an effective-medium-field micromechanics (EMFM) approximation or a self-consistent averaging method adapted to the encountered microstructures (high shape factor with vertical grains h~400 nm, diameter d~10-30 nm, textured or not, with varying porosity concentration $P = 1- \rho/\rho_{dense}$). More details on the EMFM method, can be found in Ref. [191].

Its applicability is later illustrated through its application to thin layers of $(CoCrCuFeNi)_{1-x}(Al_x, Nb_x)$ and $CoCr(Cu,Mn)FeNiN_x$ high entropy alloys with different texture and porosity, elaborated by magnetron sputtering with various concentration of oxygen impurities in the vacuum chamber [8-10]. Well characterized mass density (ρ), porosity (P~5-20%), grain size (5-30 nm), columnar grown grains with <111>-textured (FCC phase), <011>-textured (BCC phase) or isotropic were obtained and some of their elastic properties (G, E_{IT} and C_{33} measured by well-adapted techniques, such as BLS, PLU and nanoindentation.

Regarding the effective properties of the columnar structure of interest, two cases of zero void and nonzero void are considered. For each case, three configurations are defined with respect to the relative orientation of the cylinders' generators and the crystalline direction of the constituting grains. Properly speaking, in these configurations, either crystalline directions (100) or (111) or (011) are parallel with the cylinders'

generators. The columns are assumed to be composed of a single grain and all columns share the same relative orientation with respect to their constituting grains.

2.2 Synthesis, structural and chemical properties of materials

In this section we present the materials studied in this thesis, how they were synthetized and their main structural and chemical properties.

2.2.1 Synthesis of "simple nitrides" and multicomponent metallic alloys films

2.2.1.1 Epitaxial "Simple nitrides" films

A first set of samples was elaborated and experimentally studied prior the beginning of this thesis. The transition metal nitrides (*TMN*) included the (*i*) *TM* metals from IVB group *TiN*, *ZrN* and pseudo binary *TiN-ZrN* solid solutions; (ii) *TM* metals from the VB group *TaN*, *NbN*, *VN*. These "simple" epitaxial thin films were deposited on magnesium oxide *MgO-(001)*, (001) and (111) substrates, using DC magnetron sputtering by Prof. Gregory Abadias at PPRIME Institute (Poitiers University). We recall below the process elaboration conditions and main chemical and structural properties of *TiN-ZrN* and *TaN* systems, we will focus in.

(*i*) Epitaxial *TiN*, *ZrN* and *TiN-ZrN* solid solutions on *MgO*

$Ti_{1-x}Zr_xN$ films , $0 \leq x \leq 1$, were deposited on one-side polished 5×5 mm^2 *MgO (001)* and 10×5 mm^2 *MgO (110)* substrates by DC reactive magnetron co-sputtering from elemental 7.5 cm diameter *Ti* (99.995% purity) and *Zr* (99.2 % purity) targets under $Ar+N_2$ plasma discharges. The targets are arranged in a confocal configuration, located at 18 cm from the substrate holder and with an incident angle of 25° with respect to the substrate

normal. The deposition chamber is equipped with a load-lock system, which allows maintaining a base pressure lower than 5.10^{-6} Pa thanks to a cryogenic pump. The *Zr/Ti* ratio was varied in the whole composition range by controlling the respective power of the *Ti* and *Zr* targets, while operating cathodes at constant power (**Table 2.2**).

Table 2.2: Growth conditions and elemental composition of $Ti_{1-x}Zr_xN_y$ thin films.

Sample	*Ti* Target Power	*Zr* Target Power	P_{N2} (Pa) x10^{-3}	R (nm/s)	Thickness *h* (nm)	*Ti* (at.%)	*Zr* (at.%)	*N* (at.%)	x	y
TiN-M14-33	300	/	5.0	0.13	425	48.4	/	51.6	0	1.06
TiZrN-M15-32	300	105	3.6	0.19	283	35.7	12.2	52.1	0.25	1.09
TiZrN-M16-38	300	105	2.8	0.21	175	33.8	12.2	54	0.26	1.17
TiZrN-M16-39	250	200	2.7		183.5	21.2	22.8	56.0	0.52	1.27
TiZrN-M14-2	250	220	12	0.14	413	19.3	26.0	54.7	0.57	1.21
TiZrN-M16-37	195	300	3.5	0.31	184	12.2	30.0	57.8	0.71	1.37
ZrN-M16-36	/	300					46.4	53.6	1	1.16

The N_2 flow rate was optimized for each film composition to maximize deposition rate while ensuring formation of nearly stoichiometric nitride compounds (0-8 at. % metal under-stoichiometry is found). This corresponded to sputtering conditions under metallic target mode, based on a previous investigation of the hysteresis behavior of the *Ti-Zr-N* system [192]. Note that separate injection gas lines are used, the N_2 being injected in the vicinity of the substrate using a circular ring. The pumping speed of the cryo-pump was fixed at 100 $l.s^{-1}$ using a throttle valve. During deposition, gas pressure was monitored by a Baratron type gauge, while the N_2 partial pressure was determined using a MKS MicroVisionPlus mass spectrometer. The total working pressure was in the 0.20-0.26 Pa range, depending on the targeted *Zr* content. Prior to film deposition, the *MgO* substrates

were ultrasonically degreased in ethanol bath for 5 min and blow-dried using nitrogen. After insertion in the high-vacuum chamber, they were maintained at 600°C during 1h using a resistive heater and then sputter-etched, in pure *Ar* discharge, by applying a bias voltage of –60 V during 90s to remove surface contaminants and improve surface quality. Targets were also sputter-cleaned during 3 min in pure *Ar* discharge. All films were deposited at a substrate temperature of 600°C, and applying a bias voltage of –60 V. The substrate was rotated at 15 rpm throughout the deposition to ensure an even deposition rate and composition uniformity across the substrate. Two films series were synthesized: a first one with film thickness *h* around 100-180 nm, to obtain reliable film thickness determination from X-ray reflectivity (XRR, see **Figure 2.6**), as necessary input for determination of longitudinal sound velocity from PLU.

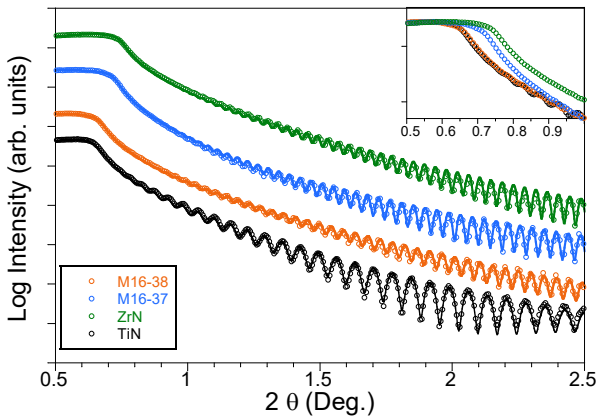

Figure 2.6: XRR scans (symbols) and best-fit curves (solid lines) from $Ti_{1-x}Zr_xN_y$ films on *MgO(001)* substrate. The insert is a magnification around the critical angle.

Thicker films ($h > 300$ nm) were deposited in a second batch, using same deposition conditions, but only increasing the deposition time, and were used to obtain more direct

and accurate measurements of the transverse sound velocity from BLS. For complementary elemental analysis, Si wafers were also employed for this second series.

Film composition was determined from electron probe micro-analysis using a wavelength dispersive Oxford Instruments spectrometer unit attached to a JEOL 7001F-TTLS scanning electron microscope operated at 10 kV. A special calibration and correction procedure were employed to account for *Ti* Lλ and *N* Kα lines overlap, allowing determination of *N* content with an accuracy better than 1 at.%.

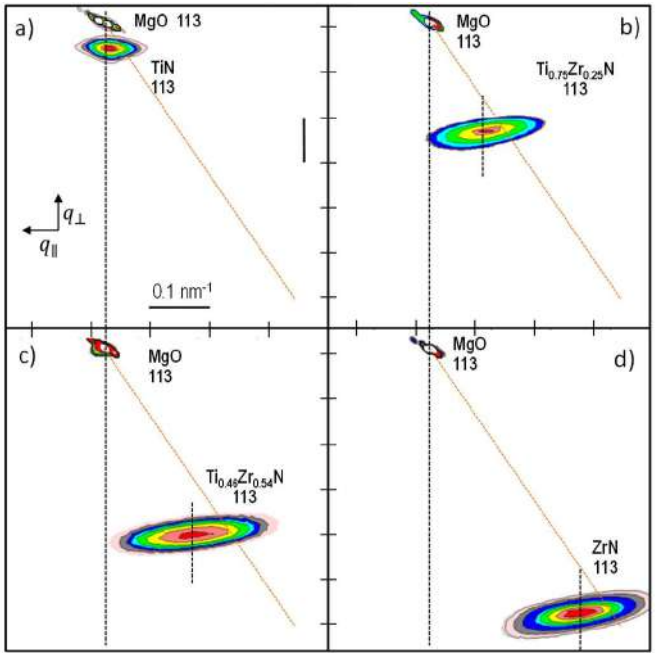

Figure 2.7: Reciprocal space mapping around the (113) reflection of a) *TiN*, b) *$Ti_{0.75}Zr_{0.25}N$*, c) *$Ti_{0.43}Zr_{0.57}N$* and d) *ZrN* films on *MgO (001)* substrate.

Film crystallinity, orientation, lattice parameters and mass density were determined using X-ray diffraction (XRD) and XRR, respectively. XRR scans (see Figure 2.6) were acquired in a four-circle Seifert XRD 3000 diffractometer, using *Cu* Kα_1 radiation (λ= 0.15406 nm) exclusively, in line focus configuration. The primary optics consists of a two-

reflection *Ge*(220) monochromator and a selection slit of 0.1 mm to remove *Cu* $K\alpha_2$ contribution; the secondary optics is composed of a scattered-radiation slit of 0.26° and a scintillation detector defined by an opening angle of 0.018°. XRR scans were fitted based on the optical model of Parratt using Analyze software to obtain the mass density, ρ, film thickness h, and surface roughness. ω-2θ scans (2θ= 31-65°) were acquired using the same parallel-beam configuration, while reciprocal space maps (RSM) around asymmetric 113 reflections (see **Figure 2.7**) were obtained using a 0.05°divergence detector slit.

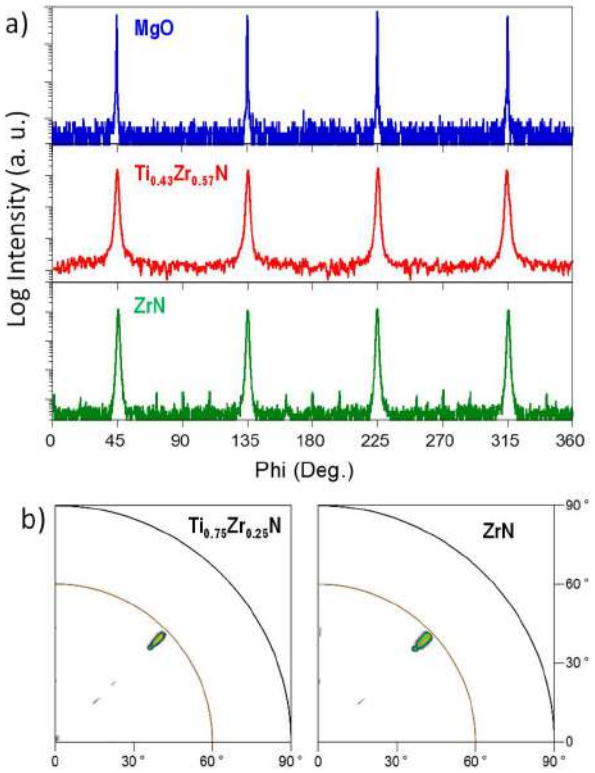

Figure 2.8 - a) Phi scans of the 111 reflections from *$Ti_{0.43}Zr_{0.57}N$* and *ZrN* films deposited on *MgO (001)* substrates, recorded at *ψ=54.74°*. The corresponding phi scan is also shown for the *MgO* substrate. b) Sectors of 111 pole figures from *$Ti_{0.43}Zr_{0.57}N$* and *ZrN* films deposited on *MgO* (001) substrate.

Pole figures, off-axis phi-scans (see

Figure 2.8) and ω-rocking curve scans were obtained in a divergent beam Bragg-Brentano geometry using the same Seifert diffractometer, but operating in point focus with *Cu* Kα radiation (λ= 0.15418 nm), a 1.0 mm diameter primary collimator, a *Ni* filter to remove *Cu* Kβ radiation and a scintillation detector defined with an acceptance angle of 0.13°. It evidenced the cube-on-cube growth of the *TiZrN* films on the *MgO* substrate. Structural properties are provided in **Table 2.3**.

Table 2.3 - Structural parameters extracted from XRD and XRR of $Ti_{1-x}Zr_xN_y$ films.

Sample	ρ (g/cm^3)	ω_{rms} (nm)	$\epsilon_{\parallel}$ (%)	$\epsilon_{\perp}$ (%)	a_0 (nm)
TiN-M14-33	5.1	2.3	0.21	0.13	0.4245
TiZrN-M15-32	6.1	1.3	0.39	0.23	0.4352
TiZrN-M16-38	5.8	1.0			
TiZrN-M16-39	6.25	0.8	0.90	0.49	0.4449
TiZrN-M14-2	6.4	1.8	1.34	0.74	0.4444
TiZrN-M16-37	7.0	1.6	0.84	0.41	0.4508
ZrN-M16-36	7.4	1.7	0.55	0.24	0.4581

(*ii*) Epitaxial *TaN* on *MgO*

TaN films (~150 nm thick) were grown by direct current (DC) reactive unbalanced planar magnetron sputtering in a load-locked high-vacuum (base pressure < 8×10^{-6} Pa) chamber with a target-to-substrate separation of 18 cm. Films were deposited on single-crystal *MgO (001), MgO (110) and MgO (111)* substrates at a growth temperature T_s=570°C and using a constant substrate bias voltage of –60 V. A 3 in. *Ta* (99.998 % purity) target was sputtered at constant DC power (200 W) in an *Ar* (30 sccm)-N_2 (4 sccm) plasma discharge at a total pressure of 0.65 Pa, the N_2 gas being injected in the close vicinity of

the substrate via a circular ring. The N_2 flow rate (corresponding to a N_2 partial pressure of 0.05 Pa) was adjusted so as to obtain stoichiometric *TaN* films, based on earlier studies on the growth of polycrystalline *TaN* films on *Si* [2, 192]. Deposition time was fixed to 25 min.

Elemental composition was investigated by wavelength-dispersive X-ray spectroscopy (WDS) microanalysis unit from Oxford Instruments attached to a JEOL-7001F-TTLS scanning electron microscopy operated at 10 kV. It is of importance to notice that films were found to be nearly stoichiometric (see **Table 2.4**).

The crystal structure and crystal orientation were characterized by X-ray diffraction (XRD) using a four-circle Seifert XRD 3000 diffractometer equipped with *Cu* tube, operated under different configurations. θ–2θ scans were recorded in line focus mode using a monochromatic beam (*Cu* Kα_1 radiation of wavelength λ= 0.15406 nm obtained from a two-crystal *Ge*(220) monochromator) and a scintillation detector defined by an opening angle of 0.018° as secondary optics. The same parallel beam configuration was used to collect reciprocal space map (RSM) around asymmetric 113 reflection of the *TaN/Mg(001)* film, using a 0.05°divergence detector slit. Pole figures, off-axis φ-scans and ω-rocking curves were acquired using the Seifert XRD 3000 diffractometer operating in point focus mode with *Cu* Kα radiation (wavelength λ= 0.15418 nm), a *Ni* filter to remove *Cu* Kβ reflections, and a scintillation detector defined with an acceptance angle of 0.21°.

X-ray reflectometry (XRR) was employed to determine the thickness *h*, mass density ρ_{XRR} and surface roughness η of the *TaN* films. Scans were recorded using the Seiffert XRD 3000 diffractometer in line focus mode using the same primary and

secondary optics as θ–2θ scans described above. XRR scans were fit to theoretical curves calculated from the optical formalism of Parratt [193] using Analyze proprietary software and assuming a three layer model (surface layer/*TaN* film/ *MgO* substrate). The room temperature electrical resistivity ρ_{300K} was measured using a standard four-point probe (with collinear geometry) set-up. Structural properties and electrical resistivity are provided in **Table 2.4**.

Table 2.4 – Deposition parameters, structural parameters extracted from XRD and XRR and electrical resistivity of *TaN* films.

Sample	Deposition temperature (°C)	p_{N2} (Pa)	h (nm)	Ta/N ratio	ρ_{XRR} (g/cm^3)	a_0 (nm)	ω_{rms} (nm)	$\epsilon_{\parallel}$ (%)	$\xi_{\perp}$ (nm)	ρ_{300K} (μΩ.cm)
TaN(001)	570	0.05	154	0.96	15.6	0.4359		22		/
TaN(110)	570	0.05	148	/	15.7	/				/
TaN(111)	570	0.05	/	/	/	/				252

2.2.1.2 *(CoCrCuFeNi)$_{1-x}$(Al$_x$, Nb$_x$)* polycrystalline films

Polycrystalline solid solutions of *(CoCrCuFeNi)$_{1-x}$(Al$_x$, Nb$_x$)* MCAs were also previously investigated within the PhD work of B. Braeckman [7] under the supervision of Pr. D. Depla at Gent University. Experimental results obtained during his PhD work will be compared to our theoretical predictions. We briefly recall here, some information on the deposition process and important microstructural characteristics (chemical composition, crystalline phase, lattice parameter, mass density and porosity fraction). Information on the samples is summarized in **Table 2.5**.

(CoCrCuFeNi)$_{1-x}$Nb$_x$ films were deposited by sputtering powder targets at various deposition conditions. In addition to the *CoCrCuFeNi* base metal, four powders targets were prepared with a nominal *Nb* atomic concentration of 5, 10, 15, and 23 at.% *Nb*. A constant discharge current of 0.09 A with a typical discharge power of 40 W, was used for all depositions. The *Ar* gas pressure (p) and target-substrate distance (d) were varied ($p{\cdot}d$= 2.8, and 3.85 Pa.cm) as film thickness between 305 and 800 nm. The deposition conditions did not influence the film's chemical composition. As the *Nb* concentration increases, the lattice distortion of the FCC solid solution increases as well because *Nb* is a larger element than the five TMs. From Braeckman results [7], it was argued that the critical solute concentration for which the crystalline solid solution phase becomes unstable, can be calculated with the topological model of Egami [194] and further extended to MCAs by [195]. When the Goldschmidt corrections for the atomic radii are taken into account, Egami's model predicts that at 18.2 at.% *Nb* the crystalline solid solution becomes topologically unstable. However, the XRD results (see **Figure 2.9**) indicate that the amorphization already occurs at lower *Nb* concentrations, i.e. at 15 at.% *Nb* [6]. Moreover, if the standard deviation on the fit parameter in Egami's model is taken into account, the amorphization should occur between 13.9 and 22.8 at.% *Nb*. Hence, for the *(CoCrCuFeNi)$_{1-x}$Nb$_x$* system, Egami's model gives a fair, but rather crude prediction of the amorphization threshold. Grains size are in are very tiny in the range 0 - 6 nm (0 is for amorphous phase) and are embedded by an amorphous shell at the grain boundary [9].

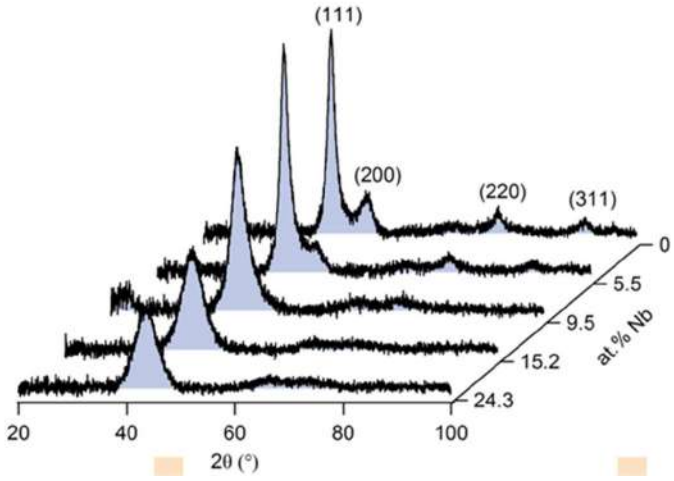

Figure 2.9 - XRD patterns of the *(CoCrCuFeNi)$_{1-x}$Nb$_x$* films as a function of the *Nb* atomic concentration (films deposited at 2.8 Pa·cm). The patterns were normalized to the respective film thickness (from [6, 7]).

The *(CoCrCuFeNi)$_{1-x}$Al$_x$* films were synthesized by a joined effort of Belgian and French research groups. F. Boydens (Ghent University), H. Hidalgo, P. Dutheil, A.-L. Thomann (Université d'Orléans, France), and M. Jullien (Université de Lorraine, France) performed the depositions [5]. These depositions were performed in a vacuum chamber with a lower base pressure, approximately 10^{-5} Pa. Hence, the impurity flux is an order of magnitude lower than during the other experiments. This should be kept in mind if one wants to compare the properties of the different HEAs. Four powder targets (T1, T2, T3, T6) with different compositions were made [5]. The composition of the targets and the average composition of the corresponding films remained very close. The standard deposition conditions were: 0.5 Pa *Ar* pressure, a constant discharge current of 0.09 A, a target-substrate distance of 9 cm, room temperature substrate and a grounded substrate holder were used. The phase formation was determined with XRD. No intermetallic compounds were detected in any of the samples.

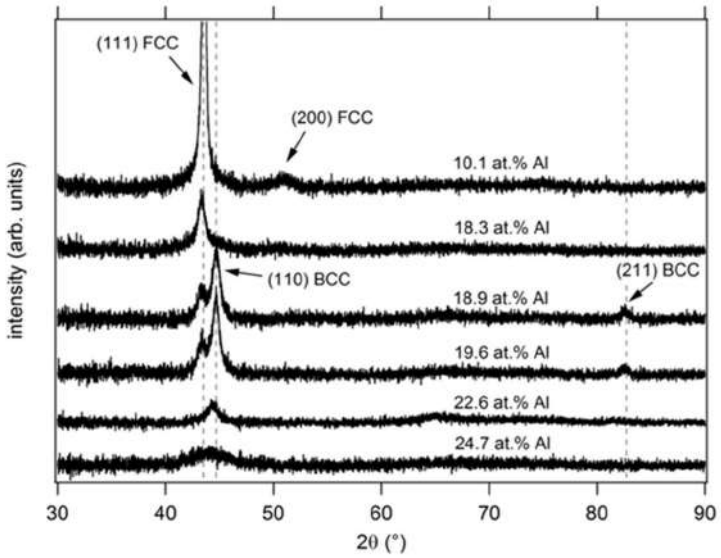

Figure 2.10 – A selection of XRD patterns to indicate the transition from FCC to BCC solid solutions. At 24.7 at. % *Al*, the film is XRD-amorphous (from Refs. [5, 7]).

Figure 2.10 presents a selection of XRD patterns from [5, 7]. The phase formation in the $(CoCrCuFeNi)_{1-x}Nb_x$ alloys was explained by a critical lattice distortion due to the incorporation of the larger *Nb* atoms. The same principle is also valid for the $(CoCrCuFeNi)_{1-x}Al_x$ films. Again, *Al* has a larger atomic radius as compared to the base elements, and an increase in the *Al* fraction increases the FCC lattice distortion. In contrast to elemental *Nb*, *Al* exhibits the same crystalline structure as the *CoCrCuFeNi* solid solution, i.e. the FCC structure. Hence, the Goldschmidt correction should not be used, and the atomic radius of elemental *Al* can be directly employed. Egami's topological model predicts that the FCC solid solution becomes unstable at 21.8 at. % *Al*. This threshold seems to be an acceptable prediction, as for *Al* concentrations larger than 19.6 at. % *Al*, only single-phase BCC-structured or amorphous films are formed. The instability of the close-packed FCC structure is predicted well by Egami's topological model. Nevertheless, the

amorphous phase is preceded by the BCC structure. Already at 16.5 at.% *Al*, a mixed FCC/BCC structure is formed. Just as the amorphous phase, the BCC structure is more able to incorporate larger atoms, and to cope with a severe lattice distortion. FCC structures consist of both octahedral and close-packed tetrahedral atomic clusters, whereas BCC structures only consist of octahedral clusters. Close-packed tetrahedral structures are more resistant against deformation, and the incorporation of larger elements in the FCC lattice increases the lattice distortion energy. The transition from the metastable FCC structure to the more open BCC structure relaxes the distortion energy. The reason why the amorphous phase is preceded by the BCC structure in the $(CoCrCuFeNi)_{1-x}Al_x$ alloys, and not in the $(CoCrCuFeNi)_{1-x}Nb_x$ alloys should be explained by the interaction between *Al* and *TMs*. Due to the peculiar electronic structure of *Al*, i.e. the outer shell contains three electrons, it prefers to transfer electrons to the incompletely filled *d*-shells of TMs, and thereby form strong bonds. This was evidenced by the atomic-bond shortening due to the strong *sp-d* orbital hybridization. Tang et al. pointed out that for TMs with a partially-filled d-shell, the BCC structure is close to the FCC structure in terms of stability [85]. Hence, the incorporation of an element rich in valence electrons, drives the system to a BCC structure.

Table 2.5 - Growth conditions, phase identification, elemental composition and porosity fraction (*P*) of *(CoCrCuFeNi)$_{1-x}$(Al$_x$, Nb$_x$)* films.

Sample	Power W	*p·d* Pa.cm	*a* (nm)	Mass density (g/cm^3)	Phase	*h* (nm)	*x*	*P*
CoCrCuFeNi	40	2.8	0.359	8.590	FCC	659	0	~0
CoCrCuFeNiNb$_{0.055}$	40	2.8	0.360	8.565	FCC	739	0.055	~0
CoCrCuFeNiNb$_{0.089}$	40	2.8	0.363	8.545	FCC	908	0.089	~0
CoCrCuFeNiNb$_{0.145}$	40	2.8	0.3577	8.743	Amorphous	676	0.145	~0
CoCrCuFeNiNb$_{0.23}$	40	2.8	0.3577	8.630	Amorphous	620	0.23	~0
CoCrCuFeNiAl$_{0.09}$	40	4.5	0.360	7.46	FCC	364	0.09	0.05
CoCrCuFeNiAl$_{0.096}$	40	4.5	0.360	7.26	FCC	295	0.096	0.07
CoCrCuFeNiAl$_{0.101}$	40	4.5	0.360	7.56	FCC	485	0.101	0.03
CoCrCuFeNiAl$_{0.168}$	40	4.5	0.361	6.93	FCC	390	0.168	0.06
CoCrCuFeNiAl$_{0.196}$	40	4.5	/	6.82	FCC	/	0.196	0.05
CoCrCuFeNiAl$_{0.165}$	40	4.5	0.286	6.53	BCC	308	0.165	0.12
CoCrCuFeNiAl$_{0.174}$	40	4.5	0.286	6.61	BCC	415	0.174	0.10
CoCrCuFeNiAl$_{0.189}$	40	4.5	0.287	6.23	BCC	398	0.189	0.14
CoCrCuFeNiAl$_{0.196}$	40	4.5	0.287	6.51	BCC	392	0.196	0.09
CoCrCuFeNiAl$_{0.226}$	40	4.5	0.290	6.13	BCC	/	0.226	0.13
CoCrCuFeNiAl$_{0.246}$	40	4.5	0.2875	6.13	BCC	512	0.246	0.11

Subscript in the sample list denotes *Nb/Al* atomic concentration. E.g., *CoCrCuFeNiNb$_{0.055}$* is alloyed with 5.5 at. % Nb.

2.2.2 Synthesis of bulk CoCrCuFeNi and CoCr(Cu, Mn)FeNiN$_x$ films

2.2.2.1 Polycrystalline bulk *CoCrCuFeNi*

CoCrCuFeNi bulk HEA ingot was synthetized by arc melting at IMR (Shenyang, China) by Pr. Dong and homogenized by several heating cycles. Several disk pieces 1” and 2” diameter, 3 mm thick were prepared to serve as targets for films growth a new batch of

CoCrCuFeNi-N films, and small cylinders (1 mm diameter, 2 mm height, 21.3 mg mass) for DSC (heat capacity C_P) and VSM analysis (magnetic state). The results of films' growth will be compared to a previous batch synthetized with a compacted powder composite target [10]. The measured heat capacity at room temperature is C_p(293 K) = 390 J/(kgK) while a paramagnetic behavior is observed from the hysteresis loop (see Figure 2.11) with a magnetization at 20 kOe of 1.59 emu/g close to the value (1.505 emu/g) reported by [119].

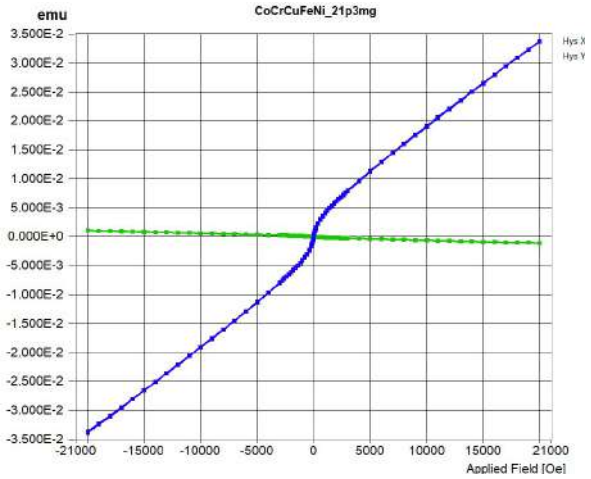

Figure 2.11 – Hysterisis loop of a *CoCrCuFeNi* cylinder ($d \approx 1$ mm, $h \approx 2$ mm height, $V = 2.68\ 10^{-3}$ cm^3, $m = 21.3$ mg). $M(H) \approx 1.3\ \frac{emu}{cm^3}$ or $1.59\ \frac{emu}{g}$ at a magnetic field $H = 20$ kOe.

Tensile tests samples were also prepared for mechanical characterizations at IMR. Diameter was $\phi = 3$ mm, initial length $L_0 = 15.0$ mm and traverse velocity $V_t = 1$ mm/mn. A typical stress-strain curve is shown in **Figure 2.12**. The mechanical properties (elastic limit $Rp_{0.2}$, ultimate strength Rm, ductility A, striction Z, strain elastic limit ε_e and Young's modulus E) are reported in **Table 2.6**. While the yield stress is comparable to the one (230

MPa) found by [119], our Young's modulus is three times higher and ductility four times lower.

Table 2.6 – Structural (a_0, ρ), mechanical (σ_y, σ_f, A, Z, ε_P), thermal (λ, D, C_p) and magnetic properties of homogenized *CoCrCuFeNi*.

a_0	ρ	λ	D	C_P (293K)	M (20 kOe)	$\sigma_{y0.2}$	σ_f	A	Z	ε_c	E
nm	g/cm^3	W/(mK)	mm^2/s	J/(kgK)	emu/cm^3	MPa	MPa	%	%	%	GPa
0.3596	7.9645	15	4.83	390	1.3	261.2	336.0	12.3	14.13	0.1	164

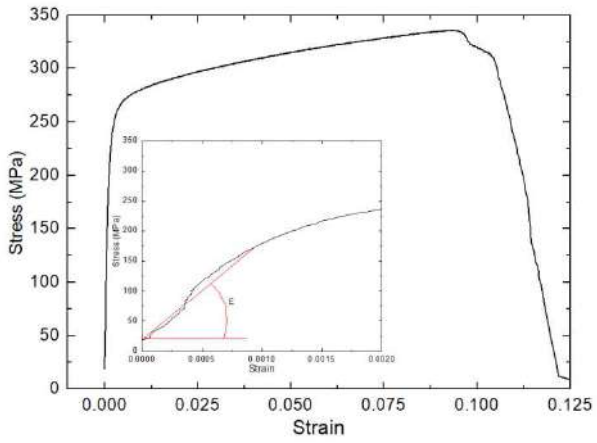

Figure 2.12 – Tensile stress-strain curve of *CoCrCuFeNi* rod with diameter of 3 mm. The insert shows the Young's modulus measured by the initial slope.

X-ray diffraction (see **Figure 2.13**), scanning electron microscopy and electron dispersive spectroscopy (see **Figure 2.14** and **Figure 2.15**) were conducted at LSPM.

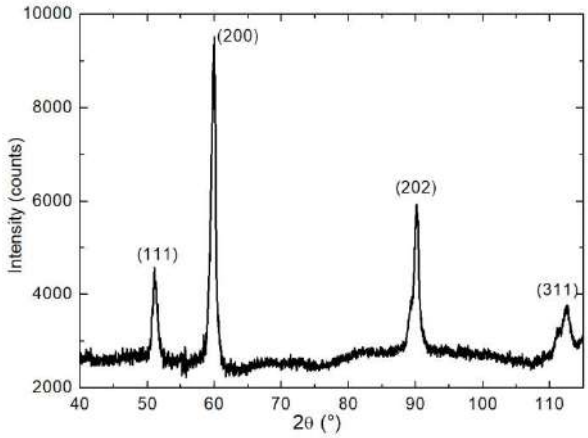

Figure 2.13 – XRD pattern (λ_{Co} = 0.1789 nm) of bulk as-cast and homogenized FCC *CoCrCuFeNi*.

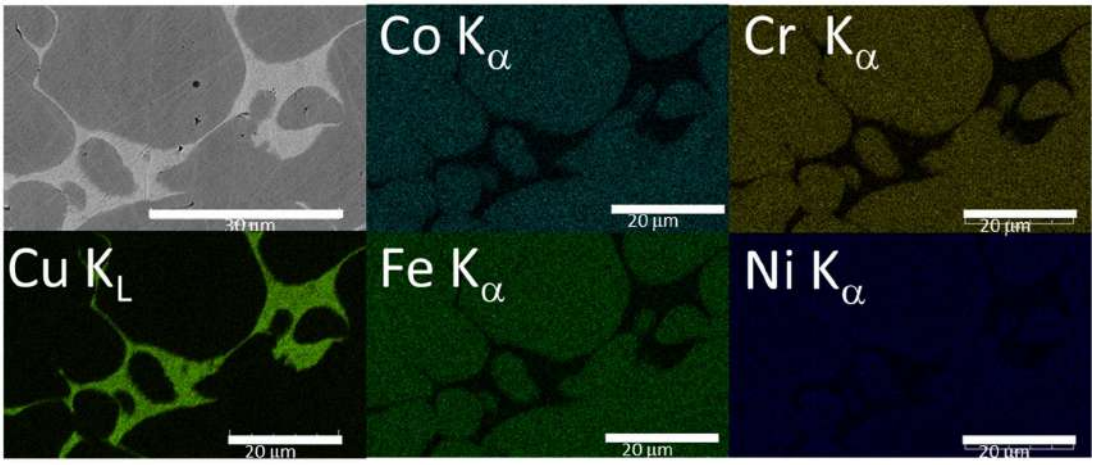

Figure 2.14 – Typical SEM microstructure of as-cast *CoCrCuFeNi* and EDS maps of alloying elements at the same location.

The structure is FCC with a lattice parameter a_0 = 0.3596 nm, near equiatomic concentration and some *Cu* (*Ni* to a less extent) segregation appearing at the grain boundaries (GBs) delimiting a rich-*Cu* (~88 at. %) interdendrite (ID) narrow phase (~5-10 µm width) and larger dendrite phase of *CoCrCuFeNi* grains (~30 µm) with a *Cu* gradient near GBs (see **Figure 2.15** and **Figure 2.16**). Microstructure is similar to the one observed

in Ref. [196]. It is clear that peaks pattern resembles a FCC structure and it is confirmed by the d_{hkl}/d_{111} ratios as-discussed also in [197] study of ball milled HEA. The lattice parameter of this FCC phase was estimated to be 0.3602 nm. The lattice parameter of as-cast *CoCrFeNiCu* alloy [119] was reported to be 0.3579 nm, which is also in agreement with the value measured in the present work. EBSD analysis (see **Figure 2.16**) has been done around the area of one nanoindentation mapping delimited by larger indent mark. The indented two grains have a crystallographic orientation close to the <001>.

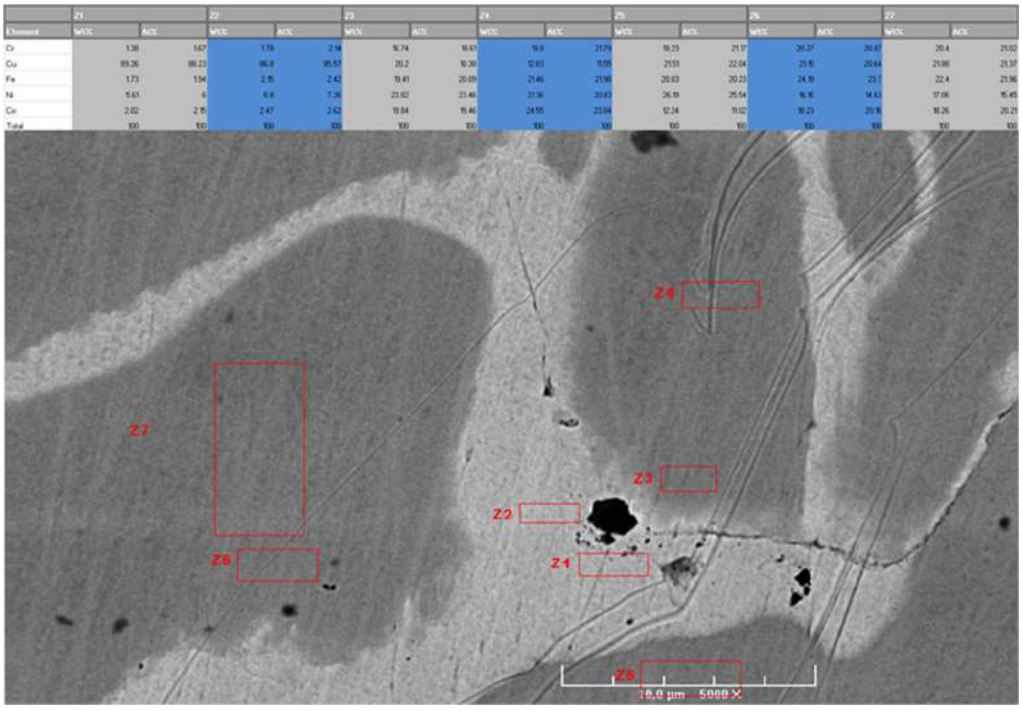

Figure 2.15 - SEM microstructure of as-cast *CoCrCuFeNi* and local EDS analysis at different locations (z1-z7).

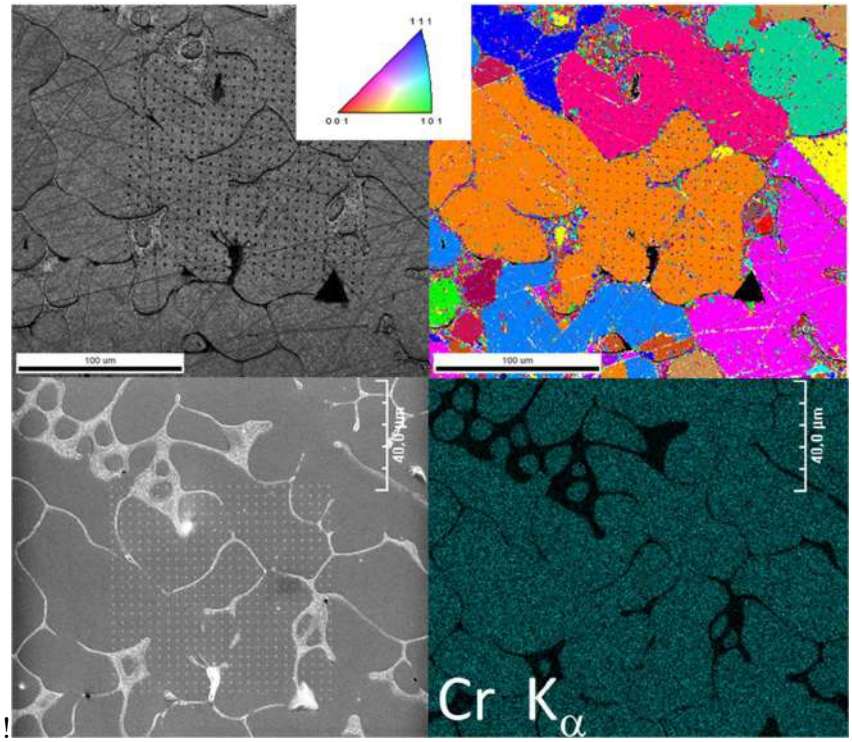

Figure 2.16 - SEM microstructure of as-cast *CoCrCuFeNi*, EDS mapping of *Cr* element and EBSD analysis at the same location. Indents from nanoindentation mapping are visible.

Thermal conductivity and a map with thermal contrast were also measured over the same area by a modulated thermoreflectance microscopy technique, in collaboration with Pr. Daniele Fournier and Pr. L. Belliard (@INSP). For the mapping, a pump laser is modulated at 1.8 MHz to heat the sample and a superimposed probe beam detected the change of sample reflectivity at the same frequency across a lock in amplifier. Using the DC signal, reflected by the sample surface, an optical image could be recorded in order to locate the grain boundaries (see **Figure 2.17a**). In same time, the modulated sample reflectivity is mapped and normalized by the optical image to shed light on thermal contrast (see **Figure 2.17b**). The resulting signature is correlated with lateral thermal properties change of the sample. By this way, spatial variation of photo thermal coefficient, which links the optical

index with the temperature, may be revealed and compared to a composition map. The variation of thermal diffusion length and all thermal barriers, playing the role of thermal resistance is also a source of signal. As we can notice the inner grain thermal signature is nearly uniform but all the boundaries exhibited a huge fluctuation in **Figure 2.17b** prove that thermal properties are nearly constant for different grain orientations in opposition with the rich copper segregated zones (black areas).

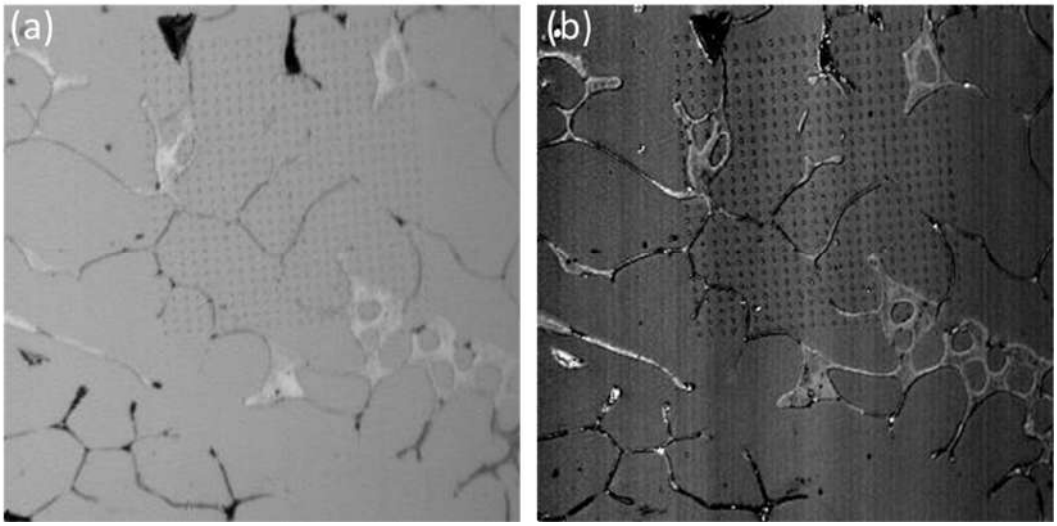

Figure 2.17 - (a) Optical image, scale 286x286µm^2. The indentation marks as well as the rich copper grains are clearly visible. (b) Thermal image obtained on the same area for a modulation frequency of 1.8 MHz.

The thermal conductivity was measured by considering the pump moving along a line and the probe fixed in the middle, for different modulation frequency. Then, the amplitude and phase of the reflected probe light is fitted by a numerical model providing the thermal conductivity λ = 15 W/(mK). Finally, using the mass density 7.9645 ± 0.002 g/cm^3 measured by the picnometer method, we can calculate the thermal diffusivity $D = \lambda/(\rho C_p)$ = 4.83 10^{-6} m^2/s.

2.2.2.2 Polycrystalline *CoCr(Cu, Mn)FeNiN$_x$* films

Polycrystalline solid solutions of *CoCr(Cu, Mn)FeNiN$_x$*, MCAs were studied nearly at the same time within the PhD work of R. Dedoncker under the supervision of Pr. D. Depla at Gent University. His first experimental results obtained on *CoCrCuFeNiN$_x$* films deposited using a powder target on a silicon substrate [10] were repeated but with the bulk HEA solid target (1" in diameter) within a new high vacuum chamber, and compared to our theoretical predictions. A second close system *CoCrMnFeNiN$_x$* made again from a powder target was considered in order to have comparisons when *Cu* is replaced by the magnetic *Mn*, avoiding segregation issues observed for *CoCrCuFeNi*. We briefly recall here, some information on the deposition process and important chemical and microstructural characteristics and difference of films deposited both on silicon and Kapton® flexible substrate. Films on Kapton were specifically designed for later tensile tests that will be described in the last chapter 7, serving as a presentation of future perspective works assessing brittleness/ductility behavior of films.

Magnetron sputtering depositions were performed in a stainless ultrahigh vacuum chamber pumped by a combination of a rotary and turbomolecular pump with a 1-inch diameter planar cylindrical magnetron. The base pressure was monitored by a Penning Gauge (Compact Full Range gauge, Pfeiffer Vacuum), which is less than 10^{-4} Pa when using silicon substrates, while for Kapton substrates, the base pressure was slightly higher.

Table 2.7 - Growth conditions, phase identification, elemental composition of *CoCrCuFeNiN$_x$* films. Thin films and thick films batches are distinguished.

N (at.)	*RN*	Power W	$p \cdot d$ (Pa. cm)	*a* (nm)	Mass density (g/cm^3)	Phase identification	*h* (nm)	Target	*P* (Pa)
0	0	40	3.2	0.359	8.5	FCC	361	solid	0.5
0.06	2	40	3.2	0.362	8.3	FCC	459	solid	0.5
0.08	3	40	3.2	0.366	8.2	FCC	439	solid	0.5
0.09	4	40	3.2	0.367	8.2	FCC	441	solid	0.5
0.11	5	40	3.2	0.371	8.2	FCC	423	solid	0.5
0.13	6	40	3.2	0.371	8.2	FCC	426	solid	0.5
0.14	7	40	3.2	0.373	8.1	FCC	434	solid	0.5
0.15	8	40	3.2	0.374	8.1	FCC	418	solid	0.5
0.17	10	40	3.2	0.377	8	FCC	451	solid	0.5
0.18	12	40	3.2	0.378	7.9	FCC	451	solid	0.5
0.22	16	40	3.2	0.382	7.8	FCC	408	solid	0.5
0.24	20	40	3.2	0.386	8.1	FCC	429	solid	0.5
0.28	25	40	3.2	0.389	7.9	FCC	433	solid	0.5
0.28	30	40	3.2	0.393	8.1	FCC	455	solid	0.5
0.30	40	40	3.2	0.398	7.9	Amorphous	449	solid	0.5
0.31	50	40	3.2	/	7.6	Amorphous	273	solid	0.5
Thin films above, thicker ones below									
0.02	0			0.361	8.6	FCC	1162	powder	0.5
0.13	12			0.373	8.2	FCC	1134	powder	0.5
0.15	16			0.378	8.1	FCC	1159	powder	0.5
0.17	20			0.385	7.9	FCC	1154	powder	0.5
0.19	25			0.390	7.8	FCC	1138	powder	0.5
0.20	30			0.393	7.6	FCC	1278	powder	0.5
0.21	35			0.394	7.6	FCC	1211	powder	0.5
0.24	40			0.397	7.5	FCC	1294	powder	0.5
0.26	50			0.401	7.4	FCC	1180	powder	0.5

The Argon and nitrogen gas flows were controlled by the MKS mass flow controllers. The argon flow rate was set to 20 standard cubic centimeters per minute (sccm) to reach a partial *Ar* pressure of 0.5 Pa. The nitrides were deposited in the Ar-N_2 mixture

gas at a flow rate of 20 standard cubic centimeters per minute with the total gas pressure (P_{Ar}+P_{N_2}) being maintained at 0.5Pa. The ratio of the N_2 partial pressure (P_{N_2}) to the total gas pressure, denoted as *RN* ($RN = \frac{P_{N_2}}{P_{N_2}+P_{Ar}}$), was manipulated to control *N* concentration of films.

The magnetron was powered by a Hüttinger 1500DC power supply. The discharge current was fixed at 0.08 A. The target to substrate distance was fixed at 63 mm for *CoCrCuFeNiN*$_x$ deposition and 32 mm for *CoCrMnFeNiN*$_x$ deposition. The silicon substrates were cut from 0.55 mm thick (111) oriented silicon wafer.

Note, for both *CoCrCuFeNi* and *CoCrMnFeNi*, there exists two series as shown in **Table 2.7** and **Table 2.8**, respectively, either with a low thickness below 500 nm, or a higher thickness above 1000 nm. Among which the author deposited the thinner films while the thicker ones were provided by Robin Dedoncker (PhD student) @Ghent University. The purpose was to evaluate influence of deposition conditions, the thickness effect, repeating experiments and ensuring higher accuracy of V_L longitudinal sound velocity measurements by picosecond laser ultrasonic.

Mass density of the films was measured by X-Ray-Reflectivity (XRR). The thicknesses of thin films were measured by a profilometer. *N* content was measured by Wavelength-Dispersive-Spectroscopy (WDS).

Table 2.8 - Growth conditions, phase identification, elemental composition of *CoCr(Mn)FeNiN*$_x$ films. Thin films and thick films batches are distinguished.

N (at.)	*RN*	Power W	$p \bullet d$ (Pa. cm)	*a* (nm)	Mass density (g/cm^3)	Phase identification	*h* (nm)	Target	*P* (Pa)
0	0	40	1.6	0.358	7.9	HCP/ Amp.	355	powder	0.5
0.09	2	40	1.6	0.358	7.9	FCC/ Amp.	453	powder	0.5
0.12	3	40	1.6	0.367	7.9	FCC/ Amp.	394	powder	0.5
0.15	4	40	1.6	0.370	7.9	FCC/ Amp.	441	powder	0.5
0.17	5	40	1.6	0.374	7.9	FCC/ Amp.	397	powder	0.5
0.18	6	40	1.6	0.374	7.8	FCC/ Amp.	400	powder	0.5
0.20	8	40	1.6	0.381	7.8	FCC/ Amp.	380	powder	0.5
0.24	10	40	1.6	0.395	7.7	FCC/ Amp.	478	powder	0.5
0.27	12	40	1.6	0.393	7.6	FCC/ Amp.	454	powder	0.5
0.30	16	40	1.6	0.398	7.6	FCC	438	powder	0.5
0.32	20	40	1.6	0.402	7.6	FCC	365	powder	0.5
0.34	25	40	1.6	0.403	7.5	FCC	423	powder	0.5
0.37	30	40	1.6	0.406	7.5	FCC	452	powder	0.5
0.38	40	40	1.6		7.5	FCC	104	powder	0.5
0.40	50	40	1.6	0.410	7.5	FCC	396	powder	0.5
Thin films above, thicker ones below									
0.03	0			0.359	8.2	FCC	1192	powder	0.5
0.12	12			0.371	8	FCC	1214	powder	0.5
0.16	16			0.378	7.8	FCC	1181	powder	0.5
0.19	20			0.390	7.6	FCC	1195	powder	0.5
0.22	25			0.397	7.6	FCC	1231	powder	0.5
0.23	30			0.400	7.5	FCC	1314	powder	0.5
0.26	35			0.404	7.5	FCC	1261	powder	0.5
0.28	40			0.408	7.4	FCC	1283	powder	0.5
0.30	50			0.410	7.4	FCC	1269	powder	0.5

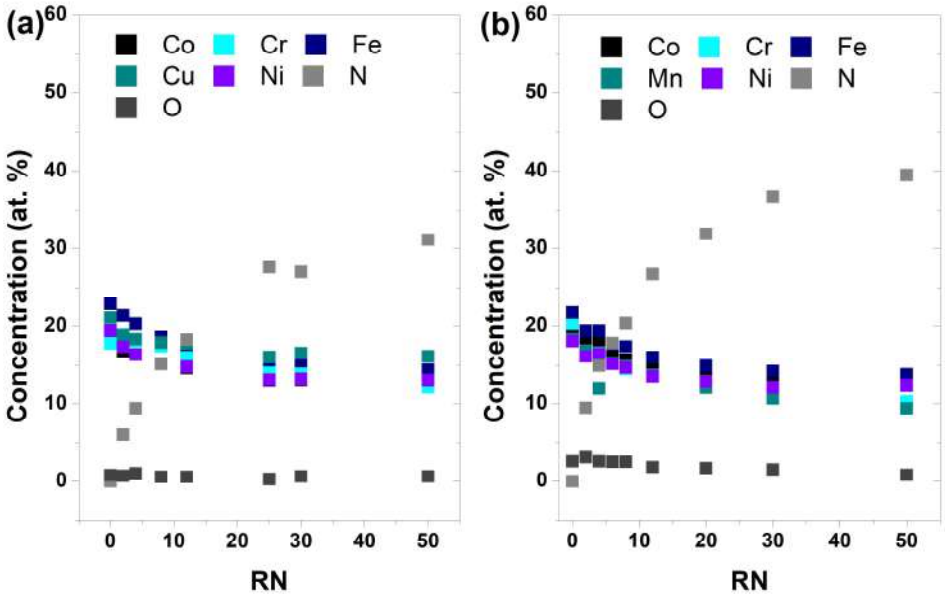

Figure 2.18 - The elements mapping of thinner (a) *CoCrCuFeNiN$_x$* and (b) *CoCrMnFeNiN$_x$* as a function of *RN*. The metallic elements were measured by EDX. The N and contamination O were measured by WDX.

The gradual increase of *N* concentration was observed as *RN* increasing for both series as shown in **Figure 2.18**. The highest *N* concentration reached was 39.5% and 31.1% for *Mn* and *Cu* series respectively. Higher *N* concentrations cannot be reached because of target poisoning when nitrides form on the surface of the target.

Oxygen impurity level with the typical value of 2 at. % was higher in the *Mn* alloy batch than the *Cu* alloy one due to a powder target was used. With a solid *CoCrCuFeNi* target, the oxygen contamination was less than 1 at. %. A gradual decrease of *O* concentration can be seen in *Mn* series as *N* concentration increasing, which is not obvious for the *Cu* series. The metallic elements concentration shows an almost equimolar character for all the films, with a standard deviation of less than 2.5% for most of the samples.

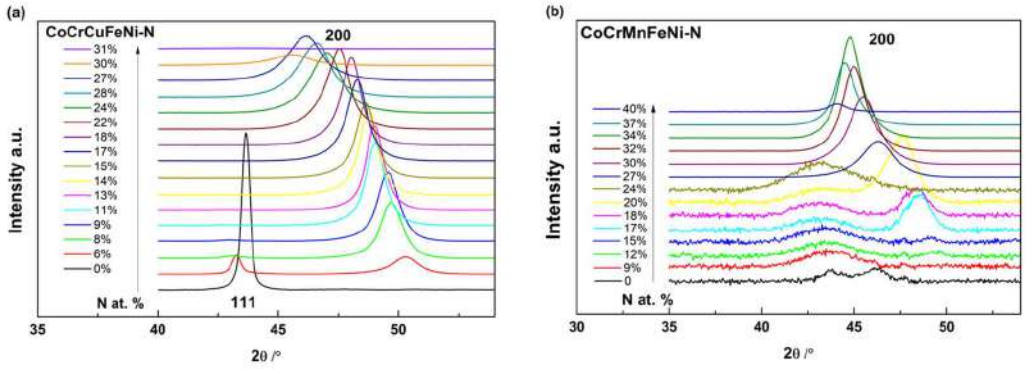

Figure 2.19 - The XRD *θ-2θ* pattern for (a) *CoCrCuFeNiN$_x$* and (b) *CoCrMnFeNiN$_x$* thin films batch. *N* concentration of each sample is given, which increases from bottom to top as indicated by the black arrow. The XRD intensity of *CoCrMnFeNiN$_x$* in *N* concentration range from 0% to 24% are magnified due to low peak intensity.

With the addition of *N*, the appearance of the peak between 45° to 50° is the main feature of the *Cu* series as shown in **Figure 2.19a**. This peak corresponds to the (200) plane of a *NaCl*-type cubic phase. A smooth peak shift to lower *2θ* values with increasing *N* suggests a smooth increase of *d*-spacing and the lattice parameter. Above 9% *N* concentration, only one peak is visible, indicating the films might be well (200)-textured at higher *N* concentrations. At low *N* concentrations, there exists also the peak corresponding to the (111) plane of the *CoCrCuFeNi* FCC phase. The highest intensity of (111)-peak was found in the *N*-free *CoCrCuFeNi* sample, suggesting a preferred (111) growth orientation. However, this *N*-free *CoCrCuFeNi* sample is not completely <111> textured because a (200)-peak can also be seen. With the increase of *N* content, the (200)-peak intensity starts to increase at 6 at. % *N* addition. Meanwhile the (111) peak intensity decreases and vanishes at 9 at. % *N*. Further increase of *N* over 22 at. % *N* leads to a decrease of (200) peak intensity, with the peak width increasing at the same time. This

behavior indicates that the crystallinity of the *CoCrCuFeNiN$_x$* cannot be maintained at high *N* concentrations.

N-free metallic *CoCr(Cu,Mn)FeNi* films with different thicknesses were deposited on *Si*, aiming to provide more comparisons to mechanical properties of the bulk material as well as to evaluate the thickness effects.

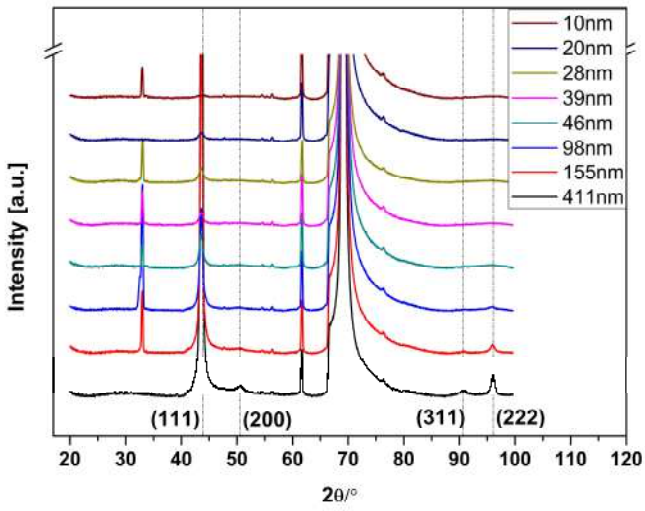

Figure 2.20 - XRD patterns of *CoCrCuFeNi* with different thicknesses deposited on *Si* substrate. Lattice planes of FCC *CoCrCuFeNi* were indicated by the dash lines. Other peaks without any indication come from *Si* substrate.

The pure metallic *CoCrCuFeNi* thin films are polycrystalline with several grain orientations revealed by XRD in **Figure 2.20**. The close packing (111) planes have dominant peak intensity among all the peaks, which is more significant when the thin becomes thinner as other peaks can barely be seen. The lattice parameter remains nearly constant (~0.3595 nm) close to the one measured in the bulk sample, except for the thicker film (~0.353 nm), a sign of residual stresses changes. The films were further characterized by optoacoustic techniques to provide the elastic properties as a function of film thickness.

Furthermore, *N*-free metallic *CoCr(Cu,Mn)FeNi* films with different thicknesses were deposited on Kapton substrate for tensile tests as it will be presented in chapter 7. As shown in **Figure 2.21**, the films were found to be polycrystalline for all thicknesses. The derived stress-free lattice parameter is 0.3596 nm (thickness > 80 nm), in accordance with the DFT value of 0.3564 nm (<1% difference) and measured one (0.3596 nm) in the bulk material.

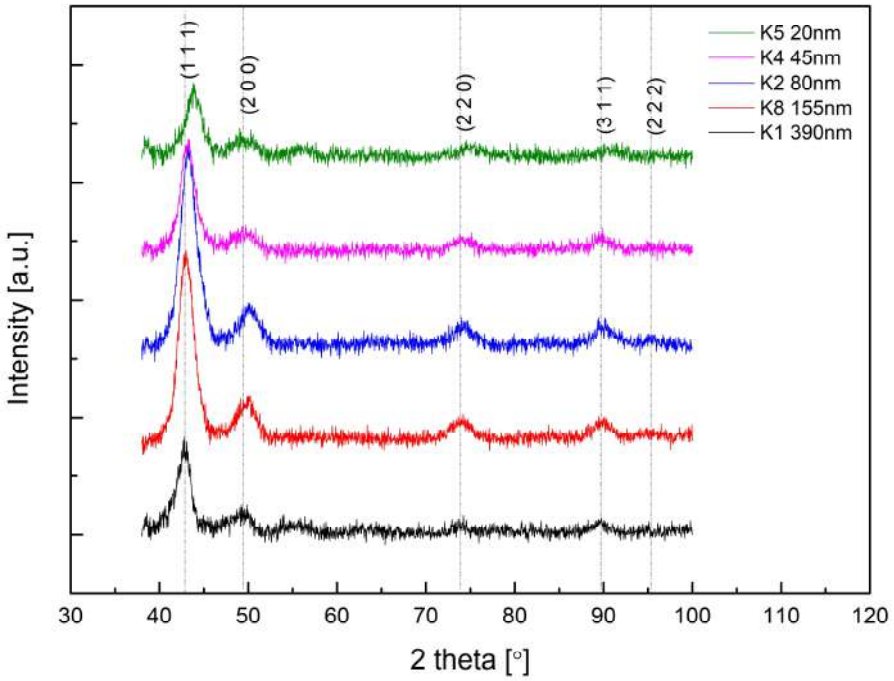

Figure 2.21 - XRD pattern of *CoCrCuFeNi* deposited on Kapton with different thickness.

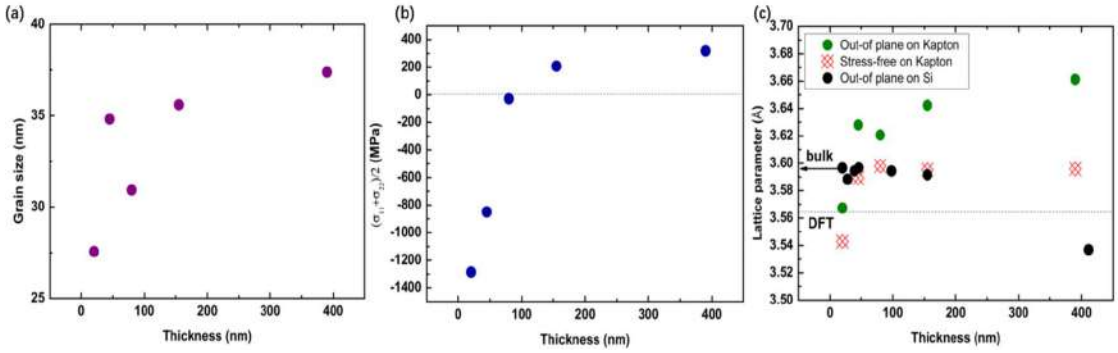

Figure 2.22 - (a) Grain size (b) residual stress and (c) lattice parameter as a function of the thickness of *CoCrCuFeNi* deposited on Kapton®.The values of DFT, bulk, as well as films on *Si* are together given as a comparison.

The grain size in **Figure 2.22a** was derived from Scherrer equation according to the peak width. The grain size lies in the range from 25 to 40 nm and increases with thickness. The in-plane residual stress was measured by the $sin^2(\psi)$ method as summarized in **Figure 2.22b**. It was found that on Kapton substrate, *CoCrCuFeNi* thin films (<100 nm) were in compression while thicker ones (100-400 nm) were in tension by contrast. It offered the possibility to compare the stress-free lattice parameters vs. the thickness, to the DFT one and reference bulk material (**Figure 2.22c**). A very good agreement was found for thicknesses above 80 nm.

2.3 Structural and chemical characterizations techniques

This section recalls briefly the principles of the main structural and elemental characterization techniques employed in this work, with a special emphasis on those necessary to the analysis of sound velocities (V_L, V_T) (thickness h, phase identification, crystallographic orientation) measured by our optoacoustic techniques and their relation to elastic constants $C \sim \rho V^2$ (ρ is the mass density). Most of these characterizations were done

by our collaborators: B. Braeckman, R. Dedoncker and D. Depla @Gent University and G. Abadias @PPRIME Institute, Poitiers University. In the particular case of phase and residual stresses analysis of *CoCr(Cu,Mn)FeNi*, additional XRD measurements were performed by Li Linwei at Paris Saclay University (Pr. Vincent Ji group). We will not provide all details of the equipment in all locations.

2.3.1 X-ray reflectivity and x-ray diffraction

2.3.1.1 X-ray reflectivity

The film density was measured with X-ray reflectivity (XRR). A Bruker D8 Advance was equipped with a scintillation detector @Gent while a Seiffert XRD 3000 diffractometer in line focus mode @PPRIME. In both cases, a *Cu* Kα radiation was used. The samples were scanned from 0.3° to 3° with a step size of 0.01°. The obtained XRR patterns were fitted by using the WinGIXA software @Gent or using Analyze proprietary software @PPRIME. A three-layer model with a topmost oxidized layer, SiO_2 layer on a *Si* substrate or a modified surface layer on the binary/ternary nitrides films on *MgO* substrate, was used in the fitting procedure. For a selection of samples, the density was also calculated by using Parratt's method [193] and the critical angle of total reflection (θc). The complex refraction index can be written as: $n = 1\text{-}\delta\text{-}i\beta$ [198], where β is related to the linear absorption coefficient of the material (μ) and the wavelength of the X-rays (λ). The parameter δ represents the dispersion and is linked to the material density (ρ). If the chemical composition and critical angle are known, the film density (in g/cm^3) can be calculated with:

$$\rho = 1203\ \theta_c^2\ E_X^2 \frac{\sum_{i=1}^{n} c_i M_i}{\sum_{i=1}^{n} c_i f_{1,i}} \qquad (2.19)$$

where c_i, M_i, and $f_{1,i}$ are respectively the atomic fraction, atomic mass, and first atomic scattering factor of the i^{th} element [199]. EX is the energy of the X-rays (8.0478 keV for Cu Kα$_1$ radiation and 6.93037 keV for CoKα$_1$ radiation). Common relative uncertainty on the film density is 2 %.

2.3.1.2 X-ray diffraction

Bragg's law gives a general relationship between the wavelength of the incident X-ray and the spacing of atomic planes [200]:

$$n\lambda = 2dsin\theta \qquad (2.20)$$

where n is the order of reflection; λ is the wavelength of the X-ray; d is the interplanar spacing of the crystal and θ is the incident angle. **Figure 2.23** illustrates the diffraction with respect to Bragg's law.

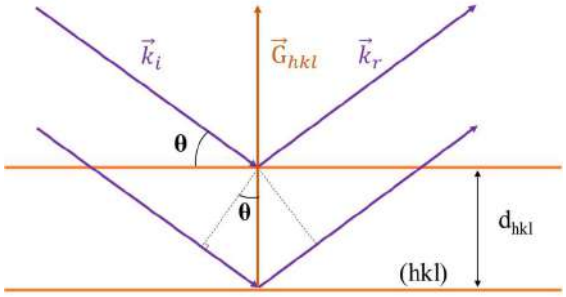

Figure 2.23 - Schematic illustration of Bragg's law in XRD.

Both phase identification and residual stress determination were performed employing PANalytical X'Pert MRD system with a copper radiation source (λ = 0.154 nm).

Grazing incidence X-ray diffraction with a fixed incident angle of 0.5° was carried out for phase identification and stress determination of thin films. Different incidence beam configurations were installed for phase and stress analysis. For the former, a mirror equipped with a mask of 5 mm and a divergence slit of 1/8° were chosen to guarantee an intense monochromatic quasi parallel beam in one dimension and thus formed a radiated area of 2 × 34.5 mm^2 on the specimen surface. For stress analysis, a lens with a collimator set as 7 mm in width and 5 mm in length was used to form a quasi-parallel beam in two dimensions, generating a radiated area of 8 × 680 mm^2 with respect to a psi angle of 0°. Both analyses were conducted using an ultra-fast detector (X'Celerator) equipped with an anti-scatter slit of 5.5 mm and a soller slits assembly of 0.4 rad to balance the efficiency and resolution.

(*i*) *Phase analysis*

The operation voltage and current were set as 45kV and 40mA respectively. 12-hour 2θ scan for each specimen was carried out from 38° to 100° with a step size of 0.04° and time per step of 3200 seconds. Diffraction pattern obtained was analyzed thanks to the software HighScore Plus (version 3.0e).

(*ii*) *Stress analysis*

For *CoCrCuFeNi* thin films on flexible substrate discussed in chapter 7, the residual stress measurements and data treatments are performed by PhD student Li Linwei at Paris Saclay university (Pr. Vincent Ji group) with respect to the European standard NF EN 15305 (version of April 2009) [201]. The classical $sin^2(\psi)$ method was chosen for residual

stress determination in this work, of which the principle can be described briefly in the following:

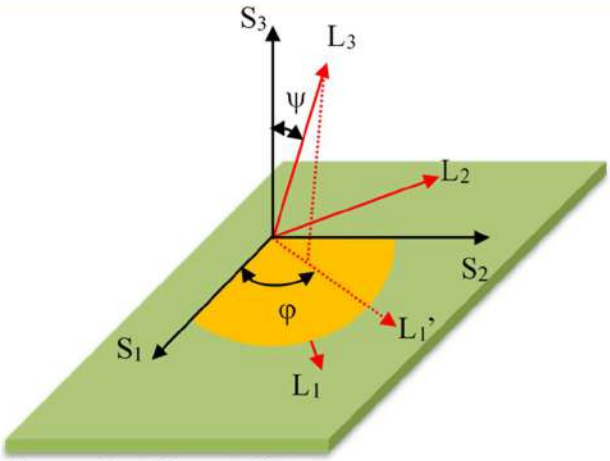

S1, S2 and S3: the specimen's coordinate system

L1, L2 and L3: the laboratory's coordinate system (L_3 is the normal direction of the diffraction lattice planes (hkl))

φ: the angle between S_1 (the direction in the sample plane defined artificially) and L_1' (the projection direction of L_3 and the direction of the stress σ_φ measured)

ψ: the angle between the sample normal and the normal of diffraction lattice planes

Figure 2.24 - The geometry related to residual stress determination.

According to elastic mechanics, with consideration of macroscopically isotropic crystalline material, the strain in the direction L_3 (shown in **Figure 2.24**) can be given by:

$$\varepsilon_{\psi\varphi}^{\{hkl\}} = \left(\frac{1+\nu}{E}\right)(\sigma_{11}\cos^2\varphi + \tau_{12}\sin 2\varphi + \sigma_{22}\sin^2\varphi)\sin^2\psi + \left(\frac{1+\nu}{E}\right)\sigma_{33}\cos^2\psi - \left(\frac{\nu}{E}\right)(\sigma_{11}+\sigma_{22}+\sigma_{33}) + \left(\frac{1+\nu}{E}\right)(\tau_{13}\cos\varphi + \tau_{23}\sin\varphi)\sin 2\psi \quad (2.21)$$

where σ_{11}, σ_{22} and σ_{33} are the normal stress components in the direction of S_1, S_2 and S_3; τ_{12}, τ_{13} and τ_{23} are the shear stresses in the planes defined by correlated coordinates.

The strain defined by the angle of ψ and ϕ can also be expressed as:

$$\varepsilon_{\psi\varphi}^{\{hkl\}} = ln\left(\frac{d_{\psi\varphi}}{d_0}\right) \cong \frac{d_{\psi\varphi} - d_0}{d_0} \tag{2.22}$$

where $d_{\psi\varphi}$ denotes the spacing of selected lattice planes; d_0 denotes the strain-free lattice spacing of the same lattice places as the ones of $d_{\psi\varphi}$.

Combining the above two equations, yields the relationship between the stress induced spacing change with stress components and elastic constants.

The issue of thin films belongs to the biaxial stress analysis scope ($\sigma_{33} = \tau_{13} = \tau_{23} = 0$), and $\varepsilon_{\psi\varphi}^{\{hkl\}}$ can thus be given by:

$$\varepsilon_{\psi\varphi}^{\{hkl\}} = \left(\frac{1+\nu}{E}\right)(\sigma_{11}\, cos^2\,\varphi + \tau_{12}\, sin\, 2\varphi + \sigma_{22} sin^2\varphi)\, sin^2\,\psi - \left(\frac{\nu}{E}\right)(\sigma_{11} + \sigma_{22}) \tag{2.23}$$

from which a linear relation is found between $\varepsilon_{\psi\varphi}^{\{hkl\}}$ and $\sin^2\psi$, and consequently a plot of strain as a function of $\sin^2\psi$ can be used to determine residual stress. In practice, the occurrence of curve deviations is due to the instrument causes, but sometimes it is caused by the out-of-plane stress which is assumed as zero. In this work, these deviations were treated as the shear stresses involved with planar normal stresses.

Considering the high-resolution configurations of XRD instrument, the relatively severe peak shifting caused by low Bragg angle chosen can be ignored. It is critical to choose an appropriate reflect angle with sufficiently high peak intensity in order to guarantee the accuracy of peak position. Therefore, the *d*-spacing change of (111) plane families was selected. 2θ scan was conducted centering around 43.5° with a deviation of ± 2.5° respectively at seven selected psi angles from -51° to 51°, where the step size was set as 0.05° and the time per step as 3200 seconds. For planar principal stress determination, each set of 2θ scan was repeated at the three phi angles of 0°, 10° and 170° respectively. Twenty-one peaks measured corresponding to various psi and phi angles were recorded for each specimen in total, which were analyzed using the software X'Pert Stress (version 1.0a). Considering the errors of normal and shear stresses deriving from the instrument and data treatment, a quarter of stress value was set as the maximum limit of error.

2.3.2 Scanning electron microscope, energy and wavelength dispersive X-ray dispersive spectroscopy

The film composition was measured with energy-dispersive X-ray spectroscopy (EDX) in combination with a scanning electron microscope (SEM) @LSPM (A. Garcia Sanchez and O. Brinza) or @ PPRIME institute (Pr. G. Abadias). The typical error on the chemical analysis is within 1 at. %. For accurate N concentration determinations, wavelength-dispersive X-ray spectroscopy (WDS) was employed instead, because EDX can lead to high level of errors in the case of *N* or *O* measuring.

2.4 Methods for films' mechanical properties assessment

This section recalls briefly the principles of the main characterization techniques employed in this work, with a special emphasis on the mechanical properties of thin films mostly done at LSPM.

2.4.1 Tensile test coupled to a Keyence microscope

This technique newly developed @LSPM, is used at the end this thesis to illustrate some perspectives. We aim to have access to supplementary mechanical properties such as fracture toughness, plastic deformation and yield strength of thin films and nanostructures to correlate to the elastic properties. Here, we coupled a micro-tensile test device (DEBEN®) to a confocal KEYENCE microscope (See **Figure 2.25**). Specially prepared films (DRAFT group, @Gent unversity on flexible substrate) such as Kapton, permitted to strain the film and observe the cracks appearance and development, followed by the buckling, by acquiring sequential pictures. Later analysis of these pictures (on-set crack appearance, cracks density, distance between cracks, buckles …) in combination with mechanical models permits the measurements of plastic deformation (ε_p) and fracture toughness K_{Ic} of the film.

Figure 2.25 – KEYENCE confocal microscope coupled to the micro-tensile test DEBEN device.

2.4.2 Nanoindentation

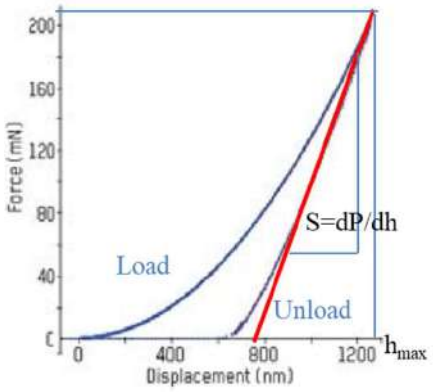

Figure 2.26 - Schematic illustration of the loading-unloading cycle during nanoindentation measurements.

The hardness (H) and indentation modulus (E_{IT}) of the MCAs films were measured with a nanoindentation device (XP model from MTS/Agilent). Nowadays, this technique is a conventional one and commonly used in most of R&D Lab for measurement of the indentation test Young's modulus (E_{IT}) and the hardness (H). This will be used for

comparison to our elastic properties measurements by optoacoustic methods and providing complementary information on the plasticity behavior.

For this purpose, a Berkovich indenter penetrated into the films acquiring at the same time the required force. To omit any contribution of the substrate, only the films with a thickness of minimum 400 nm were measured, and the indentation depth was below 40 nm. The force and indentation depth were measured during the loading-unloading cycle. After calibrating the effective contact area function using a fused-silica calibrate, an analysis of the maximum indentation load (P_{max}), maximum displacement (h) and effective contact area (A) allows calculating (H) and (E_{IT}) [202]:

$$H = \frac{P_{max}}{A} \tag{2.24}$$

The elastic unloading stiffness ($S = dP/dh$) is defined as the slope of the unloading curve during the initial stages of unloading (see **Figure 2.26**). The indentation modulus is then:

$$E_{IT} = \frac{S}{2\beta}\sqrt{\frac{\pi}{A}} \tag{2.25}$$

where β is a dimensionless parameter to account for the deviations in stiffness due to the lack of axial symmetry of pyramidal indenters. The indentation modulus is related to the Young's modulus as follows:

$$\frac{1}{E_{IT}} = \frac{1-\nu^2}{E} + \frac{1-\nu_i^2}{E_i} \tag{2.26}$$

where ν_i, E_i, ν, and E are respectively the Poisson's ratio and Young's modulus of the indenter and film. The nanoindentation measurements were performed by Dr. F. Tétard @LSPM.

2.4.3 Picosecond laser ultrasonic (PLU)

The PLU technique introduced by H. J. Maris in the 1980s [203] derives from the well-known optical pump-and-probe scheme (see **Figure 2.27**). A femtosecond laser pulse (the pump beam) is absorbed at the sample surface. This absorption generates, by thermal expansion, a longitudinal acoustic wave that propagates through the system, perpendicularly to the free surface. Partly reflected and transmitted at all the interfaces of the sample (see **Figure 2.27**), the acoustic wave in return is then probed at the free surface. It is detected from the reflectivity change of the sample surface using a variable time-delayed laser pulse, commonly called the probe beam (see **Figure 2.27**). For a monolithic film onto a substrate, sharp reflectivity changes are periodically detected, so-called echoes, separated by a constant time delay as in a standard sonar technique. These acoustical features superimposed at periodic time of arrival (time of flight, *TOF*) on the photo-thermal decaying background, as illustrated in **Figure 2.28**, in case of *CoCrCuFeNi* films with variable thickness. The real and imaginary parts of the relative change in the surface transient reflectivity $\Delta r(t)/r_0$ induced by such acoustical strain may be measured by interferometric or reflectivity measurements [204]. Consequently, if the thickness (h) of the layer is known, PLU gives a direct access to the vertical longitudinal sound velocity ($V_L = 2h/TOF$). Additionally, in-plane surface acoustic waves could be generated in the

GHz frequency range, if the size of the laser excitation area is small enough [205] and detected using a classical interferometer [206].

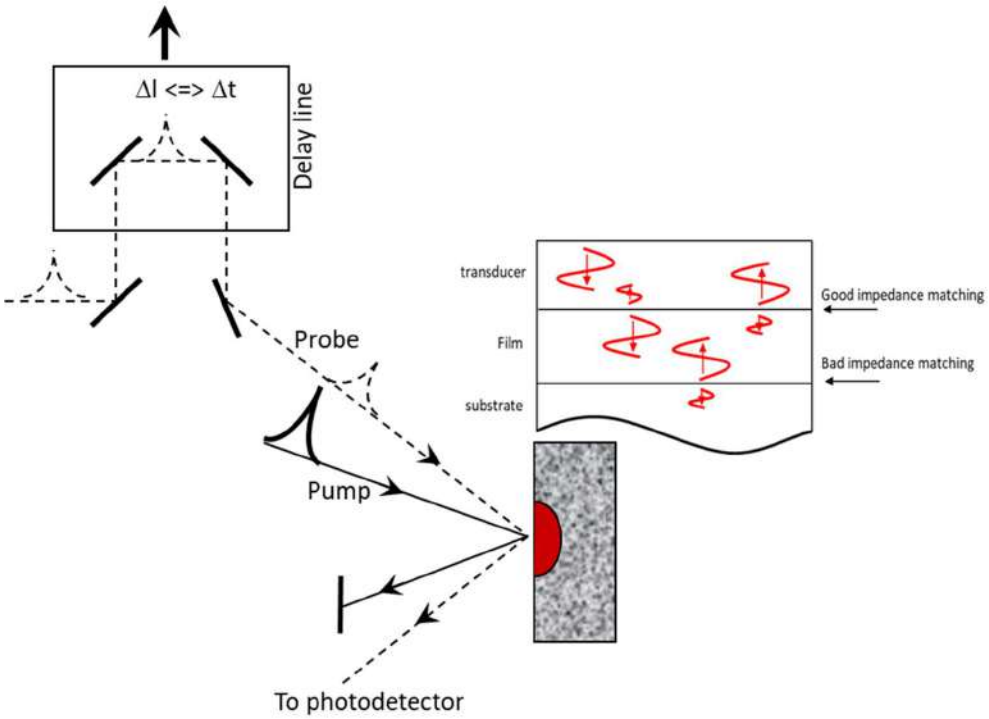

Figure 2.27 – Schematic sketch of the PLU pump-probe setup and echoes traveling forth and back in the film.

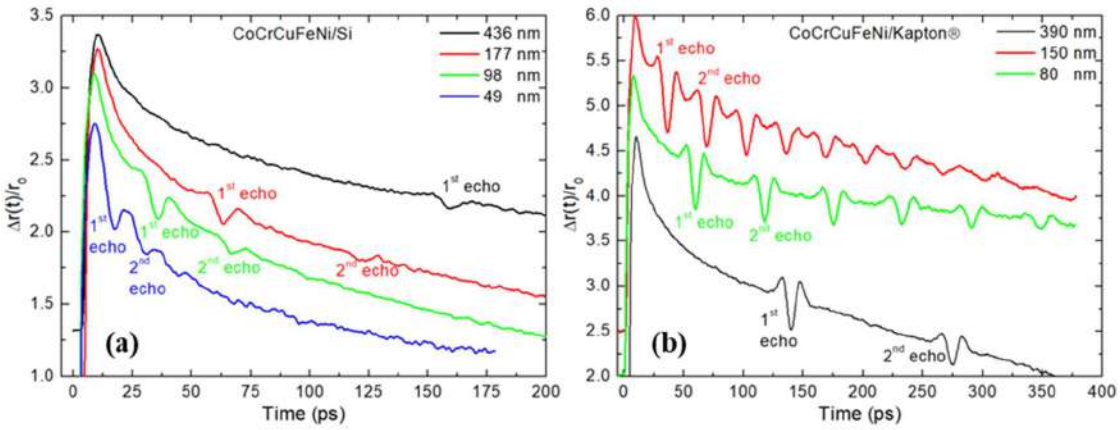

Figure 2.28 – Transient reflectivity of *CoCrCuFeNi* films vs. thickness, (a) films on silicon substrate, (b) films on Kapton substrate.

One of the advantages of this powerful technique is the large frequency domain of the generated acoustic waves, mainly imposed by the optical properties of the materials. By this way, a frequency range from 100 MHz up to 1 THz is routinely achieved, overcoming by three orders of magnitude the bandwidth limitations associated to standard piezoelectric sensors. Ultra-short acoustic waves have been used successfully to investigate acoustic properties in various systems, such as thin films [204, 207], multilayer [208, 209], isolated dots [210] or phononic crystals [211, 212].

In the present case of metallic and nitrides thin films, a standard picosecond laser ultrasonic approach is convenient to extract the longitudinal sound velocity along the normal of the film-plane, V_L. In the experimental set-up (@INSP with collaboration of E. Charron, Pr. L. Belliard and Dr. B. Perrin, we used a mode-locked *Ti*:Sapphire laser source, operating at 800 nm with a repetition rate around 79.3 MHz. The pump beam is modulated at 1.8 MHz to improve the signal-to-noise ratio. The longitudinal velocity is simply defined by $V_L = 2h/\Delta t$, where Δt is the time delay between two consecutive echoes, measured with an accuracy better than 1 ps (see **Figure 2.28**). obviously, the accurate knowledge of the film thickness h is also crucial. A particular effort has been made for measuring accurately the thicknesses: by XRR for thin films (< 200 nm) and mechanical profilometer for the thicker ones. Representative PLU measurements showing the relative change in surface reflectivity, $\Delta r(t)/r_0$, versus time are reported in **Figure 2.28**, for *CoCrCuFeNi* films with different thickness on silicon and Kapton® substrate, showing the modification of time of flight.

Another strong advantage of the PLU technique is its ability to measure directly/selectively the vertical C_{33} elastic constant along the normal of the film plane, from the relation $C_{33} = \rho (V_L)^2$. Thus, the result should be the same for highly textured polycrystalline films as for epitaxial ones, enabling the knowledge of one single-crystal elastic constant, in the case of (001) orientation (i.e. c_{11}), or a combination of c_{ij}*'s* for other orientations (e.g., in the case of (111) orientation $(c_{11}+c_{12}+4c_{44})/3$ or in the case of (011) orientation $(c_{11}+c_{12}+2c_{44})/2)$, among three (resp. five) for cubic (resp. hexagonal) materials.

2.4.4 Brillouin light scattering (BLS)

BLS has proved to be very efficient technique for achieving a complete elastic characterization of thin films and multilayered structures [213]. In a BLS experiment, a monochromatic light beam is used to probe the thermally excited acoustic waves which are naturally present in the investigated medium. The power spectrum of these excitations is mapped out from frequency analysis of the light scattered within a large enough solid angle. Because of the wave vector conservation rule in the phonon–photon interaction (see **Figure 2.29**, $\boldsymbol{Q}_2 = \pm(\boldsymbol{k}_s - \boldsymbol{k}_i)$), the wavelength of the revealed elastic waves with wave vector $\boldsymbol{Q}_2$ is of the same order of magnitude as that of light (incident and scattered optical wave vector $\boldsymbol{k}_i$ and $\boldsymbol{k}_s$) and then is much larger than the interatomic distances, so that the material can be described as a continuous effective-medium.

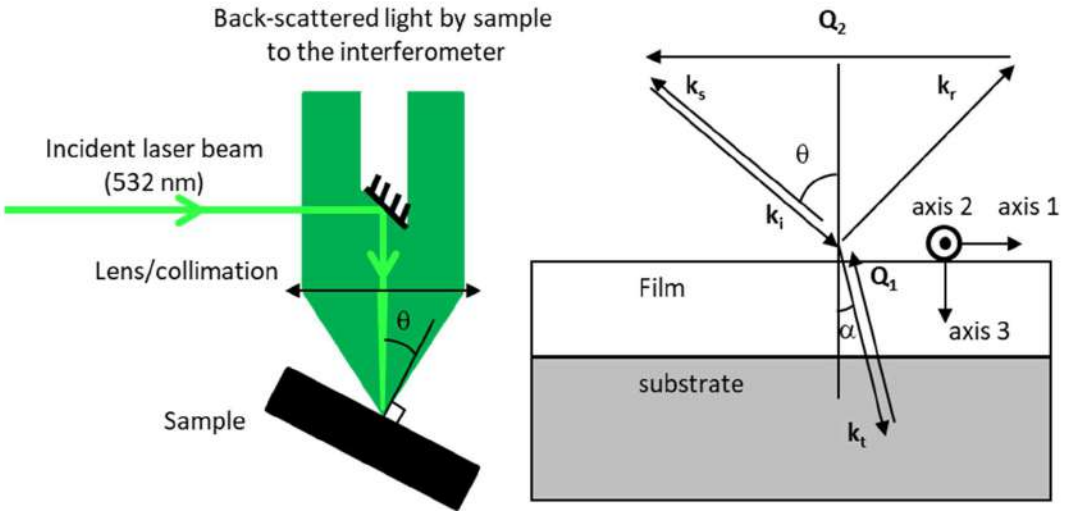

Figure 2.29– Schematic sketch of the BLS interaction and wave vectors definition: (k_i, k_s, k_r) of the incident, back-scattered and reflected light, and of the surface acoustic waves (Q_2).

Here, we used the backscattering interaction geometry (see **Figure 2.29**), so that the modulus value of the wave vector (Q_2) of the probed surface acoustic waves travelling parallel to the film-plane is fixed experimentally to the value $Q_2 = 2k_i \sin(\theta)$, where k_i denotes the incident optical wave vector in air and θ the incidence angle of the light with respect to surface normal. The acoustical wavelength (Λ) is simply defined as $\Lambda = 2\pi/Q_2$ and the velocity (V) of a surface acoustic wave is obtained from the frequency measurements (f) thanks to the relation $V = f * \Lambda$. For a ratio $h/\Lambda > 1$, the slower surface acoustic waves, namely the Rayleigh surface wave, will be no longer influenced by the substrate, neither by the film' thickness. Thus, the Rayleigh wave velocity will measure property of the film only, as for a bulk material [214] closely related to the transverse velocity, hence to its shear elastic constant C_{44}. The BLS spectra were obtained at room temperature in air, with typical acquisition times of 2-3 h. The light source was a YAG solid laser with single mode of 532 nm. Typically 200-300 mW of a naturally p-polarized

(vertical) light was focused on the surface of the sample and the backscattered light was analyzed by means of a Sandercok-type 3 + 3 pass tandem Fabry–Perot interferometer (see **Figure 2.30**).

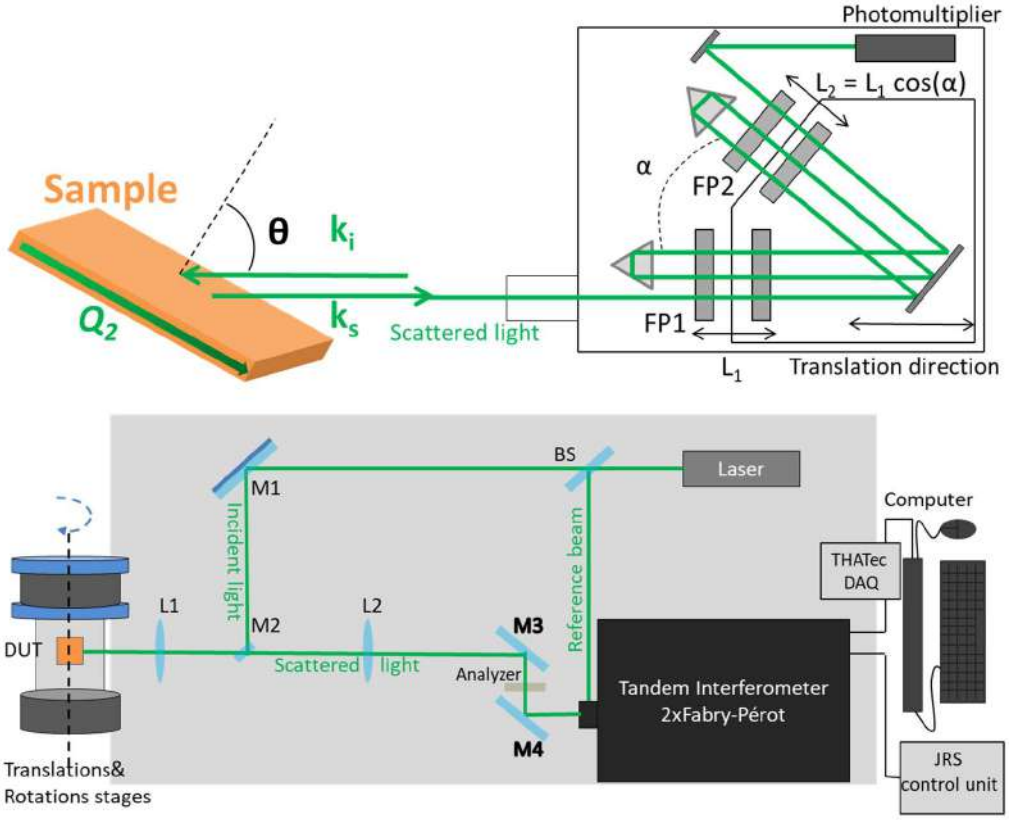

Figure 2.30 – BLS setup in the backscattering geometry showing the optical paths and the tandem Fabry Pérot designed by J.R. Sandercock.

The transmission of the light inside the tandem Fabry Pérot interferometer is described in **Figure 2.31**. The free spectral range (FSR) is defined by $FSR = c_0/2L_1$, c_0 being the speed of light ($c_0 = 3*10^8$ *m/s*) and L_1 the distance between each glass plate of FP1. $L_1/L_2=20/19$ is fixed by the angle between each FP in the design.

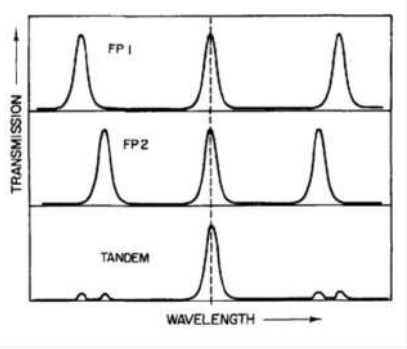

Figure 2.31 – Transmission of light within each Fabry Pérot (FP) and in tandem operation after superposition of one transmission order for each.

Typical BLS spectra are reported in **Figure 2.32** for the binary *TaN*, *CoCrCuFeNi* thin films and bulk, together with their corresponding fit using our home-made programs [215].

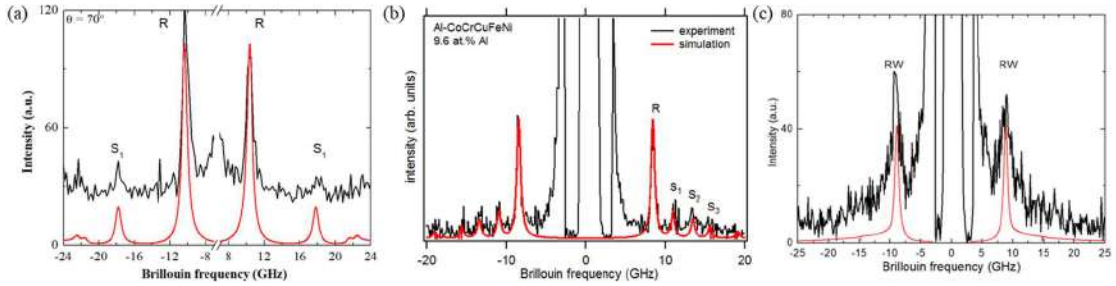

Figure 2.32 – (a) One typical BLS spectrum of *TaN* ($h = 154$ nm) film on the *MgO(001)* substrate for an angle of incidence $\theta = 70°$. The fit of the spectrum considering the ripple mechanism at the free surface is also provided at the bottom (red line). *R* and S_1 denote the Rayleigh surface wave and the first Sezawa wave, respectively. (b) Typical BLS spectrum of $(CoCrCuFeNi)_{1-x}Al_x$ film (h = 485 nm) for an incidence angle of 65° and the best-fit simulation (red line). (c) BLS spectrum of Bulk *CoCrCuFeNi* for an incidence angle of 65° and the best-fit simulation (red line).

For opaque layers, such as the present metallic and nitride films with metallic character, the scattering mechanism is restricted to the scattering of light by the dynamical corrugation of the free surface by acoustic waves travelling parallel to the film plane [216]. Thus, we can only observe the surface acoustic waves with a sagittal polarization (first

component along the $\boldsymbol{Q}_2$ direction and the second is vertical). For films with thicknesses around the acoustic wavelength (~0.3 µm) and deposited on a substrate with higher acoustic phase velocity ("slow" film on "fast" substrate), the surface acoustic waves with a sagittal polarization are: the Rayleigh wave *(R)* and the so-called Sezawa guided waves $(S_1–S_n)$ [216] at higher frequencies. The frequency (velocity) and number of these *Si* surface modes are dependent on both the thickness and the elastic constants of the film and of the substrate, whereas the velocity of the Rayleigh surface wave, V_R, is mainly dependent on the transverse velocity $V_T = (C_{44}/\rho)^{1/2}$ [217] through the relation $V_R = \beta V_T$, where β~0.92 is a slightly varying function of the whole elastic constants of the film.

The film thickness h and the mass density (ρ) of the films were preliminary measured by XRR with accuracy better than 2%, as necessary inputs to determine the eigen frequencies by solving the acoustical problem. Two distinct symmetry assumptions were considered depending on film composition and resulting microstructure (crystal structure, texture): for polycrystalline not textured cubic MCAs films, isotropic elastic properties were considered, requiring only two independent elastic constants c_{11} and $c_{44} = (c_{11} - c_{12})/2$, while for textured ones with strong (111), (011) or (001) texture an effective medium with hexagonal (transverse isotropic) symmetry was assumed. In this case, the characterization of the elastic properties of such films requires the knowledge of five independent effective elastic constants, namely C_{11}, C_{33}, C_{44}, C_{13} *and* C_{66}. The fifth elastic constant, $C_{66} = (C_{11} - C_{12})/2$ enabling measurement of the C_{12} constant, can only be determined from measurements of the phase velocity of shear horizontal modes (Love modes) but are not observed here because of their low "bulk-like" scattering mechanism

efficiency. The four first ones influence the Rayleigh and Sezawa surface modes observed in the BLS spectra [207, 216]. In all cases, the C_{33} elastic constant is first measured by PLU and then considered as a fixed known parameter in the fitting procedure of our BLS spectra.

In case of epitaxial film with cubic symmetry, BLS is able to probe the in-plane anisotropy by varying the in-plane propagation direction of generalized surface waves, by simply rotating the sample. Then, for cubic materials with three unknown single crystal elastic constants (c_{ij}'s), at least c_{44} and $c' = (c_{11}-c_{12})/2$ elastic constants could be *a priori* determined [218], avoiding the limitation encountered in the case of hexagonal or polycrystalline textured films. Unfortunately, in the present case, rotation of samples along the normal did not provide the expected information, instead a full spectrum fitting procedure of both the Rayleigh and one Sezawa mode (at least) was performed in order to evaluate both c_{44} and c_{12}, independently, $c_{11} = c_{33}$ being selectively measured by PLU, on a (001) epitaxial film.

CHAPTER 3. “SIMPLE” NITRIDES FILMS OF TRANSITION METALS: ROLE OF VACANCIES

The aim of this work is to measure directly the 3 independent single crystal elastic constants of thin films binary and ternary materials with cubic symmetry, namely c_{11}, c_{12} *and* c_{44}. By using epitaxial thin films growth on *MgO* substrates with specific orientations (001), (011) and (111), no more effective average of properties as for polycrystalline materials is needed. To measure selectively the elastic constants of these thin film materials, we combined two acousto-optic techniques: picosecond laser ultrasonic (PLU) and Brillouin light scattering (BLS). The results were first compared to DFT calculations considering a defect-free lattice. VASP [12, 176] was used to perform the DFT calculations, employing the projector augmented plane wave pseudopotentials under the generalized gradient approximation (GGA) with a Perdew-Burke-Ernzerhof exchange and correlation functional [219]. We found that the influence of defects (metal and nitrogen vacancies in this case) cannot be ignored. The studied transition metal nitrides include the (*i*) metals from IVB group *TiN*, *ZrN* and pseudo binary *TiN-ZrN* solid solutions; (*ii*) metals from the VB group *TaN*, (*NbN* and *VN* not discussed in this thesis). Epitaxial thin films were deposited using magnetron sputtering by Prof. Gregory Abadias @PPRIME institute, Poitiers University.

3.1 Measurement of the elastic constants

3.1.1 TiN-ZrN system: picosecond laser ultrasonic and Brillouin light scattering

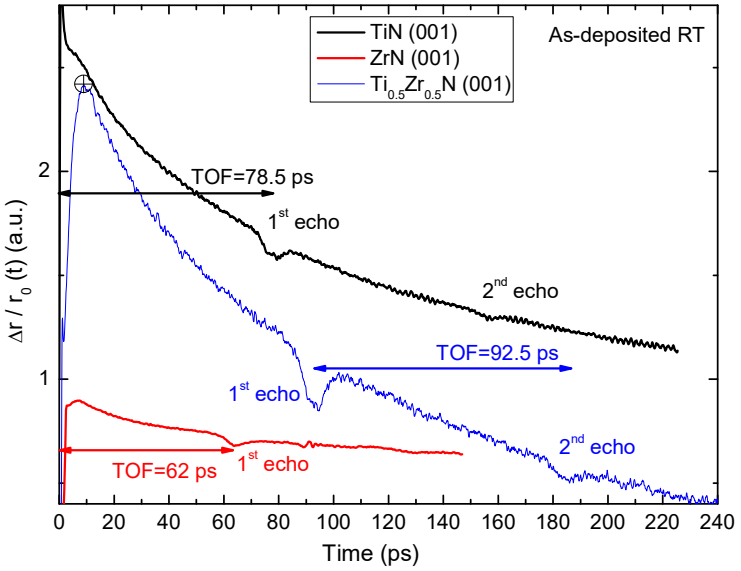

Figure 3.1 - Relative change of reflectivity as a function of time measured by the PLU technique for the *TiN, ZrN* and *$Ti_{0.5}Zr_{0.5}N$* films on *MgO* (001) substrate.

From the transient reflectivity change, the time that ultrasonic pulses need to travel back and forth the thin film can be determined and is denoted by *TOF* as shown in **Figure 3.1**. Knowing the thickness *h* of the film, the measured *TOF* enables the measurement of sound velocity $V_L = 2h/TOF$.

In the present case of $Ti_xZr_{1-x}N_y$ $(0 \leq x \leq 1)$ epitaxial films, a standard picosecond ultrasonic approach is convenient to extract the longitudinal sound velocity along the normal of the film-plane, $V_L[001]$ and $V_L[011]$. Each velocity is related to a set of elastic constants through $c_L = \rho(V_L)^2$, following the equations **(Eq. 3.1)** and **(Eq. 3.2),** respectively.

$$\rho V_L^2[001] = c_{11} \tag{3.1}$$

$$2\rho V_L^2[011] = c_{11} + c_{12} + 2c_{44} \tag{3.2}$$

with ρ being the mass density of the film. Unfortunately, the third orientation (111) that cannot be obtained by growth on *MgO(111)* or on sapphire substrates does not provide a novel independent equation. Indeed, the velocity along (111) direction is given by the equation (**Eq. 3.3**), which will also be useful later for *TaN*.

$$3\rho V_L^2[111] = c_{11} + 2c_{12} + 4c_{44} \tag{3.3}$$

The Brillouin light scattering (BLS) laser-based technique allows measuring sound velocity of a few kinds of surface acoustic waves (V_{SAW}) in thin films and coatings and thus estimating single-crystal elastic constants (ρV^2), in the case of epitaxial films, if the mass density ρ of the film is known. The Rayleigh surface wave velocity V_R ($V_R = \beta V_T$, β~0.9) is known to be closed to the shear wave velocity (V_T) and much more dependent on the shear elastic constant $c_T=\rho(V_T)^2$ ($c_T = c_{44}$ for [100] direction of propagation in a (001) plane). We show for example the measured Rayleigh wave velocity in **Figure 3.2** as a function of film thickness (h) over acoustic wavelength(Λ) ratio (h/Λ) for *MgO* the substrates, *TiN* and *ZrN*. *ZrN* is more sensitive to the ratio, whereas *TiN* doesn't show large dependence.

Sound velocities and elastic constants of binary *TiN* and *ZrN* and several *TiZrN* are listed below in **Table 3.1**.

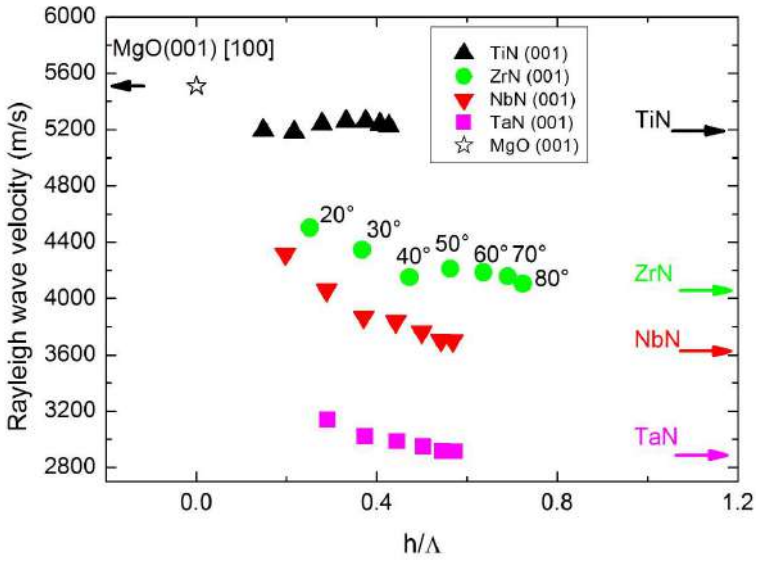

Figure 3.2 - The sound wave velocity dispersion of R as a function of the film thickness (*h*) over the acoustic wavelength (*Λ*) ratio *h/Λ*.

Table 3.1: Sound velocities measured by PLU and BLS on (001)- and (011)-$Ti_{1-x}Zr_xN_y$ epitaxial films and the derived elastic constants. Mass density were measured from XRR.

Sample	*Ti* (at.%)	*Zr* (at.%)	*N* (at.%)	V_L(m/s)	c_L(GPa)	V_T(m/s)	c_T(GPa)
TiN-M14-33_001	48.4	/	51.6	10295	572	0	1.06
TiN-M14-33_011	48.4	/	51.6	9974	557	/	/
TiZrN-M15-32_001	35.7	12.2	52.1	9159	512	5153	162
TiZrN-M16-38_001	33.8	12.2	54			4983	144
TiZrN-M16-38_011	33.8	12.2	54	8569	426		
TiZrN-M16-39_001	21.2	22.8	56.0	8864	491	4561	130
TiZrN-M16-39_011	21.2	22.8	56.0	8536	455		
TiZrN-M14-2_001	19.3	26.0	54.7	8930	510	4760	145
TiZrN-M16-37_001	12.2	30.0	57.8	7991	447	4536	144
TiZrN-M16-37_011	12.2	30.0	57.8	7723	417		
ZrN-M16-36_001		46.4	53.6	8889	585	4191	130
ZrN-M16-36_011		46.4	53.6	7576	424		

3.1.2 TaN system: picosecond laser ultrasonic and Brillouin light scattering

We first measured selectively with the picosecond laser ultrasonic (PLU) technique the longitudinal bulk sound wave velocity V_L and elastic constant $c_L = \rho(V_L)^2$ of the *δ-TaN* epitaxial films with different crystal orientations: (001), (011) and (111). The relative change of the transient reflectivity, $\Delta r(t)/r_0$, is shown in **Figure 3.3** for the different orientations. At least, two echoes are clearly visible for all films.

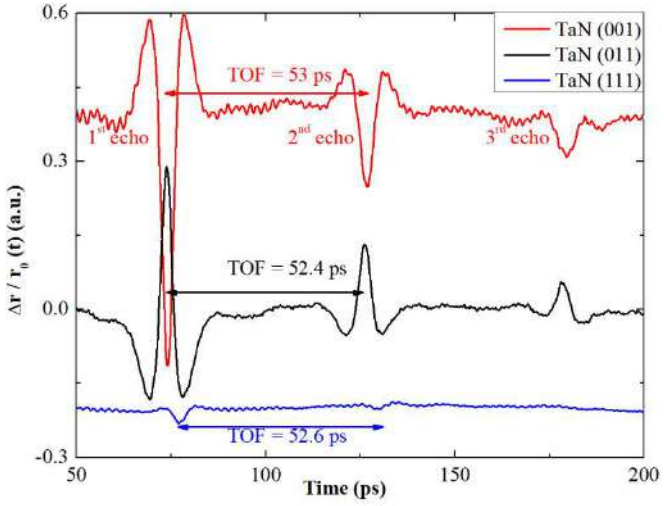

Figure 3.3 - (a) Transient reflectivity change of *δ-TaN*-(001), -(011) and -(111) epitaxial films. From the time of flight (TOF), the film thickness (*h*) and the mass density (*ρ*), one can measure selectively c_{11} = 530 GPa, $(c_{11}+c_{12}+c_{44})/2$ = 502 GPa and $(c_{11}+2c_{12}+4c_{44})/3$ = 498 GPa, respectively.

Considering the value of 530 GPa for the c_{11} elastic constant as obtained from the $Ta_{0.93}N/MgO(001)$ film by PLU, the two other elastic constants, c_{44} and c_{12}, could be determined by BLS. c_{44} is found to be mostly dependent on the Rayleigh surface wave (R), while c_{12} is related to the first Sezawa wave (S_1), see **Figure 3.4a**. c_{44} and c_{12} were extracted from the sound velocity dispersion curve for different angles of incidence θ (30-80°), see **Figure 3.4b**, by fitting each BLS spectrum considering the ripple mechanism at the free

surface [220, 221]. The experimental sound velocities (V_L, V_R and V_T) and the related elastic constants (c_L and c_T) obtained for the different *TaN* epitaxial films are summarized in **Table 3.2**.

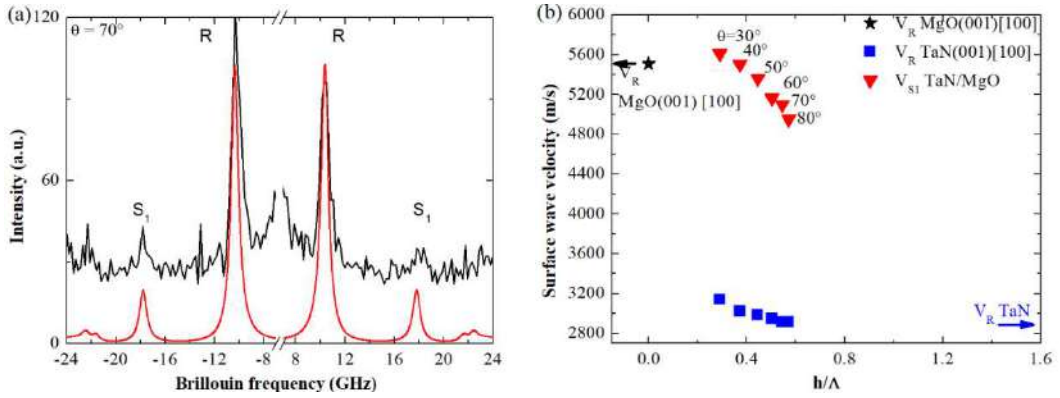

Figure 3.4 - (a) One typical BLS spectrum measured on the *$Ta_{0.93}N$/MgO(001)* sample (*h*=154 nm) at an angle of incidence θ = 70°. The fit of the spectrum considering the ripple mechanism at the free surface is also provided at the bottom (red line). R and S_1 denote the Rayleigh surface wave and the first Sezawa wave, respectively. (b) The sound wave velocity dispersion of R and S_1 as a function of the film thickness (*h*) over the acoustic wavelength (*Λ*) ratio *h*/*Λ*. Fitting parameters are c_{44} = 137 ± 3 GPa and c_{12} = 130 ± 5 GPa, considering c_{11} = 530 GPa fixed to the PLU measured value.

Table 3.2 - Experimental sound velocities and related elastic constant of *TaN* epitaxial films. c_{12} = 130 ± 5 GPa was determined by fitting the first Sezawa surface acoustic wave (S_1) of the *$Ta_{0.93}N$/MgO(001)* sample. Mass density from X-ray reflectivity (XRR) was used: ρ_{XRR} = 15.6 g/cm³.

Orientation	V_L (m/s)	c_L (GPa)	V_R[100] (m/s)	V_T[100](m/s)	c_T(GPa)	Poisson ratio
(001)	5830	530	2830	2963	137	0.197
(011)	5656	502	-	-	-	
(111)	5635	498	-	-	-	

3.2 Computational procedures

3.2.1 TiN-ZrN system

The structural short-range order (SRO) of the alloy was modelled with supercells generated with the special quasirandom structure (SQS) method introduced by Zunger [179]. Based on the fcc lattice we used the size of *(2×2×2)* for the supercell with 64 atoms. This supercell size and shape has been shown to result in converged elastic constants for $Ti_{0.5}Al_{0.5}N$ [222]. SQS supercells were derived for defect-free compounds with $x = 0.25$ $(x = 0.75)$ and $x=0.5$, as well as for defected structures. We considered 4 types of randomly distributed vacancies for the defected structures, namely, *Ti* vacancy, *Zr* vacancy, mixed *Ti-Zr* vacancy and *N* vacancy. The atomic configurations were obtained by optimizing the Warren-Cowley pair SRO parameters in the first seven nearest-neighboring shells. Since the configurational disorder breaks the local cubic point symmetry, we used the symmetrization procedure suggested by Tasnádi [223]. That is, we calculated nine elastic constants independently and then we derived the cubic-averaged ones, to be the three independent single crystal elastic constants c_{11}, c_{12}, c_{44}, of a cubic material. The elastic constants were calculated by total energy calculations with using ± 0.5 % distortions.

The total energy calculations were performed using the Vienna ab initio simulation package (VASP) [12, 176]. The exchange correlation functional was approximated by the Perdew-Burke-Ernzerhof generalized gradient functional (GGA) [219]. The valence electron configuration is $3p^6 3d^3 4s^1$ for Ti and $4s^2 5s^1 4p^6 4d^3$ for *Zr*. The plane-wave cutoff energy （520eV） and the Monkhorst-Pack sampling of the Brillouin zone (*6×6×6*, with the spacing of k-points <0.2/Å) were tested and convergence was achieved. In obtaining

the ground structure we optimized the volume, the shape and lattice coordinates (tag ISIF was set to 3 in VASP).

Monovacancy formation energy was calculated for 3 different compositions ($Ti_{0.25}Zr_{0.75}N$, $Ti_{0.5}Zr_{0.5}N$ and $Ti_{0.25}Zr_{0.75}N$) separately. Unlike binary nitrides which have well defined Me/N monovacancy with the same surrounding environment everywhere, disordered ternary nitrides may exhibit different chemical environments for each vacancy. For example, in ternary *Ti-Zr-N* system, the number of *Zr* atoms surrounding a vacancy and their spatial distribution may differ from another vacancy site and play a role in determining the vacancy formation energy. In order to take chemical environments into account, we created multiple configurations with only one vacancy by removing each time one atom from each site in the defect-free SQS supercell *(2×2×2)*. Hence, we obtained a set of monovacancy formation energies for the 3 ternary compositions, which were further correlated to the number of *Zr* atoms in the neighboring shells.

The monovacancy formation energy ΔE_X^{vac} for *X*-type vacancy is calculated based on the formula:

$$\Delta E_X^{vac}|Ti_xZr_yN_z = E(X)|Ti_xZr_yN_z - E|Ti_xZr_yN_z \quad (3.4)$$

where *X* represents either *Ti, Zr or N*, *E(X)* denotes the energy of defected structure with one *X*-type vacancy and *E* is the energy of the corresponding defect-free structure.

3.2.2 TaN system

The valence electron configuration is $5p^6\ 5d^3\ 6s^2$ for Ta and $2s^2\ 2p^3$ for N. A *2×2×2* cubic supercell consisting of 64 lattice sites is chosen to model the defected Ta_xN and TaN_x

compounds ($x \leq 1$). The plane-wave cutoff energy was always set to 800 eV and the $8\times8\times8$ Monkhost-Pack k-vector sampling of the Brillouin zone was checked to provide total energy accuracy of about 1 meV/at, elastic stress tensor convergence within 2 kbar and the elastic constants convergence within 10 GPa, for tested configurations. Atomic positions as well as shape and volume of the unit cell were allowed to relax.

To compare various systems in terms of their thermodynamic stability, the formation energy, E_f, was calculated. The *TaN* defect-free structure was proposed by Balasubramanian *et al*. [64] as another reference choice considering it is more relevant in the case of thin film growth. In this case, the formation energy is lowered by the tantalum chemical potential difference, $\Delta\mu_{MS} = \mu_{Ta} - \mu_{TaN} = 1.768$ eV/at., between bcc-*Ta* and *TaN* reference states ($\mu_{TaN} = -13.572$ eV/at).

Moreover, several defected or non-stochiometric structures were investigated with different degree of ordering/clustering of the metal cation or nitrogen anion vacancy. Metal vacancies, nitrogen vacancies and Schottky defects (containing equivalent number of metal and nitrogen vacancies) were considered as possible defects. DFT calculations have been carried out for a defect concentration up to 20%, with respect to the total (metal + nitrogen) lattice sites. The Alloy Theoretic Automated Toolkit (ATAT) was employed to generate the special quasi-random structures (SQS) [181], representing random distribution of vacancies (denoted as "random" configuration). The short-range order parameters were optimized for pairs up to seventh order and to fifth order for triplets. Besides, we considered ordered distribution of vacancies (denoted as "symmetric" configuration) by removing atoms with certain site symmetries from the $2\times2\times2$ supercell. Hence, in the symmetric

configurations, all the defected structures remain cubic. Finally, to evaluate the vacancy clustering effect, we simulated certain cluster configurations, by removing the neighboring cations or anions in the supercell. In the case of Schottky-type defects, SQS were again adopted to remove randomly identical number of metal and nitrogen atoms.

We searched for additional stable structures offering ordered *Ta* and *N* vacancies with different concentrations by employing the UNiversal CLuster Expansion (UNCLE) code [224]. The identified structures and their properties are described in the Appendix A (see **Figure A.1** and **Table A.3**). This complementary approach based on cluster expansion (CE) calculations enabled us to scrutinize the 0-25% ordered-vacancy concentration interval.

The lattice constant a of defected δ-TaN structures was calculated from $a = (V_0)^{1/3}$, where V_0 is the equilibrium volume corresponding to the conventional cubic cell. Our structural models are based on $2\times2\times2$ supercells constructed from the conventional cubic cell, therefore we took $V_0 = V/8$ where V is volume of the fully relaxed supercell with or without defect(s). Due to supercell finite size effect, the relaxed defected supercells do not have, in general, cubic shape anymore. However, the defected materials will macroscopically possess the cubic symmetry, so that evaluating a from the supercell volume will effectively average the local atomic distortions and provide the correct estimation of the lattice constant for the macroscopically cubic material.

We investigated elasticity of selected TaN_x structures by employing the stress-strain method [225, 226]. Fourth-order elasticity tensor c relates the stress, σ, linearly to the strain, ε, according to the Hooke's law

$$\sigma = c\varepsilon \tag{3.5}$$

By convenience, instead of using the fourth-order tensor c in a three-dimensional space, it is often replaced by a 6×6 matrix. In the following, c will represent this matrix of elastic constants in the so-called Voigt's notation. To evaluate elastic constants corresponding to structures with arbitrary symmetry, we adopt the methodology proposed by Moakher and Norris [227]. First, the squared norm of the elasticity matrix c is defined as

$$\|c\|^2 = (c, c) \tag{3.6}$$

The scalar product (c, c) can be calculated in various ways depending on how c is represented. Assuming the Euclidean metrics and the case of 2D representation, Eq. (3) takes the form

$$\|c\|^2 = \sum_{i,j}^{6} c_{ij}^2 \tag{3.7}$$

Simplifying the general 6×6 matrix $C = (C_{ij})$ with 21 independent constants, we must project it onto a convenient symmetry class and hence, decrease the number of independent elastic constants. Thus, we search for a matrix C_{sym} of a specific symmetry class such that the norm $\|C - C_{sym}\|$ is minimal. Rigorous derivation of the projectors for all crystal symmetry classes can be found in Refs. [227, 228]. In this work, we restricted the search to a cubic or a tetragonal symmetry when we used the SQS method.

$$\begin{pmatrix} \varepsilon & 0 & 0 \\ 0 & 0 & \frac{1}{2}\varepsilon \\ 0 & \frac{1}{2}\varepsilon & 0 \end{pmatrix}, \begin{pmatrix} 0 & 0 & \frac{1}{2}\varepsilon \\ 0 & \varepsilon & 0 \\ \frac{1}{2}\varepsilon & 0 & 0 \end{pmatrix}, \begin{pmatrix} 0 & \frac{1}{2}\varepsilon & 0 \\ \frac{1}{2}\varepsilon & 0 & 0 \\ 0 & 0 & \varepsilon \end{pmatrix} \quad (3.8)$$

To calculate the elastic constants, we employed the above deformation matrices with ε equals to ± 0.004, as in the stress-strain method. They are equivalent for materials of cubic symmetry. However, for SQS structures we used, elastic tensor can barely maintain cubic symmetry due to randomly distributed vacancies. One usually gets elastic constants by averaging relevant elastic constants. The 3 independent elastic constants (c_{11}, c_{12} *and* c_{44}) were obtained from the following averaging process,

$$c_{11} = \frac{1}{3}(c'_{11} + c'_{22} + c'_{33}) \quad (3.9)$$

$$c_{12} = \frac{1}{6}(c'_{12} + c'_{23} + c'_{13} + c'_{21} + c'_{31} + c'_{32}) \quad (3.10)$$

$$c_{44} = \frac{1}{3}(c'_{44} + c'_{55} + c'_{66}) \quad (3.11)$$

where *c'* denotes the element in the full elastic tensor and can be calculated directly using the stress-strain method.

3.3 Energetics, phase stability and structural properties

3.3.1 TiN-ZrN system

Dispersed *monovacancy formation energies* were found for *Ti-Zr-N* compounds as shown in **Figure 3.5**. Geometric analyses of the coordination suggest that the dispersed

metallic (*Ti & Zr*) monovacancy formation energies can be better described in terms of the numbers of *Zr* neighbors in the first and second nearest metallic shells around the vacancy. For each composition, *Ti/Zr* monovacancy formation energy decreases with the number of *Zr* atoms in the second nearest neighbor shell increasing.

Ti/Zr monovacancy formation energy can be well separated into 3 groups corresponding to the 3 compositions. The data points lie well on the 3 planes as indicated in **Figure 3.5**. Accordingly, we fitted *Ti/Zr* monovacancy formation energy for the 3 compositions as a function of *Zr* occupations in the first and second nearest metallic shells around the vacancy, as denoted by n_1 and n_2 respectively.

The *Ti* monovacancy formation energy are formulated as

$$\Delta E_{Ti}^{vac}|Ti_{0.75}Zr_{0.25}N = -0.39861 - 0.01675n_1 + 0.14592n_2 \quad (3.12)$$

$$\Delta E_{Ti}^{vac}|Ti_{0.5}Zr_{0.5}N = -0.90357 - 0.00782n_1 + 0.16351n_2 \quad (3.13)$$

$$\Delta E_{Ti}^{vac}|Ti_{0.25}Zr_{0.75}N = -1.25794 - 0.01411n_1 + 0.15363n_2 \quad (3.14)$$

The *Zr* monovacancy formation energy are formulated as

$$\Delta E_{Zr}^{vac}|Ti_{0.75}Zr_{0.25}N = -0.60698 - 0.00706n_1 + 0.08428n_2 \quad (3.15)$$

$$\Delta E_{Zr}^{vac}|Ti_{0.5}Zr_{0.5}N = -0.7961 - 0.00712n_1 + 0.11434n_2 \quad (3.16)$$

$$\Delta E_{Zr}^{vac}|Ti_{0.25}Zr_{0.75}N = -1.09788 - 0.00893n_1 + 0.15707n_2 \quad (3.17)$$

The negative coefficients before n_1 means that more *Zr* atoms in the first nearest shell of the vacancy will lower the vacancy formation energy. The coefficients of n_2 are

positive in all cases, and have a larger absolute value than the negative coefficient before n_1, suggesting that the metal vacancy formation depends strongly on the number of *Zr* atoms in the second nearest metallic shell and more *Zr* in the second nearest shell suppresses the vacancy formation.

To compare *Ti/Zr/N* vacancy formation energy for different compounds, it is necessary to assume that the chemical potential for *Ti/Zr/N* does not change with *Zr* concentration increasing. The separation of monovacancy formation energy into different groups implies that *Ti/Zr* monovacancy formation energy in *Ti-Zr-N* does depend not only on the *Zr* coordination numbers in the first and second nearest shells, but also on the chemical composition of the compound, or the *Ti/Zr* ratio. In **Figure 3.5a** and **Figure 3.5b**, the $Ti_{0.75}Zr_{0.25}N$ monovacancy energy sets lie on the top while $Ti_{0.25}Zr_{0.75}N$ lie at the bottom, indicating *Ti/Zr* vacancy formation energy decreases as *Zr* concentration increasing.

A thorough description of the vacancy formation energy for ternary nitrides requires larger supercells containing other correlation functions. Apart from this, it is also necessary to include concentration and configurational corrections due to the concentration and correlation functions change resulting from removing one atom from the supercell. A more sophisticated study of metal vacancy formation energy in a similar $Ti_{0.5}Al_{0.5}N$ ternary system can be found in Rev. [222].

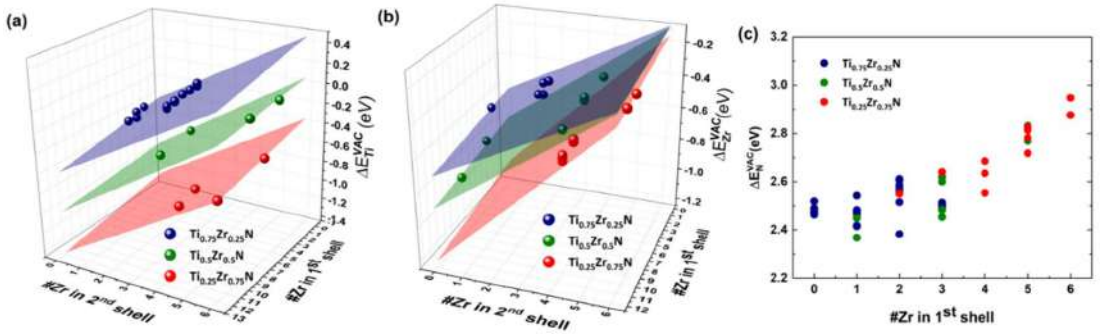

Figure 3.5 - (a) Mono *Ti* vacancy (b) mono *Zr* vacancy formation energy as a function of numbers of *Zr* atoms in the first and second nearest neighboring shells (c) *N* vacancy formation energy as a function of the number of *Zr* atoms in the first nearest neighboring shell, for $Ti_{0.75}Zr_{0.25}N$ (blue), $Ti_{0.5}Zr_{0.5}N$(black), $Ti_{0.25}Zr_{0.75}N$(red). The planes are the guides for the eye.

The nitrogen vacancy formation energy in **Figure 3.5c** generally increases when more *Zr* atoms occupy the metallic 1st shell around the vacancy center. This is consistent with the fact that for the simple binary nitrides, *TiN* has a smaller *N* vacancy formation energy (2.414eV) than *ZrN* (3.090eV). The energy disperse implies that there are other factors influencing *N* vacancy formation energy other than numbers of *Zr* neighbors in the nearest neighbor shell. To demonstrate, we found that the relative positions of *Zr* atoms at the octahedron vertices of the first nearest metallic shell around the vacancy site, can alter *N* vacancy formation energy. The *N* vacancy formation energy is 0.2 eV higher when two *Zr* atoms occupy the adjacent vertices than two *Zr* atoms occupy the opposite vertices, despite the numbers of coordination *Zr* are the same.

As shown in Figure 3.6, lattice parameters and mass density increase almost linearly with the addition of Zr and a good agreement between DFT and experiments was reached. For TiN and ZrN, thin films provide similar lattice parameters, i.e., 4.245 and 4.581 Å respectively, to the bulk value, 4.241 and 4.578 Å [228]. Our calculated lattice

constants are 4.252 and 4.596Å, respectively for TiN and ZrN, in line with 4.253 and 4.618 Å calculated by Holec *et al* [229]. The experimental values for both films and bulk are smaller than the DFT predicted defect-free lattice parameters. This might be due to the application of GGA exchange-correlation functions in DFT calculations, since it is known that DFT almost always overestimate the lattice constants with GGA.

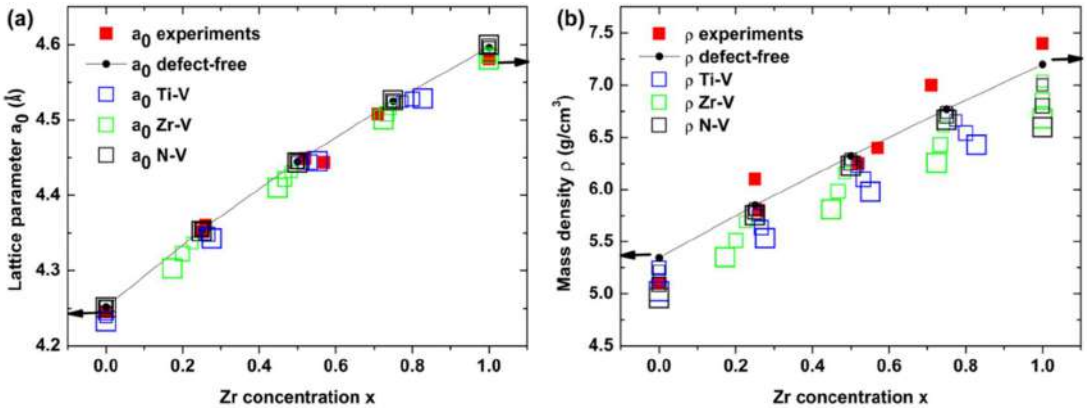

Figure 3.6 - (a) Stress-free lattice parameter deduced experimentally (red square) from reciprocal space mapping as a function of *Zr* concentration, *x*, compared to bulk materials (arrows) and DFT calculations with *Ti* (blue square), *Zr* (green square), and nitrogen (black square) vacancies. (b) Mass density deduced from XRR as a function of *Zr* concentration, *x*, compared to bulk materials and DFT calculations with vacancies. The line and are the defect-free calculations. Increasing size of symbols indicates increasing vacancy concentration (up to 3/64). These symbols have the same meaning hereafter.

As revealed by DFT, among the 3 vacancies types, only *Zr* vacancies lead to obvious lattice parameter reducing because of its large atomic size. Quantitatively, 4.7 at. % *Zr* vacancies result in 1.2 %, 0.8 %, 0.5 % and 0.3 % reduction of the lattice parameter for $Ti_{0.75}Zr_{0.25}N$, $Ti_{0.5}Zr_{0.5}N$, $Ti_{0.25}Zr_{0.75}N$ and *ZrN*, respectively. *Ti* vacancies only play a role in *TiN*. 4.7 at. % *Ti* vacancies decreasing the lattice parameter by 0.4 % for *TiN*. With *Ti* vacancies, no lattice shrink can be observed for *Zr*-rich compounds. The

influence of *N* vacancies on lattice parameters is unnoticeable within all compositional range.

Mass density in **Figure 3.6b** increases linearly from *TiN* to *ZrN*. Theoretically, both *Ti* and *Zr* vacancies decreases the mass density. On the other hand, *N* vacancy affects only the mass density of binary nitrides, not the ternary. No vacancy is responsible for several over dense samples, as measured by XRR.

3.3.2 TaN system

The calculated formation energy at 0 K of different defected and defect-free δ-TaN_x structures are shown in **Figure 3.7**. When we compare to the defect-free $Fm\bar{3}m$ cubic phase (E_f = –0.875 eV), the *P4/nmm* tetragonal phase is found to have a lower formation energy (E_f = –0.925 eV) and is thermodynamically, mechanically and dynamically stable, as previously established in the recent work of Hu *et al*. and confirmed by the present calculations (see Appendix). From first-principles calculations, Hu *et al*. [230] concluded that the presence of point defects (*Ta* or *N* vacancies in low concentration, ~2%) or *C* or *O* impurities did not prevent the cubic to tetragonal phase transformation. Nonetheless, considering the small grain size of thin films (a few tens of nm) with low local coordinated sites on the surfaces or interfaces, they argued that such size effect could induce a stabilization of the *TaN* cubic phase, compared to its bulk counterpart. Many other non-stochiometric crystalline Ta_yN_x compounds were numerically investigated by Weinberger *et al*. [231] using first-principles methods but these authors did not discuss the case of the *P4/nmm* tetragonal phase.

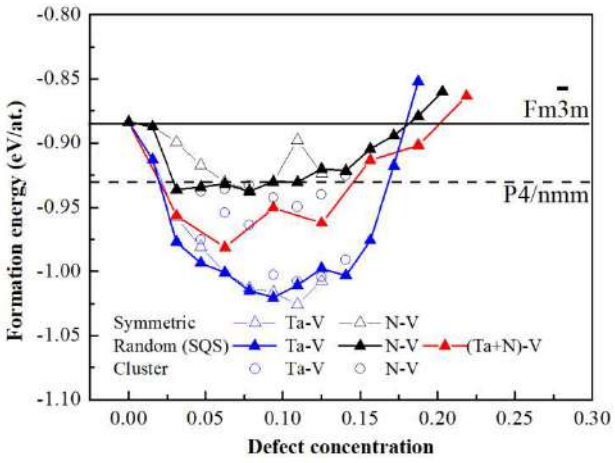

Figure 3.7 - Formation energy in *δ-TaN* phase as a function of defect (*Ta*, *N* or (*Ta*+*N*) vacancy) concentration in supercell. Ordering/clustering configurations of atom species have been considered. The horizontal lines indicate the formation energy of the cubic *Fm*$\bar{3}$*m* (solid line) and tetragonal *P4/nmm* (dashed-line) defect-free *TaN* structures. Not shown, formation energy of the cubic *NbO*-type *Pm*$\bar{3}$*m* simulating 25 at. % ordered Schottky defects is -0.727 eV/at., much higher than others.

From **Figure 3.7**, it is observed that the introduction of metal or nitrogen vacancies as well as Schottky defects stabilizes the cubic structure compared to the tetragonal one, for defect concentration in the 2.5-17.5 % range. The lowest formation energy of −1.02 eV is found for $Ta_{0.78}N$ (11 % *Ta* vacancy), as also predicted by Koutná *et al.*[232], whatever the defect configuration is. Nitrogen vacancies appear less energetically favorable than metal vacancies, whereas Schottky defects have intermediate formation energy between that of metal and nitrogen vacancy, depending certainly on their configuration/interaction. One can notice that formation energy of the cubic *NbO*-type (*Pm*$\bar{3}$*m*) simulating 25 at. % ordered Schottky defects is -0.727 eV/at., is much higher than any other structures, indicating that such high amount of Schottky defects is not expected. For instance, the formation energy of one metal vacancy, one nitrogen vacancy and one Schottky-defect pair

in *δ-TaN* is -3.345, +0.068, and –4.520 eV, respectively. These formation energies are in line with the values of –3.4 eV (*Ta* vacancy) and 0 eV (*N* vacancy) calculated by Balasubramanian *et al*. [64] if one considers the *TaN* reference state, instead. In agreement to previous calculations by Koutná *et al*. [232]our results also confirm that the configuration of defects does not play a significant role on the stabilization of both types of defects in this particular system, contrarily to *MoN* [232, 233]. Moreover, the results on perfectly ordered Ta_yN_x compounds from CE method (**Table A.3**) or the "symmetric" cubic supercell reproduce well the variation of the formation energy with defect concentration obtained using a supercell with a "cluster" configuration or the SQS methodology with a random configuration (see **Appendix.A.2** for definition of supercells).

Our DFT calculations for *δ-*TaN_x compounds illustrate a monotonous decrease of the lattice parameter *a* from 4.426 to 4.305 Å as the vacancy concentration increases up to 20 % (see **Figure 3.8a**). The evolution of *a* appears sensitive to the type of defects, a stronger decrease being found for metal vacancies (blue symbols). Comparable trends were predicted previously from first-principles calculations by Stampfl and Freeman [234], Grumski *et al.* [235] and Koutná *et al*. [232]. **Figure 3.8a** additionally evidences a greater influence of defect configuration for metal vacancies, lower *a* values being obtained for ordered *Ta* vacancies ("symmetric" configuration, open blue triangles). It is also supported by the calculation of 25 at. % ordered Schottky defects simulated by the *NbO*-type structure, providing a lattice parameter as low as 4.252 Å. It is even lower than the extrapolated one from SQS randomly distributed Schottky defects. The sensitivity of the lattice constant to the type and defect concentration (> 2%) could explain the large spread of structural parameters reported in the literature.

When we compare in **Figure 3.8** the experimental stress-free lattice parameter a_0 = 4.375 Å to the calculated a values of defected TaN_x structures, one should expect a maximum of ~6% ordered tantalum vacancy (open blue triangles) or ~11% random Schottky pair (red triangles) concentration to find a closer agreement between experimental and theoretical values. Taking into account the measured composition of the $Ta_{0.93}N/MgO(001)$ sample, this would suggest the presence of ~3.5 % metal vacancy and ~8% Schottky defect concentration in this film. Note that the relative difference between the lattice constant values of the defect-free *TaN* compound and the defected $Ta_{0.93}N(001)$ film is −1.2 %, corresponding to 3.6 % reduction in the unit cell-volume.

Following the approach of Koutná *et al*. [232] to provide a quantitative estimation of the lattice parameters, we fitted the calculated values for defect concentrations below 0.12, with linear functions of the defect concentration, x, (see **Figure 3.8a**):

$$a = a(0) - \beta x \tag{3.18}$$

Here, $a(0)$ is the lattice parameter of defect-free δ-*TaN* (4.426 Å). Our fitted β values are 0.830, 0.338, and 0.48 Å for ordered (symmetric) *Ta* vacancies, random *N* vacancies and Schottky defects (*Ta*+*N* vacancies), respectively. They compare well to the previous values of 0.747, 0.358, and 0.573 Å reported by Koutná *et al*. [232]. In general, metal deficient Ta_xN structures show much greater volume decrease upon vacancy introduction than their nitrogen deficient counterparts. Similar trends have been reported by Gu *et al*. for δ-HfN_x compounds [236].

Interesting features are observed for the evolution of mass density with defect concentration: a significant decrease is found as the metal vacancy or the Schottky pair concentration increases, whereas the introduction of nitrogen vacancy leads to a slight increase (see **Figure 3.8b**). One can also notice that the mass density is rather insensitive to the defect configuration. When we compare in **Figure 3.8b** the experimental mass density obtained from XRR (ρ = 15.6 g/cm^3) to the calculated values of defected δ-Ta_yN_x structures, one can easily observe that it lies outside the range of accessible values. However, the calculation of mass density from XRR data was carried out without considering any defect in the lattice. If one calculates the mass density from XRD data, considering the previous defect concentration inferred in the $Ta_{0.93}N/MgO(001)$ sample yields a value of ρ_{XRD} ~ 13.7 g/cm^3 (solid line), consistent with DFT calculations. This is a reduction of ~12 % respectively to ρ_{XRR} value. It means that in the present case, the mass density has to be evaluated from the volume of the fcc lattice $(a_0)^3$ and the total mass considering ~3.5 % *Ta* vacancy and ~8 % Schottky pair. Part of the remaining apparent experimental overestimation is intrinsically coming from the overestimation of cell-volume by the GGA approximation (a few percent).

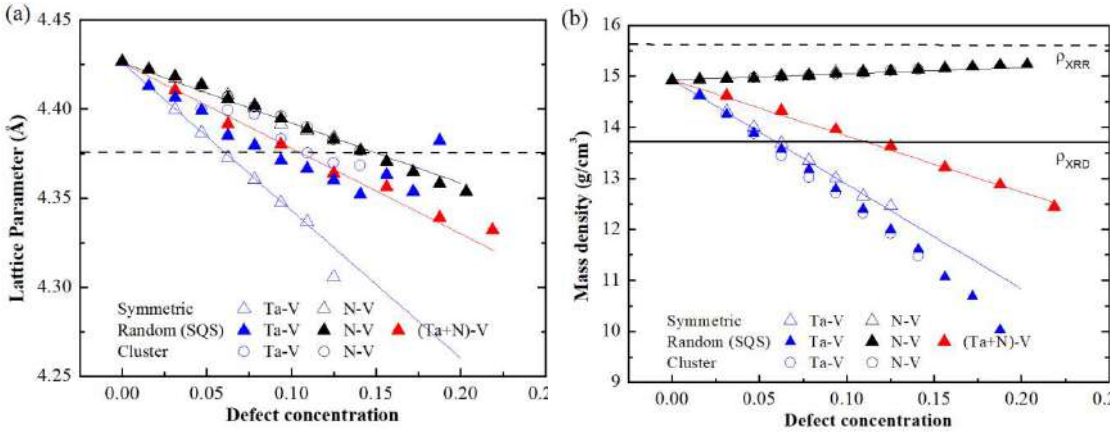

Figure 3.8 - Calculated (a) equilibrium lattice parameter and (b) mass density as a function of defect (*Ta, N or (Ta+N)* vacancy) concentration in *δ-TaN* structures. The solid lines are linear fit to the data for vacancy concentration below 12 % according to Eq. (3.18). The horizontal lines indicate our experimental data obtained from XRD (a_0 = 4.375 Å and ρ_{XRD} = 13.7 g/cm^3 for the defected structure) and XRR (ρ_{XRR} = 15.6 g/cm^3).

3.4 Sound velocities and elastic constants: DFT vs. experiments

3.4.1 TiN-ZrN system

Thin films with (001) orientation allow direct measurement longitudinal $V_L[001]$ and $V_T[001]$, which are correlated to c_{11} and c_{44} of a cubic crystal, respectively. $V_L[001]$ and $V_T[001]$ in **Figure 3.9a** and **Figure 3.9c** respectively both decrease clearly with *Zr* addition. For *TiN*, $V_L[001]$ obtained from the (001) single crystal films are 10828m/s, in close agreement to 10770 m/s measured by [237] for stoichiometric *TiN*, slightly higher than the DFT value of 10442m/s. The $V_T[001]$ we measured from the same sample is 5601m/s, higher than 5247m/s[238], 5370m/s[239] measured on single crystals by an acoustic microscope and BLS respectively, but in good accordance with 5572m/s from DFT calculations in this study. *ZrN* has the value of 8889 and 4191m/s respectively for $V_L[001]$ and $V_T[001]$, in agreement to 8572m/s and 3944m/s from DFT. The decreasing trend was well reproduced by DFT calculations. However, the experimental $V_L[001]$ values are lower than defect free structures from DFT calculations while the opposite was found for $V_T[001]$. The largest discrepancy for $V_L[001]$ appears as large as 1000m/s, at $x = 0.75$, accounting for ~12% with reference to the defect-free value. Other compounds allow better agreements with a deviation below ~7%. Theoretical calculations considering the presence of metal *(Ti/Zr)* and *N* vacancies up to 4.6 at. % provide a better agreement to experimental

$V_L[001]$ and $V_T[001]$. Both metal and *N* vacancies lead to a significant reduction of $V_L[001]$. With 4.6 at. % of vacancies, the absolute reduction can reach around 500 to 1000 m/s for all compounds, making the experimental $V_L[001]$ comparable to DFT. Regarding the vacancy influence on $V_T[001]$, metal and N vacancies behave differently. $V_T[001]$ is more sensitive to metal vacancies for all the nitrides under study. For instance, with 4.6 at. %, both *Ti* and *Zr* vacancies were found to increase $V_T[001]$ up to ~12 % in the whole composition range, leading to an overall satisfactory agreement to the values measured by BLS. $V_T[001]$ is not sensitive to *N* vacancies except for *ZrN*. A minor increase of 6% was found with 4.6 at. % *N* vacancies for *ZrN*, but still much smaller than 12 %, the value contributed by the same amount of *Zr* vacancy.

The longitudinal velocity along (110) crystallographic orientation in **Figure 3.9b** decreases from 9918 m/s for *TiN* to 7746 m/s for *ZrN* theoretically. The PLU measurements provide the same decreasing trend as well as good quantitative agreements. Slightly slower sound velocities were found for $x=0.25$ and 0.75 with a difference below 500 m/s, with respect to the defect-free values. Of the three types of vacancies, only *N* vacancy has a significant influence on this sound velocity. 4.6 at. % *N* vacancy can lead to 4 % decrease of $V_L[110]$.

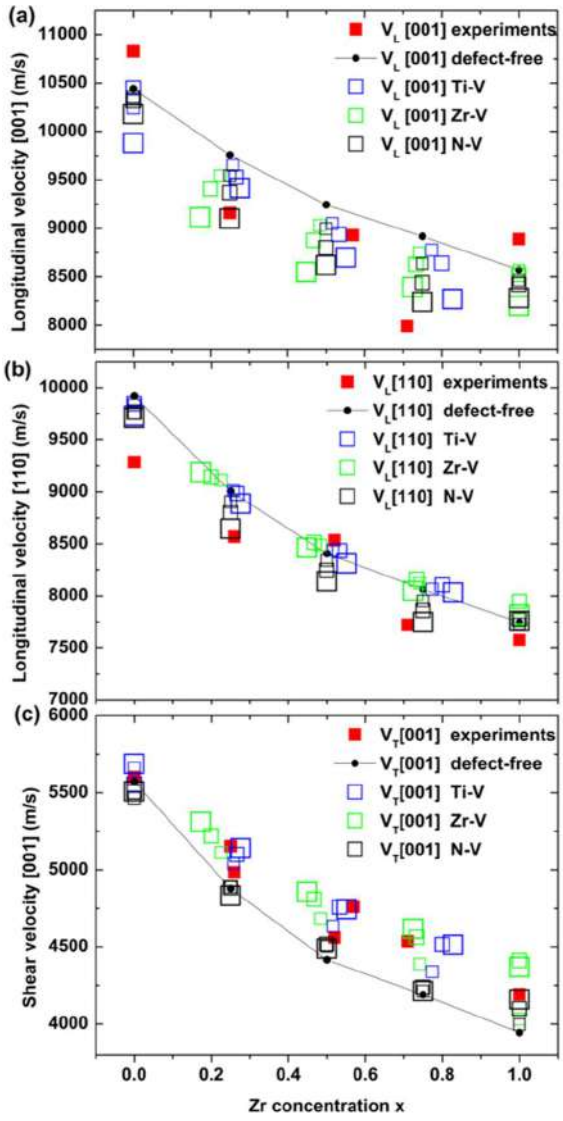

Figure 3.9 - Sound velocities measured as a function of *Zr* concentration, *x*: a) V_L along (001), b) V_L along (011) and c) V_T along (001). The solid line corresponds to the defect-free calculation.

Table 3.3 – DFT calculated single crystal elastic constants of $Ti_xZr_{1-x}N$ and Voigt-Reuss-Hill averages

Sample	c_{11} (GPa)	c_{12} (GPa)	c_{44} (GPa)	Zener ratio A	B (GPa)	G (GPa)	G/B	Poisson ratio $\nu_{(001)}$	c_{12}-c_{44} (GPa)
ZrN	529	111	112	0.5359	250	144	0.576	0.17	-1
$Ti_{0.25}Zr_{0.75}N$	538	104	119	0.5484	249	152	0.610	0.16	-15
$Ti_{0.5}Zr_{0.5}N$	540	107	123	0.5681	251	155	0.617	0.16	-16
$Ti_{0.75}Zr_{0.5}N$	557	113	139	0.6261	261	168	0.645	0.16	-26
TiN	583	137	166	0.7444	286	186	0.650	0.19	-29

The single crystal elastic constants and moduli are given in **Table 3.3**. The single crystal elastic constants are in line with the values calculated in [229] for *ZrN* (c_{11}=523GPa, c_{12}=111 GPa, c_{44}=116 GPa) and *TiN* (c_{11}=575 GPa, c_{12}=130 GPa, c_{44}=163 GPa). The elastic constants for the ternary $Ti_xZr_{1-x}N$ also found general agreements to our previous work calculated with ultrasoft pseudo-potentials [240]. The elastic moduli were calculated with ELATE program [241]. The *G/B* ratio is associated with ductility, with a critical value of 0.57 separating brittle and ductile materials. Although the ratio all exceeds 0.57, its decrease with *Zr* addition suggests the increase of ductility. The Cauchy pressure $(c_{12}$-$c_{44})$ with the addition of *Zr* indicates enhancement of the metallic bonding character by Zr alloying. **Figure 3.10a** illustrates that c_{11} decreases gradually from *TiN* to *ZrN*. For the binary nitrides, very close experimental c_{11} were obtained comparing to DFT. The deviation between experiments and DFT is relatively large for the ternary and increases

with *Zr* addition. The largest deviation of 175 GPa was found for *x=0.75*. It was found from calculations that metal and *N* vacancies contribute equally in reducing c_{11}. With 4.6 at. % vacancies, a reduction of ~100 GPa for c_{11} is expected, with reference to the defect-free compounds. The difference between the as measured c_{44} and the defect-free value predicted by DFT is typically within 20 GPa, where the experiments provide a higher value. 4.6 at. % metal vacancies can bring about a c_{44} increase of ~10 GPa. As contrast, *N* vacancies cannot strengthen c_{44} for *Ti-Zr-N* nitrides. A decrease of c_{44} for TiN due to *N* vacancies was even observed. These suggest metal vacancies influence rather than niotrogen.

Corresponding to $V_L[110]$, the elastic constant $(c_{11}+c_{12}+2c_{44})/2$ decreases theoretically as *Zr* content is increasing, from 526 to 432 GPa. Both metal and *N* vacancies lead to a reduction of 11 % for $(c_{11}+c_{12}+2c_{44})/2$ with 4.6 at. % vacancies. The most significant reduction was found for *TiN*, 4.6 at. % *N* vacancy results in a decrease of 58 GPa, accounting for 11%.

c_{12} in **Figure 3.10d** was not measured directly, but from the combination of $V_L[001]$, $V_L[110]$ and $V_T[001]$ on two samples. The data shows large degree of scattering. In contrary, theoretical c_{12} varies smoothly with *Zr* addition, ranging from 137 to 111 GPa, from *TiN* to *ZrN*. Furthermore, the vacancies, have very small influence on c_{12} comparing with other elastic constants. The deviation between DFT and experiments exceeds 55% and reach even up to 120%, certainly beyond the acceptable error range. This may be an indication of non-equivalent structural state for both samples with different crystallographic growth direction, leading to different elastic properties.

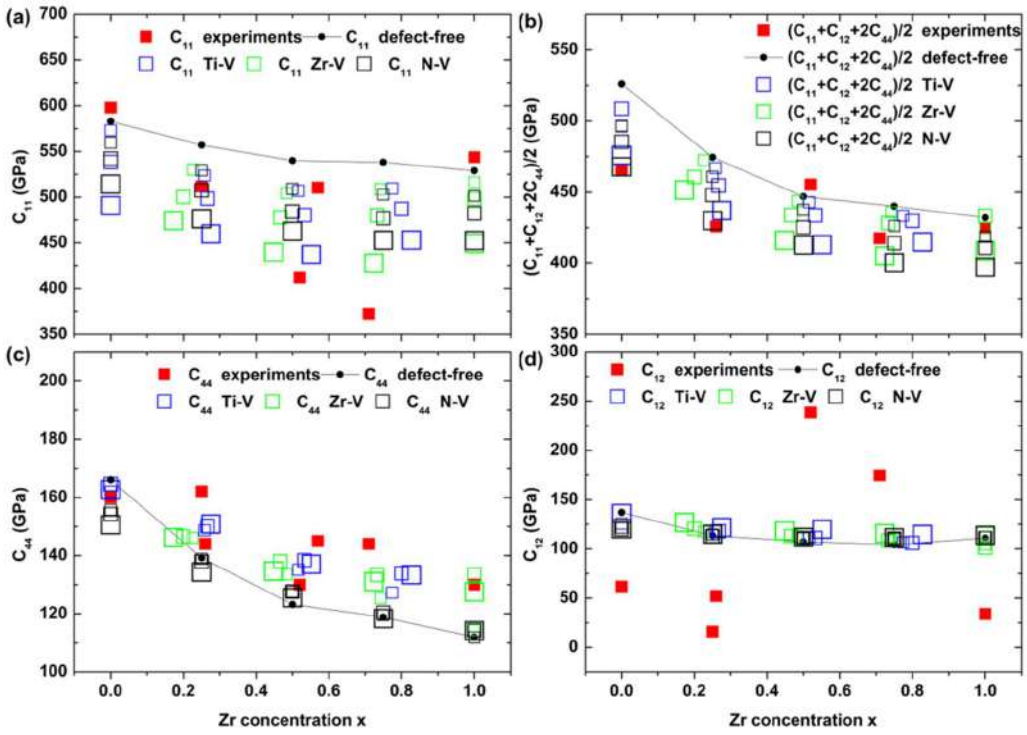

Figure 3.10 - Elastic constants measured as a function of *Ti* concentration, *x*: a) c_{11}, b) $c_{11}+c_{12}+2c_{44})/2$, c) c_{44} and d) c_{12} (deduced from a-c). The solid line corresponds to the defect-free calculation.

In general, V_L and V_T measured from epitaxial $Ti_xZr_{1-x}N$ films with (001) or (110) orientations and derived elastic constants agree well to the DFT predictions. $V_L[001]$ and c_{11} are below the defect free value while $V_T[001]$ and c_{44} are slightly higher than the defect free value. Considerations of vacancies further ensure better quantitative comparison. The physical origin is well explained in [189] where the vacancies reduce the occupations of the directional *p-d* covalent bonding and non-shear-resistant *d-d* metallic bonding, which leads to c_{11} softening and c_{44} stiffening, respectively. The experimental elastic constants are dispersive both as can be seen from our measurements and from literature. One possible reason is that nitrides can sustain a large amount of vacancies, resulting in different stoichiometry, which has significant influence on the elastic properties [237] compared to

lattice parameter. Besides, elastic constants are sensitive to microstructures, porosity, and textures in thin films [240, 242], these parameters are cumbersome to be accurately determined hence quite easy to be ignored.

With the combination of DFT calculations and optoacoustic techniques, it is possible to evaluate the influence of vacancies on elastic constants and estimate the vacancy type and concentration. The comparison of V_T and c_{44} to DFT calculations indicates the existence of metal vacancies for all compounds, since *N* vacancies don't play a huge role in c_{44} determination. This has also been confirmed by the elemental compositions as shown in **Table 2.2** that the *N*/metal ratio is slightly over 1. Vacancies also lead to significant reduction of $V_L[001]$ and c_{11}, as revealed by both experimental and DFT data. And the reduction increases with the vacancy concentration. The largest discrepancy of $V_L[001]$ and c_{11} between experiments and DFT were found at $x= 0.75$ where the largest *N*/metal ratio of 1.37 was reported in **Table 2.2**, suggesting the existence of the highest metal vacancy concentrations. This is also consistent with our vacancy formation energy calculations, from which we found lower metal vacancies formation energy at high *Zr* concertation. The (110) orientated thin films were used to probe $V_L[110]$, from which $c_{11}+c_{12}+2c_{44}$ can be derived. The relatively lower experimental $V_L[110]$ indicates that N vacancies are possibly presented because of metal vacancies alone cannot reduce $V_L[110]$. This is, however, contrary to the *N*/metal ratio which is above 1, but can be explained by the coexistence of both metal and *N* vacancies.

Our strategy to derive c_{12} employs two different sets of samples with either (001) or (110) orientations deposited at the same condition simultaneously. From the (001) oriented sample, c_{11} and c_{44} are determined while the complex elastic constant of

$c_{11}+c_{12}+2c_{44}$ is determined from the (110) oriented sample. As it has been shown, the accurate c_{12} determination cannot be achieved by manipulating the three elastic constants measured from two different samples. The reason for the non-feasibility is that the two samples are not comparable elastically even if they were deposited in the same condition, at the same time. They might have different microstructures, porosity, defects, etc., due to different substrates and growth directions.

3.4.2 TaN system

The vertical longitudinal sound velocity $V_L[001]$ of bulk wave propagating along the growth direction (001) and the transverse sound velocity $V_T[100]$ propagating along the in-plane (100) direction of the $Ta_{0.93}N/MgO(001)$ sample have been selectively measured by the PLU and BLS techniques, respectively (see **Figure 3.3**，**Figure 3.4**). This provides a selective measurement of c_{11} and c_{44} single-crystal elastic constants. The remaining independent elastic constant, namely c_{12}, has been determined by the fitting of several BLS spectra obtained at different angles of incidence (see **Figure 3.4**). It enables the calculation of the Poisson ratio $\nu = c_{12}/(c_{11}+c_{12}) = 0.197$. Additionally, vertical longitudinal sound velocity $V_L[011]$ and $V_L[111]$ of bulk wave propagating along the (011) and (111) growth directions of the $TaN_{0.99}/MgO(011)$ and $TaN/MgO(111)$ samples, respectively, have been selectively measured by PLU (see **Figure 3.3**). The measured sound velocities and elastic constants are reported in **Table 3.2**.

The obtained experimental single-crystal elastic constants from the $Ta_{0.93}N/MgO(001)$ sample are the following: $c_{11} = 530 \pm 10$ GPa, $c_{12} = 130 \pm 5$ GPa and $c_{44} = 137 \pm 3$ GPa. This yields a Zener anisotropy ratio $A = 2c_{44}/(c_{11}-c_{12})$ equal to

0.685. This value is significantly larger than the value of $A = 0.16$ predicted by DFT calculations for the perfect δ-TaN compound. However, both A values are <1, signifying that the elastically stiffest direction is along [001] for δ-TaN compound. This is reflected also by the fact that $V_L[001] > V_L[011] > V_L[111]$. Note that the calculated $V_L[011]$ and $V_L[111]$ velocities (5471 and 5347 m/s, respectively) from the $Ta_{0.93}N/MgO(001)$ sample slightly differ from the measured ones (5656 and 5635 m/s, respectively) on the $TaN_{0.99}/MgO(011)$ and $TaN/MgO(111)$ samples (compare solid and dashed lines in **Figure 3.11c-d**) but remain below $V_L[001]$ (5830 m/s). This is contributed to different film compositions, associated with different point defect concentrations (see below), depending on crystal growth orientation despite the films being deposited in the same batch.

Comparisons of DFT calculations considering defected δ-TaN_x structures and experimental results are collected in **Figure 3.11** for V_L and V_T. All sound velocities show different trends with increasing defect concentration and configuration type. If we restrict the discussion to Schottky-type defects, one can see that $V_L[001]$ is decreasing, while $V_T[100]$ and $V_L[111]$ are first increasing until a plateau is reached. For the specific (011) crystal orientation, Schottky defects have surprisingly no noticeable influence on the longitudinal sound velocity until ~15 % defect concentration, with $V_L[011]$ being equal to ~5625 m/s. This value agrees with the experimental value of 5656 m/s of the $TaN_{0.99}/MgO(011)$ sample; however, a stiffening of $V_L[011]$ is predicted when considering metal vacancies, especially for "symmetric" configuration up to ~12%. Nevertheless, for the two other crystal orientations, the predicted trends provide a mean to estimate the influence of the defect concentration on the elastic response of TaN_x compounds.

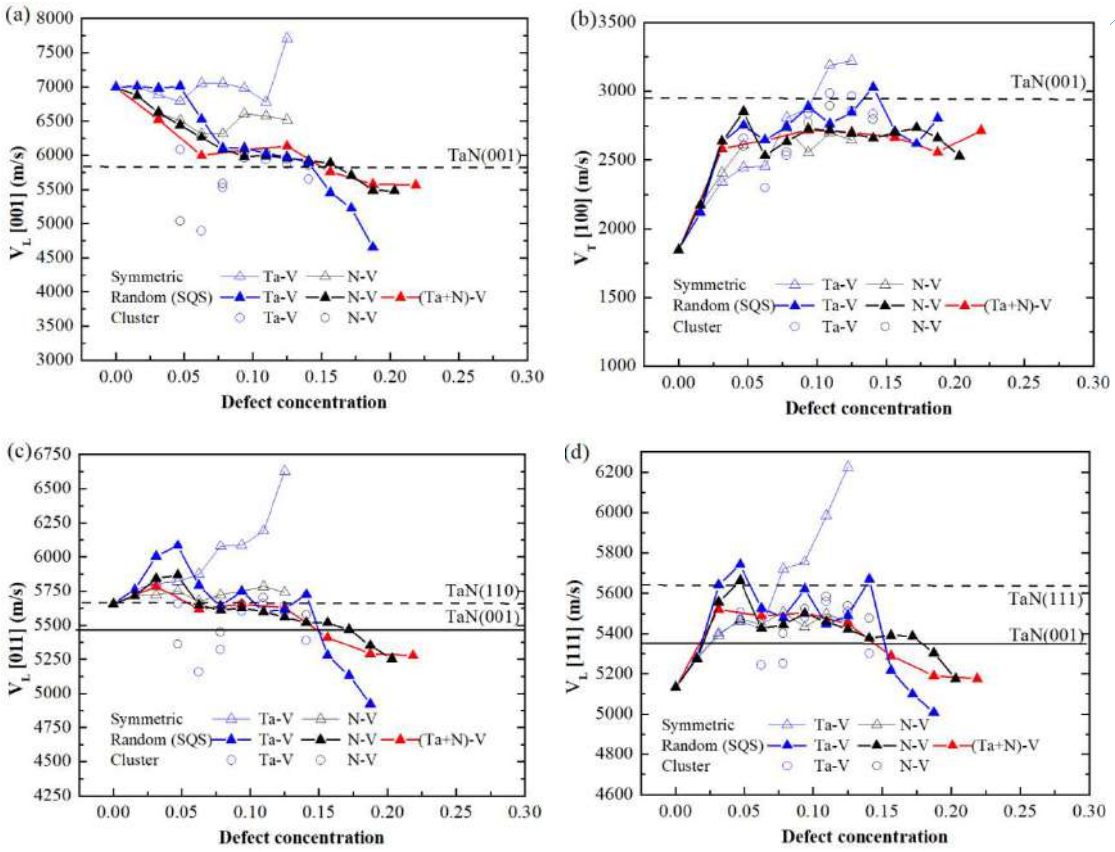

Figure 3.11 - Calculated sound velocities as a function of defect *(Ta, N or (Ta+N)* vacancy) concentration in *δ-TaN* structures. (a) $V_L[001]$, (b) $V_T[100]$, (c) $V_L[011]$, (d) $V_L[111]$. The horizontal dashed-lines indicate our experimental data selectively measured by PLU and BLS (a-b) on the $Ta_{0.93}N/MgO(001)$ film and PLU (c-d) on $TaN_{0.99}/MgO(011)$ and $TaN/MgO(111)$ films, respectively. In (c-d) the solid line is calculated from experimental C_{ij}'s of the $Ta_{0.93}N/MgO(001)$ sample.

Measured $V_L[001]$ (5830 m/s) and $V_T[100]$ (2963 m/s) are 20% lower and 76 % higher than the defect-free calculated values, 6994 and 1848 m/s, respectively (see **Appendix**). Interestingly, considering the presence of metal or nitrogen vacancies allows explaining these huge discrepancies, see **Figure 3.11**. At least 7 % up to 15 % Schottky defects have to be considered to match the experimental $V_L[001]$ value of the $Ta_{0.93}N/MgO(001)$ sample. This range of defect concentration is consistent with the previous discussion on the structural parameters (a_0 and ρ), see **Figure 3.6**. It is also

remarkable that it corresponds to the lowest formation energy of the defected δ-TaN_x structure, see **Figure 3.7**. For $V_T[100]$, accounting for Ta vacancies in addition to Schottky defects would enable to reach the experimental value above the "plateau". A lower defect concentration is expected, from 2.5% up to 12 % Schottky defects, for the *TaN/MgO(111)* sample.

Figure 3.12 displays the evolutions of the computed single-crystal elastic constants, c_{11}, c_{12} and c_{44}, as well as a combination of these data, as a function of defect concentration, and their comparison with experimental data. c_{11} and B have the same decreasing trend as defect concentration is increasing, pointing towards a more compliant material (see **Figure 3.12a** and **Figure 3.12c**, respectively). The experimental values, c_{11} = 530 GPa and B = 263 GPa, are ~20-27% lower than the calculated values of defect-free *TaN* compound, c_{11} = 731 GPa and B = 325 GPa (**Table A.1**). One has to consider the presence of 10-15% vacancies (*Ta* vacancies and/or Schottky pairs) to obtain a satisfying agreement with experimental data, in agreement with the previous estimations for lattice parameter (mixing of 3.5 % *Ta* vacancy and 8 % Schottky). On the other hand, a stiffening of the C_{44} elastic constant is observed with defect incorporation and the value saturates around 100 ± 15 GPa for defect concentration >5 %, see **Figure 3.12d**. The experimental value, c_{44} = 137 GPa, is ~180 % higher than the computed value of 50 GPa of the defect-free *TaN* compound but could be approached by considering at least 11 % defect concentration. Note that a value of 122 GPa is derived for c_{44} if one considers ρ_{XRD} instead of ρ_{XRR}. Similarly, the c_{12} elastic constant is found to first increase and then remains practically constant with introduction of defects, see **Figure 3.12b**, although its variations are less pronounced than for c_{44}. The present DFT calculations demonstrate that

introduction of vacancy-type defects into δ-TaN structure in concentration up to ~10% leads to a more compliant (from B = 325 to ~280 GPa) and less anisotropic (from A = 0.16 to 0.55) material. Electronic structure calculations (not reported here) of density of states (DOS) show that the presence of vacancies in TaN_x structures leads to a reduced number of *p-d* bonding states (integrated in the –10 to –4 eV interval), which weakens the bond strength, and could explain the observed c_{11} softening. The DOS at the Fermi level, corresponding to *d-d* metallic bonding states, is also reduced with introduction of either metal or nitrogen vacancy with respect to perfect *δ-TaN*, likely at the origin of c_{44} stiffening [36, 243]. Similar trends were reported by Jhi *et al*. [189] in sub-stoichiometric NbC_x compounds (same group-5 metal).

The value of 502 GPa, as measured by PLU for the modulus $(c_{11}+c_{12}+2c_{44})/2$, along the [011] direction of the $TaN_{0.99}/MgO(011)$ sample, compares well to the calculated values of defected structures over a wide range of concentration, see **Figure 3.12e**. While Ta vacancies and Schottky defects tend to decrease $(c_{11}+c_{12}+2c_{44})/2$ for concentrations larger than 5%, this modulus is found to be rather insensitive to N vacancy concentration, having a value of 480 ± 20 GPa for nitrogen deficient structures with concentration up to 15%. Although it is unrealistic to predict from the trends shown in **Figure 3.12e** which defect concentration would match at best the experimental

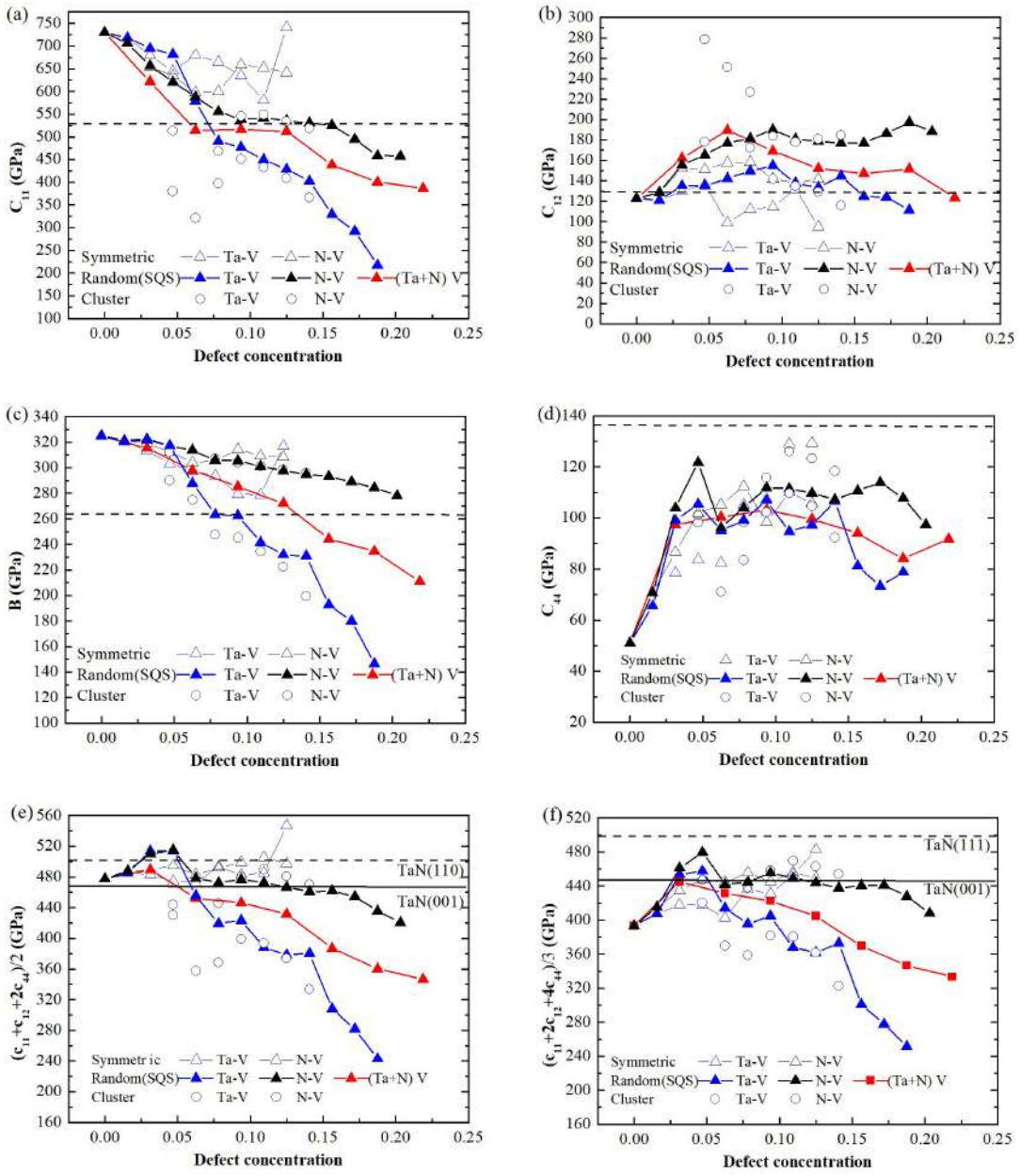

Figure 3.12 - Calculated elastic constants as a function of defect *(Ta, N or (Ta+N)* vacancy) concentration in *δ-TaN* structures. (a) c_{11}, (b) c_{12}, (c) $B = (c_{11}+2c_{12})/3$, (d) c_{44}, (e) $(c_{11}+c_{12}+2c_{44})/2$ and (f) $(c_{11}+2c_{12}+4c_{44})/3$. The dashed-line indicates our experimental data selectively measured by BLS (b-d) and PLU (a) on the *$Ta_{0.93}N$/MgO(001)* film, and by PLU (e-f) on *$TaN_{0.99}$/MgO(011)* and *TaN/MgO(111)* films, respectively. In (e-f) the solid line is calculated from experimental C_{ij}'s of the *$Ta_{0.93}N$/MgO(001)* sample.

$(c_{11}+c_{12}+2c_{44})/2$ value, the findings do not contradict the earlier statement that the $TaN_{0.99}/MgO(011)$ film showed the best crystalline quality and is stoichiometric.

For $(c_{11}+2c_{12}+4c_{44})/3$, an increase from 395 to 460-480 GPa is noticed with increasing defect concentration up to 5%, followed by a substantial softening for higher defect concentrations, see **Figure 3.12f**. The value of 498 GPa, as measured along the (111) direction of the *TaN/MgO(111)* sample by PLU, would be approached by considering a defect concentration of at least 5%. Schottky defects alone could not provide a closer agreement as for the (001)-oriented *TaN* film, which may indicate that this film is not stoichiometric. The relative difference between the defect-free and the defected film (minimum 5 % defect concentration) is –25%.

As energetics, of cubic and tetragonal structures may remain very close for small amounts of defect (< 2.5%), we should compare the elastic properties of the defected $Fm\bar{3}m$ cubic structure and of the defect-free *P4/nmm* tetragonal phase. As presented in **Table A.1** and in Ref.[230], the elastic properties of *P4/nmm(I)* are closed to the ones of *P4/nmm*. Whereas the c_{44} elastic constant (120 GPa) is comparable to our experimental value (137 GPa), the c_{33} elastic constant (262 GPa) is very different from both that of defect-free *δ-TaN* (731 GPa) and experimental value (530 GPa). This rules out the possible stabilization of a tetragonal structure in our as-deposited *TaN* films and further suggests that the cubic phase contains a defect concentration higher than 2.5 %.

3.5 *TaN* system: static and dynamical mechanical stability

There are three independent elastic constants in a solid crystal with cubic symmetry: c_{11}, c_{12}, and c_{44}. With no external stresses applied, its static mechanical stability

requires that $c_{44} > 0$, $c' = (c_{11} - c_{12})/2 > 0$, and $B = (c_{11} + 2c_{12})/3 > 0$ [244]. This first static criterion is easily verified, and the present findings confirm that as-deposited *TaN* films are mechanically stable. The same holds for the calculated *δ-TaN* structures as well as ordered TaN_x $(x \leqslant 1)$ and Ta_xN $(x \leqslant 1)$ compounds computed by CE (see **Appendix**, **Table A.2 and Table A.3**). The second criterion concerns the dynamical mechanical stability that can be inferred from vibrations calculations. The phonon dispersion properties of several ordered structures (defect-free $Fm\bar{3}m$ and *P4/nmm TaN*, Ta_3N_4 and Ta_4N_3 compounds with $Pm\bar{3}m$ structure having 12.5 % *Ta* and *N* vacancy concentration, see **Table A.3**) were calculated by PHONONPY code [245] within the harmonic approximation, using density functional perturbation theory (DFPT) calculations implemented in VASP. Details of the calculations and results are reported in **Appendix.A.3**.

The imaginary frequencies indicate dynamic instability for defect-free *δ-TaN* (see **Appendix**, **Figure A.2**), while *P4/nmm TaN* is thermodynamically more stable (as already discussed, see **Figure 3.7**) and dynamically stable (see **Figure A.3**). At low vacancy concentrations (< 2.5 %, see **Figure 3.7**), the cubic structure is still energetically not favorable and could easily transform to the more dynamically stable tetragonal phase after atomic relaxation [230]. However, for much higher defect concentration, defected *δ-TaN* structures become energetically more stable, similarly to the ordered defected structures with 12.5% *Ta* or *N* vacancy concentration. The phonon calculations on these two phases show that imaginary frequencies were not totally vanished though but can be suppressed by introducing more vacancies and/or ordering configuration. This suggests that vacancies,

known as cubic *TaN* phase-stabilizer from energetics, can indeed decrease the dynamic instability as well.

3.6 Summary and conclusions

B1-rocksalt epitaxial $Ti_{1-x}Zr_xN$ films with (001) and (110) orientations were deposited by magnetron sputtering. The sound velocities (V_L, V_T), the elastic constants $(c_{11}, (c_{11}+c_{12}+2c_{44})/2, c_{44})$ were measured using a unique combination of the picosecond laser ultrasonic and the Brillouin light scattering techniques. The lattice constants, mass density, vacancy formation energy, the single-crystal elastic constants c_{11}, c_{12} *and* c_{44}, of cubic $Ti_{1-x}Zr_xN$ with *Ti/Zr/N* vacancies were calculated as a function of *Zr* composition, x, using first principles DFT calculations in combination with SQS method. The combination of the vacancy involved DFT calculations and optoacoustic techniques, revealed the existence of metal and N vacancies inside the as-deposited $Ti_{1-x}Zr_xN$ films, and their different role in modifying different elastic constants, i.e., c_{11}, c_{12} *and* c_{44} and combinations. Existence of metal vacancies is expected for rich-Zr solid solutions, with favoured positions in the vicinity of depleted Zr region. The decreasing of c_{11} and rising c_{44} due to vacancies is commonly encountered for other transition metal nitrides and carbides. The calculations considered maximum 4.6 at. % vacancies which already provided good comparisons to experiments.

In contrast to $Ti_{1-x}Zr_xN$, influence of defects on the elastic properties of TaN is much more important and cannot be ignored. In case *TaN*, for (001)-orientation, BLS provides the measurement of c_{44} (137 ± 3 GPa) and c_{12} (130 ± 5 GPa) single-crystal elastic constants, while PLU provides the third independent one, c_{11} (530 ± 10 GPa). For (011)- and (111)-

orientations, PLU provides selectively the following additional combinations, $(c_{11}+c_{12}+2c_{44})/2$ and $(c_{11}+2c_{12}+4c_{44})/3$, respectively. Electrical resistivity measurements show evidence of point defects in the films despite a composition close to 1:1 stoichiometry. Point defects (metal and nitrogen vacancies) are considered in our first-principles calculations to find closer agreement between experimental and theoretical lattice parameter, mass density, sound velocities and elastic constants. Sound velocities and elastic constants are found to be particularly sensitive to the presence of vacancies, resulting into a more compliant and less anisotropic material. While only ~ – 1 % mismatch is found between predicted defect-free and experimental lattice parameters, huge differences of – 27 % and + 180 % are observed for c_{11} and c_{44}, respectively. These discrepancies can be rationalized by considering the presence of point defects (metal vacancy and/or Schottky defect) in concentration ~11% in the as-deposited *TaN* films, a compositional value that corresponds to the lowest formation energy of δ-TaN_x phase.

CHAPTER 4. THE BASE METALLIC HEA CoCrCuFeNi, BULK AND FILMS

We characterized at different scale thermal, structural and mechanical properties of the *CoCrCuFeNi* bulk HEA elaborated by arc-melting, as a reference for comparison to our films. The samples were synthesized by Pr. L-M Dong and co-workers at the Institute of Metal Research (Shenyang, China) and later used as a target for *CoCrCuFeNi* metallic alloy and *CoCrCuFeNi*N_x nitride film's depositions. First theoretical calculations including magnetic ordering with spin polarization of each element were conducted on this base HEA, before considering addition of 6th metallic element (*Al* and *Nb*) or nitrogen.

4.1 DFT simulations

4.1.1 EMTO-CPA and VASP-SQS spin-polarized calculations

4.1.1.1 Energetics: relaxed and unrelaxed atomic positions and magnetic ordering

Both CPA and supercell SQS calculations predict higher formation energy for the paramagnetic (PM) state than ferromagnetic (FM) state, indicating the FM state is more favourable at 0K for *CoCrCuFeNi* HEA. One can estimate the Curie temperature (T_c) from DFT calculations according to the formula based on mean field approximations,

$$T_c = \frac{2(E_{PM} - E_{FM})}{3k_B(1-c)} \quad (4.1)$$

where E_{PM} and E_{FM} are the total energies per atom for the PM and FM state, respectively, k_B is the Boltzmann constant, and c is the concentration of the non-magnetic elements in

the alloy. The T_c was calculated to be 234 K from EMTO-CPA calculations while 72 K from VASP-SQS calculations. Existing value based on EMTO methods from Huang [246] gives similar value of 251 K, while a smaller value of 172 K was found by Wang [119] measured by a SQUID magnetometer.

From our VSM characterizations, PM state was found for the bulk *CoCrCuFeNi* and thin films on *Si* substrate at RT (293 K). By contrast, FM state was found for thin films deposited on Kapton® from both VSM and FMR. It is surprising to find different magnetic configurations for the same material with different substrates. The origin is not known yet.

Table 4.1 – Formation energy, lattice parameter, mass density, elastic constants and Zener ratio simulated with EMTO-CPA and VASP-SQS, for both PM and FM *CoCrCuFeNi* state.

	E_f *(eV/at.)*	a **(nm)**	ρ *(g/cm^3)*	c_{11} **(GPa)**	c_{12} **(GPa)**	c_{44} **(GPa)**	B **(GPa)**	A $2C_{44}/(C_{11}-C_{12})$
EMTO-PM	0.235	0.35568	8.533	235	165	151	188	4.31
EMTO-PM **[246]**	-	0.35561	8.537	224	155	151	178	4.37
EMTO-PM **[247]**		0.35574	8.527	227	154	165	179	4.52
EMTO-FM **[246]**	-	0.35721	8.423	209	150	142	170	4.81
VASP-PM	0.138	0.35644	8.478	211	135	114	160	3.0
VASP-FM	0.131	0.35644	8.478	206	132	116	157	3.13
VASP-FM Atoms fixed	0.145	0.35632	8.486	239	161	118	187	3.02

4.1.1.2 Structural properties: lattice parameter and mass density

FM state has a slightly larger lattice parameter (0.357nm) than the PM state (0.352nm) as calculated by EMTO-CPA. Supercell calculations by VASP provide a

medium value (0.356nm) in between FM and PM states. The predicted mass density for the equimolar HEA has the value 8.478 g/cm^3 from VASP calculations. EMTO gives a slightly higher value for the PM state while a lower one for the FM state.

4.1.1.3 Sound velocities and elastic constants

We evaluate separately the magnetic and atomic relaxations effects on elastic constants. We first consider the effects of different magnetic configurations. EMTO and VASP calculations provide the same conclusion in this case. The differences between the calculated FM and PM elastic constants from EMTO calculations reported in [246] are small, i.e., 15 GPa (7 %), 5 GPa (3 %) and 9 GPa (6 %) for c_{11}, c_{12} *and* c_{44}, respectively. The difference is even smaller if calculated by VASP with atomic relaxations considered, i.e., 5 GPa (2 %), 3 GPa (2 %) and 2 GPa (2 %) for c_{11}, c_{12} *and* c_{44}, respectively. We conclude that, the magnetic configuration does not have significant influence on elastic constants for *CoCrCuFeNi* HEA.

To evaluate the atomic position relaxation effects, we further performed VASP supercell calculations with atomic positions fixed. This corresponds to EMTO calculations which do not include atomic relaxations. With atomic positions fixed, we obtained a significantly higher elastic constants for c_{11} and c_{12}, of FM *CoCrCuFeNi*, with the difference corresponding to 33 GPa (16 %) and 29 GPa (22 %) respectively, by comparing to the fully relaxed calculations. Surprisingly, C_{44} is not affected by atomic relaxations. Larger c_{11} and c_{12} leads to a higher bulk modulus B for the atom-fixed configuration. Note that c_{11}, c_{12}, and B from EMTO predictions, are also higher comparing to the fully relaxed SQS calculations, emphasizing the necessity of considering atomic relaxations in

calculating elastic constants for MCAs, avoiding overestimations of some elastic constants and moduli.

Note that elastic constants from EMTO calculations are sensitive to the derivation of bulk modulus as demonstrated in [248]. This leads to a certain uncertainty between calculations from different authors. But in general, we see that EMTO calculations from both our own calculations and literatures provide a more rigid material, namely a higher c_{11}, c_{12} and bulk modulus B, as well as a higher value for c_{44}, than SQS supercell methods. The higher value of c_{44} was also reported in other materials [249, 250], which might be a systematic output of EMTO methods.

Elastic constants c_{11}, c_{12} and c_{44} calculated from VASP with atomic relaxations for the ground state FM *CoCrCuFeNi* have the value of 206, 132 and 116 GPa, respectively. The material is anisotropic with a Zener ratio above 3. Using ElAM (Elastic Anisotropy Measures) program [251], Young's modulus (E) along different crystallographic orientations is plotted in **Figure 4.1a**, respective to the crystal axis <100>. E along the most rigid direction, i.e., E_{111} has a maximal value of 279 GPa, while E along the soft direction, E_{001} has a minimal value of 102 GPa. This last value is in good agreement to the one (~70 GPa) measured by Zhang [252] from compression of <100> oriented micro-pillars, considering the general reduction of Young's modulus due to size effects [253] and to the existence of the softer *Cu*-rich second phase in this HEA. Shear modulus depends on both the shear plane and shear direction in the plane. Shear modulus minimal and maximal values were found respectively, in (110) and (001) planes, with G_{min} = 37 (<-110> direction in (110) plane) and G_{max_001} = 116 GPa (<3 17 0> direction in (001) plane).

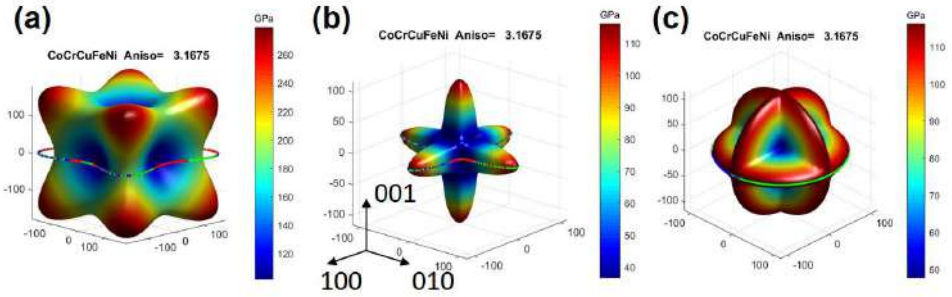

Figure 4.1 - Orientation dependence of (a) Young's modulus *E*, (b) minimum shear modulus, (c) maximum shear modulus *G*, for *CoCrCuFeNi*. The input elastic constants were calculated by VASP-SQS, considering FM state and atomic positions relaxations.

Table 4.2 - Hill average of isotropic, (111)- and (001)-textured FCC *CoCrCuFeNi* elastic moduli and sound velocities.

Orientation	*B* (GPa)	G_{xz} (GPa)	E_z (GPa)	*Poisson ratio* ν		V_L (||z) (m/s)	V_T (xz) (m/s)
Isotropic	156	73	190	0.2983		5466	2934
(111)	156	55	279	ν_{xy} = 0.3832	ν_{xz} = 0.1567	6057	2547
(011)	156	66	217	ν_{xy} = 0.3277	ν_{xz} =0.2482	5654	2790
(001)	156	116	102	ν_{xy} = 0.1224	ν_{xz} =0.5623	4929	3699

The Voigt-Reuss-Hill (VRH) average provides a simple way to estimate the elastic constants and moduli of a textured/isotropic polycrystal in terms of its crystallographic texture and the single crystal elastic constants of the constituting crystals. The average elastic properties of more often encounter isotropic, (111)- and (001)-textured FCC *CoCrCuFeNi* are given in **Table 4.2**.

4.2 Experimental: micro- vs. macro-scale

In order to provide a mean for a direct comparison between experiments and previous DFT calculations of *CoCrCuFeNi* properties, we first privileged the techniques which allow measurements of bulk samples with larger grain size at the microscale (the grain): XRD (intra-granular and phase sensitive), nanoindentation (mapping with indent spacing of order of 10 μm), PLU (surface wave propagation imaging on a 100x100 μm^2 area and thermal conductivity contrast), BLS (Rayleigh surface wave velocity mapping in one grain vs. the propagation direction). Other methods such as the standard tensile tests, the pulse echo ultrasound and DSC techniques provided macroscopic average properties of the bulk polycrystalline *CoCrCuFeNi*, having also a fraction of segregated *Cu*-rich phase at the grain boundaries. Most of these techniques are also used to further characterize films' properties with much finer grains and better homogeneity.

4.2.1 Structural properties: lattice parameter and mass density

The structure is FCC with a lattice parameter $a_0 = 0.3596$ nm, near equiatomic concentration and some *Cu* (*Ni* to a less extent) segregation appearing at the grain boundaries (GBs) delimiting a rich-*Cu* (~88 at. %) interdendrite (ID) narrow phase (~5-10 μm width) and larger dendrite phase of *CoCrCuFeNi* grains (~30 μm) with a *Cu* gradient near GBs. Microstructure is similar to the one observed in Ref. [196]. The lattice parameter of this FCC phase was estimated to be 0.3602 nm. The lattice parameter of as-cast *CoCrFeNiCu* alloy [119] was reported to be 0.3579 nm, which is also in agreement with the value measured in the present work. All these values agree within less than 1 % with the DFT (SQS) 0.35644 nm. The mass density as measured by the piconometer 7.964 g/cm^3

is 6.5 % lower than that of DFT (8.478 g/cm^3) that indicates the presence of equivalent fraction of porosity.

4.2.2 Mechanical properties: nanoindentation and tensile tests

Nanoindentation mapping has been done on the area shown in **Figure 2.16**. The nano-hardness varies from 1 GPa (in the *Cu*-rich segregated area) to ~ 7 GPa (in the inner HEA grains) with an average value $H \sim 5$ GPa. It does compare well to the hardness (~ 8 GPa) measured in our different batches of *CoCrCuFeNi* films [9, 254], but seems to be slightly higher that the reported average value for both the FCC matrix and the *Cu*-rich phase (~ 3 GPa) by Zhang *et al.* [255] for as-cast *CoCrCuFeNi-Gd$_x$* alloys. The indentation modulus E_{IT} from nanoindentation ranged from 55 to 233 GPa. The larger value corresponds to the intra-granular area of HEA, while the small value corresponds to the less rigid *Cu*-rich segregation's area. EBSD mapping reveals that the nanoindentation went through grains with several different orientations including rigid (111), (011) and soft (001). Note that the *CoCrCuFeNi* is highly anisotropic, with maximum E_{111} and minimum E_{001} equal to 279 GPa and 102 GPa, respectively. Overall, the mean value (199 ± 18 GPa) from nanoindentation across several grains matches well with the DFT (SQS) prediction and Hill isotropic average Young's modulus (190 GPa). On the other hand, the tensile test provides a Young's modulus of 150 GPa and a yield strength of 260 MPa, in close agreement to other results ($E \sim 170$ GPa and $\sigma_y = 320$ MPa) from nanoindentation and compression tests, respectively [255] . In the tensile test, the fact that the fracture happened at a very low strain 10 percent while the ultimate strength was low ($\sigma_f = 330$ MPa) suggests the existence of voids, as already mentioned above for the lower mass density.

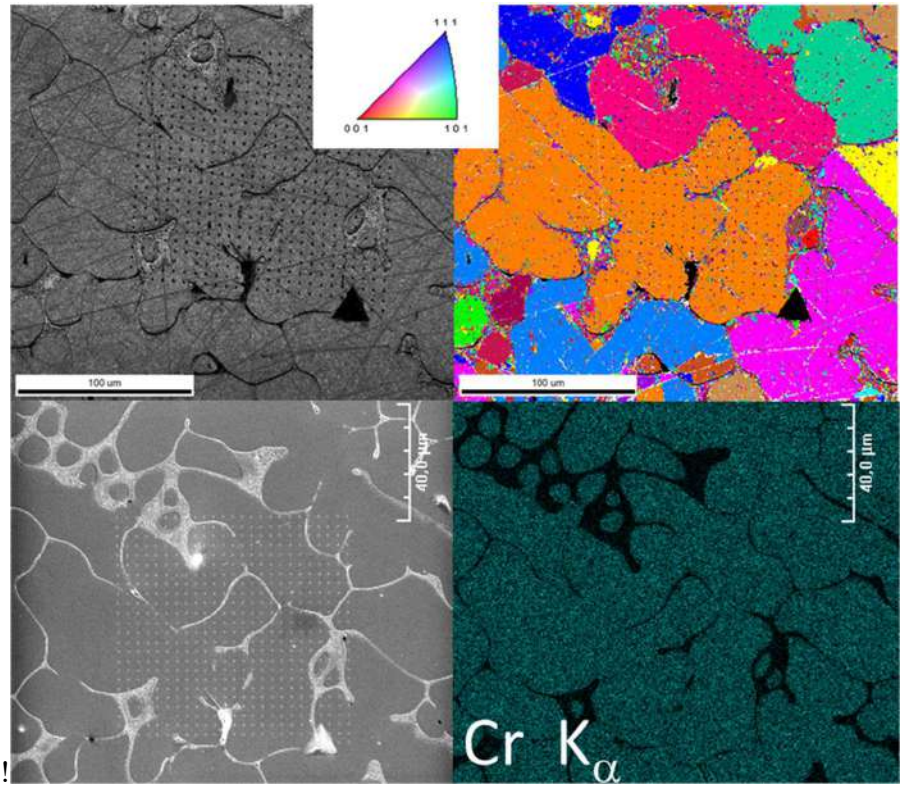

Figure 4.2 - SEM microstructure of as-cast *CoCrCuFeNi*, EDS mapping of *Cr* element and EBSD analysis at the same location. Indents from nanoindentation mapping are visible.

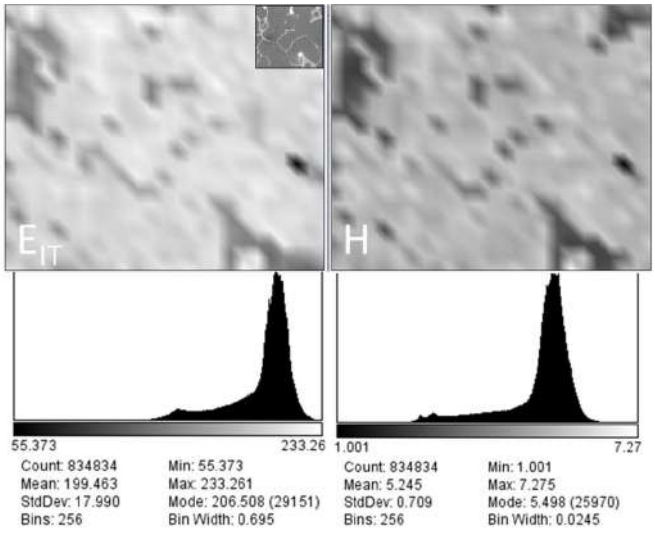

Figure 4.3 – Mapping of the indentation modulus (E_{IT}) and nanohardness (H) of bulk *CoCrCuFeNi*. The value (in GPa) is indicated by the color of the mapping. Statistics (mean and standard deviation) are given at the bottom.

4.2.3 Thermal properties: thermal diffusivity (D), conductivity (λ) and heat capacity (C_P)

Investigations by modulated thermoreflectance microscopy have been performed over the same large area as for nanoindentation tests. In such approach, a pump laser is modulated at 1.8 MHz to heat the sample and a superimposed probe beam detected the change of sample reflectivity at the same frequency across a lock in amplifier. Using the DC signal, reflected by the sample surface, an optical image could be recorded in order to locate the grain boundaries, **Figure 2.17a**. In same time, the modulated sample reflectivity is mapped and normalized by the optical image to shed light on thermal contrast **Figure 2.17b**. The resulting signature is correlated with lateral thermal properties change of the sample. By this way, spatial variation of photo thermal coefficient, which link the optical index with the temperature, may be revealed and compared to a composition map. The variation of thermal diffusion length and all thermal barriers, playing the role of thermal

resistance is also a source of signal. As we can notice the inner grain thermal signature is nearly uniform, but all the boundaries exhibited a huge fluctuation in **Figure 2.17**, a proof that thermal properties are nearly constant for different grain orientations in opposition with the rich copper segregated zones.

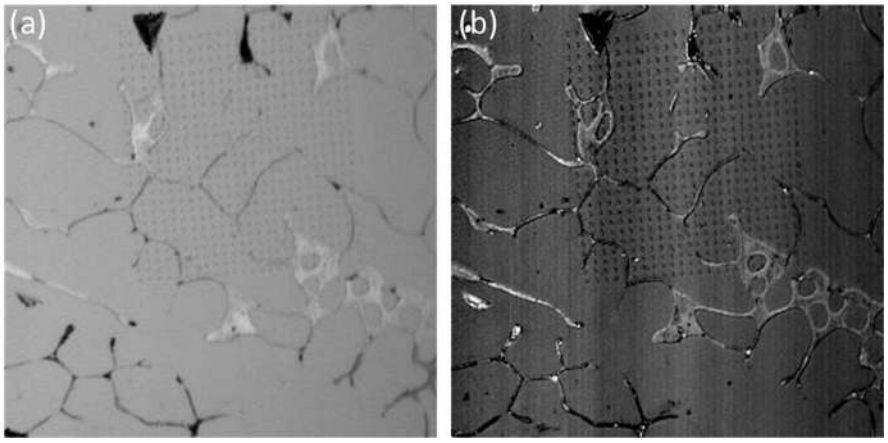

Figure 4.4 – (a) Optical image, scale 286×286 µm². The indentation marks as well as the rich copper grains are clearly visible. (b) Thermal image obtained on the same area for a modulation frequency of 1.8 MHz.

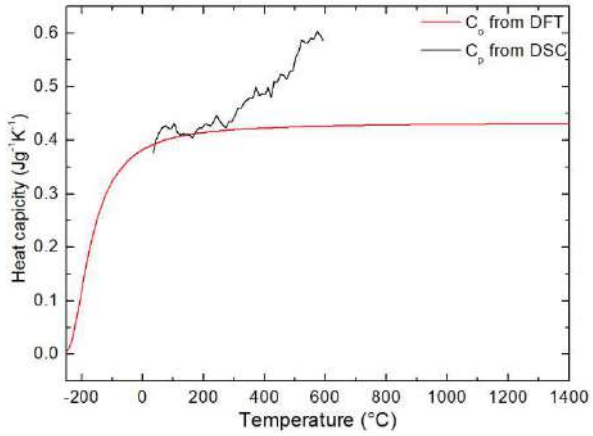

Figure 4.5 – Heat capacity vs. temperature of *CoCrCuFeNi*, measured by DSC and calculated from DFT within a Debye model simulation.

The heat capacity was measured by DSC from room temperature to 500 °C and compared to the Debye model estimate, in **Figure 4.5**. At room temperature, we found $C_P \sim 390$ J/(kgK) which agrees well with DFT and Debye model simulation.

The thermal diffusivity was measured by thermoreflectance microscopy within a single CoCrCuFeNi grain. Inside the HEA grain, the diffusivity value is 5×10-6 m2/s, as shown in Figure 4.6, while at the grain boundary with more Cu segregation, the diffusivity was about 6 times larger (~ 3×10-5 m2/s). Wang et al. [256] measured the macroscopic thermal conductivity of CoCrCuFeNi with a laser flash method. Their value equals to 4.7×10-4 m2/s at 297 K, which is two decades higher than our intra-granular result, due to the contribution of Cu-enriched phase. Indeed, the thermal diffusion coefficient of the solid Cu element is about 1.12×10−3 m2/s, suppose that the difference between the volumetric heat capacity of HEA and Cu-rich phase is negligible. We

therefor use the heat capacity from DSC for both phases in order to get their thermal conductivity. Using the above measured volumetric heat capacity 3.106 J/K/m^3, we derived the thermal conductivity for a single grain HEA and *Cu*-rich phase, 15 and 102 W/m/K respectively. Hence, the existence of *Cu*-rich segregation of much higher conductivity will increase a lot the macroscopic averaged thermal conductivity of this high entropy alloy.

Many more experiments were also done on *CoCrCuFeNi*, $(CoCrCuFeNi)_{1-x}(Nb_x, Al_x, N_x)$ thin films in collaboration with Pr. Daniele Fournier (@INSP), who is gratefully acknowledge, varying the porosity fraction and the chemical composition. Their analysis and correlations to the microstructure and chemical composition is still under progress and will not be reported in this thesis.

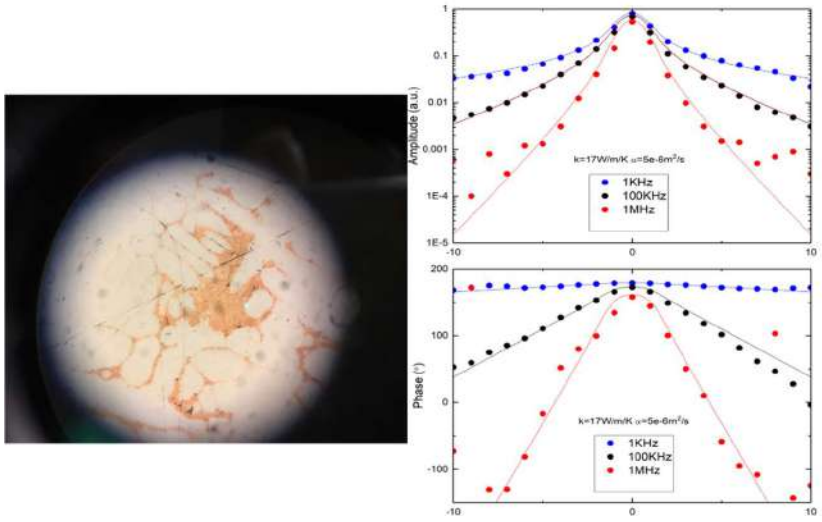

Figure 4.6 – Bulk *CoCrCuFeNi* surface showing *Cu* segregation (yellow) and *CoCrCuFeNi* grain (grey). Thermal conductivity (λ) and diffusivity (*D*) were measured within one single *CoCrCuFeNi* grain (probing diameter = 10 µm) using thermoreflectance microscopy. Best values of 15 W/m/K and 5 10^{-6} m^2/s were found by fitting the amplitude and phase of the probe signal. The experiments were conducted with 3 modulated laser frequencies, at 1 kHz, 100 kHz and 1 MHz.

4.2.4 Sound velocities and elastic constants: pulse echo techniques, BLS and PLU

Longitudinal and shear sound velocity of the bulk at RT were measured by the pulse echo ultrasound (5 MHz transducer) and BLS (on five different grains of the indentation map in **Figure 4.1**), with the respective average value of 4545 ± 20 m/s and 2885 ± 20 m/s. The derived average elastic constants are 128 ± 1 and 81 ± 1 GPa for C_{33} and C_{44}, respectively. The DFT predicted isotropic polycrystalline longitudinal and shear sound velocity are 5466 and 2934 m/s, respectively, with C_{33} and C_{44} corresponding to 253 and 73 GPa. The deviation of the longitudinal sound velocity V_L and elastic modulus C_{33} are much larger, which might be due to the voids and the soft *Cu*-rich segregation phase contributions to this macroscopic measurement. In case of BLS, the sampling of grains is

reduced, but is not influenced by *Cu* segregated phase and voids in the bulk, offering a satisfactory comparison of V_T and C_{44} to DFT ones.

Further intra-granular analysis was successively performed by PLU, generating with a point source and imaging bulk and surface acoustic waves, propagating at the surface of one grain. An illustration is provided in **Figure 4.7**, for the big grain having (001) orientation (see **Figure 2.16**, orange grain labelled **1**). The fourth order cubic symmetry is easily recognized from mapping of the detected vertical displacement $u_z(x, y, t_0+i200$ ps) by interferometry, t_0 being the launching time. For both direction of propagation, *X1* = [100] and *X2* = [110], the analysis of the time and position of each wave having a fast (F) or a low (L) motion, provided two or three sound velocities $V_{L1} = \sqrt{C_{L1}/\rho}$, $V_{L2} = \sqrt{C_{L2}/\rho}$ and $V_F = \sqrt{C_F/\rho}$.

A detailed discussion of the full numerical analysis (all directions) of such experiment can be found in Ref. [256, 257]. Here, we restrict ourselves to provide some more data to compare to DFT and later to thin films. From a quick semi-analytical analysis of wave propagation in a (001) plane of cubic symmetry made by Stoneley [258], the following conclusions could be obtained: $V_{L1} = \sqrt{C_{L1}/\rho}$ along [100] direction should be identified to Rayleigh surface velocity V_R, and the lowest shear wave velocity along the [110] direction to $V_{T1} = \sqrt{C_{T1}/\rho}$ with $C_{T1} = (c_{11} - c_{12})/2$. The fast sound velocity, $V_F = \sqrt{c_F/\rho}$ can be identified to the longitudinal sound velocity $V_L = \sqrt{c_{11}/\rho}$ along [100] direction. The numerical search [258] of V_R that remains slightly below $V_{T2} = \sqrt{c_{44}/\rho}$ will provide the remaining constant c_{44}. We measured $V_R[100]$ = 3080 ± 46 m/s (i.e. V_{T2} [100] = 3348 ± 50 m/s), V_{T1} [110] = 2540 ± 173 m/s and V_L [100] = 5310 ± 174 m/s.

We used the VASP-SQS mass density ($\rho = 8.478$ g/cm^3) instead of the composite experimental one, to deduce the single crystal elastic constant: $c_{11} = 239 \pm 14$ GPa, $c_{12} = 109 \pm 14$ GPa, $c_{44} = 95 \pm 3$ GPa and $B = 152 \pm 14$ GPa. This ***first direct*** measurement in a single (001) grain of our bulk *CoCrCuFeNi* HEA is quite encouraging and compared reasonably well to VASP-SQS (see **Table 4.1**), taking into account respective accuracy and some disorientation of this grain from the perfect (001) plane. Accessing such single-crystal elastic properties necessitates usually the single crystal growth of the material by a Bridgman technique, and its analysis by employing resonant ultrasound spectroscopy [259] or dynamical vibration analysis [114].

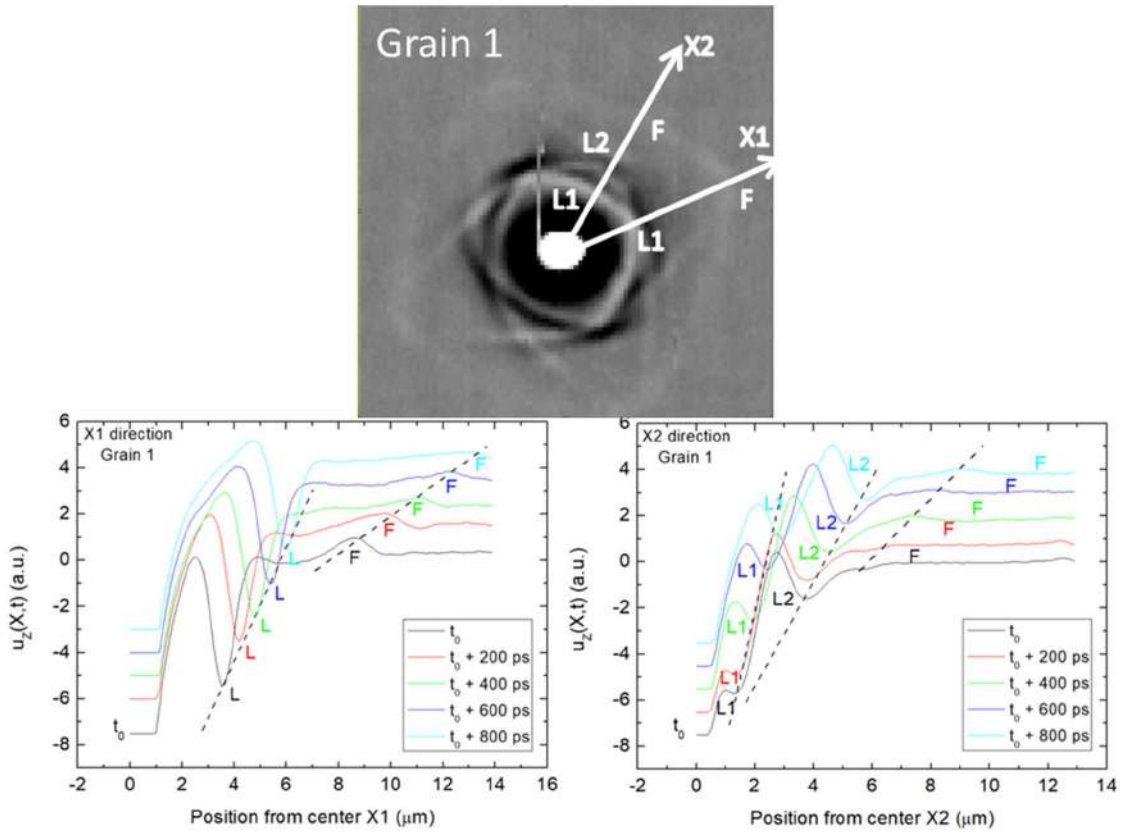

Figure 4.7 – At the top, surface and bulk acoustic waves generation (t_0) and imaging (t_0+200 ps) of their propagation in a grain with (001) orientation. Snapshots with a time-step of 200 ps, along the two high symmetry direction, *X1* = [100] and X2 = [110] are provided in the bottom. L and F denotes the low-velocity and fast-velocity acoustic wave.

As a supplementary comparison (process elaboration, shape and microstructure), *CoCrCuFeNi* metallic thin films were deposited from this bulk HEA target by magnetron sputtering, varying their thicknesses and the substrate. Their elasticity was further studied by PLU and BLS to probe the longitudinal and shear sound velocity of *CoCrCuFeNi* polycrystalline films. Previous works done by Braeckman *et al.* [254] with films deposited from a composite compacted powder target on silicon, showed that V_L and V_T of as-deposited <111>-textured dense thin films are 6100 and 2600 m/s, with the corresponding

C_{33} ~ 300 GPa and C_{44} ~ 52 GPa. C_{33} is slightly below than the VASP-SQS DFT value of 310 GPa, while Young's modulus $E_{(BLS+PLU)}$ ~ 150 GPa and indentation test modulus E_{IT} ~ 190 GPa are in the range of the previous values measured in the bulk, but remain both far below the simulated E_{111} (279 GPa). There is certainly some details of the microstructure that are not well considered in order to reach a better agreement for the Young's modulus, such as a core shell structure with an oxide (disordered/amorphous) surrounding the grains [9]. Such shell material may induce a softening of some elastic constants or moduli, depending on its thickness and elastic properties.

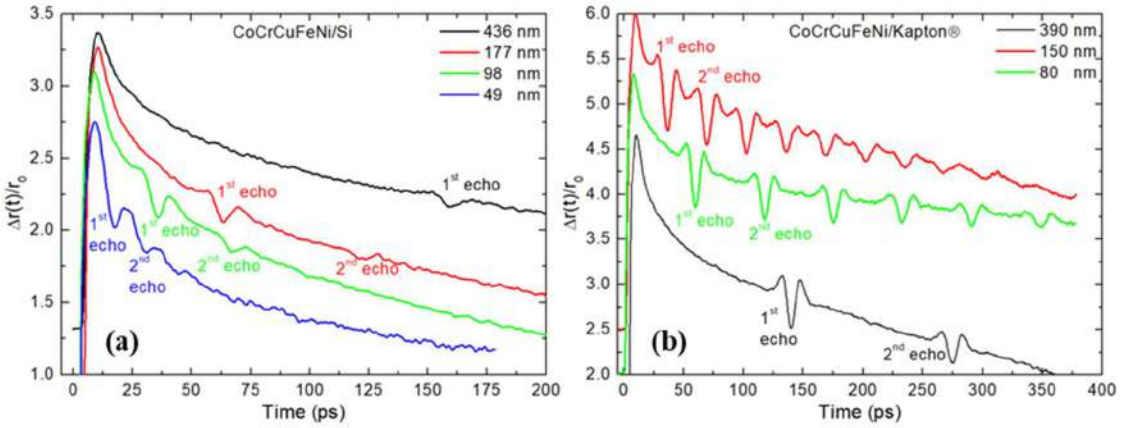

Figure 4.8 – Transient reflectivity of *CoCrCuFeNi* films vs. thickness, (a) films on silicon substrate, (b) films on Kapton substrate.

In this work, the influences of two different substrates (*Si* and Kapton®) as well as thicknesses were evaluated. The depositions were done in a high vacuum chamber. More details about the deposition and microstructure can be found in Chapter 2. The sound velocities and elastic constants measured by our optoacoustic techniques, BLS and PLU, are listed in **Table 4.3**. The transient reflectivity measured by PLU is shown in **Figure 2.28** for both films on silicon or Kapton substrates. It demonstrates the quality of the

measurements of echoes vs. the thickness (50-400 nm). The amplitude of echoes is even higher in case of Kapton as the impedance contrast (ρV) with the film is higher, favouring the reflexion at the interface and detection at the free surface.

Table 4.3 - Sound velocities and elastic constants of as-deposited polycrystalline *CoCrCuFeNi* thin films

Substrate	Thickness (nm)	ρ(g/cm^3)	V_L(m/s)	C_{33} (GPa)	V_T(m/s)	C_{44} (GPa)
Si	436	8.6	5626±60	272±20	2737±25	64±2
	177		5520±60	262±20	2823±25	69±2
	98		5297±60	241±20	/	/
	49		5600±200	270±30	/	/
	28		/	/	/	/
Kapton®	390	8.6	5455±60	256±5	/	/
	150		5455±60	256±5	/	/
	80		4938±200	209±20	/	/

Note that BLS analysis of thin films (< 250 nm) is no more direct, because Rayleigh wave sound velocity will become dispersive, varying with thickness and being influenced by the presence of the underlying substrate. This can be partially overcome if

we use a full simulation of surface waves within a multilayer structure (film + substrate). Besides, we observed that the thickness measured by mechanical profilometry on soft substrate might involve larger errors than on *Si* substrate. Recall that V_L and V_T calculated by DFT for non-textured *CoCrCuFeNi* polycrystals are 5466 and 2934 m/s, respectively,

in very close agreement to the results from the as-deposited films. The accordance might result from the chemical and microstructural homogeneity for deposited thin films as compared to the bulk material. The higher experimental value is due to the contribution from the most rigid <111> orientation in the case that the film is not perfectly isotropic but has a preferred growth orientation, which is reflected from XRD pattern when the <111> peak has a dominant intensity.

The substrates or the thickness did not show obvious influences on the elastic properties of deposited *CoCrCuFeNi* films, at least on the longitudinal sound velocity and elastic constants.

4.3 Summary and conclusions

We performed first DFT calculations on our reference base HEA alloy: *CoCrCuFeNi*. The comparison between EMTO-CPA and VASP-SQS, which enable mimicking the randomness of such FCC solid solution, showed negligible influence of magnetic ordering FM or PM on structural or elastic properties. More relevant, atomic positions relaxations must be considered if one wants to reach better accuracy level on the elastic property predictions. EMTO-CPA does not permit such atomic position relaxation and leads to a systematic overestimation of elastic constants in comparison to VASP-SQS. Then VASP-SQS is privileged assuming a FM state rather than PM, that will simplify future comparison of chemical alloying (*Nb*, *Al* and *N*) from one supercell to another.

A second level of comparison is done between DFT simulations and several experiments (XRD, nanoindentation, PLU, BLS, pulse echo ultrasound and tensile tests) that can distinguish between intra-granular vs. macroscopic properties, and on bulk and

films (different process elaboration and microstructure). A good agreement is found for bulk and films stress-free lattice parameters (< 1 %) whereas mass density of the bulk material exhibiting some voids, is ~ 6 % lower than the one of films (~ 8.6 g/cm^3) or DFT which agreed very well to the film. A first direct PLU measurement of sound velocities (V_L and V_T) and single crystal elastic constants in a single (001) grain of the bulk *CoCrCuFeNi* HEA compared reasonably well to VASP-SQS, taking into account respective accuracy and some disorientation of this grain from the perfect (001) plane. These single crystal elastic constants (experimental and DFT) enabled an overall good prediction of macroscopic average properties (sound velocities and elastic constants and Young modulus), if one considered the correct texture and segregation of *Cu*.

CHAPTER 5. THE BASE HEA CoCrCuFeNi THIN FILMS: THE ROLE OF A 6TH ELEMENT ADDITION

(CoCrCuFeNi)$_{1-x}$(Al, Nb)$_x$ thin films were deposited by magnetron sputtering at Ghent University using compacted powders target, in the group of Prof. D. Depla. By varying the (*Al, Nb*) concentration, phase transitions were observed as well as crystallographic texture changes. By adding *Al*, the FCC to BCC phase transition took place at ~20 at. % *Al* addition, while for ~15 at. % *Nb* addition an FCC to amorphous transition happened. Besides phase transition, in the case of *Al* alloying, films were meanwhile porous which also plays a role in material properties. DFT calculations were not only able to capture the phase transitions from energetics, but also provided good predictions of structural (lattice parameter and mass density) and elastic properties. Elastic properties were calculated and compared to available optoacoustic measurements. EMTO-CPA was used due to its superior efficiency (accuracy and computing time) for calculating multicomponent metallic alloys. As a comparison, we performed VASP calculations combined with SQS to evaluate the influence of local lattice distortion, or atomic relaxation which is not been considered in EMTO calculations. AIMD calculations were carried out for the amorphous phase.

5.1 DFT calculations and the Debye model

5.1.1 VASP-SQS

The first-principles electronic-structure calculations were performed using: (*i*) the Vienna ab initio simulation package (VASP) [13, 260] employing projector augmented-

wave (PAW) potentials [261] with the special quasirandom structures (SQS) [262] generated by the alloy theoretic automated toolkit program (ATAT) [16]; (*ii*) the exact muffin-tin orbitals (EMTO) method [14] with the coherent potential approximation (CPA). The SQS and CPA techniques are used to mimic the disordered solid solutions. The formation energy per atom (ΔH) is obtained from the following relation:

$$\Delta H(x) = \frac{1}{N}\left(E((CoCrCuFeNi)_{1-x}Me_x) - \left(n_{Me}E_{Me} + \frac{(N - n_{Me})}{5}\sum_i E_i\right)\right) \quad (5.1)$$

with E being the total energy of $(CoCrCuFeNi)_{1-x}(Nb_x, Al_x)$, E_i and E_{Me} the reference energy of the transition metals (*Co, Cr, Cu, Fe, Ni*) and the metallic element *Me* (Al or Nb) in their bulk state, N and n_{Me} the total number of atoms and *Me* atom count in the supercell.

Supercells with 64-atoms were build using equiatomic FCC and BCC *CoCrCuFeNi* with (4, 9, 14 and 19) atom sites randomly substituted by *Nb* or *Al* atoms and collinear magnetic moments (ferromagnetic FM state). Hence, *Nb* or *Al* atomic concentration spanned 0-30 at. %. Note that exceptionally for the base *CoCrCuFeNi* alloy, we've used a supercell containing 80 atoms. Potentially, there is an uncertainty in the energy of different configurations due, for example, to the permutations in the atomic positions of different atomic species in equiatomic HEAs. The challenge is even greater when the magnetic disorder in HEAs is considered. Accuracy was verified by comparing energetics to larger supercells with 125 atoms (twenty-five *CoCrCuFeNi*). The Perdew-Burke-Ernzerhof (PBE) exchange correlation functional [263] in the generalized gradient approximation (GGA) was employed to perform the self-consistent calculations and compute the total energies. We used uniformly distributed *k*-points in the irreducible Brillouin zones with *k*-

points spacing equals to 0.2 per Å, according to the Monkhorst-Pack scheme [264], for both FCC and BCC phases, and an energy cut-off of 500 eV. The electronic energy-convergence criterion was set to 10^{-5} eV/cell. VASP-SQS energetics calculations were performed considering no relaxation of atoms within the supercell (total energy per atom, E_{nr}) and allowing atomic relaxation (total energy per atom, E_r), the difference providing the relaxation energy between the non-relaxed and the relaxed supercell $\Delta E_r = E_{nr} - E_r > 0$. This relaxation energy is associated to the following (*LLD,* **Figure 2.3**) quantity [184] that quantifies the local lattice distortion:

$$LLD = \frac{1}{N}\sum_i \sqrt{(x_i - x_i')^2 + (y_i - y_i')^2 + (z_i - z_i')^2} \tag{5.2}$$

with (x_i, y_i, z_i) and (x_i', y_i', z_i') being the unrelaxed and relaxed positions of atoms i in the cell-coordinates and N is the total number of atoms in the supercell (80 for the base *CoCrCuFeNi* and 64 for others with *Al* or *Nb* addition) of alloys.

The relaxation energy will be compared to the elastic-strain energy ΔH_{el}, defined in [101, 265] as

$$\Delta H_{el} = \sum_{i=1}^{N} c_i B_i \frac{(V_i - V)^2}{2V_i} \tag{5.3}$$

$$V = \frac{\sum_{i=1}^{N} c_i B_i V_i}{\sum_{i=1}^{N} c_i B_i} \tag{5.4}$$

where c_i, B_i and V_i are the concentration, bulk modulus and the atomic volume of component i, respectively.

Another empirical parameter which is considered in this work, the atomic size difference δ, is defined following Zhang et al [95] as,

$$\delta = \sqrt{\sum_{i=1}^{N} c_i \left(1 - \frac{r_i}{\bar{r}}\right)^2} \tag{5.4}$$

with r_i being the atomic radius for component i, $\bar{r}(= \sum_{i=1}^{N} c_i r_i)$ being the average atomic radius.

5.1.2 EMTO-CPA

In the case of EMTO, the single-site coherent-potential approximation (CPA) was used to treat the (*Al* or *Nb*) substitutional and magnetic disorders [15, 17, 18, 266]. Using the CPA, one completely ignores the atomic short-range order and local lattice relaxation effects, whereas recent findings confirmed the absence of severe local lattice distortion in the parent alloy *CoCrMnFeNi* [267]. The scalar-relativistic approximation and soft-core scheme was used to solve the one-electron Kohn-Sham equations. The Green's function was calculated for 16 complex energy points to integrate the valence states below the Fermi level. We included *s*, *p*, *d*, and *f* orbitals in the basis sets. To ensure enough accuracy for the elastic constants, we used *25×25×25* uniformly distributed *k*-points in the irreducible Brillouin zones for both FCC and BCC phases. The electrostatic correction to the CPA was described using the screened impurity model [268] with screening parameter 0.6 and 0.9 for *Al* and *Nb* alloying, respectively. The EMTO approach has been successfully applied in the first-principles study of the physical properties of multicomponent HEAs [118, 126, 269-272]. These previous studies indicated that the EMTO-CPA method is a powerful and

suitable method assessing energetics, structural, elastic and magnetic properties of HEAs. At room-temperature, the $(CoCrCuFeNi)_{1-x}(Nb_x, Al_x)$ alloys have the paramagnetic (PM) FCC structure at *(Al, Nb)*-low levels and gradually transform to the PM BCC or amorphous structure with increasing *(Al, Nb)* content according to Sun *et al.* [273]. However, in *Al*-low alloys, the theoretical Curie temperature of the thermodynamically unstable BCC phase is above the room-temperature [37]. Due to the low Curie temperature, here we assume the PM state for all compositions in EMTO-CPA calculations while in the case of VASP-SQS we are restricted to ferromagnetic (FM) rather than PM in order to limit the influence of supercell atomic configurations difference for each concentration. The PM state was simulated by the disordered local magnetic moment (DLM) model [274-276]. Within the DLM approach, a PM $(CoCrCuFeNi)_{1-x}(Nb_x, Al_x)$ alloy is described as alternatively *Co* ↑ *Co* ↓ *Cr* ↑ *Cr* ↓ *Cu* ↑ *Cu* ↓ *Fe* ↑ *Fe* ↓ *Ni* ↑ *Ni* ↓ (*Al* ↑ *Al* ↓; *Nb* ↑ *Nb* ↓), with equal amount of spin up (↑) and spin down (↓) atoms. Hence, even though the calculations were performed at 0 K, the effect of the loss of magnetization above the Curie temperature was captured in the total energy.

There are three independent elastic constants in a cubic lattice: C_{11}, C_{12}, and C_{44}. Mechanical stability requires that $C_{44} > 0$, $C' = (C_{11} - C_{12})/2 > 0$, and $B = (C_{11} + 2C_{12})/3 > 0$ [277]. In the present study, the cubic elastic constants of PM $(CoCrCuFeNi)_{1-x}(Nb_x, Al_x)$ alloys were calculated using EMTO-CPA and those of FM $(CoCrCuFeNi)_{1-x}(Nb_x, Al_x)$ by VASP-SQS, as a function of the chemical composition and crystal structure (FCC and BCC). At each composition x, the simulated equilibrium volume and bulk modulus were obtained from a Morse-type function [278] fitted to the *ab-initio* total energies calculated for nine uniformly distributed volumes between 11.0 Å^3/atom and 14.0 Å^3/atom. There are

magnetic transitions within this interval and some alloy components develop local magnetic moments with increasing volume, which slightly deteriorates the quality of the numerical fit especially for the bulk modulus. Thus, the alloying trend is considered using a larger volume interval in order to keep the numerical noises consistent.

5.1.3 AIMD

Additionally, in order to discuss the structural properties of the amorphous phases, ab initio molecular dynamics (AIMD) simulations were performed using the plane-wave pseudo-potential as-implemented in VASP [261]. The plane-wave cutoff energy was set to 296 eV. The simulations were performed at the Γ point only and magnetism was not considered during these AIMD simulations, as a detailed study of the amorphous phase was initially out the scope of this work. We built three cubic supercells of 256 atoms corresponding to the compositions of $(CoCrCuFeNi)_{0.899}Nb_{0.101}$ (10.1 at. % *Nb*), $(CoCrCuFeNi)_{0.84}Nb_{0.16}$ (16.0 at. % *Nb*) and $(CoCrCuFeNi)_{0.742}Nb_{0.258}$ (25.8 at. % *Nb*). AIMD simulations were performed initially above the melting temperature, at 2000 K, using a Nose-Hoover thermostat [279] in a NVT canonical ensemble. The simulation lasted for 9 ps, until reaching the liquid state equilibrium. Then, it was followed by a cooling process where the temperature smoothly went down to 300 K within 3000 simulations steps to reproduce the experimental cooling procedure, but much faster. A micro-canonical ensemble was utilized during the cooling process. Finally, a 9 ps NPT simulation was used to equilibrate the final structures at 300 K. The time step was fixed at 3 fs for all AIMD calculations. For the statistics, we used the last 1000 frames of the trajectory to calculate the atomic radial distribution function (RDF), atomic volume and mass density in order to

compare with XRD and XRR results. As for the analysis of XRD experiments of the amorphous phase, an equivalent FCC lattice parameter ($a\sqrt{2} = 2D$) is calculated from the average interatomic distance (D) deduced from the RDF. Since the elastic properties vary slightly with temperature within the interval 0-300 K that we examine here, we calculate only the 0K elastic constants of the amorphous structures for the sake of saving computational costs. As for force calculations when accuracy is needed, we took magnetism (FM configuration) into consideration and employed a higher cutoff energy of 500 eV. The formation energy was calculated also at 0K for a better comparison to other structures.

5.1.4 Averaged polycrystalline elastic properties

We used a standard technique [280] to calculate the single crystal elastic constants c_{ij}'s and obtained the effective elastic properties polycrystalline C_{ij} according to Hill approximation [26] which correspond to the arithmetic mean of Voigt and Reuss estimates, in the case of the dense $(CoCrCuFeNi)_{1-x}Nb_x$ <111>-textured solid solutions (~0 porosity). For the porous $(CoCrCuFeNi)_{1-x}Al_x$ solid solutions the elastic properties difference between the matrix and the voids is too large. Therefore, the micro mechanical effective medium field, developed by Li [27] was used. This method permits to account for the crystallographic texture and porosity. In a previous work [8], we used an analytical model [281] that was restricted to porous configurations with isotropic symmetry approximated with spherical components. The simulated effective elastic moduli and single-crystal elastic parameters are used to calculate sound velocities and to compare with raw experimental results.

5.1.5 *DFT or experimental sound velocities and Debye temperature*

DFT calculations and the independent measurement of V_L and V_T data from PLU and BLS experiments also allows for the evaluation of the average sound velocity V_m in the polycrystalline film according to:

$$\frac{3}{V_m^3} = \frac{1}{V_L^3} + \frac{2}{V_T^3} \tag{5.5}$$

In the Debye model, the heat capacity and cohesion energy depend on the so-called Debye temperature θ_D θ_D, which is related to V_m and V_a through the following equation:

$$\theta_D = \frac{\hbar}{k}\left(\frac{6\pi^2}{\mathrm{V_a}}\right)^{1/3} V_m \tag{5.6}$$

where $\hbar$ and k are the Planck's and Boltzmann's constants, respectively, and V_a is the atomic volume. This parameter can be convenient to follow phase transitions, discussing either mechanical and topological lattice instability, related to V_m and V_a, respectively.

Using the two experimental effective elastic constants, C_{33} and C_{44}, we can calculate, the isotropic Young's modulus E, shear modulus G ($G = C_{44}$) and the bulk modulus B, assuming an *isotropic* approximated medium and using the following relationships:

$$E = C_{33} - \frac{(C_{33} - 2C_{44})^2}{C_{33} - C_{44}} \tag{5.7}$$

$$G = C_{44} \tag{5.8}$$

$$B = C_{33} - \frac{4}{3}C_{44} \tag{5.9}$$

Throughout the whole document, C_{ij} and c_{ij} elastic constants will denote effective elastic constants and single crystalline from first principles, respectively.

5.2 Formation energy, phase stability, relaxation/elastic energy and local lattice distortion

EMTO-CPA and VASP-SQS formation energy of FCC and BCC crystalline phases are plotted in **Figure 5.1a** and **Figure 5.1b** for the $(CoCrCuFeNi)_{1-x}Nb_x$ and the $(CoCrCuFeNi)_{1-x}Al_x$ HEA, respectively. Ab-initio molecular dynamics formation energy for the *Nb*-rich $(CoCrCuFeNi)_{1-x}Nb_x$ amorphous phase are also added in **Figure 5.1**, instead of VASP-SQS for the BCC phase, which is not stable. We distinguished between the results of EMTO-CPA and VASP-SQS, as the relaxation of atomic positions was only allowed for the latter case. Phase transition from FCC to BCC is predicted at ~ 23-25 at.% *Al* while FCC remains the stable phase in the case of *Nb* alloying until phase transformation to an amorphous state at ~ 15 at. % *Nb*. These ab initio predictions are in agreement with a simple topological model originally proposed by Egami and Waseda [194] and extended by Senkov and Miracle [282] for interstitial solutes, that enabled estimation of the critical concentration of *Al* and *Nb*, ~ 22 at. % [5] and ~ 19 at. % [6], respectively.

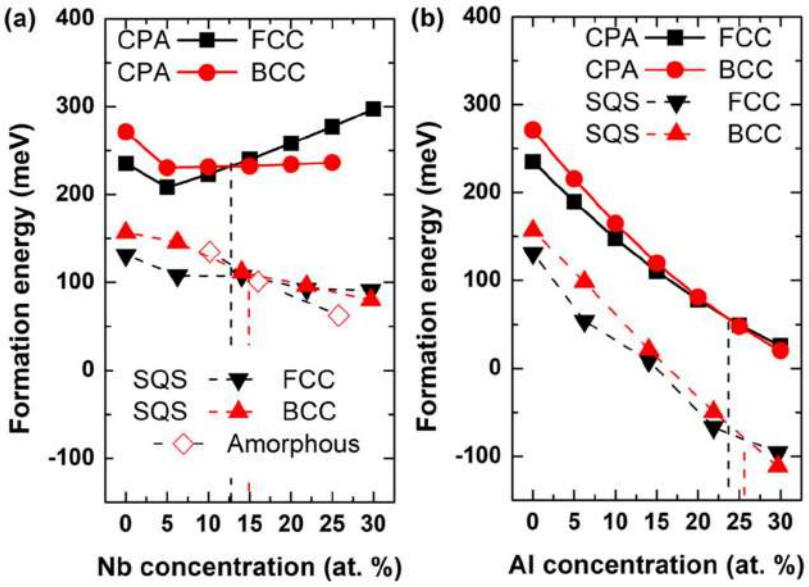

Figure 5.1 - Formation energy calculated by EMTO-CPA and VASP-SQS for (a) *(CoCrCuFeNi)$_{1-x}$Nb$_x$* and (b) *(CoCrCuFeNi)$_{1-x}$Al$_x$*. with FCC, BCC and amorphous structures. The energy cross between different structures is indicated by vertical dashed lines.

However, as inferred from XRD results [6], the amorphization already occurs at lower *Nb* concentrations, i.e. ~ 15 at. % *Nb*, in perfect agreement with the ab initio prediction. This could be related to the high effective quenching rate during sputter deposition which enables higher glass formation ability and effectively decreases the critical solute concentration before transition from crystalline to amorphous state. For a high enough concentration of the alloying element *Al* or *Nb*, a transition from the BCC or from the FCC crystalline phase to the amorphous phase is observed from XRD patterns [5, 6]. We confined such computationally expensive AIMD calculations of the energetics to the amorphous phase of *(CoCrCuFeNi)$_{1-x}$Nb$_x$*. Although we did not include magnetic contributions during the amorphization cooling process, the phase transition is still well predicted from the energetics calculations.

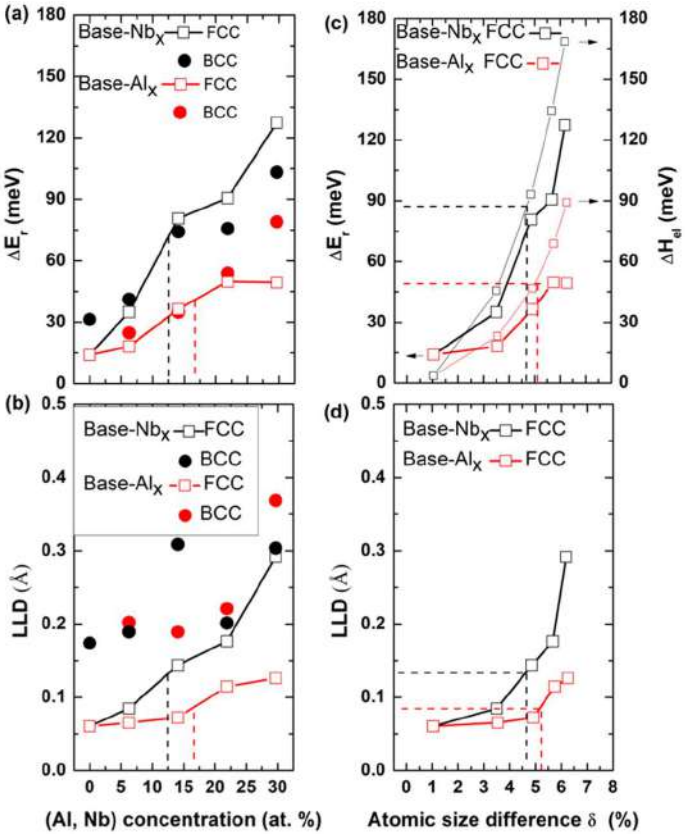

Figure 5.2 - (a) Atomic relaxation energy (ΔE_r) and (b) local lattice distortion (*LLD*) as a function of (*Al, Nb*) concentration for FCC and BCC $(CoCrCuFeNi)_{1-x}(Al_x,Nb_x)$. (c) ΔE_r, the elastic-strain energy (ΔH_{el}) (d) *LLD* as a function of atomic size difference for FCC $(CoCrCuFeNi)_{1-x}(Al_x,Nb_x)$. Critical concentration for phase transition is indicated by dashed lines. $(CoCrCuFeNi)_{1-x}(Al_x,Nb_x)$ is denoted as base-$(Al,Nb)_x$ in the figure.

Relaxation energy $\Delta(E_r)$ and local lattice distortion *LLD* of FCC and BCC supercells were evaluated from the VASP-SQS calculations with and without atomic relaxations. They are plotted in **Figure 5.4a** and **Figure 5.4b**, respectively, as a function of Nb and Al concentrations. Clear correlation can be seen between relaxation energy $\Delta(E_r)$ and local lattice distortion *LLD*. Indeed, Tian *et al* [249] has demonstrated that $\Delta(E_r)$ depends linearly on the square of *LLD* in FCC $Cu_{1-x}Au_x$ solid solution at small strains. We found that $\Delta(E_r)$ and *LLD* increase with *Nb/Al* addition, moreover, *Nb* can increase $\Delta(E_r)$

and *LLD* more rapidly with reference to same amount of *Al*. Elastic-strain energy ΔH_{el} was calculated for both alloys using the tool offered by Andreoli *et al.* [101] and exhibits a clear correlation with $\Delta(Er)$ from both aspects of trend and value, as shown in **Figure 5.2c**, indicating that the atomic relaxation energy $\Delta(Er)$ is mainly associated to elastic-strain energy and has an elastic nature. A critical atomic size difference δ value of ~4.6-5.2 (%) before the transition onset is obtained for both alloys with FCC structure, in good line with the criterion to form stable single phase multicomponent solid solution which requires $\delta \leq 6$ % as proposed in [283]. Further *Nb/Al* addition beyond the critical concentration (12.5 at. % and 17 at. % for *Nb* and *Al*, respectively) leads to larger atomic size difference, hence atomic relaxation energy or elastic strain energy. When this elastic energy, whether denoted as $\Delta(E_r)$ *or* almost equally as ΔH_{el}, reaches the thresholds that the FCC structure can sustain, phase transition will be triggered. The thresholds elastic energy for FCC $(CoCrCuFeNi)_{1-x}Nb_x$ ($\Delta(E_r)$= 80 meV) is higher than FCC $(CoCrCuFeNi)_{1-x}Al_x$ ($\Delta(E_r)$= 36 meV) as shown in **Figure 5.2c**. At this critical δ, The FCC $(CoCrCuFeNi)_{1-x}Nb_x$ transforms to amorphous while FCC $(CoCrCuFeNi)_{1-x}Al_x$ transforms to BCC. As shown in **Figure 5.2a**, $\Delta(E_r)$ keeps increasing for the BCC $(CoCrCuFeNi)_{1-x}Al_x$, which finally reaches 79 meV at 30 at. % Al, arriving at the same level of $(CoCrCuFeNi)_{1-x}Nb_x$ (80 meV) where the amorphization occurs. It is interesting to note that, experimentally we saw the BCC to amorphous transition for $(CoCrCuFeNi)_{1-x}Al_x$ at around 25 at. % to 30 at. % Al addition, which means no matter from BCC $(CoCrCuFeNi)_{1-x}Al_x$ or FCC $(CoCrCuFeNi)_{1-x}Nb_x$ phase, the amorphous transition has nearly the same $\Delta(E_r)$ energy threshold around 80 meV.

The atomic size difference δ can be correlated to *LLD* in **Figure 5.2d**. Together with the chemical bonding difference between Al and Nb, these two factors might be the reason for the distinct behaviors observed for $(CoCrCuFeNi)_{1-x}Nb_x$ and $(CoCrCuFeNi)_{1-x}Al_x$, of their $\Delta(E_r)$, *LLD*, ΔH_{el} and phase transition. Despite the importance of elastic-strain in describing phase stability, it should not account alone for the the FCC to BCC phase transition occured in $(CoCrCuFeNi)_{1-x}Al_x)$ because the calculation neglecting the atomic relaxations is able to predict the FCC to BCC phase transition as well.

Valence electron concentration (*VEC*) concept is also used to evaluate the phase stability type of HEA [97, 98], FCC ($VEC \geq 7.8$) or BCC ($VEC \leq 6$). As for above δ and Ω parameters, *VEC* was calculated using the AlloyTool software [284] for both alloys, $(CoCrCuFeNi)_{1-x}(Nb_x, Al_x)$ showing *VEC* > 8 until 22 at. % *Nb* and 14 at. % *Al*, respectively. For both alloys with FCC structure, the elastic-strain energy ΔH_{el} remains below 6.8 kJ/mol (70.8 meV) which agrees with the new criterion of FCC single phase stability, established by Andreoli et al. [101]. This is in good agreement with our *ab-initio* results, too. One should notice that this last empirical approach has *no computational cost*!

Lastly, as mentioned by Kube *et al.* [102], we observed that HEAs (e.g., $(CoCrCuFeNi)_{1-x}Al_x)$ with the same relaxation energy $\Delta(E_r)$ in **Figure 5.2a**, BCC phase can sustain greater *LLD* over FCC as shown in **Figure 5.2b**, which means BCC can accommodate a large atomic size difference while maintaining a low elastic-strain energy penalty.

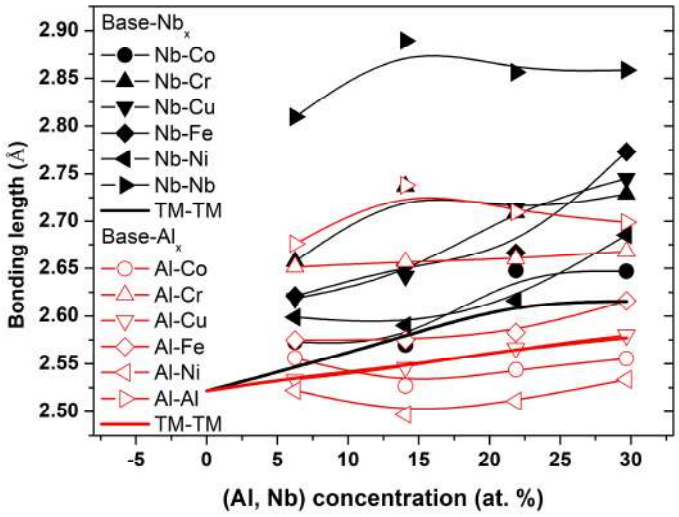

Figure 5.3- Bonding length between different species in FCC *(CoCrCuFeNi)$_{1-x}$(Nb$_x$, Al$_x$)* phases vs. niobium and aluminium concentration. TM-TM represents the average bonding length between 3*d* transition metal elements (TM, i.e., *Co, Cr, Cu, Fe and Ni*). Note that there is no (*Al*, *Nb*)-TM bonding for the base alloy (0 at. %).

We studied the bonding length between different species of FCC phase *(CoCrCuFeNi)$_{1-x}$(Al,Nb)$_x$*. Large orbital overlapping between *Al* and TMs is revealed in **Figure 5.3** by the short bonds formed between *Al* and TMs, comparing to Nb and TMs. The two strongest bonds, i.e., *Al-Co* and *Al-Ni* bonds, even shorter than the major TM-TM bonds, consequently make a contribution to alloy cohesive energy, as can be seen from **Figure 5.1b** that *Al* addition leads to lower formation energies. The bonding length distribution is also in line with the mixing enthalpy, e.g., *Al-Ni* with the shortest bonds, *Al-Cr* with the longest bonds have respectively the lowest and highest mixing enthalpy among all the *Al*-TM pairs. As a contrast, all *Nb*-TM bonds have greater bonding length than the TM-TM bonds, which means *Nb* will not contribute positively to the bonding. Therefore, *Nb* addition results in an increasing trend for alloy formation energy. The electronic structure origin of different behavior between *Al* and *Nb* addition is that *Al* allows the strong

p-d (*Al*-TM) hybridization, while in the case of *Nb*, the *d-d* or *s-d* (*Nb*-TM) interaction is relatively weak.

5.3 Structural properties: lattice parameter, phase transition and mass density

Lattice parameters of $(CoCrCuFeNi)_{1-x}Nb_x$ and $(CoCrCuFeNi)_{1-x}Al_x$ measured from more intense peaks of x-ray diffraction patterns (see Refs. [5, 6]) are summarized in **Table 2.5**, and shown in **Figure 5.4a** and **Figure 5.4b**, respectively. They are compared to our *ab-initio* calculations of crystalline FCC, BCC and amorphous phase. A clear trend between the chemical composition and the phase formation is observed. More specifically, at low *Al* concentrations, a single FCC solid solution is formed. At higher *Al* concentrations, the BCC solid solution starts to emerge, and a mixed duplex FCC/BCC solid solution is formed. At even higher *Al* concentrations, from ~20 at. % *Al*, a single BCC solid solution is formed. The film with the highest *Al* fraction (24.7 at. % *Al*) exhibits an amorphous phase. Preferred (111) and (011)-orientation are observed for the FCC and BCC phase, respectively, deposited with low $p_{Ar}.d_{TS}$ values.

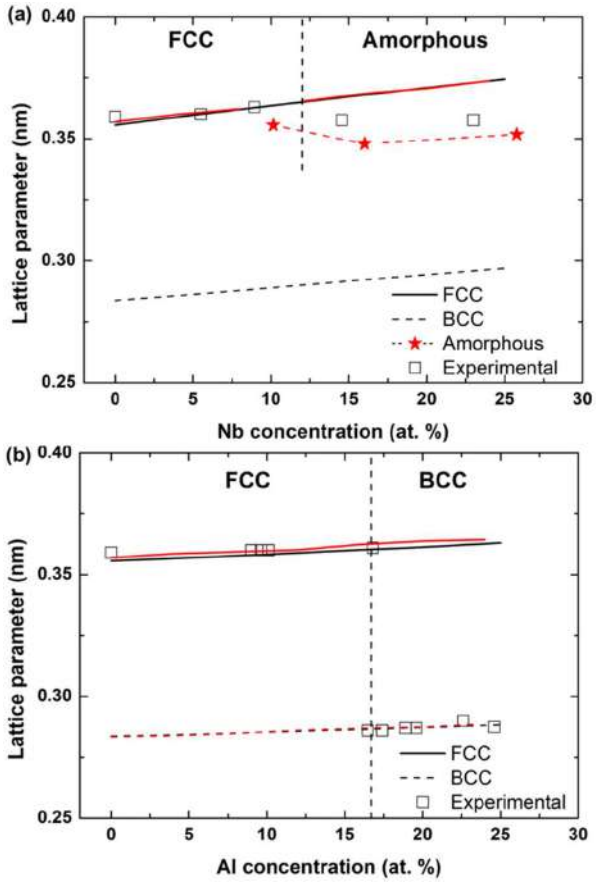

Figure 5.4 - Experimental (void square) and calculated lattice parameter of FCC cell (solid line), BCC cell (dashed line) and the amorphous phase (red-dotted line with asterisks) vs. (a) niobium and (b) aluminium concentration, for the *(CoCrCuFeNi)*$_{1-x}$*(Al*$_x$*,Nb*$_x$*)* high entropy alloys. Red lines are related to VASP-SQS simulations. The vertical dotted lines at 17 at. % *Al* and 12.5 at. % *Nb* indicate the FCC to BCC and the FCC to amorphous structural transitions, respectively.

The simulated partial correlation functions after cooling at 300 K, of the melts at 2000 K for three compositions *(CoCrCuFeNi)*$_{0.899}$*Nb*$_{0.10}$, *(CoCrCuFeNi)*$_{0.84}$*Nb*$_{0.16}$ and *(CoCrCuFeNi)*$_{0.742}$*Nb*$_{0.258}$ of amorphous *(CoCrCuFeNi)*$_{1-x}$*Nb*$_x$ (see **Figure 5.5** as an example for a melt) have been calculated, and the average interatomic distances evaluated. Then, equivalent lattice parameters in these amorphous phases, assuming a FCC lattice host, have been calculated both experimentally, from XRD results and using

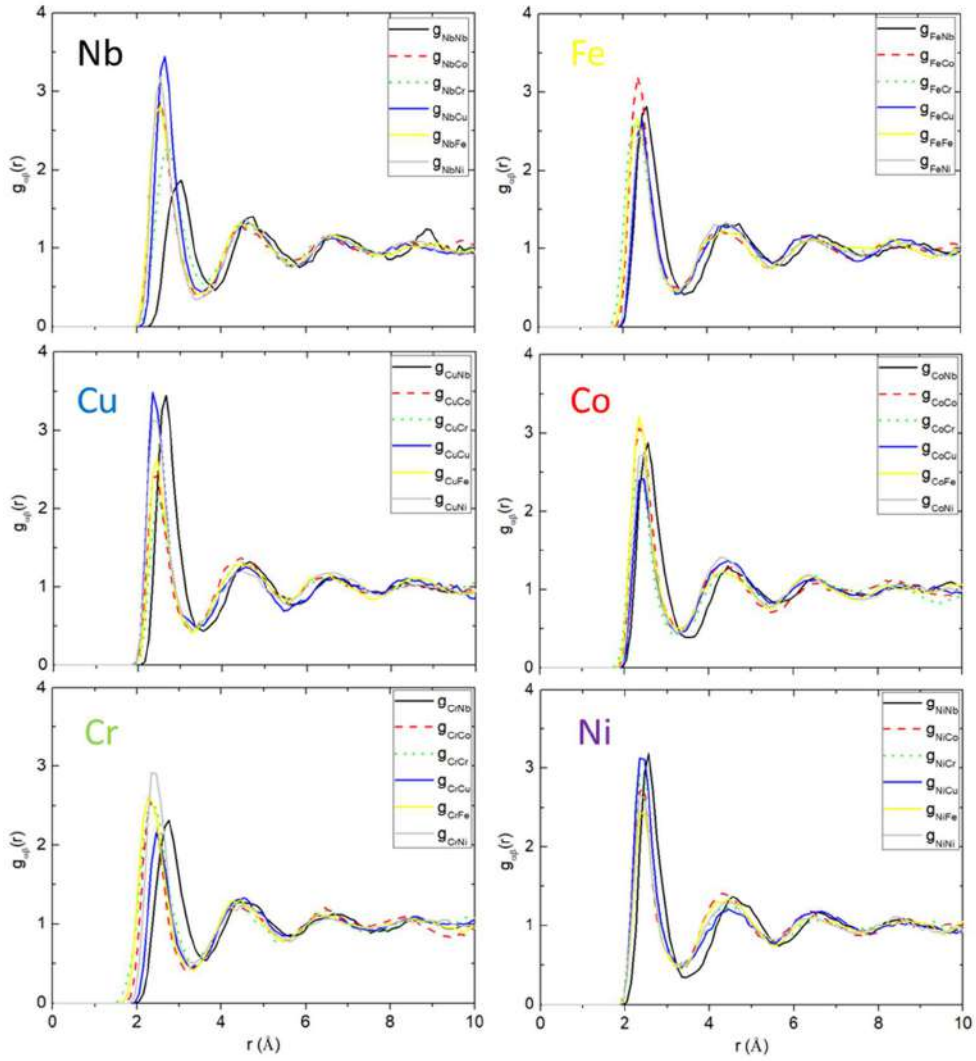

Figure 5.5 - AIMD (256 atoms) simulated partial pairs correlation functions of the melt *CoCrCuFeNiNb$_{0.95}$* (16 at.% *Nb*) from NVT canonical at 2000 K after the simulation time of 9 ps, showing Cu clustering and short-range ordering between *Nb-(Cu, Ni, Cr, Fe)*, *Fe-(Co, Cr)* and *Cr-(Ni, Co, Fe)* pairs.

Ehrenfest equation (**eq. 2.9**) [187], and theoretically by calculating the average interatomic distances from radial distribution function (RDF). Then, it can be seen from **Figure 5.4**, that the FCC phase is maintained during alloying of *Nb* until ~12.5 at. %, when the transition to the amorphous phase occurs, thus inducing a small drop of "lattice parameter".

From pair correlation functions of $(CoCrCuFeNi)_{0.84}Nb_{0.16}$ (16 at.% *Nb*) melt at 2000 K in

Figure 5.5, one can notice the limited *Cu* clustering and short-range ordering between *Nb-(Cu, Ni, Cr, Fe)*, *Fe-(Co, Cr)* and *Cr-(Ni, Co, Fe)* pairs, which were expected to be retained after cooling in the solid state. There are some differences with a similar calculation of Gao and Alman [285] but limited to the melt of $(CoCrCuFeNi)_{1-x}Al_x$. In the case of $(CoCrCuFeNi)_{0.794}Al_{0.206}$ melted at 1,873 K, the simulated RDF can be compared to our $(CoCrCuFeNi)_{0.84}Nb_{0.16}$ melt at 2000 K. *Nb* addition leads to less short-range ordering and segregation in the liquid structure, suggesting that the atoms are much more randomly distributed than in the case of $(CoCrCuFeNi)_{0.794}Al_{0.206}$, for which bonds formation between *Al* and TM elements are favored. As a result, higher glass formation ability is expected and a single amorphous phase should be promoted in *Nb*-rich alloys compared to *Al*-rich ones, after solidification from the melt. One should expect similar results from a vapor-solid process for film's growth.

It is easy to identify from the abrupt step of the lattice parameter, the onset of FCC to BCC structural phase transition around 17 at. % *Al* and FCC to amorphous ~ 12.5 at. % *Nb*. **Figure 5.4a** indicates that, as the experimental interatomic distance of the amorphous phase is lower than the one calculated for the hypothetical FCC crystalline solid solution, the amorphous phase exhibits a more compact way to distribute the atoms for larger *Nb* concentrations.

The predicted and experimental mass density evolution of $(CoCrCuFeNi)_{1-x}(Nb_x, Al_x)$ as a function of *Al* or *Nb* concentration, are shown in **Figure 5.6**. One can again notice the FCC to BCC phase transition around 17 at. % *Al* and FCC to amorphous at

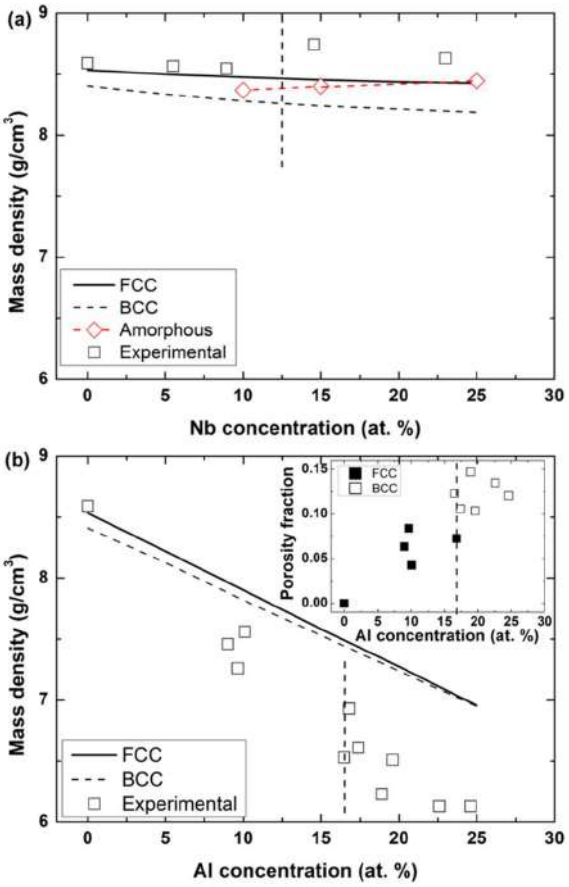

Figure 5.6- Experimental (void square) and calculated mass density of FCC cell (solid line), BCC cell (dashed line) and the amorphous phase (red-dotted line with asterisks) vs. (a) niobium and (b) aluminium concentration, for the $(CoCrCuFeNi)_{1-x}(Al_x, Nb_x)$ high entropy alloys. The vertical dotted lines at 17 at. % *Al* and 12.5 at. % *Nb* indicates the FCC to BCC and the FCC to amorphous structural transitions, respectively.

~ 12.5 at. % *Nb*. Furthermore, one can distinguish the difference between both deposition processes. In case of *Al* alloying, we obtained under-dense thin films with increasing porosity *P*, defined by:

$$P = 1 - \frac{\rho}{\rho_{bulk}} \quad (5.10)$$

where ρ and ρ_{bulk} are respectively the mass density of the $(CoCrCuFeNi)_{1-x}Al_x$ film and the corresponding value from first-principles calculations.

The porosity increases as a function of the aluminum concentration, in both FCC (0-17 at. %) and BCC (17-25 at. %) phases, reaching the highest value of 16 %, as shown in the inset of **Figure 5.6b**. The influence of the porosity should be considered later for the estimations of effective elastic properties and sound velocity. In the case of alloying with heavier *Nb* atoms, only the mass density slowly grows theoretically. One should bear in mind that the peening effect guarantees the densification of the films over the full range of concentrations. The segregation of *Nb* phase (ρ=8.57g/cm^3) is also a possibility that may lead to an over-dense polycrystalline film above 10 at. % *Nb*, as observed from **Figure 5.6a**.

5.4 Sound velocities Debye temperatures and elastic constants

Before discussing experimental measurements and their comparison with numerical results, we compare the corresponding elastic constants of the single crystal $(CoCrCuFeNi)_{1-x}(Nb_x, Al_x)$ in the FCC phase calculated from EMTO-CPA and VASP-SQS simulations (**Figure 5.7a** and **Figure 5.7b**) and those of $(CoCrCuFeNi)_{1-x}Al_x$ in the BCC phase(**Figure 5.7c**). In our calculations, FM and PM were considered for VASP-SQS and EMTO-CPA simulations, respectively. Our calculations of the base FCC *CoCrCuFeNi* considering both PM and FM magnetic states compare well with EMTO data of Ref. [246]. The main results (formation energy, lattice parameter and elastic constants) are reported in

Table 4.1. Data are comparable for each method with either PM or FM state with maximum difference below a few percent. The major difference appears between the elastic constants when comparing EMTO to VASP. The maximum difference of + 10 % , +20 % and +30 % are observed for c_{11}, c_{12} *and* c_{44}, respectively. This difference for c_{12} and c_{44} is roughly maintained but decreases for c_{11} when alloying with *Nb* and *Al* (see **Figure 5.7**). Most of elastic constants have a common softening trend with *Nb* and *Al* addition. This difference is mainly due to the lack of atomic positions relaxation in EMTO-CPA. Similar conclusions are drawn when comparing VASP calculations with relaxed and unrelaxed atomic positions, but with no influence on the c_{44} elastic constant that is nearly not affected. Hence, we propose that there is an intrinsic difference between EMTO and VASP when evaluating this elastic constant.

We will assume that difference in magnetic configuration plays a minor role on elastic constants in our alloys compared to atomic relaxation, avoiding the more difficult calculations of the paramagnetic phase, when we have to compare between different supercell random configurations and chemical concentrations, with SQS method. Tian et al. [270] provided comparison between SQS and CPA for $(CoCrCuFeNi)_{1-x}Al_x$ and for Cu_xAu_{1-x} alloys [184]. The two methods generally give the same trend on elastic constants, but always bigger elastic constants from EMTO-CPA as we found for $(CoCrCuFeNi)_{1-x}(Nb_x, Al_x)$ alloys.

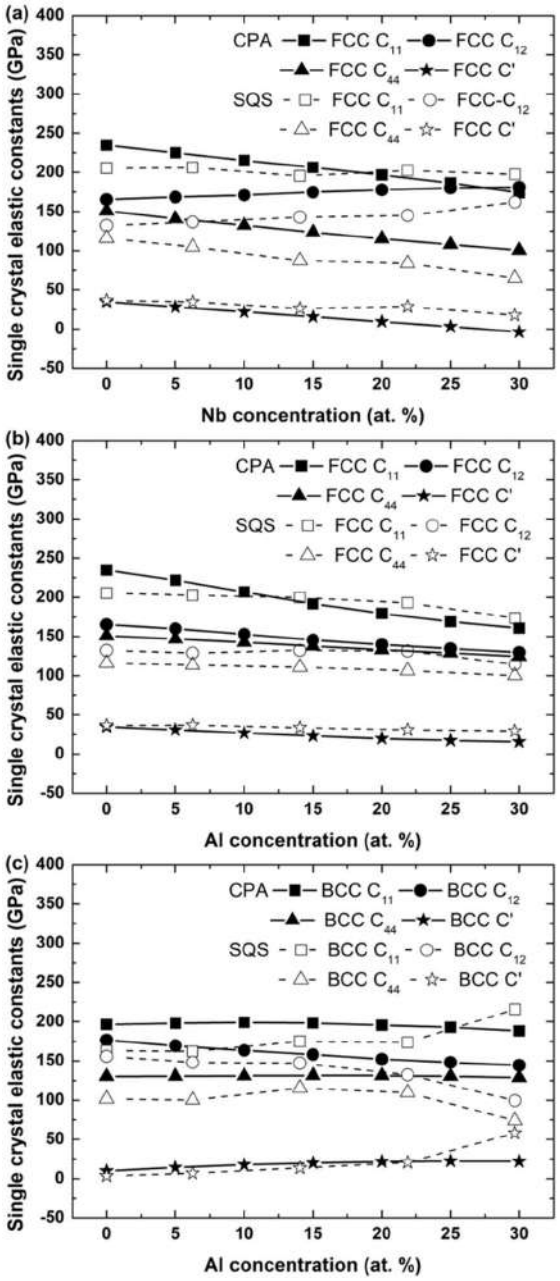

Figure 5.7- The calculated single crystal elastic constants of the FCC $(CoCrCuFeNi)_{1-x}(Nb_x, Al_x)$ as a function of (a) niobium concentration, and (b) aluminum concentration, and of the BCC $(CoCrCuFeNi)_{1-x}(Nb_x, Al_x)$ (c). (Solid line) and (dashed line) are from EMTO-CPA and VASP-SQS calculations, respectively.

Although both approaches can provide the phase transition from energetics, i.e., the FCC to BCC transition when alloying *Al*, VASP-SQS method is able to provide more

accurate elastic constants because the atomic relaxation is taken into account, especially in the case when the atomic relaxation effect is not negligible, e.g., when atoms of greater sizes are added into the lattice and increasing lattice local distortion. The single crystal elastic constants (c_{11}, c_{12} and c_{44}) will be used later as input for micro-mechanical self-consistent calculations of effective elastic properties of our polycrystalline materials considering their crystallographic texture, <111> crystallographic orientation for FCC structure and <110> for BCC one, including changes in porosity fraction of $(CoCrCuFeNi)_{1-x}Al_x$ alloy. Five independent averaged effective elastic constants will be calculated, namely, C_{11}, C_{12}, C_{13}, C_{33} and C_{44} corresponding to a macroscopic hexagonal symmetry. In case of the rich-*Nb* amorphous phase having isotropic elastic symmetry, AIMD and stress-strain method provides directly the two independent elastic constants $C_{11} = C_{33}$ and $C_{44} = (C_{11} - C_{12})/2$. Hence, predicted sound velocities $\langle V_L \rangle = \sqrt{C_{33}/\rho}$ and $\langle V_T \rangle = \sqrt{C_{44}/\rho}$ as well as the Debye temperature $\langle \theta_D \rangle$, can be calculated for each alloy concentrations and compared to the following raw experimental results.

Typical transient relative reflectivity from PLU and a Brillouin light scattering spectrum at 65° angle of incidence are shown in **Figure 5.8a** and **Figure 5.8b**, respectively, for $(CoCrCuFeNi)_{0.9}Al_{0.1}$ film. From time of flight of echoes and Rayleigh wave velocity, longitudinal and transverse sound velocities of $(CoCrCuFeNi)_{1-x}(Nb_x, Al_x)$ have been measured, as a function of *Nb* and *Al* concentration. These raw data are plotted in **Figure 5.8a** and **Figure 5.8b** and are compared to theoretical simulations.

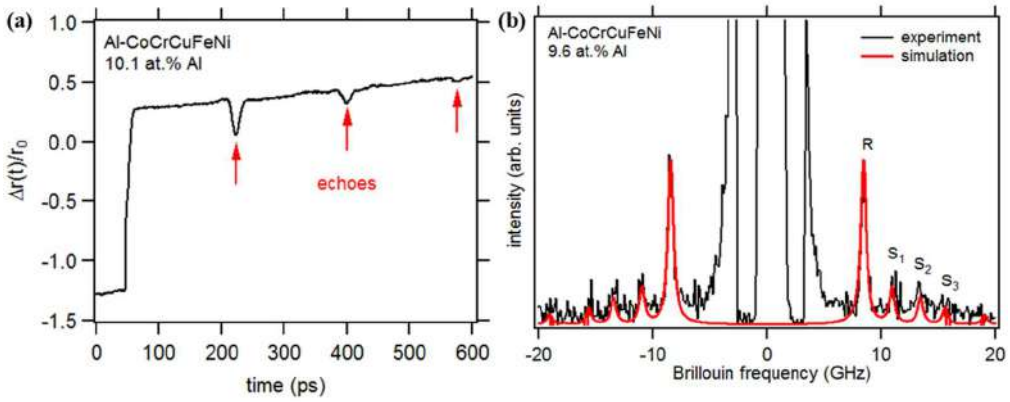

Figure 5.8 - Typical transient relative reflectivity from (a) picosecond laser ultrasonic technique and (b) Brillouin light scattering spectrum at 65° angle of incidence.

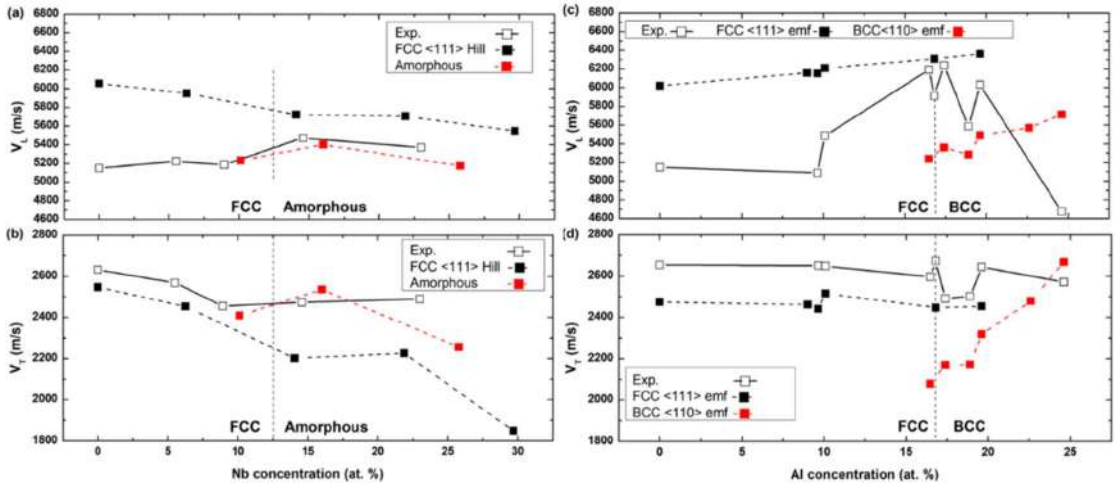

Figure 5.9 - The calculated (dashed line with filled square) and experimental (solid line with void square) sound velocities of *(CoCrCuFeNi)$_{1-x}$(Nb$_x$, Al$_x$)* (a) V_L and (b) V_T vs. niobium concentration; and (c) V_L and (d) V_T vs. aluminium concentration. It employed the micro-mechanical effective medium field (EMFM) results of FCC (111) and BCC (110) textures, as well as porosity for Al alloying. Amorphous rich-*Nb* alloys were calculated by AIMD. The vertical dotted lines at 17 at. % *Al* and 12.5 at. % *Nb* indicates the FCC to BCC and the FCC to amorphous structural transitions, respectively.

Comparable trends with either *Nb* or *Al* alloying are obtained for V_L and V_T. V_T decreases only a little (from ~2650 m/s) reaching a minimum velocity in the vicinity of the

phase transition: ~2500 m/s, and then remains nearly constant in *Nb*-rich amorphous phase while increasing a bit more for *Al*-rich BCC phase. The films with a mixed FCC/BCC, BCC or amorphous phase show a clear separation from the FCC phases. There is a limited softening in the mixed $(CoCrCuFeNi)_{1-x}Al_x$ FCC/BCC duplex region in comparison to what is expected for pure BCC, indicating a partial transformation as observed from XRD experiment below 20 at. % *Al*. The trends and relatively good quantitative agreement is found between numerical results and experimental V_T of $(CoCrCuFeNi)_{1-x}(Nb_x, Al_x)$ crystalline and amorphous phases

V_L changes only a little until 10 at. % (~5150 m/s) and then increases, reaching a maximum velocity in the vicinity of the phase transition: 5500 m/s for ~12.5 at. % *Nb* and 6200 m/s for ~17 at. % *Al*, and then decreases only a little in *Nb*-rich amorphous phase while a bit more for *Al*-rich BCC stucture. Again, the films with a mixed FCC/BCC, BCC or amorphous phase show a clear separation from the FCC phases. Here, V_L softening in the mixed $(CoCrCuFeNi)_{1-x}Al_x$ FCC/BCC region lies between what is expected for pure FCC and BCC. The experimental V_L are lower than the calculated values for fine-grained materials in the FCC phase for both alloys, even for the base alloy and *Nb*-alloyed dense films, therefore excluding effects of porosities. For comparison, it was found from self-consistent averages that 5 % porosity induced ~10 % softening of C_{44} and ~8 % softening of C_{33} for both FCC and BCC phases.

This could be attributed to the nature of the films: nanocrystalline solid solutions with grain size of few nm [9] with a large number of grain boundaries. Furthermore, the grain boundaries are probably enriched in oxygen due to the relatively high impurity-to-

metal flux ratio during film growth (low deposition rate and moderately good vacuum base pressure) [9]. Both effects, the oxygen contamination and the presence of a large fraction of disordered/amorphous grain boundaries causes a decrease of the average atomic bond strength, hence produces an extrinsic cause of softening of longitudinal modulus C_{33} and Young's modulus of the material [286].

This softening of C_{33} in comparison with the numerical estimation in FCC phase is visible in **Figure 5.10**. One should notice that visibility of this effect seems to disappear when approaching and after the phase transition from FCC to amorphous phase (~12.5 at. % *Nb*). The whole material ($(CoCrCuFeNi)_{1-x}Nb_x$ alloy) has narrower grain size (3-10 nm) and will be highly disordered or amorphous, meaning core and shell grain have closer properties. But it is still visible for $(CoCrCuFeNi)_{1-x}Al_x$ alloys which have larger grain size (8-18 nm), after the FCC to BCC transition and mixed phases region, until the amorphous transition (~25 at. % *Al*). This is supporting the existence of an amorphous or highly disordered interphase at nano-sized grain boundaries. As mentioned in our previous work [9], while the oxygen impurity-to-metal flux ratio is increased, the grain boundaries are no longer purely metallic. An oxide tissue is formed [9], leading to certain proportion of covalent bonds modifying the effective elastic and plastic properties of the grain boundaries and of the core-shell grains. At least, the influence of this nanometer size oxide tissue interphase should be considered in further analysis, trying to identify its average thickness and properties by direct observations or using inverse numerical method modeling some physical effective properties such as, for example: elastic, electrical and thermal properties. This approach is currently under progress. Noticeably, this interphase

is not supposed to have marked influence on the shear modulus C_{44}, as simulations and experiments compare well for both alloys in FCC, BCC or amorphous phase.

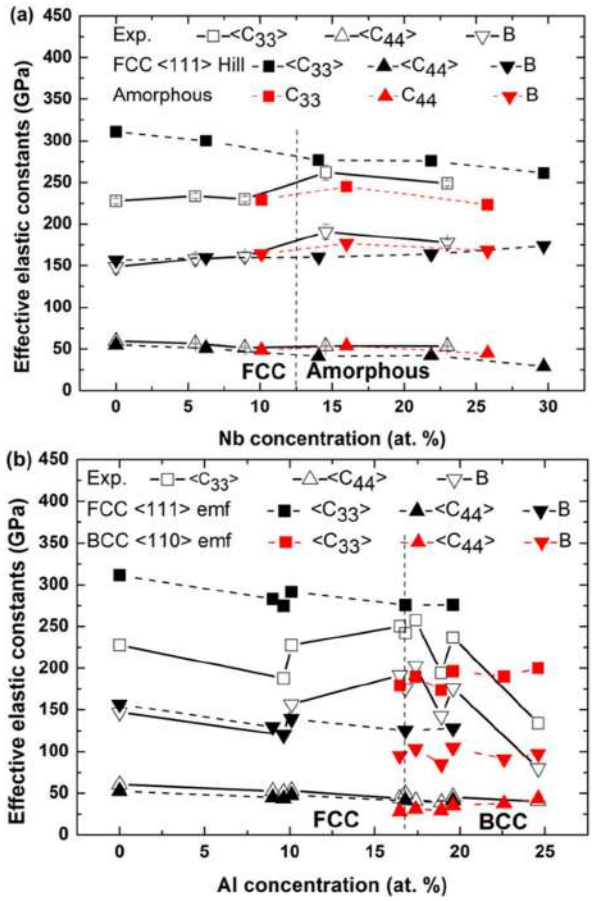

Figure 5.10 - The calculated (dashed line with filled symbols) and experimental (solid line with void symbols) C_{33}, C_{44} and *B* elastic moduli *(CoCrCuFeNi)$_{1-x}$(Nb$_x$, Al$_x$)* as a function of (a) niobium concentration, and (b) of aluminium concentration. It employed the micro-mechanical effective medium field (MF) results of FCC (111) and BCC (110) textures, as well as porosity for *Al* alloying. Amorphous *Nb*-rich alloys were calculated by AIMD. The vertical dotted lines at 17 at. % *Al* and 12.5 at. % *Nb* indicates the FCC to BCC and the FCC to amorphous structural transitions, respectively.

More intuitive material trends can be inferred from Debye temperature θ_D (**Eq. 5.6**) calculated from average sound velocities (V_m) and atomic volumes (V_a). Experimental and simulations are displayed in **Figure 5.11**.

Two different behaviors can be distinguished from its compositional dependence, in relation to the structural state, either crystalline (FCC or BCC) or amorphous. In the composition range below the previous identified phase transition (12.5 at. % *Nb* or 17 at. % *Al*), where FCC crystalline solid solutions are stabilized, one observes an abrupt decrease of θ_D, in particular at the approach of the crystalline lattice instability. This tendency involves a lower cohesion in relation to the onset instability. This result is well correlated with the decrease of inverse atomic volume 7 % and 19 %, in the vicinity of their respective phase transition, for Nb and Al alloying, respectively. As θ_D varies as $\sim(1/V_a)^{1/3}$, it contributes for 2 % and 6 % to the observed 7% and 11% continuous decrease in both systems (from ~400 K to ~350 K). The continuous decrease of θ_D is well captured by our *ab-initio* plus effective properties predictions. It evidences the same V_m softening for both systems (-5%) and that the lattice instability is mostly of mechanical origin for *Nb* alloying whereas a topological one for case *Al*. It was already partially visible from the limited variation of V_T and C_{44} for both structures, and the different trends of their mass density, atomic volume in Al case increasing much more.

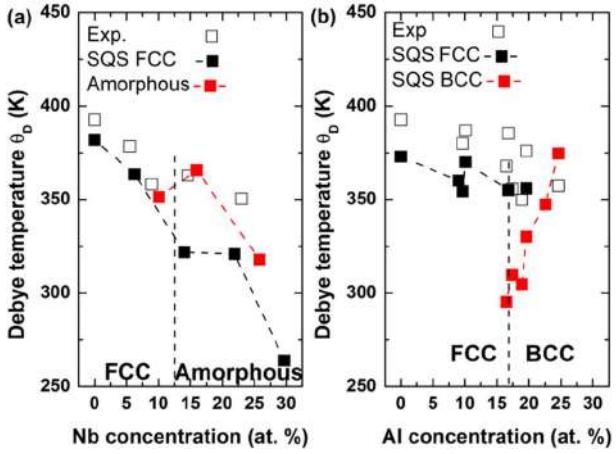

Figure 5.11 - The calculated (dashed line) and experimental (symbol) Debye temperature (a) $(CoCrCuFeNi)_{1-x}Nb_x$ and (b) $(CoCrCuFeNi)_{1-x}Al_x$ as a function of niobium and aluminium concentration. The vertical dotted lines at 17 at. % *Al* and 12.5 at. % *Nb* indicates the FCC to BCC and the FCC to amorphous structural transitions, respectively.

5.5 Summary and conclusions

Al and *Nb* addition both increased the lattice distortion while *Al* favored strong bonds formation with transition metals. *Nb* leads to fully dense films, whereas the mass density continuously decreased with an increasing porosity fraction, as a function of *Al* concentration. As inferred from x-ray diffraction, addition of *Nb* leads to a phase transition from FCC to amorphous state ~ 12.5 at. % *Nb* while in the case of *Al*, the transition from FCC to BCC appears ~ 17 at. % *Al*, before the final amorphous phase ~ 25 at. % *Al*.

The experimental phase and structural properties agree well with the DFT calculations, using either the exact Muffin-Tin orbitals (EMTO) method together with the coherent potential approximation (CPA) or the SQS method with pseudo-potentials using VASP that allows accounting for the relaxations of atomic positions. In terms of elastic constants, CPA calculations tend to provide more rigid elastic constants (c_{12}, c_{44}) due to absence of atomic relaxations as well as an intrinsic problem of EMTO to overestimate c_{44}. c_{11} is a special case where the relative value depends on alloying content. Briefly, the atomic relaxation effects should be carefully checked when using CPA to calculate elastic properties.

Empirical atomic size difference δ and elastic-strain energy ΔH_{el} were validated by DFT calculated local lattice distortion *LLD* and relaxation energy $\Delta(E_r)$ and these parameters were found to play a role in describing phase transitions. The phase transition

from FCC to amorphous or FCC to BCC occurred at a critical δ(4.6–5.2 %) value, in accordance to the common criterion ($\delta \leq$ 6%). Much stronger *LLD* for *Nb* than for *Al* addition to FCC *CoCrCuFeNi* were found. At the critical transition point, *Nb* addition in *CoCrCuFeNi* necessitates an increasing elastic-strain energy ΔH_{el} ~8 kJ/mol (83 meV, slightly above Andreoli *et al.* criterion 6.8 kJ/mol [101]) and relaxation energy $\Delta(E_r)$~81 meV and (for 14 at. % Nb) associated to its higher lattice distortion before phase transformation, whereas for FCC $(CoCrCuFeNi)_{1-x}Al_x$, the threshold relaxation energy is $\Delta(E_r)$~36 meV and elastic-strain energy ΔH_{el} ~5.1 kJ/mol (53 meV) at the phase transition ~17 at. % Al. Additionally, *VEC* calculated for both $(CoCrCuFeNi)_{1-x}(Nb_x, Al_x)$ alloys showed *VEC* > 8 until 22 at. % Nb and 14 at. % *Al*, respectively, allowing FCC phase stability in good agreement with our *ab-initio* predictions.

PLU and BLS optoacoustic techniques measured the sound velocity of longitudinal (V_L) and transverse (V_T) acoustic waves provided the effective elastic constants of the films, C_{33} and C_{44}. A*b-initio* calculations of single crystal elastic constants were complemented by a self-consistent averaging micro-mechanical model to derive the simulated effective elastic constants and sound velocities for each crystallographic texture of FCC (111) and BCC (110) polycrystalline phases. *Ab-initio* molecular dynamics calculations were performed for the particular case of *Nb*-rich amorphous phase of $(CoCrCuFeNi)_{1-x}Nb_x$ and all numerical results (lattice parameter, mass density, phase stability, elastic constants and sound velocities) were compared to their experimental counterpart, considering the porosity fraction in the particular case of $(CoCrCuFeNi)_{1-x}Al_x$, that may induce an extrinsic softening of the material elastic properties. For comparison, it was found from self-

consistent averages that 5 % porosity induced ~10 % softening of C_{44} and ~8 % softening of C_{33} for both FCC and BCC phases. Good comparison is obtained for V_T and C_{44} that vary only little with chemical composition. Decrease of Debye temperature is mainly due to the atomic volume increase for $(CoCrCuFeNi)_{1-x}Al_x$ system, identifying the origin of lattice instability and phase transition of topological and not mechanical origin.

Nevertheless, as the comparisons between the predicted and the experimental V_L and C_{33} were not satisfactory enough in the FCC phase (still over-estimate) and before the appearance of the amorphous or the BCC phase, the formation of an amorphous or highly disordered interphase at the grain boundaries [9] due to the presence of oxygen impurities in the deposition chamber, is suspected to play a non-negligible role in the acoustic and elastic effective properties response of the base metallic films. It should be considered in further analysis. One should notice that such interphase should not influenced noticeably V_T and C_{44} properties. Further investigations are in progress to identify its properties by considering more independent information, such as thermal and electrical properties.

CHAPTER 6. MULTICOMPONENT INTERSTITIAL ALLOYS AND NITRIDES CoCr(Cu, Mn)FeNi-N_X

CoCr(Cu,Mn)FeNi-N_x thin films were deposited by reactive magnetron sputtering in a ultrahigh vacuum chamber at different nitrogen pressures. The crystal structure was studied by the standard XRD. Optoacoustic techniques were used to measure the shear and longitudinal wave velocity, specifically by Brillouin light scattering (BLS) and picosecond laser ultrasonic (PLU), respectively. Magnetic properties were studied by ferromagnetic resonance spectroscopy (FMR) but are not discussed in this thesis. Additionally, by using stretchable substrate glued on piezo-actuators, we were able to obtain their magnetostriction coefficient. Metallic films deposited on polymer substrate were deformed under the micro-tensile test machine to study the crack propagation and buckles formation and results on *CoCrCuFeNi* films will be presented in the last *chapter 7*. Numerically, we explored structural, magnetic and mechanical properties at the atomic scale by density functional theory (DFT) combined with Special Quasi-Random Structures (SQS). The evolution of structural, mechanical and magnetic properties as a function of *N* concentration can be well understood combing DFT calculations.

6.1 Energetics of *CoCr(Cu,Mn)FeNi-N_x*

The first-principles spin-polarized electronic-structure calculations were performed with the Vienna ab initio simulation package (VASP) [36, 37] using projector augmented-wave (PAW) potentials [38]. The Perdew-Burke-Ernzerhof (PBE) exchange correlation functional [41] in the generalized gradient approximation (GGA) was employed to perform

the self-consistent calculations and compute the total energies. We used uniformly distributed k-points in the irreducible Brillouin zones according to the Monkhorst-Pack scheme [42] with a k-points spacing of 0.2/Å. A plane wave cut-off energy of 520 eV was chosen to ensure the accuracy of force calculations. The electronic energy-convergence criterion was set to 10^{-5} eV/cell and a force convergence criterion of 0.02 eV/Å was used during ionic relaxation.

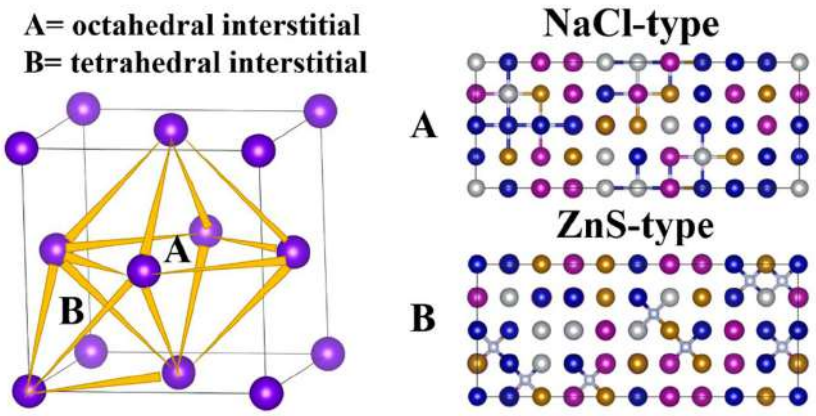

Figure 6.1: Two types of interstitials in an FCC lattice, denoted by A and B, representing the octahedral and tetrahedral interstitials respectively. Fully occupation of A or B sites leads to *NaCl* or *ZnS*-type structures, respectively.

We employed the special quasi-random structures (SQS) [262] to model the chemical randomness of metallic elements and the random distribution of nitrogen at octahedral or tetrahedral interstitial sites. The structures were generated by ATAT [16] by optimizing the Warren–Cowlley short range order parameters to 6^{th} nearest neighbors for pairs and to 4^{th} nearest neighbors for triplets. Initially supercells containing totally 80 metallic atoms were built. Various numbers of nitrogen atoms were later added randomly by SQS, into the octahedral or tetrahedral interstitial sites respectively as shown in **Figure 6.1**, leading to the formation of octahedral interstitial alloy or tetrahedral interstitial alloy

with different *N* concentrations. Full *N* occupation forms the *NaCl*- or *ZnS*-type stoichiometric nitride, respectively.

The formation energy per atom (ΔH) is obtained by,

$$\Delta H(x) = \frac{1}{n}\left(E(CoCr(Cu,Mn)FeNiN_x) - \left(\frac{x}{2}E_{N_2} + \sum_i E_i\right)\right) \qquad (6.1)$$

where *n* is the total number of atoms in the supercell, *E* is the total energy of *CoCr(Cu,Mn)FeNiN*$_x$. E_{N_2} and E_i are the energy of N_2 molecular and the metallic elements (*Co, Cr, Cu, Mn, Fe and Ni*) in their ground state respectively.

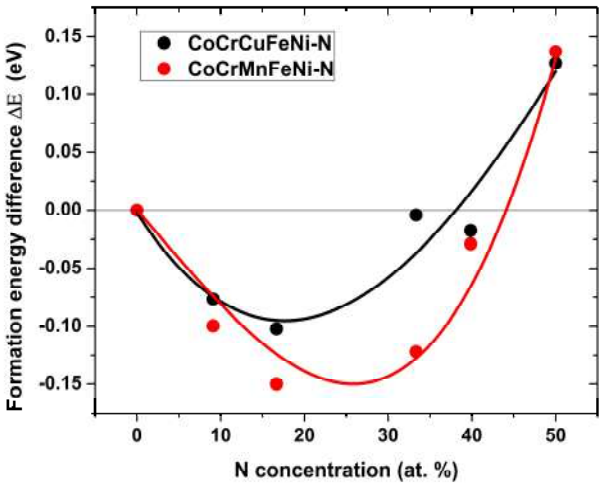

Figure 6.2 - The formation energy difference ($\Delta E = E_{octahedral} - E_{tetrahedral}$) between the octahedral interstitial configurations and tetrahedral interstitial configurations for *CoCrCuFeNiN*$_x$ and *CoCrMnFeNiN*$_x$ respectively. The curves are only a guide to the eyes.

The formation energy difference is defined as the energy difference between the octahedral and tetrahedral interstitial configurations. A negative value suggests the octahedral interstitial filling is more favorable, and vice versa. A positive value for the

energy difference emerged at and only at ~50 at. % *N*, meaning that the *ZnS*-type structure is more energetically favorable than *NaCl*-type for both stoichiometric *CoCrCuFeNiN* and *CoCrMnFeNiN*. As can be seen from **Figure 6.2**, the tetrahedral interstitials are not favorable in a large concentration interval from 0 to ~40 at. % *N*. This range covers all the samples we've synthesized. In the following (elastic properties) calculations we will consider octahedral interstitial filling only.

The tetrahedral interstitial configurations at low *N* concentrations (e.g., 9 at. % and 16.7 at. % *N*) were unstable for both *CoCrCuFeNi*N_x and *CoCrMnFeNi*N_x. The *N* interstitials moved to octahedral interstitial sites spontaneously during atomic relaxation. This instability can be understood by comparing the radius of the octahedral and tetrahedral holes in an FCC lattice, see **Figure 6.1**. The size ratio of octahedral hole to the atomic spheres is 0.414. As a contrast, the ratio of tetrahedral hole to the atomic spheres is 0.225. The atomic radii of *N* is 65 pm and the other metallic elements have an average atomic radius 137 pm (*Cr* 140 pm, *Mn* 140 pm, *Fe* 140 pm, *Co* 135 pm, *Ni* 135 pm, *Cu* 135 pm), giving a ratio (0.46) far above 0.225. Consequently, the *N* interstitial will prefer the larger octahedral hole where Coulomb repulsion force is smaller.

6.2 Structural properties *CoCr(Cu,Mn)FeNi-*N_x

For both *CoCrCuFeNi*N_x and *CoCrMnFeNi*N_x, the lattice parameters increase with more N content as revealed by XRD and DFT, and the mass density decreases with *N* addition. DFT calculations with octahedral and tetrahedral interstitials provide similar values and the same trend. However, to compare lattice parameters quantitively, one have to bear in mind that the generalized-gradient approximation (GGA) tends to overestimate

the lattice constants up to 3% [287]. Besides, residual stress in thin films can also lead to discrepancies as stress-free lattice parameters were not evaluated in case of films deposited on Si substrate. For instance, we found for *CoCrCuFeNiN_x* with high *N* concentrations, the thick films exhibit compressive stress, resulting in an expanded out-of-plane lattice parameter.

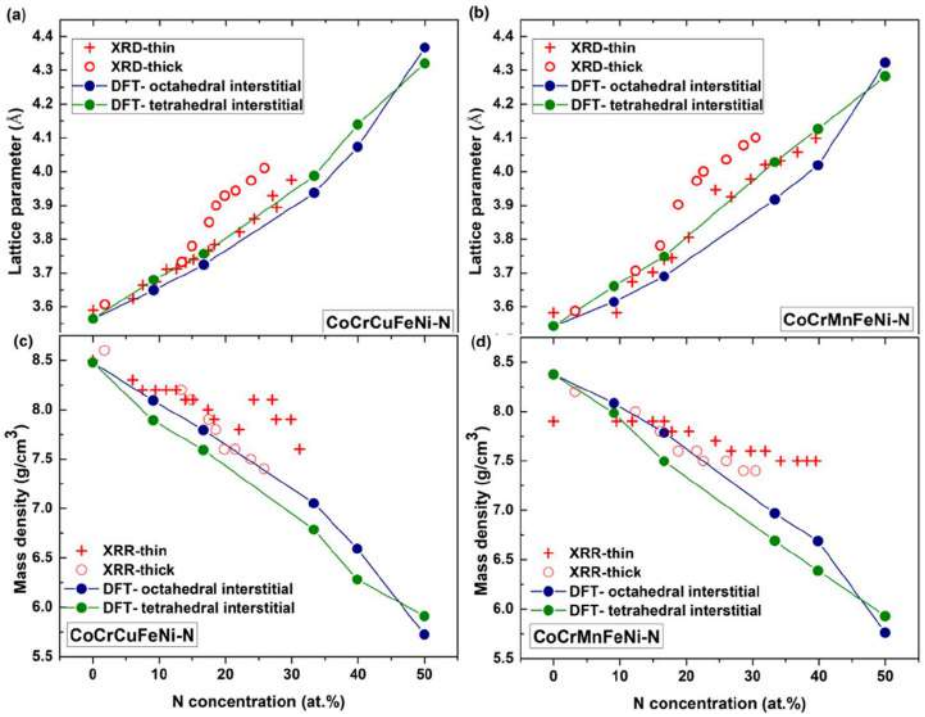

Figure 6.3 - The XRD and DFT lattice parameters as a function of the N concentration for (a) *CoCrCuFeNiN_x* and (b) *CoCrMnFeNiN_x*, and XRR and DFT mass density for (c) *CoCrCuFeNiN_x* and (d) *CoCrMnFeNiN_x*.

Hence, using the stress-free lattice parameter for comparisons to DFT is a priority. It was already demonstrated in *chapter 2* for CoCrCuFeNi films on Kapton, but it is a huge effort to perform such systematic experimental evaluation.

The discrepancy of experimental and DFT calculated lattice parameters and mass density is relatively large when *N* addition is less than 20 at. %, as shown in **Figure 6.3**. An obvious augmentation of the lattice parameter with reference to the thin films as well as DFT predictions can be seen from the thick *CoCrCuFeNi*N_x and *CoCrMnFeNi*N_x films above ~20 at. % *N*.

As reported by Klimashin et al. [233], the ordering of N vacancies (in NaCl structure) is favored at high *N* concentrations for *Mo*N_x. To study the *N*-ordering effects on lattice parameters in *CoCrCuFeNi*N_x or *CoCrMnFeNi*N_x, we considered several structures as listed in **Figure 6.4**. These structures contain ordered *N* interstitials and have already been identified from both experiments and theories. For instance, Takahashi *et al*. has synthesized the $Pm\bar{3}m$-Fe_4N phase and measured the elastic moduli [288] with the value of 157 ±11 GPa and 159 ±17 GPa, respectively for thin films and a bulk-like sample, which is in good agreement with the DFT calculated value of 162 GPa. The *N* ordering structure for $P6_322$-Ni_3N [289] and the reversible *N*-order-disorder transition for $P6_322$-Fe_3N [290] were confirmed by Leineweber *et al.* through neutron scattering. The $Pm\bar{3}m$-Cu_3N has open-packed anti-ReO_3 structure with one *N* occupies the vertices of a cubic cell while three *Cu* atoms occupy six face centers. $Pm\bar{3}m$-Cu_3N is metastable and can decompose into *Cu* and N_2 around 300°C [291]. The $Pm\bar{3}m$-*WN* has the *NbO*-type structure. It has the same stoichiometry as the defect-free *NaCl*-type compounds but contains 25 at. % ordered Schottky vacancies. The transition from *NbO*-type *WN* with ordered vacancies to *NaCl*-type *WN* with disordered vacancies can be triggered by electron beam irradiation as reported by Xing et al.[292]. Liu et al. carried out systematic calculations on *3d* transition metal mononitride with *NbO*-type structures[293], they found the *NbO*-type nitrides have

similar cohesive energy to the *NaCl*-type ones, of which *CoN*, *NiN* and *CuN* even have lower energies. The lower energy for the *NbO*-type MoN_x than the *NaCl*-type was also reported in Ref. [233].

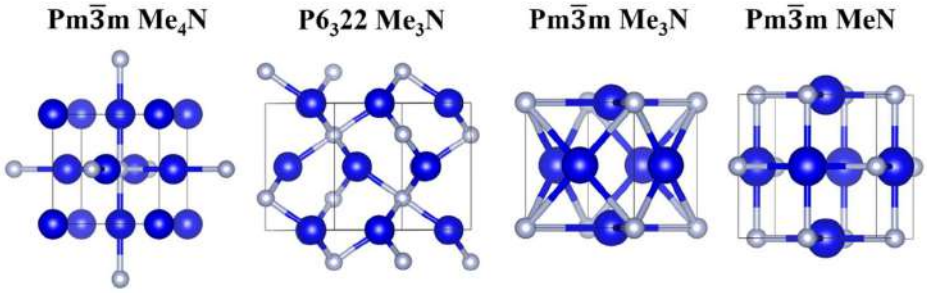

Figure 6.4 - Structures with ordered *N* distributions ranging from 20 to 50 at. %.

We evaluated the *N*-ordered structures for $CoCrCuFeNiN_x$. The structures were built by SQS with the same parameters described in the methods section. Our simulated powder diffraction pattern of the hexagonal $P6_322$- $CoCrCuFeNiN_{1.67}$ (Me_3N) displays a most intense peak at 44.09º with a corresponding *d*-spacing of 2.053Å, whereas the thick sample with similar *N* concentration has the peak at 45.18º with a corresponding *d*-spacing of 2.005Å. The $Pm\bar{3}m$-$CoCrCuFeNiN_{1.67}$ (Me_3N) is not stable and didn't provide a reasonable structure after relaxation. The calculated structural parameters are listed in **Table 6.1**, together with the values of disordered octahedral/tetrahedral interstitials and the experimental values at 20 at.% and 25 at.% *N*. However, none of these calculations provide reasonable explanations to the discrepancy of lattice parameter over 20 at. % *N,* suggesting this lattice expansion after 20 at. % *N* has other origin. Further check of oxygen impurity influence is undergoing.

Table 6.1 - Lattice parameters of the *N*-ordered *CoCrCuFeNiN_x*.

Sample	Space group	Lattice parameters	Reference lattice
CoCrCuFeNi$N_{1.25}$	$Pm\bar{3}m$	3.787	3.755[a], 3.798[b], 3.801[c], 3.926[d]
CoCrCuFeNi$N_{1.67}$	$P6_322$	a=4.640, c=4.407	3.813[a], 3.870[b], 3.876[c], 3.994[d]
CoCrCuFeNi$N_{1.67}$	$Pm\bar{3}m$	/	
CoCrCuFeNiN_5	$Pm\bar{3}m$	3.833	4.368[a], 4.324[b]

*a: *NaCl*-type lattice with disordered *N* vacancies calculated by DFT. *b: *ZnS*-type lattice with disordered *N* vacancies calculated by DFT. *c: Lattice parameters as measured from thin films. *d: Lattice parameters as measured from thick films

The mass density measured by XRR is presented in **Figure 6.3**. The decreasing trend is in good line with DFT predictions. It happens because the initial metallic lattice is expanded by additional *N* atoms, and the relatively light *N* atoms don't add significant mass into the system. In the case of *CoCrMnFeNiN_x*, the films were found less dense under 15 at. % *N*. This is probably due to the used powder target. We always get dense *CoCrCuFeNiN_x* films deposited with the solid target. Contrarily, films become over dense at higher *N* concentrations over 20 at. %, especially for the thin films.

6.3 Sound velocities, elastic constants, indentation test modulus and hardness

6.3.1 Single crystal elastic constants of CoCr(Cu,Mn)FeNiN_x

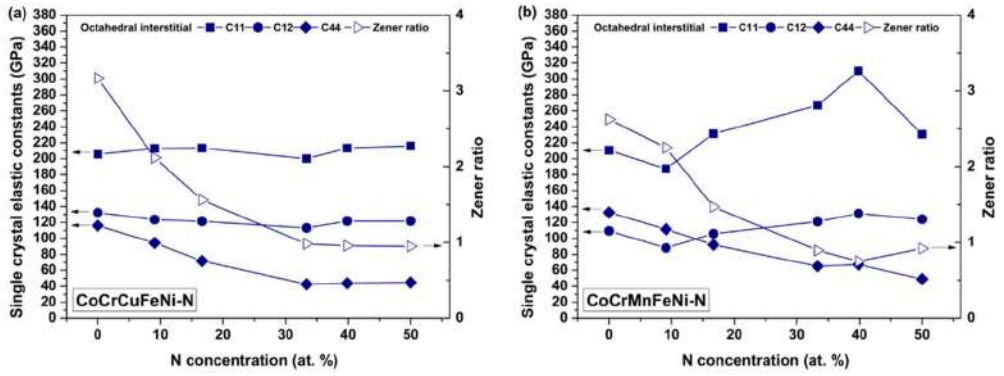

Figure 6.5 - Single crystal elastic constants and the Zener anisotropy ratio of (a) *CoCrCuFeNiN_x* and (b) *CoCrMnFeNiN_x* as a function of the *N* concentration. The calculations were performed on the octahedral *N* interstitial filling configurations. The black arrow indicates the corresponding *y*-axis.

Single crystal elastic constants for *CoCrCuFeNiN_x* and *CoCrMnFeNiN_x* with octahedral *N* interstitials were calculated using DFT. The three independent elastic constants for a cubic material (c_{11}, c_{12} *and* c_{44}), as well as the Zener anisotropy ratio are plotted in **Figure 6.5**. The Zener anisotropy ratio ($A = \frac{2c_{44}}{c_{11}-c_{12}}$) quantifies how far a material is from being elastically isotropic ($A = 1$). Clear trends show that *A* decreases with *N* alloying and reaches the isotropic criterion above ~35 at. % *N* for both *CoCrCuFeNiN_x* and *CoCrMnFeNiN_x*. It is also revealed that FCC *CoCrCuFeNi* and *CoCrMnFeNi* are highly anisotropic with an *A* value of 3.168 and 2.624 respectively. In terms of single crystal elastic constants, c_{11} behaves very differently for the two systems. For *CoCrCuFeNiN_x*, c_{11} almost keeps constant with *N* addition, whereas it increases from 210 GPa to 310GPa for *CoCrMnFeNiN_x*, accounting for a + 47% growth. The variation of c_{12} for *CoCrCuFeNiN_x* is insignificant. For *CoCrMnFeNiN_x*, an obvious decrease occurs at 9 at. % *N* then a slight increase follows. A softening of c_{44} is quite significant with *N*

addition as for *CoCrCuFeNiN_x* and *CoCrMnFeNiN_x*, c_{44} decreases from 116 GPa to 45 GPa and from 132 GPa to 49 GPa respectively.

6.3.2 Sound velocities and elastic constants-CoCrCuFeNiN_x

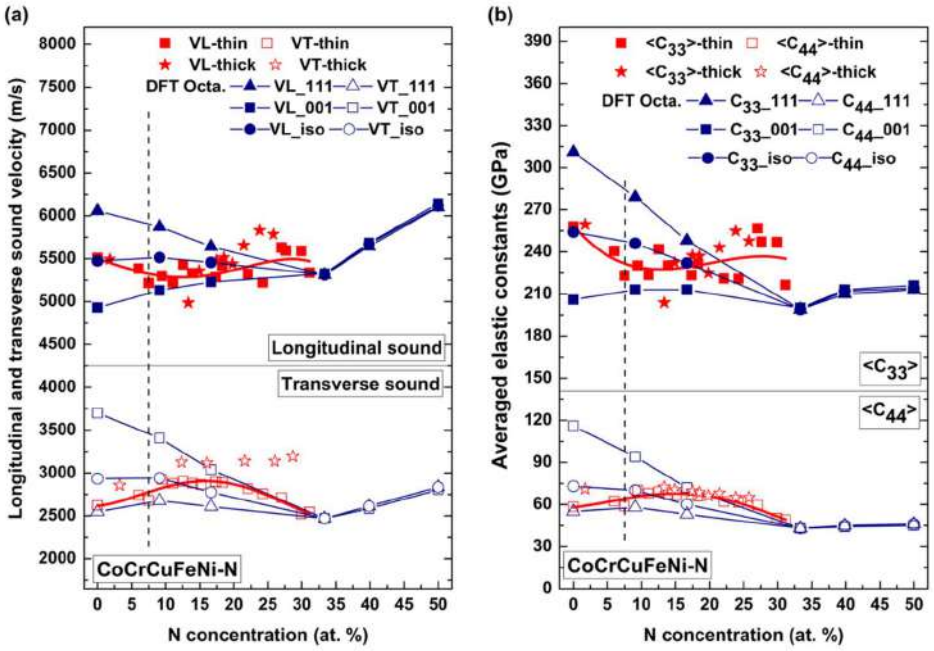

Figure 6.6 - (a) The longitudinal sound velocity V_L and shear sound velocity V_T (b) the derived elastic constants C_{33} and C_{44} for *CoCrCuFeNiN_x*. The effective sound velocities and elastic constants are calculated from the Voigt-Reuss-Hill (VRH) average, considering isotropic, <111>-textured and <001>-textured polycrystals. The dashed line is an indicator for the texture change observed from XRD.

Based on the single crystal elastic constants, the effective sound velocities and elastic constants for polycrystals can be calculated by the Voigt-Reuss-Hill (VRH) average. In **Figure 6.6**, we've considered the isotropic average for the as deposited nitrides, the <111>-textured and <001>-textured average. It has been mentioned that the cubic *CoCrCuFeNi* and *CoCrMnFeNi* are highly anisotropic. The <111> crystallographic orientation is the stiffer one while the <001> is the softest one. Hence the <111>-textured

average is the upper boundary while the <001>-textured average is the lower boundary, and the isotropic lies in between, as depicted in **Figure 6.6**. The difference between the three averages diminishes with *N* concentration due to the decrease of anisotropy, and finally disappears at ~33 at. % *N* when the nitrides become elastically isotropic (*A*~1).

The experimental trends presented in **Figure 6.6** are in accordance with our previous findings of the elastic properties of *CoCrCuFeNi*N_x as a function of the deposition parameter *RN* rather than *N* content [10]. Here, in terms of the experimental longitudinal sound velocity V_L and elastic constant C_{33}, a decreasing trend was observed at the early beginning of *N* addition (before the dashed line in **Figure 6.6**). Meanwhile, the shear sound velocity V_T and C_{44} was found to increase at this stage. The two different trends are well explained by DFT calculated average along the <111> orientation as expected. Comparing to V_L and C_{33}, V_T and C_{44} are more sensitive to the texture change for *CoCrCuFeNi*, since the change from <111> texture to <001> texture leads to a 45 % variation for V_T and a 110% variation for C_{44}. The relatively low values of V_T and C_{44} confirm the main orientation being <111> before the dashed line, in agreement to XRD observation. Note that the values of V_L and C_{33} in this composition range are lower than the calculated <111>-textured average. This maybe because the *CoCrCuFeNi* film is not perfectly <111>-textured and/or disordered core-shell structure forming at the grain boundaries with the oxygen impurities. Minor grains fraction of other orientations can significantly decrease V_L and C_{33} due to high anisotropy. Further *N* addition leads to a plateau between 10 at. % to 20 at. % *N* for V_T and C_{44}. Within this composition range, V_T and C_{44} have reached their maximum values. The high plateau results from joint contribution of the gradual change of <111> to <001> texture which increases V_T and C_{44}, and chemical effect of *N* addition

which decreases V_T and C_{44} along the <001> orientation. The texture change can be inferred not only from V_T and C_{44} as they deviate from the <111>-textured average, but also from V_L and C_{33} as they approach the <001>-textured average. The texture change is almost completed at ~20 at. % *N*, because at this point, both V_L and V_T have reached the theoretical value of <001>-textured average. At the next stage, more *N* addition results in a decrease of V_T and C_{44}. The experimental values for the thin series fit very well to DFT averages along the <001> orientation. On the other hand, V_L and C_{33} quite scatter and cannot provide a significant increasing or decreasing trend. Note that, unlike V_T and C_{44}, V_L and C_{33} are sensitive to the thickness measurement which might contribute the scattering of data points. Thick samples deposited under a different condition clearly provide higher values for V_T and V_L especially at high *N* concentrations above 20 at. %. These samples also provide larger lattice parameters as shown in **Figure 6.3**, and then we cannot expect same results for elastic properties, too. The explanation for the discrepancies is still unclear.

6.3.3 Sound velocities and elastic constants-CoCrMnFeNiN_x

V_L and $\langle C_{33} \rangle$ slightly decrease before 10 at. % *N*, then increase until reaching 40 at. % *N*. This trend is well reproduced by DFT calculations, with either isotropic average, <111> or <001>-textured average. This strong tendency is mainly attributed to the chemical influence of *N* addition, which affects significantly the elastic properties comparing to *CoCrCuFeNi*N_x, as shown for single crystal elastic constants depicted in **Figure 6.5**. The same trend was also found for V_T and C_{44}, in the case of the thin series. Moreover, the values of V_T and C_{44} for this series are obviously lower than the lowest

predictions (<111>-textured) from DFT, which has not been encountered in the case of *CoCrCuFeNiN_x*. To understand the origin of the low value, we recall that, in amorphous materials, the shear modulus is about 30 % smaller than in the corresponding crystals [294]. This is because there exists a variety of atomic environments in the unrelaxed amorphous phase, the rearrangements of atoms occurring easily under a macroscopic strain for those atoms in the environment with unstable topology.

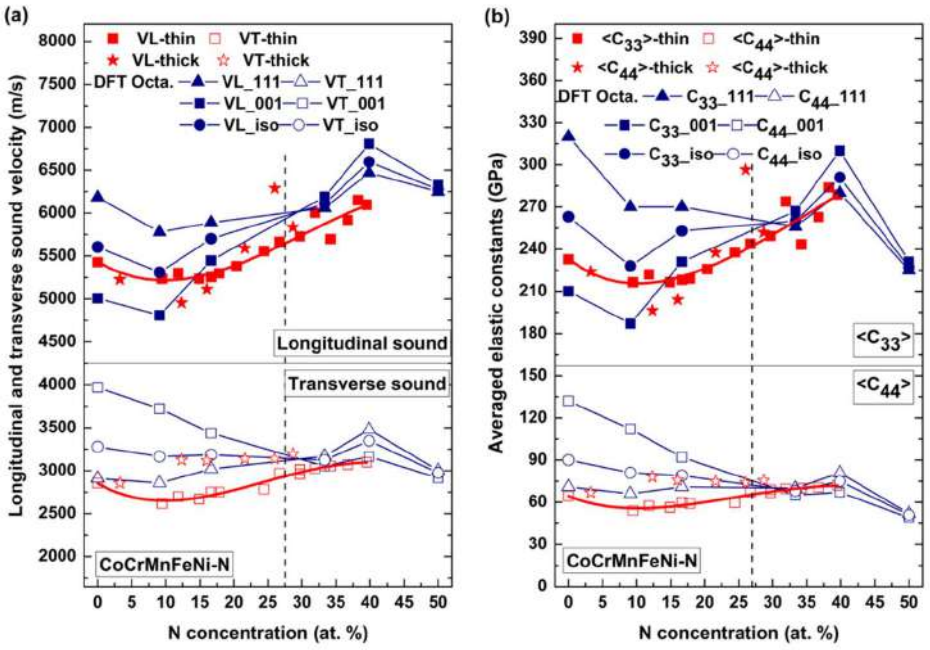

Figure 6.7 - (a) V_L and V_T (b) the derived elastic constants C_{33} and C_{44} for *CoCrMnFeNiN_x*. Highly intense XRD (002) peak appears after the dashed line for the thin series (refer to Figure 2.19b).

The existence of amorphous phases in *CoCrMnFeNiN_x* is well captured by the broad XRD peaks in **Figure 2.19b**, as well as the low mass density as shown in **Figure 6.3d**. These amorphous phases contribute to the softening of the effective shear modulus.

As a contrast, higher V_T and C_{44} were achieved for the corresponding thick samples with dense crystalline phases. Meanwhile, it is also interesting to note that thin and thick films provide similar values for V_L and C_{33}, without being affected by the amorphous phase.

Quantitatively, we found better agreement between the thick samples and DFT calculations for V_T and C_{44}. The microstructural change from <111>-textured to isotropic was captured in **Figure 6.7a** and **Figure 6.7a**, as V_T and C_{44} initially fit very well to the <111>-textured average for the first thick sample, then superimpose with the isotropic-average over 12 at. % *N* addition. V_L and C_{33} don't provide the same scenario because the exact <111>-texture is difficult to obtain as in the case of *CoCrCuFeNi*N_x and there may be errors coming from the thickness determination, as we've mentioned before. The core-shell structure formation with oxygen impurities is also not excluded.

6.3.4 Young's modulus and hardness by Nanoindentation

As depicted in **Figure 6.8a** and **Figure 6.8b**, theoretical Young's modulus show large discrepancies between the isotropic, <111>- and <001>-textured averages due to high anisotropy. The discrepancies decrease with *N* addition until reaching ~33 at. % *N*, where the nitrides become more isotropic. A steady increasing trend was found for the experimental Young's modulus by adding *N*, for both *CoCrCuFeNi*N_x and *CoCrMnFeNi*N_x. For both cases, the experimental values lie close to the theoretical predicted range, except for the last two *CoCrCuFeNi*N_x samples which already have shown larger V_T and C_{44}. *CoCrMnFeNi*N_x provides better agreements between nanoindentation on thick samples and the isotropic average from DFT calculations. Interestingly, in the previous section, the same conclusion was drawn when we compare theoretical V_T or C_{44}

to the BLS value. Note that, many of the thin samples (~400nm) provide unreasonably low indentation Young's modulus as well as low hardness (low values were not shown in **Figure 6.8**), of which the *CoCrMnFeNiN_x* deposited from a powder target provide even worse results due to being less dense.

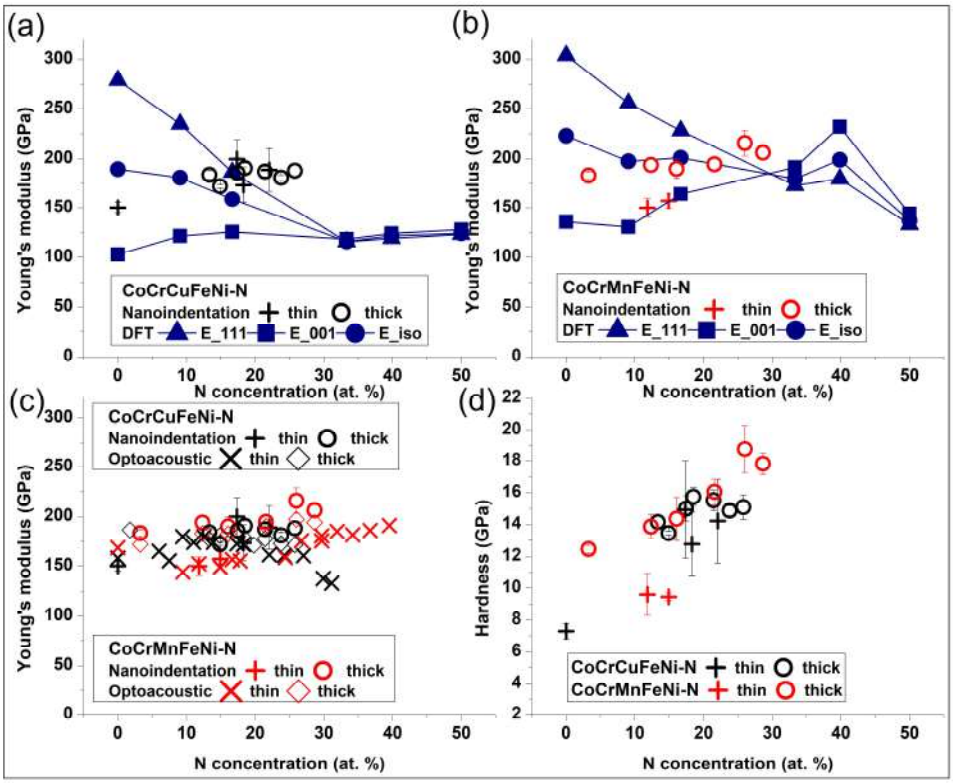

Figure 6.8 - DFT and indentation Young's modulus for (a) *CoCrCuFeNiN_x* (b) *CoCrMnFeNiN_x* (c) Indentation and optoacoustic Young's modulus for *CoCrCuFeNiN_x* and *CoCrMnFeNiN_x* (d) Indentation hardness for *CoCrCuFeNiN_x* and *CoCrMnFeNiN_x*. Samples providing unreasonable low values are removed from the figure.

For samples with issues of being porous, or not thick enough to eliminate the influence of substrate, the optoacoustic techniques can provide reasonably good elastic properties comparing to nanoindentation, such as Young's modulus as shown in **Figure**

6.8c. Despite the less dense *CoCrMnFeNi*N_x films from the thin series which provide relatively low modulus by optoacoustic measurements, satisfactory agreements can be achieved between nanoindentation and optoacoustic probing. Note that for *CoCrCuFeNi*N_x thin films with ~30 at. % *N*, optoacoustic results exhibit an extra decreasing trend comparing to nanoindentation. This is indeed reasonable because thin films have reached a higher *N* concentration, and at this *N* concentration, the decreasing tendency is in line with the DFT prediction as shown in **Figure 6.8a**. In **Figure 6.8d**, it was found that *N* incorporation increases the hardness for both *CoCrCuFeNi*N_x and *CoCrMnFeNi*N_x. *CoCrCuFeNi*N_x exhibit a maximum saturation (~16 GPa) for ~18 at. % *N*. *CoCrMnFeNi*N_x can reach a higher hardness (~19 GPa) for ~28 at. % *N* comparing to *CoCrCuFeNi*N_x.

6.4 Summary and conclusions

We have studied elastic properties of the interstitial high entropy nitride alloys, i.e., *CoCr(Cu,Mn)FeNi*N_x with various *N* concentrations from both experiments and DFT based *ab-initio* calculations. Lattice parameters, mass density, sound velocities and elastic constants were compared.

CoCr(Cu,Mn)FeNiN_x thin films with two characteristic thicknesses (~400nm and 1200 nm, denoted as thin and thick respectively) were deposited by reactive magnetron sputtering at different *N* partial pressures. Stoichiometric nitrides haven't been synthesized due to target poisoning. The maximum incorporated *N* content reached ~40 at. %. With *N* addition, XRD diffraction clearly reveals the increase of the lattice parameter and the texture change from (111) of FCC (metal phase) to (002) of another FCC (*NaCl*-type defected nitride).

The longitudinal and shear sound velocities were measured by picosecond laser ultrasonic (PLU) and Brillouin light scattering (BLS) respectively, and the corresponding elastic constants were derived. The longitudinal sound velocity V_L and C_{33} first decrease then increase with N addition for both *CoCrCuFeNi*N_x and *CoCrMnFeNi*N_x. Although the variations in *CoCrCuFeNi*N_x are relatively small. The shear sound velocity V_T and C_{44} vary slightly with *N* addition, they increase first then decrease for *CoCrCuFeNi*N_x, while they decrease first then increase for *CoCrMnFeNi*N_x.

As for DFT calculations, the atomic structures were built by SQS considering random distribution of *N* interstitials. The *ab-initio* total energy calculations first suggest that the octahedral interstitial filling is more favorable comparing to tetrahedral filling for the interstitial alloy but not for the stoichiometric compounds. Based on the octahedral interstitial configurations, the single crystal elastic constants were calculated. For *CoCrCuFeNi*N_x, c_{11} and c_{12} have no significant dependence on *N* content, while c_{44} decreases monotonously. In the case of *CoCrMnFeNi*N_x, obvious stiffening of c_{11} was observed with *N* addition. c_{12} varies slightly and c_{44} decreases monotonously as in *CoCrCuFeNi*N_x. The elastic anisotropy was found to decrease with *N* addition for both cases becoming nearly elastically isotropic above ~30 at. % *N*. The sound velocities and elastic constants were further averaged using the VRH method considering different textures observed from XRD. By comparison, we found that the different trends of V_L, V_T, C_{33}, and C_{44} obtained from optoacoustic measurements are in fact attributed to both the microstructure variations (texture and porosity) and the chemical alloying effects (*N* interstitial). In the case of *CoCrCuFeNi*N_x, a good agreement can be reached if considering <111> textured average at the beginning and <001> textured average in the later part for

DFT values. In the case of *CoCrMnFeNiN_x*, the isotropic average is preferred, and the porosity should be considered to have a softening effect on C_{33} and C_{44}. The existence of a core-shell disordered structure at the grain boundaries is also not excluded, as in the case of *CoCrCuFeNi-(Nb_x, Al_x)*, in *chapter 5*.

Comparison between the optoacoustic and nanoindentation techniques on elastic properties leads to good agreements on Young's modulus for the thick and dense films (~1200 nm). The results also agree to DFT calculations. Thin films (~400 nm) in this work tend to provide very low indentation modulus and hardness especially for *CoCrMnFeNiN_x* deposited with a powder composite target which don't have well defined XRD peaks (being broad and less intense) and are porous (observed from XRR mass density). The optoacoustic techniques might be a better choice, especially for the less dense and less thick films which nanoindentation is incapable to handle.

CHAPTER 7. CoCrCuFeNi THIN FILMS ON KAPTON SUBSTRATE

In this chapter, we present first results on fracture behaviour of pure *CoCrCuFeNi* thin films on Kapton® substrate, varying the thickness. These samples were tested in uniaxial traction, combined in situ with confocal microscopy observations of the surface. These studies made it possible to highlight the phenomenon of fragmentation, which was then analyzed with the existing theoretical models. We have a mean to estimate the fracture toughness of these thin films as well as their adhesion energy with the Kapton® substrate. This last chapter has to be considered as a more detailed example of our perspective of development of new experimental tools, in order to achieve a more complete characterization of mechanical properties of thin films on different kind of substrates.

7.1 Background

7.1.1 Fracture behaviour

The mechanical properties of thin films deposited on flexible substrates are increasingly studied because of applications in flexible electronics [295-297]. The desired characteristics include good film/substrate adhesion, good mechanical strength, and sufficient deformability to be applied to complex geometries inducing large deformations. In the case of stretchable systems, we will look for stretching of a few tens of percent, while for flexible systems a few percent. For the latter, a practical criterion is the ability to wind a flexible system around a pencil avoiding the formation of cracks in the thin film, which corresponds to about 2 % of applied strain. Another advantage of flexible substrates,

characterized by a low Young's modulus (a few GPa for polyimides such as Kapton®), is its ability to evaluate the mechanical properties of thin films deposited on top (provided an adhesion energy high enough). The uniaxial test combined with *in situ* probes (x-ray diffraction [297], atomic force microscopy [298], optical microscopy [299], electrical resistivity [300]) can indeed bring a lot of knowledge (fracture toughness, adhesion energy) by extracting quantitative data.

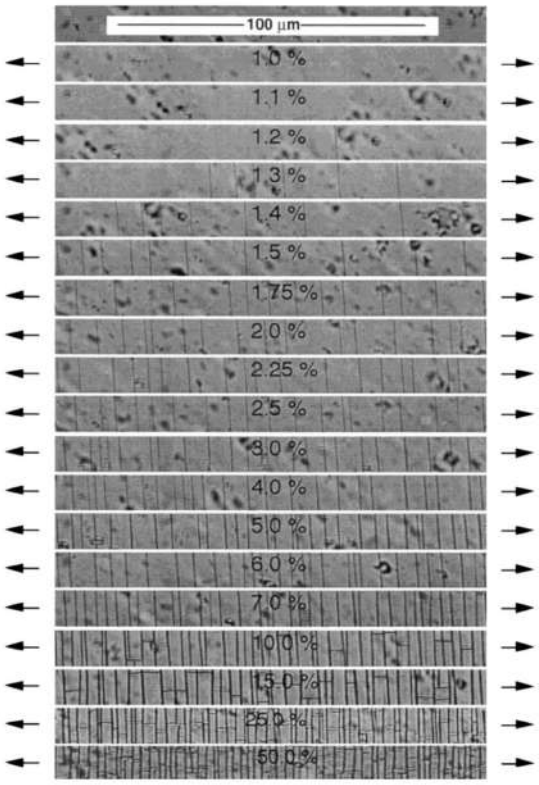

Figure 7.1 - Fragmentation morphology of the SiO_x Fragmentation morphology of the *SiOx* coating on a PET substrate at different strains parallel to the roll direction [7].

In contrast to conventional tensile testing of bulk materials, tensile testing of thin films on flexible substrates is characterized by multiple fracture of the thin film because the remaining adherent parts continue to be loaded by the substrate, which continues to be elastically or elastoplastically strained. In the case of brittle thin films, this is characterized by patterns of straight and parallel cracks [301]. Therefore, the crack density increases with the applied macroscopic strain (see **Figure 7.1**).

This can be modeled by purely analytical approaches, such as the all-elastic Xia & Hutchinson model [302] based on Beuth's work [303], Franck model [304], or by more recent numerical approaches such as finite elements [305]. These models make it possible to identify quantities as fracture thoughness K_{IC} and the energy release rate G [306-308].

Before describing the different steps, let us denote σ_∞ the reference value of the stress that would exist in an uncracked film. One critical characteristic of multi-cracked systems is the "stress transfer length" ξ, defined as the characteristic distance over which the stress σ_∞ is recovered inside the film starting from the free surface (*i.e.* zero stress) induced by a crack.

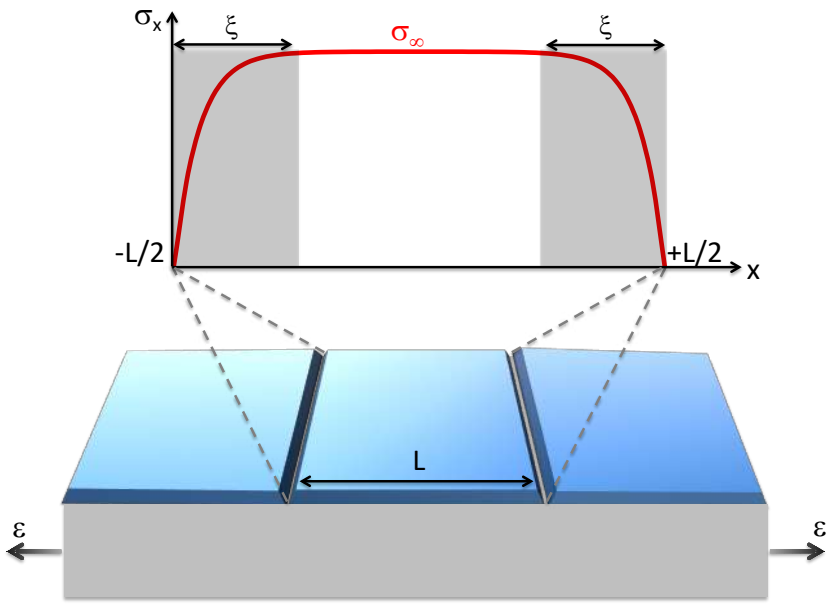

Figure 7.2 - Sketch of a fragmentation test of a thin film supported by a compliant substrate. A typical stress profile (along the tensile direction x) is plotted. ξ is defined as the stress transfer length and corresponds to the area where stress gradient occurs.

When a substrate is much more compliant than a film, the stress transfer length around a crack can be significant. Xia and Hutchinson have defined this quantity [302]:

$$\xi = \frac{\pi}{2} g(\alpha, \beta) h_f \tag{7.1}$$

where $g(\alpha,\beta)$ is a dimensionless integral of the crack opening displacement, which depends overall elastic mismatch between the film and the substrate. α and β are the so-called Dundurs parameters:

$$\alpha=\frac{\bar{E}_f-\bar{E}_s}{\bar{E}_f+\bar{E}_s},\beta=\frac{\mu_f(1-2\nu_s)-\mu_s(1-2\nu_f)}{2\mu_f(1-\nu_s)+2\mu_s(1-\nu_f)} \tag{7.2}$$

where $\bar{E}=\frac{E}{1-\nu^2}$ is the reduced modulus and $\mu=\frac{E}{2(1+\nu)}$ is the shear modulus. The determination of ξ can be done numerically or experimentally, as it will be described in the following.

Whatever the film thickness, 3 major strain domains generally characterize the evolution of fragment length as function of external strain ε as illustrated in **Figure 7.3** showing the evolution of mean fragment length as function of strain. The scales are especially there to give a typical order of magnitude for a metallic film of submicron thickness deposited on compliant substrates.

(1) Cracks appear only if the elastic energy stored in the thin film reaches the fracture energy (Griffith energy). In the first regime, the test being macroscopically homogeneous, the cracks appear non-deterministically at the places where the stresses are most localized, related to the slight microstructure heterogeneities of the thin film (grain boundaries, defects, ...). This initial fragmentation step is characterized by a crack spacing significantly exceeding the stress transfer length. During this regime, the interaction

between cracks is negligible; the rate of crack generation is governed solely by the mechanical inhomogeneity of the thin film. Therefore, in this regime, $L >> \xi$.

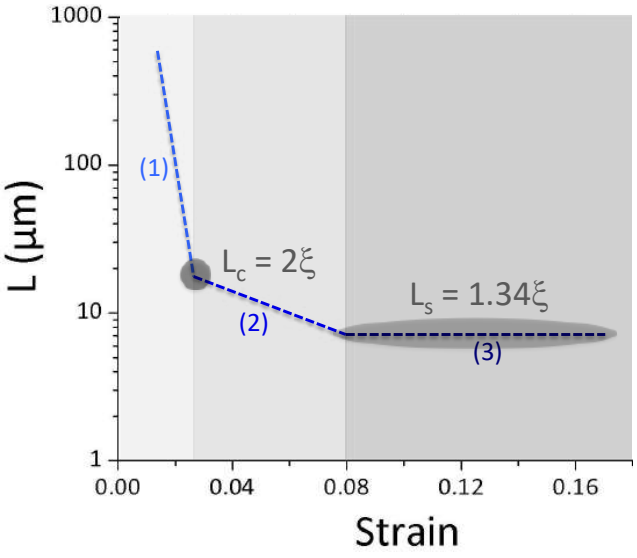

Figure 7.3 - Schematic evolution of mean fragment length as function of strain

(1) Cracks appear only if the elastic energy stored in the thin film reaches the fracture energy (Griffith energy). In the first regime, the test being macroscopically homogeneous, the cracks appear non-deterministically at the places where the stresses are most localized, related to the slight microstructure heterogeneities of the thin film (grain boundaries, defects, ...). This initial fragmentation step is characterized by a crack spacing significantly exceeding the stress transfer length. During this regime, the interaction between cracks is negligible; the rate of crack generation is governed solely by the mechanical inhomogeneity of the thin film. Therefore, in this regime, $L >> \xi$.

(2) Very quickly, once first fragments of thin films are created, the stress field between two existing cracks can be determined, the maximum being located between them; this corresponds to the second regime. The multiplication of cracks occurs when the stress

between two pre-existing cracks allows reaching the fracture energy again. Compared to the first regime, the crack propagation is slower, which results in a slope break in the "fragment length *versus* applied strain" curve. This transition between regimes (1) and (2) corresponds to the instant when the cracks begin to interact with each other. This corresponds to the particular condition $L \approx 2\xi$ (see **Figure 7.2** and **Figure 7.3)** [306].

(3) Finally, from a given crack density, it is no longer possible to reach stress levels sufficient to break the fragments. Thus, this third regime corresponds to a constant value of the mean fragment length. Rochat *et al.* [309] showed that this saturating length corresponded to $L \approx 1.34\xi$ (**Figure 7.3**).

Fundamental studies on channeling cracks in fully and partially cracked films were performed by Beuth [303], who expressed the energy release G rate of steady-state channeling cracks as a function of stress, film thickness and elastic mismatch between layer and substrate:

$$G_{Beuth} = \frac{\pi\sigma_f^2 h_f}{2\overline{E_f}} g(\alpha,\beta) = \frac{\xi\sigma_{x,0}^2}{\overline{E_f}} \tag{7.3}$$

with $\sigma_{x,0}$ the fracture stress of the film (sum of applied and residual (σ_{res}) stress along the tensile direction when first cracks appear).

Xia and Hutchinson [302] took into account multiple crack geometries and found that the energy release rate is reduced if an array of parallel cracks is channeling simultaneously or, to an even larger extent, sequentially. By following the work of Xia and Hutchinson, it is possible to express the energy release rate according to elastic and

geometrical parameters of the problem. The energy release rate for a sequential cracking process, as described above, is:

$$G_{X\&H} = \frac{\xi\sigma_x^2}{2\overline{E_f}}\left[2\tanh\left(\frac{L}{2\xi}\right) - \tanh\left(\frac{L}{\xi}\right)\right] \tag{7.4}$$

with σ_x the stress in the uncracked areas of the film during the multi-cracking phenomenon (sum of applied and *residual* (σ_{res}) stress).

More recently Franck *et al.* have proposed a complete 2-dimensional shear-lag model taking into account of the biaxial stress field in the fragments [304]. They found a more complex expression for the energy release rate:

$$G_{X\&H} = \frac{\xi\sigma_x^2}{2\overline{E_f}}\left[\frac{3\sinh^2(1/\lambda) - 1/\lambda}{\cosh^2(1/(2\lambda))} - \frac{3\sinh^2(2/\lambda) - 2/\lambda}{2\cosh^2(1/\lambda)}\right] \tag{7.5}$$

with $\lambda = {}^{\xi}/_{\boldsymbol{L}}$.

Then, assuming a fracture mode I, the fracture toughness K_{IC} can be further calculated from the energy release rate by:

$$K_{IC} = \sqrt{\overline{E_f}G} \tag{7.6}$$

For the implementation of all these models, elastic constants and moduli will be taken from *ab initio* calculation results combined with homogenization method for the polycrystalline microstructure (i.e. isotropic). The applied stress is known from the tensile

tests gage and residual stress is estimated from prior XRD experiments. Parameters ξ and L are determined from and *in situ* microscopy experiments.

7.1.2 Buckling behaviour (film/substrate adhesion)

One of the characteristics of the uniaxial fragmentation tests is that they are generally accompanied by buckling phenomenon because of compressive stresses along transverse direction (perpendicular to tensile one in the plane of the film) [304]. This phenomenon is initiated at the edge of cracks because it is where the compression stresses are the strongest. Thus, from a few % of applied strain, there is appearance of blisters (triangular or rectangular) periodically distributed on the surface of the sample (**Figure 7.4**) [310].

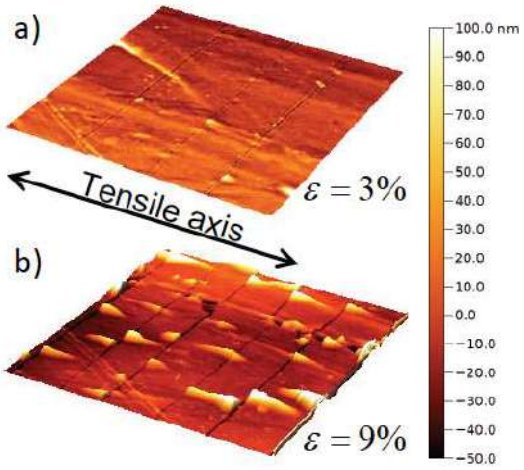

Figure 7.4 - AFM images of a) Fragmentation of a thin film during tensile test (strain = 3%), b) Buckling of thin film upper strain (9%), taken from ref. 16.

Two different failure modes might induce delamination: buckle-limited delamination and strain energy delamination [308]. Optically, the two different delamination modes are not distinguishable because both start at the fragmentation boundaries at the location of maximal compressive stress. However, buckle delamination indicates a weak adhesion of the coating to the substrate and the onset strain of delamination as a function of film thickness differs for both models. The film thickness dependence on the buckling strain for both cases can be calculated if the *residual stress* is

considered. These two modes can be distinguished by this dependency. It is in of square root inverse for strain energy mode whereas it is in squared for buckle-limited mode.

For the case of strain energy delamination, the expression of onset strain of delamination ε_{SED} follows [308, 311]:

$$\varepsilon_{SED} = \sqrt{\frac{2G_0}{\overline{E_f}\beta^2}} h_f^{-1/2} - \frac{\sigma_{res}}{\overline{E_f}\beta} \tag{7.7}$$

with $\beta = (\nu_f - \nu_s) - 2\lambda\nu_f(1 - \nu_f\nu_s)\tanh(1/(2\lambda))$ a dimensionless parameter proposed by Franck *et al.* to consider of the mean transversal strain in the fragments. Here, $\lambda = \xi/L$ has been defined for the fragmentation test in the previous section.

In the case of buckle-limited mode, the expression of onset strain of delamination ε_{BL} follows [308]:

$$\varepsilon_{BL} = \frac{\pi^2(\nu_f - \nu_s)}{12b^2} h_f^2 - \frac{\sigma_{res}}{\overline{E_f}(\nu_f - \nu_s)} \tag{7.8}$$

Finally, the thickness-dependency of buckling strain (found experimentally) will determine the delamination mode. This will be shown in the dedicated result section.

7.2 Experimental results and discussion

7.2.1 Residual stress as a function of thickness

The residual stress measured by x-ray diffraction increases with thickness. In fact, a high compressive stress is generated for a thickness of 20 nm while a tensile stress is

measured when thickness exceeds a hundred nanometers. This evolution looks characteristic of competitive columnar growth, whereby compressive stress is dominant in the early growth stages and then tensile stress dominates at later growth stages [312]. Indeed, compressive stress in sputtered films originates from defect incorporation, predominantly at the grain boundary (GB): if the grain size is small in the beginning of growth, the GB density is high that is traduced by compressive stress. Tensile stress is due to attractive forces at the column boundary; if column size increases with film thickness, the contribution of compressive stress source is lower, so the net stress is tensile. As shown by Yu & Thompson [313], the residual stress in the film due to increasing of the grain size to d from its initial value d_0 is given by:

$$\sigma_{res} = M\Delta a\left(\frac{1}{d_0} - \frac{1}{d}\right) \tag{7.9}$$

where M is the biaxial elastic modulus of the thin film and Δa is the excess volume per unit area of grain boundary.

If we assume a linear expression between grain size and film thickness, as proposed by Yu & Thompson [313], it is possible to fit the experimental data with an equation linking residual stress with thickness:

$$\sigma_{res} = K_1 - \frac{K_2}{h_f} \tag{7.10}$$

where K_1 and K_2 are fitting parameters. The best fit of the experimental data is shown in **Figure 7.5**. The expression of σ_{res} is therefore incorporated into the **eq. 7.3**, **7.4** and **7.5** for fracture behavior and **eq. 7.7** and **7.8** for buckling behavior.

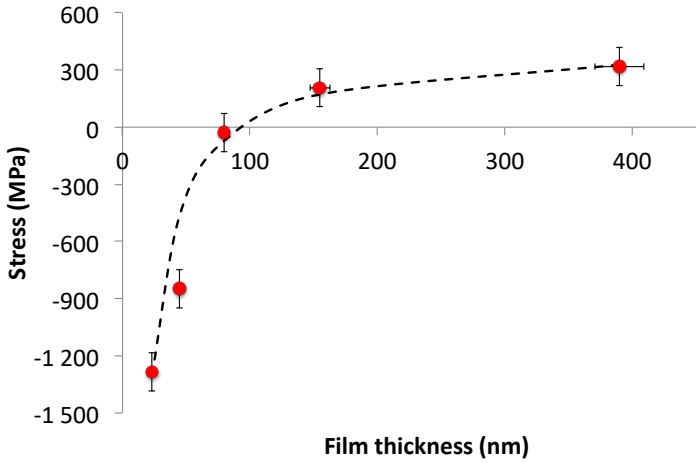

Figure 7.5 - Residual stress as function of *CoCrCuFeNi* film (deposited on Kapton® thickness, determined by x-ray diffraction.

7.2.2 Tensile tests with in-situ optical microscopy

The tensile tests were carried out using a 300 N Deben tensile machine combined with a Keyence confocal microscope. The tensile speed was 0.2 mm/min for samples 17 mm long. Therefore, the strain rate was about 2.10^{-4} s^{-1} for each sample. The **Figure 7.6 - Figure 7.10** show the experimental results for the 20 nm, 45 nm, 80 nm, 155 nm and 390 nm thick films, respectively. A few images have been selected in order to show the fragmentation and buckling phenomena during tensile tests. The following **Figure 7.6- Figure 7.10** show the evolution of the surface of the samples as a function of the strain applied to the system. The scale is obviously different because the spacing between the cracks tends to follow a scaling law (dependence on the thickness of the thin film).

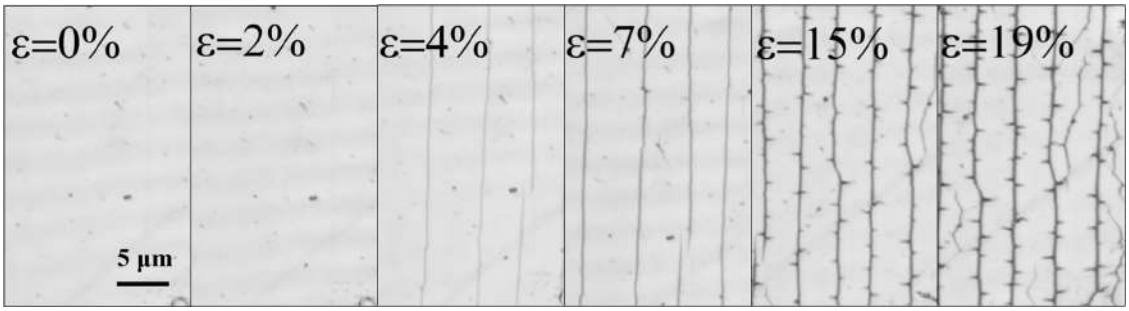

Figure 7.6 - Surface of the sample captured by confocal microscopy for different applied strains for the 20 nm thick film

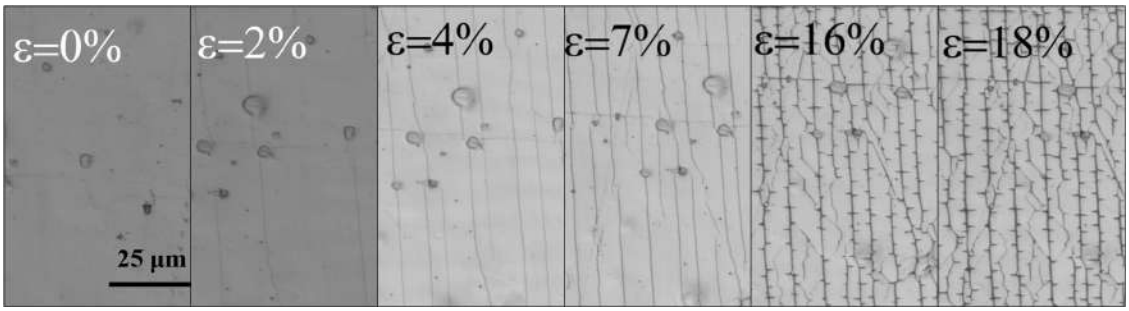

Figure 7.7 - Surface of the sample captured by confocal microscopy for different applied strains for the 45 nm thick film

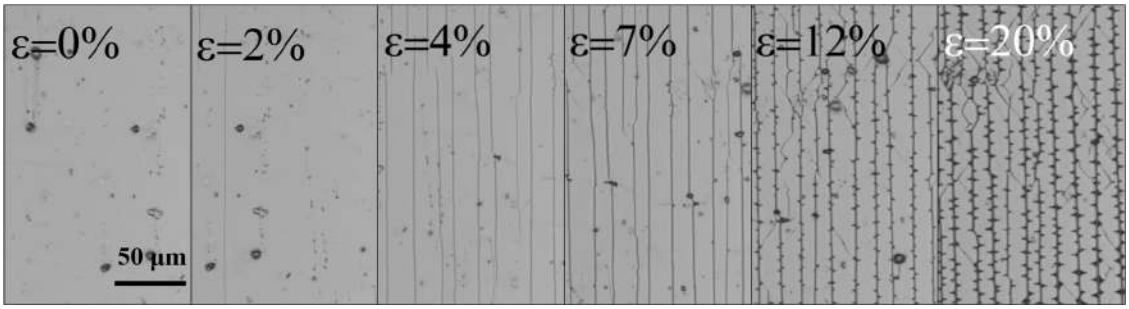

Figure 7.8 - Surface of the sample captured by confocal microscopy for different applied strains for the 80 nm thick film

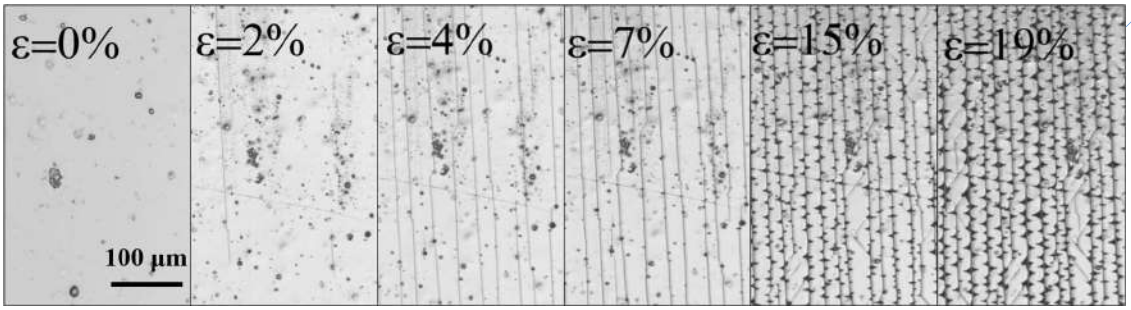

Figure 7.9 - Surface of the sample captured by confocal microscopy for different applied strains for the 155 nm thick film

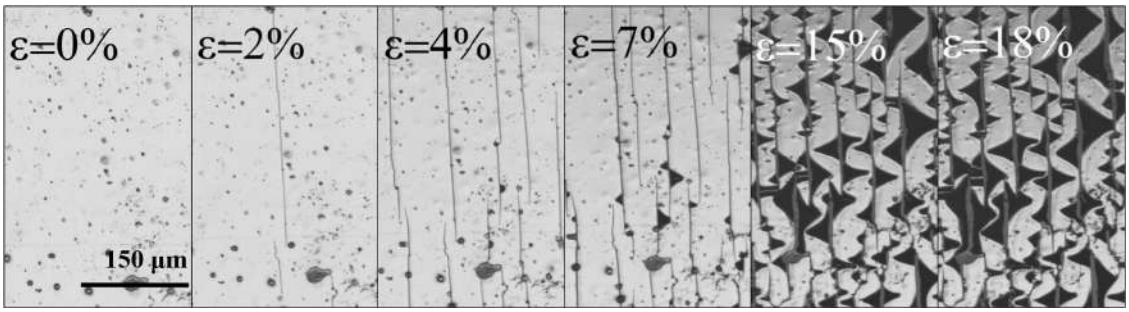

Figure 7.10 - Surface of the sample captured by confocal microscopy for different applied strains for the 390 nm thick film

Overall, for the 5 thicknesses, there are similarities of behavior, with initiation of cracks around $\varepsilon = 2\%$ and appearance of blisters between $\varepsilon = 6\%$ and $\varepsilon = 13\%$. The cracks are generally straight (especially the first ones), which is the signature of brittle materials. However, it should be noted here that a few curved cracks appear after the buckling initiation. This is not yet well understood in the community, but it should come from the complex stress fields induced by the presence of first cracks and buckles forming at the edges free-surface. This is particularly pregnant in **Figure 7.8** and **Figure 7.9**. It should also be noted that a number of initial defects (related to imperfections of the Kapton® substrate) can tend to locally influence the linearity of the cracks.

7.2.3 Quantitative analysis and discussion

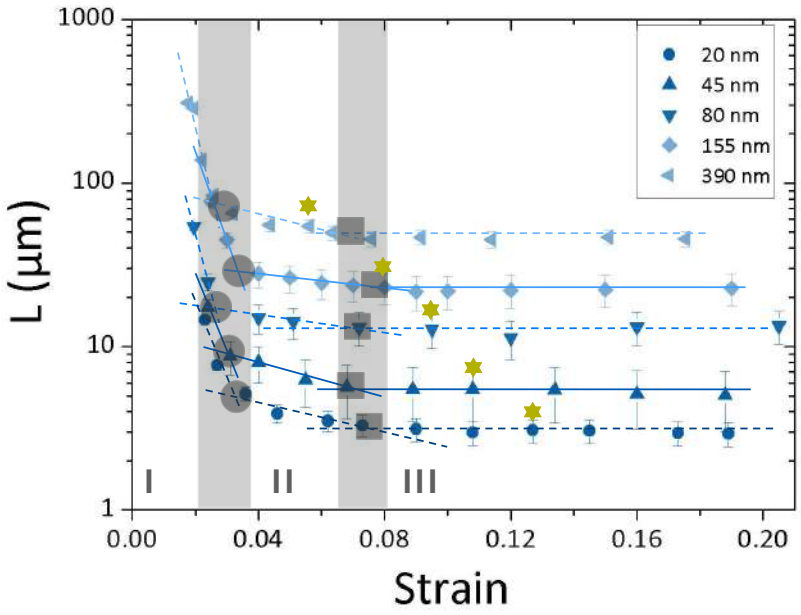

Figure 7.11 - Mean fragment length as function of external strain for the 5 thicknesses

In this part, we will give quantitative information from the images obtained by confocal microscopy. In a first part, we will use the evolution of the mean fragment length with the deformation to deduce fracture toughness values as a function of the thickness. Then in a second part, buckling initiation strain will be used to estimate the adhesion energy between *CoCrCuFeNi* films and Kapton® substrate.

The **Figure 7.11** shows the fragment length as a function of the deformation applied for each film thickness. This was determined by performing a statistic on all the images (average over 10 lines per image over the entire available field (larger than in **Figure 7.6** to **Figure 7.10**)). Furthermore, **Figure 7.11** also shows the strain value for which initiation of thin film buckling occurs (yellow stars on the graph). We find the 3 regimes as expected.

This behavior is very well described for each of the thicknesses and will allow estimating the toughness of each thin film vs. their thickness. Moreover, we see a clear evolution of the buckling strain depending on the thickness, which will allow us to determine the delamination mechanism as well as estimate the film/substrate adhesion energy.

7.2.3.1 Fracture behaviour

Figure 7.12 shows the evolution of stress transfer length as a function of the thickness. This is determined either from the fragment length *Lc* between regimes I and II [306], or from the threshold fragment length *Ls* in regime III [309].

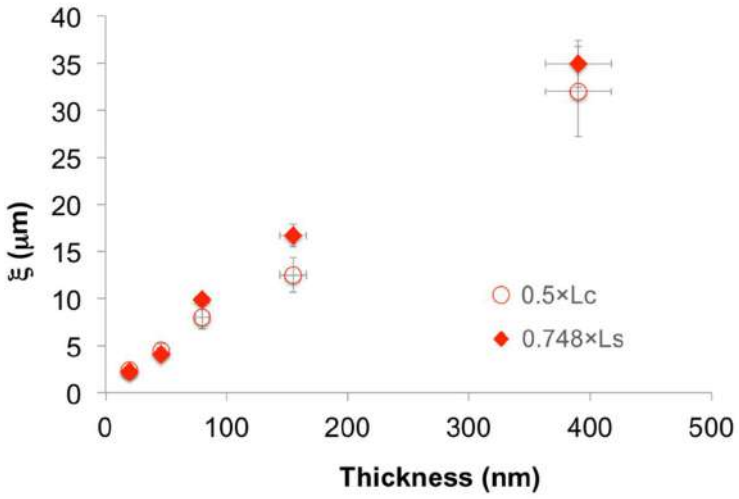

Figure 7.12 - Stress transfer length ξ as function of film thickness determined from *Lc* (fragment length at frontier between regimes I and II) and *Ls* (saturating fragment length in regime III)

We see that the two curves showing the evolution of ξ with thickness are similar and nearly superposed, which is reassuring on the quality of the experiments and the subsequent treatment. However, values derived from the saturating value *Ls* will subsequently be kept because the uncertainty on its determination is lower (because of the

number of points in the regime III and the difficulty in determining the exact boundary between the regimes I and II). It may be noted that the value of ξ varies from approximately 2 to 35 μm, which is small compared to the initial transversal length of the thin film (2 mm) but is obviously close to the fragment length when approaching the regime II.

From the values of ξ, L, applied strains ε and residual stresses σ_{res}, equations **7.3**, **7.4**, and **7.5** can be used to estimate the energy release rate G and then deduce fracture toughness K_{IC}. The elastic constants have been taken from ab-initio calculations and subsequent average over all grains assuming a non-textured thin film (found experimentally by x-ray diffraction). Thus, these values were found to be E_f = 164 GPa and ν_f = 0.325.

The Beuth model, by applying **eq. 7.3**, is a very direct method. The fracture stress along the tensile direction $\sigma_{x,0}$ has been determined from the fracture strain by applying Hooke's law, and from to the residual stress value ($\sigma_{x,0} \approx E_f \varepsilon_{fracture} + \sigma_{res}$). On the other hand, using the models of Xia & Hutchinson (**eq. 7.4**) and Franck (**eq. 7.5**), it is possible to determine K_{IC} for each applied strain. However, we have limited this analysis to the strain domain before buckling which would affect strongly this kind of analysis because the stress state in the thin film is no longer representative. This analysis has led to **Figure 7.13** and **Figure 7.14** respectively.

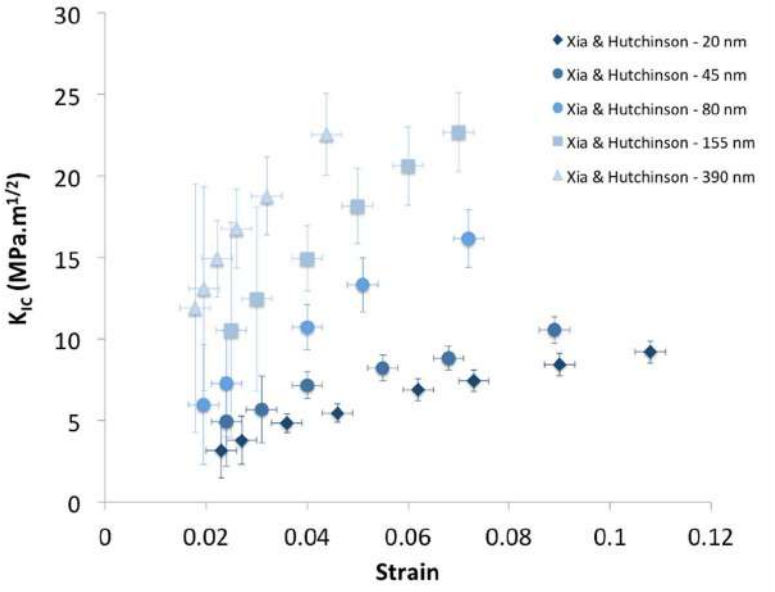

Figure 7.13 - K_{IC} as function of strain using Xia & Hutchinson model for each thickness.

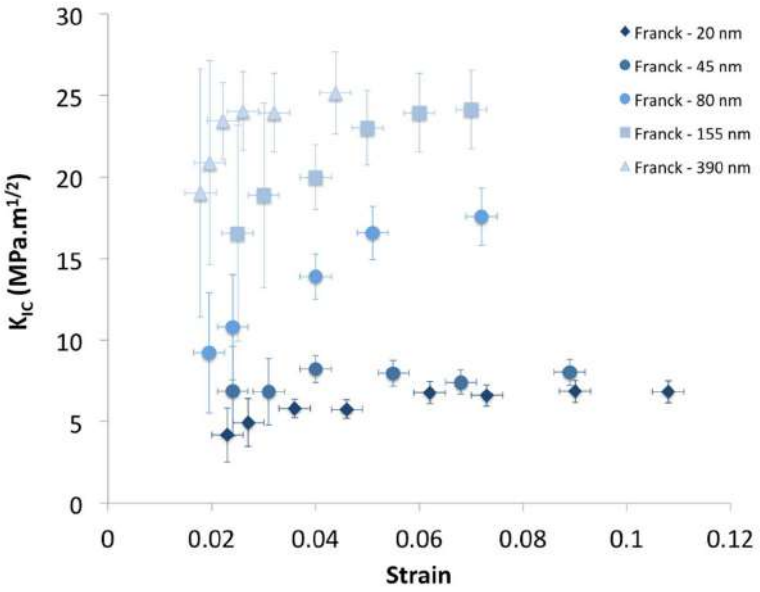

Figure 7.14 - K_{IC} as function of strain using Franck model for each thickness.

Figure 7.13 and **Figure 7.14** are very similar. They show that the toughness determined by these models is not constant with the thickness. This effect has been reported

previously [299, 304, 306] and finds its explanation in the approximations of the models: the uncertainty on **L** is quite large at the beginning of the fragmentation, the initiation of the first cracks is made to pronounced defects which is not taken into account in the models, the plasticity of the substrate is not taken into account (beyond ε = 3%) [305] and its apparent Poisson's ratio can vary during the test. Besides, we can note that the 2D Franck model makes appearing a plateau for few thicknesses once the regime II is attained (generally attributed to the actual film fracture toughness in the literature), suggesting that taking into account of transverse stress in the fragments makes more consistent the analysis (as compared to 1D Xia & Hutchinson one). Moreover, this analysis shows a significant evolution of K_{IC} with the thickness.

In order to highlight this trend, we have made an average over the data for each thickness (for Franck, Xia & Hutchinson and Beuth model). The results are shown in **Figure 7.15**. Overall, the results show an increase in K_{IC} with thickness, regardless of the performed analysis. This increase is very marked at the small thickness whereas the difference between 155 nm and 390 nm thick films is much less. This evolution can be attributed to the effects of thickness and grain size (which generally increases with thickness). Indeed, a small thickness and a high proportion of grain boundaries are generally not compatible with high toughness. Thus, this alloy whose elastic constants calculations show that it is not very ductile as compared to other FCC high entropy alloys, tends to be further weakened by its thin film microstructure (nano-sized thickness and grains).

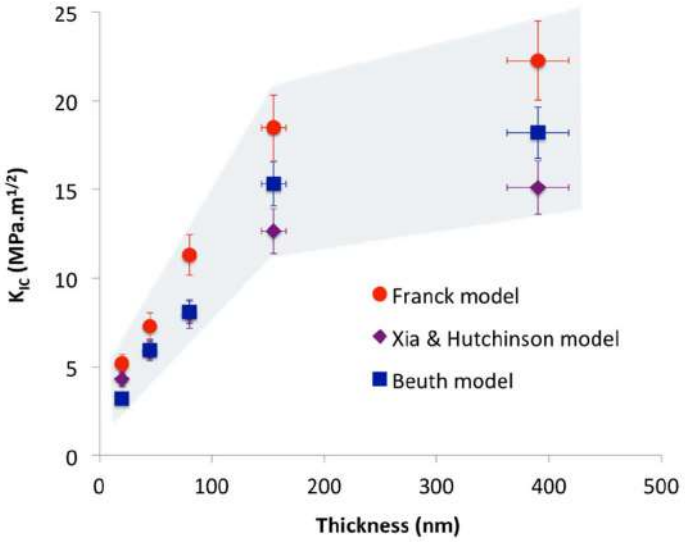

Figure 7.15 - K_{IC} as function of thickness, estimated from Franck, Xia& Hutchinson and Beuth model.

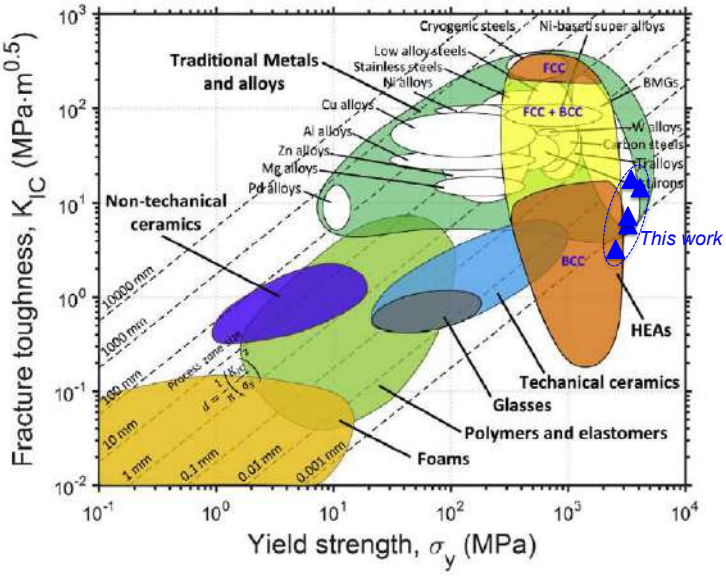

Figure 7.16 - Ashby plot of fracture toughness versus yield strength of HEAs along with traditional metals/alloys and other material classes [20]. Blue triangles show our results.

This is illustrated by **Figure 7.16** that shows a Ashby plot of K_{IC} as function of yield strength for several class of (*bulk*) materials [314]. Our results are closer to *bulk BCC*

HEA or some metallic glasses than *bulk FCC* HEA. Although only a few studies on fracture toughness of HEA thin films exist [315, 316], they until now show a brittleness less encountered for their bulk counterpart.

7.2.3.2 Buckling behavior

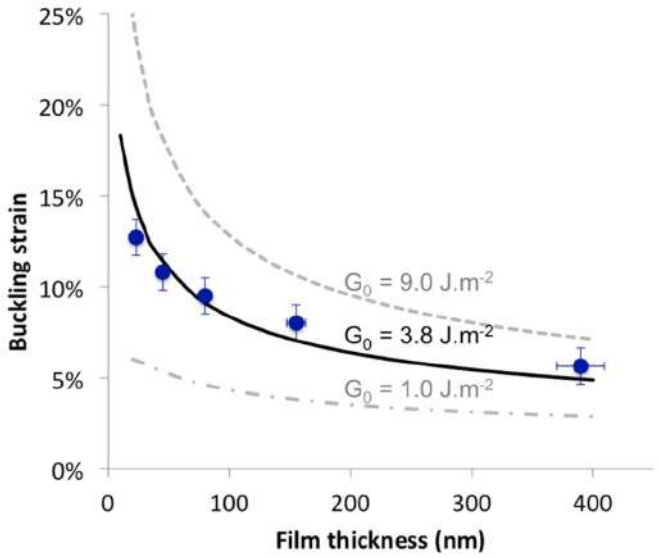

Figure 7.17 - Buckling strain as function of film thickness. Symbols are experimental data and each line is a model plot (eq. 7.7) with a given value of adhesion energy G_0.

The last paragraph of this chapter deals with the buckling behavior of thin films. This can be related to the adhesion properties between the alloy and the Kapton® substrate. It is not an intrinsic quantity of the alloy, but it can be important if these high entropy alloy systems, in particular magnetic, find an interest for the flexible magneto-electronics. First, from the experiments, we plotted the buckling strain as a function of thickness in order to verify the trend that this system follows (**Figure 7.17**). This curve shows a decrease in inverse of the root of the thickness, as is expected for strain energy delamination.

Following the **eq. 7.7**, the sole unknown is the adhesion energy G_0; all the other parameters are determined experimentally or a known from ab-initio calculations (elastic constants and moduli). Therefore, by fitting the experimental data, it is possible to determine G_0. The best fit allows obtaining adhesion energy of 3.8 J.m^{-2}. Fits for higher (G_0 = 9 J.m^{-2}) and lower (G_0 = 1 J.m^{-2}) values are also shown in the figure; these show the strong sensitivity of the model to the energy of adhesion. This value is very comparable to the other metal/polymer systems encountered in the literature, as shown in **Table 7.1**. If the brittleness of these thin films is potentially an obstacle for the uses in flexible electronics, this energy of adhesion is on the contrary very encouraging for this kind of application.

Table 7.1 - Adhesion energy for several metal/polymer systems found in literature

Film	Substrate	G_0 (J.m^{-2})
Ni	Polycarbonate	6.3 [317]
Pd	Polycarbonate	1.0 [318]
Nb	Polycarbonate	1.0 [319]
Cr	Kapton®	4.5 [320]
Au	Kapton®	1.0 [321]
Ti	Kapton®	4.7 [322]
Cu/Mo	Kapton®	2.8 [323]
Cu/Nb	Kapton®	1.1 [324]
Cu/Zr	Kapton®	1.2 [324]
Cu/Cr	Kapton®	5.0 [325]
Cu/Ta	Kapton®	4.1 [325]
CoFeB	Kapton®	5.4 [310]
CoCuCrNiFe (this work)	Kapton®	3.8

7.3 Summary and conclusions

To conclude this chapter, a complete study on the mechanical properties of *CoCrCuNiFe* thin films deposited on Kapton® was carried out. The elastic parameters and residual stresses made it possible to estimate the fracture behaviour of this alloy and its adhesion with the substrate. The analysis shows that the toughness of the alloy is rather weak compared to bulk HEA alloys of FCC structure, which can be explained for two reasons. First, the Pugh criterion (*G/B*) has shown that this alloy does not have a high ductility for a FCC crystal. Second, the specific nanocrystalline nature of PVD-deposited thin films should make the overall material more brittle than coarse-grained (micrometric) polycrystals. A typical example is nickel, which, although ductile in the bulk state, is generally brittle as a thin film (unlike gold which retains its ductile nature) [297].

Globally, toughness was found to increase with the thickness (from ≈ 2 $MPa.m^{1/2}$ to ≈ 20 $MPa.m^{1/2}$); this tends to show that this brittleness decreases by reducing the proportion of grain boundaries and the surface/volume ratio. Overall, all the thin films could however not be deformed without cracks appearing beyond 2% deformation. From an application point of view for this type of substrates used for flexible electronics, this value is a little too low to make this system a good potential candidate. On the other hand, the good adhesion value (about 3.8 $J.m^{-2}$) shows that this type of high entropy alloys can be deposited on Kapton® without any possible problem related to this property.

Subsequently, it would be interesting to find an alloy that can be naturally much more ductile, whose nanocrystalline character would be less damaging for this kind of applications. Several options are possible, *CoCrNi* alloy, for example, which is known to be extremely ductile as coarse-grained polycrystals, is very promising also in the form of thin films. In addition, the magnetic features of these alloys must be watched carefully.

Some studies on the alloys of this thesis are currently in process and show that their ferromagnetic and magnetostrictive properties could be exploitable. However, all the magnetic and magnetomechanical properties must be studied because they are so far very little known.

CONCLUSIONS AND PERSPECTIVES

The combination of BLS and PLU offers great opportunity to probe the elastic properties of thin films. However, there are still many issues to consider, e.g., the influence of vacancies as shown for epitaxial TaN and TiZrN thin films, the influence of porosity as shown for CoCrCuFeNi-Al and CoCrMnFeNi-N, and the influence of preferred or isotropic crystallographic orientations which we have always considered in this thesis. For a better comparison to DFT calculations, epitaxial thin films with well-defined microstructures and chemical composition, less porosity, are preferred to their polycrystalline counterparts. However this approach that we first thought to be the easiest one has revealed that defects have to be taken into account in our simulations. The more striking evidence being for simultaneously grew TaN/MgO cubic epitaxial films of (001), (110) and (111) orientations, we found stoichiometric by WDS chemical analysis. From the comparison of their PLU+BLS measured single crystal elastic constants to their VASP-SQS simulated ones of the defected crystal, we identified the presence of ~11 at. % Schottky defects in the TaN (001) films to explain the + 180 % and – 30 % values of c_{44} and c_{11}, compared to the defect-free material. This concentration corresponds remarkably to the minimum of calculated Schottky formation energy. Also, it is shown that the three orientations although grew at the same time, could not be considered as the same material, but have different defects concentration and elastic properties. The same observations and conclusions could be drawn for the ternary alloys $Ti_{1-x}Zr_xN$ epitaxial films but with much lower amplitude. Metal vacancies are more favorable at higher Zr concentrations.

One more trial to assess reliable experimental single crystal elastic constants to compare to DFT has been successfully achieved, but by measuring bulk and surface acoustic waves, within one large grain (~ 30 μm) with a simple orientation (001) of bulk CoCrCuFeNi HEA polycrystal. PLU demonstrated its high versatility and efficiency to generate and imaging acoustic wave propagation during several ns over a few tens of μm. It is offering nice opportunities in the future by combining characterizations of a unique large grain of bulk dense targets and those of epitaxial thin films materials, still in combination with DFT computational simulations of their properties.

To improve the accuracy of the elastic constants determination from these two optoacoustic techniques (PLU and BLS), two important parameters, namely thickness and mass density of thin films should be characterized with particular attention. On the other hand, DFT calculations are powerful and can always provide good references to experiments in respect of total energy, structure and elastic properties. This is extremely useful and inspiring especially when there are too many uncertainties from the experimental parts or when a computational driven design is employed. Although it is believed that the PVD process is nonequilibrium, DFT calculations can still predict the stable phase, structural and mechanical properties, e.g., in the magnetron sputtered thin films. In the field of high entropy alloys, although EMTO-CPA shows great advantages on its effectiveness, one should be aware of the consequence of ignoring atomic relaxation on elastic constants calculations. For materials with random features, whether it is the case of random (metals or nitrogen) vacancies in a crystal or random solutions as high entropy alloys, or the random nitrogen interstitials, SQS can provide admirable results comparable to experiments.

Regardless to the issues and successes we encountered in this work, several perspectives can be evoked:

(*i*) Porosity and oxide tissues forming at the grain boundaries commonly appear inside thin films and can affect many properties including elastic constants, thermal and electrical conductivity measured macroscopically. A quantitative description of the influence of porosity and core-shell structures on these properties for anisotropic materials is important not only for academy but also for industry. However, more sophisticated micromechanical models have to be employed [191] and hopefully can be complemented by accurate characterization of elastic as other physical properties and microstructures. If one wants to proceed to the identification of geometrical and physical properties of the core-shell structure, several properties could be investigated and numerical inverse method used for identification. (*ii*) In this thesis, we added other properties from supplementary experiments and attempted to couple elasticity to plasticity (buckle and cracks), magnetism (magnetization and magnetostriction) and thermal properties (heat capacity, thermal conductivity and diffusivity) of thin film materials. This work is tricky because other physics are involved as well as the modification of substrates. Careful characterizations must be done to exclude the influence of the substrates including residual stresses analysis. In all cases, it is meaningful and exciting to provide more insight in other physical properties just from the coupling and correlations to simple elastic constants. (*iii*) Nanoindentation is the most practical and widely used technique to determine thin film elastic and hardness properties as well as local mechanical properties in bulk materials. Thus, it is necessary to answer the question how the optoacoustic results compare or not to nanoindentation, especially for more porous materials and between different large grains

having different crystallographic orientation, where the two techniques may tend to provide very different values. (*iv*) The optoacoustic techniques are suitable for amorphous materials due to their highest symmetry, which make them promising to study metallic glasses. We found rather overall good agreement between our AIMD simulations of the HEA CoCrCuFeNi-(Nb_x, Al_x) amorphous phase encounter in this thesis. It is encouraging for further works dealing with bulk and thin film metallic glasses. (*v*) In developing hard materials supporting high external pressure, it is straightforward to couple the optoacoustic techniques to high hydrostatic pressure apparatus, such as diamond anvil cell. Effects of such high hydrostatic pressure on the mechanical and phase stability can thus be followed, again in combination with DFT simulations.

APPENDIX A. TANTALUM NITRIDE ORDERED STRUCTURES AND PROPERTIES

This appendix recalls how the ordered structures were obtained by the cluster expansion method and the design of supercells with different ordering of atoms and defects. There structural, elastic and dynamical properties are also provided for easier comparisons.

A.1 First principles calculations

A.1.1 Ordered phase and cluster expansion

Density functional theory (DFT) calculations of the energy, structure and elastic properties of mononitride *TaN* compounds with cubic *NaCl*-type ($Fm\bar{3}m$), *NbO*-type ($Pm\bar{3}m$) and tetragonal (*P4/nmm*) structures are reported in **Table A.1** and **Table A.2**. The particular case of the *NbO*-type structure simulates a cubic structure with 25 at. % Schottky defects (12.5 % *Ta* vacancy + 12.5 at. % *N* vacancy). The values computed by Hu *et al*. [58] for the tetragonal *P4/nmm(I) TaN* structure are also reported. The results of cluster expansion (CE) calculations using the UNCLE program [326], for several over- and under-stoichiometric ordered *TaN* compounds, are shown in **Figure A.1**. Their structural and elastic properties are summarized in **Table A.3**.

Table A.1 - The calculated formation energy per *TaN* unit, lattice parameters, volume per *TaN* unit, elastic constants, effective Voigt-Reuss-Hill isotropic bulk modulus (*B*), shear elastic modulus (*G*), Young's modulus (*E*), Poisson's ratio (*v*), and bulk/shear modulus ratio (*B/G*) of several mononitride *TaN* phases using the VASP code.

	NaCl- $Fm\bar{3}m$	*NbO-$Pm\bar{3}m$*	*P4/nmm(I)*	*P4/nmm*
E_{form}(eV/TaN)	–1.75(–1.71[a], –1.75[d], –1.76[e])	-1.453	(–1.84[a])	–1.86 (–1.92[a,d])
a(Å)	4.426(4.420[a], 4.414[d], 4.427[e])	4.252	(3.076[a])	2.999 (2.967[a], 2.966[d])
c(Å)			(4.575[a])	4.874 (5.119[a], 5.099[d])
V(Å^3)	21.68 (21.59[a], 21.5[d], 21.69[e])	25.63	(21.65[a])	21.93 (22.54[a], 22.43[d])
c_{11}(GPa)	731.0 (732.3[a], 706.97[b], 817[c])	419.6	(663.3[a])	578 (727.0[a])
c_{12}(GPa)	121.5 (131.2[a], 155.7[b], 112[c])	206.4	(106.9[a])	283 (158.1[a])
c_{13}(GPa)			(290.3[a])	223 (149.9[a])
c_{33}(GPa)			(253.7[a])	262 (351.0[a])
c_{44}(GPa)	49.7 (70.9[a], 208.2[b], 71[c])	49.4	(105.3[a])	120 (211.1[a])
c_{66}(GPa)			(44.0[a])	294 (104.8[a])
B(GPa)	324.6 (331.6[a], 347[b])	277.5	(324.0[a])	297 (285.8[a])
G(GPa)	113.2 (132.5[a], 144[b])	67.6	(134.8[a])	136 (160.2[a])
E(GPa)	304.2 (350.7[a], 380[b])	187.5	(355.2[a])	353 (404.9[a])
ν (*E/2G-1*)	0.343 (0.324[a], 0.32[b])	0.387	(0.317[a])	0.3017 (0.264[a])
B/G	2.868 (2.503[a], 2.41[b])	4.105	(2.403[a])	2.183 (1.784[a])

[a] Hu *et al*., [58], [b] Mota *et al*. [327], [c] Zhao *et al*. [328], [d] Kim *et al*. [59], [e] Koutná *et al*. [62].

Table A.2 - The lattice parameters, Wyckoff positions, internal coordinates, and *Ta-N* distance in the *Ta-N* octahedral of the cubic *δ-TaN* compound ($Fm\bar{3}m$) and its corresponding values in the tetragonal *TaN* phase with *P4/nmm* symmetry.

	$Fm\bar{3}m$	*P4/nmm*
a (Å)	4.426(4.420[a])	2.999 (2.967[a])
c (Å)		5.119
Ta	4a (0, 0, 0)	2c (0, 1/2, z), z=0.776(0.727[a])
N	4b (1/2, 1/2, 1/2)	2c (0, 1/2, z), z=0.319(0.165[a])
d(*Ta-N*) (Å)	2.213 (2.210[a][6[b]])	2.169 (2.169[a][4[b]]), 2.243 (2.242[a][1[b]]), 2.880 (2.877[a][1[b]])

[a] Hu *et al*. [58], [b] The number of *Ta-N* bonds with the given distance value around a *Ta* atom.

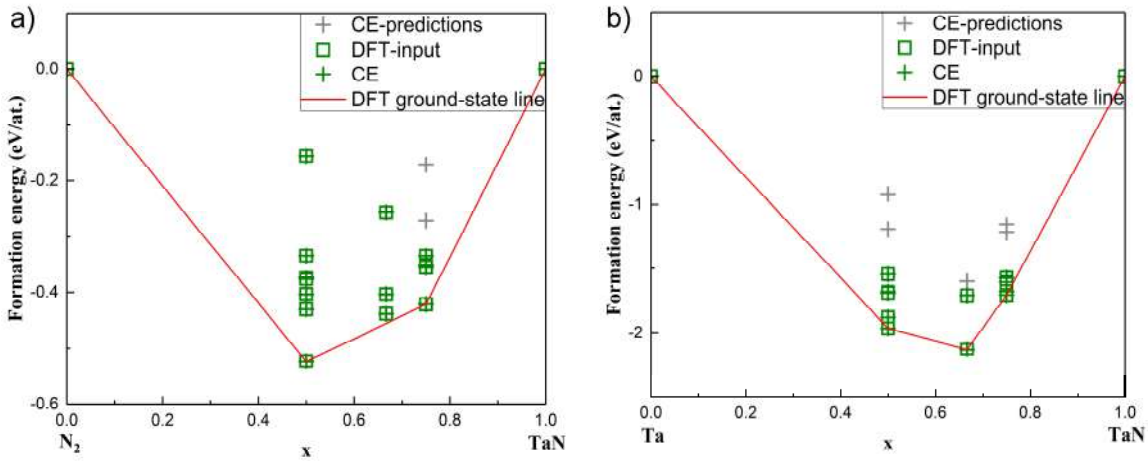

Figure A.1 - (a) Formation energy of over-stoichiometric Ta_xN $(x\leq1)$ and (b) under-stoichiometric TaN_x $(x\leq1)$ structures evaluated by the CE method. The red line is the ground state calculated by DFT. The superposition of the open green square and green cross symbols suggests a good fitting of CE parameters. The grey cross is the predicted energy of several randomly generated structures according to the fitted CE model. Note that the CE results are used to provide some additional configurations with ordering vacancies in this work, to compare to the results from disordered SQS.

Table A.3 - The calculated formation energy per atom, lattice parameters, volume per Ta_xN_y unit, elastic constants, effective Voigt-Reuss-Hill isotropic bulk modulus (B), shear elastic modulus (G), Young's modulus (E), Poisson's ratio (ν), and bulk/shear modulus ratio (B/G) of several non-stoichiometric ordered Ta_xN_y phases, identified from CE calculations.

	TaN	Ta_3N_4	Ta_2N_3	TaN_2	Ta_4N_3	Ta_2N
Space group	$Fm\bar{3}m$	*I4/mmm*	*Immm*	$I4\bar{1}/amd$	*I4/mmm*	$I4\bar{1}/amd$
Vac. conc. (*N* or *Ta*)	0/0	0.125 *(Ta)*	0.17 *(Ta)*	0.25 *(Ta)*	0.125 *(N)*	0.25 *(N)*
E_{form}(eV/atom)	-0.852	-1.066	-1.062	-0.384	-0.938	-0.840
a(Å)	4.419	4.291	9.777	4.031	4.404	4.421
b(Å)			4.036			
c(Å)		8.589	3.081	9.939	8.619	8.201
V(Å^3)	21.58	79.09	60.80	40.39	83.58	40.08
c_{11}(GPa)	686	679	341	424	660	490
c_{12}(GPa)	152.5	167	263	158	107.5	142.5
c_{13}(GPa)		101	127	135	151	194
c_{22}(GPa)			484			
c_{23}(GPa)			157			
c_{33}(GPa)		667	451	187	606	413
c_{44}(GPa)	59	148	126	70	106	123
c_{55}(GPa)			70			
c_{66}(GPa)		131	80	21	134	136
B(GPa)	330	307	263.3	210.1	305	272.6
G(GPa)	114	320.4	97.4	60.7	158.3	132.6
E(GPa)	304	860.5	259.5	164.5	404.5	342.2
ν	0.351	0.343	0.331	0.356	0.277	0.290
B/G	2.900	0.958	2.702	3.463	1.926	2.056

For Ta_2N_3 and TaN_2, the relaxed atomic arrangements show a similarity to the tetragonal *P4/nmm* phase which is also reflected on their elastic constants.

A.2 Design of SQS supercells and atoms coordinates in supercells used in this work

The design of SQS supercell by ATAT Monte Carlo method is explained in the main text. Supercells with "symmetric" configuration used in this work for DFT calculations: we considered ordered distribution of vacancies (denoted as "symmetric" configuration) by removing atoms with certain site symmetries from the 2×2×2 supercell. Hence, in the symmetric configurations, all the defected structures remain cubic. The vacancies in "symmetric" configurations are not randomly distributed as in SQS. They are created in a symmetric manner referring to the rotational symmetry in a cubic cell. The configurations are generated progressively by removing an atom from the 2×2×2 supercell by one of the following manners, (*i*) 1 cubic center atom (1 V), (*ii*) *i*+ 1 vertex of the cubic (2 V), (*iii*) 3 face centers (3 V), (*iv*) *i*+*iii* (4 V), (*v*) *i*+*ii*+*iii* (5 V), (*vi*) *iii*+ 3 edge centers (6 V), (*vii*) *vi*+*i* (7 V), (*vii*) *vi*+*ii* (8 V). Note that, the structure has still cubic symmetry (equal in 3 directions) after vacancies creation for each step.

In the case of cluster configurations, the vacancies are manually created by removing adjacent *Ta* or *N* atoms, respectively for clustered *Ta* or *N* vacancies. For example, a *N*(0) atom has 12 neighboring *N*(1-12) atoms, we first remove one *N*(0), then a neighboring *N*(1) of this first *N*(0), then a second neighboring *N*(2), ... The vacancies form a cluster in such a way. It is the same for *Ta* atoms.

For 'perfectly ordered' structures, they were found by CE method to have the lowest energies within the interested concentration range. Although they have higher symmetry comparing to SQS supercell, it is better to name them specifically such as "CE ground state

(ordered) structures", in order to distinguish from the symmetric one we generated by hands.

A.3 Dynamical mechanical stability

The phonon dispersion properties of $Fm\bar{3}m$ *TaN* and related structures were calculated by PHONONPY code [245] within the harmonic approximation, using density functional perturbation theory (DFPT) calculations implemented in VASP . For the cubic phases, the calculations were performed with a 4×4×4 supercell, while for the tetragonal phase, a 5×5×3 supercell was used, with each dimension of the supercells larger than 12 Å, in order to minimize the finite size effect. The 2×2×2 Monkhorst-Pack *k*-point mesh were applied to both cubic and tetragonal phases, respectively. An electronic energy convergence of 10^{-8} eV was adopted to ensure accurate force constant calculations.

The imaginary frequencies indicate dynamic instability for defect-free cubic *δ-TaN* (**Figure A.2**), while tetragonal *TaN* with *P4/nmm* structure is energetically favorable and dynamically stable (see **Figure A.3**). At low vacancy concentrations (< 2.5%, see **Figure 3.7**), the cubic structure is still energetically not favored and could easily transform to the more dynamically stable tetragonal phase after atomic relaxations, as predicted by Hu *et al*. [58]. However, for higher defect concentration, defected *δ-TaN* structures become energetically favorable, similarly to the ordered defected structures computed by the CE method. We further performed phonon calculations on Ta_3N_4 and Ta_4N_3 compounds ($Pm\bar{3}m$ symmetry) using "symmetric" supercell configurations, corresponding to 12.5% *Ta* and *N* vacancy concentration, respectively. The phonons calculations on these two phases (**Figure A.4** and **Figure A.5**) show that imaginary frequencies were not totally

vanished though but can be suppressed by introducing more vacancies. This suggests that vacancies, known as cubic *TaN* phase-stabilizer from energetics, can indeed stabilize the lattice dynamically as well.

δ-TaN $Fm\bar{3}m$

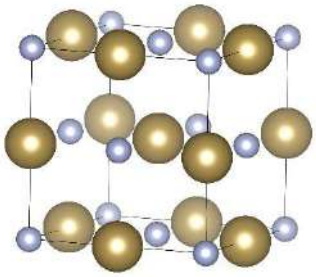

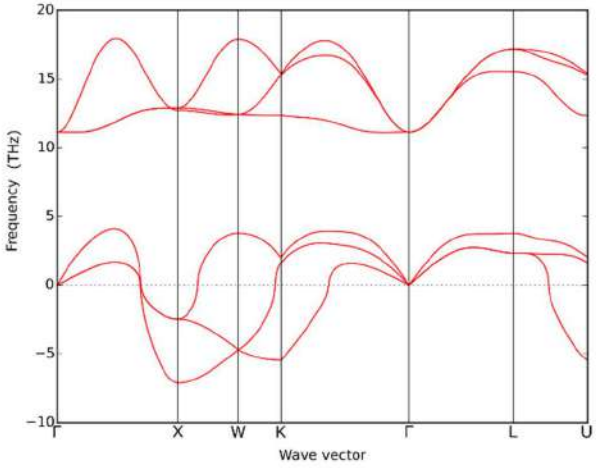

Figure A.2 - The phonon dispersion curves of *δ-TaN* (*$Fm\bar{3}m$* symmetry).

TaN P4/nmm

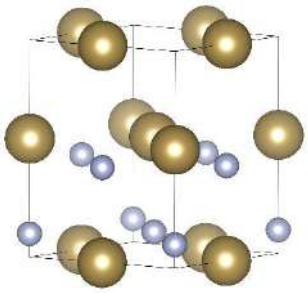

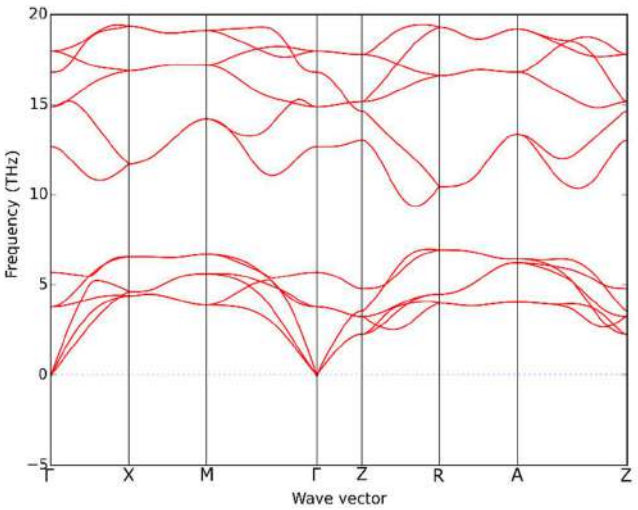

Figure A.3 - The phonon dispersion curves of tetragonal *TaN* with *P4/nmm* symmetry

Ta_3N_4 $Pm\bar{3}m$

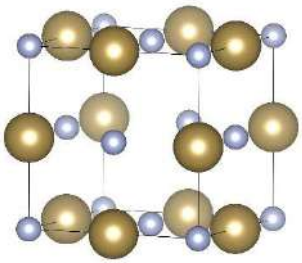

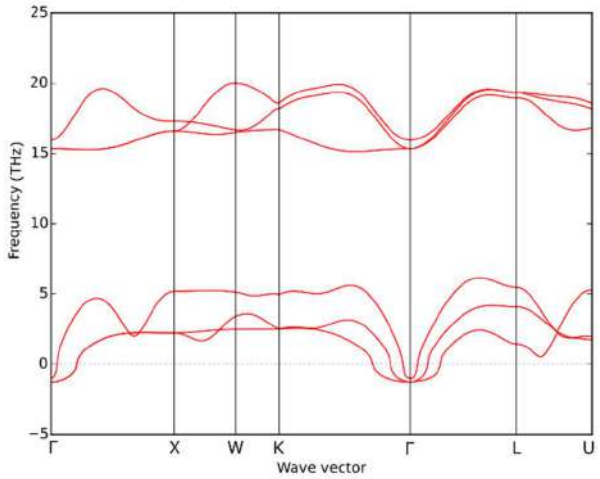

Figure A.4 - The phonon dispersion curves of Ta_3N_4 with $Pm\bar{3}m$ symmetry.

Ta_4N_3 $Pm\bar{3}m$

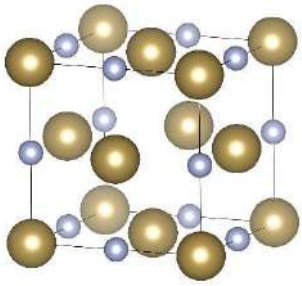

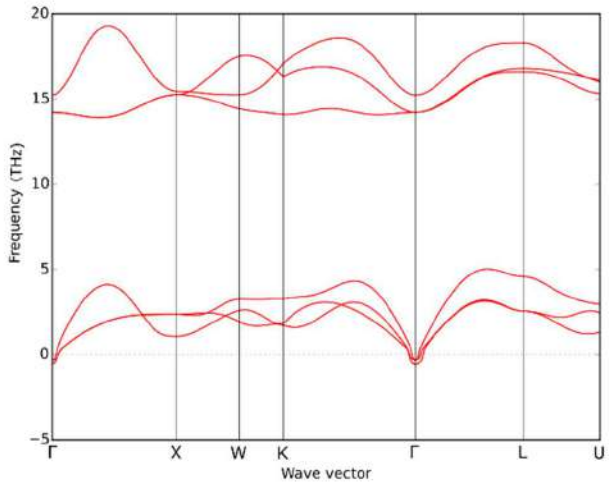

Figure A.5 - The phonon dispersion curves of Ta_4N_3 with $Pm\bar{3}m$ symmetry.

REFERENCES

1. Abadias, G., et al., *Structure, phase stability and elastic properties in the Ti1-xZrxN thin-film system: Experimental and computational studies.* Acta Materialia, 2012. **60**(15): p. 5601-5614.
2. Djemia, P., et al., *Structural and elastic properties of ternary metal nitrides TixTa1-xN alloys: First-principles calculations versus experiments.* Surface & Coatings Technology, 2013. **215**: p. 199-208.
3. Abadias, G., et al., *Electronic structure and mechanical properties of ternary ZrTaN alloys studied by ab initio calculations and thin-film growth experiments.* Physical Review B, 2014. **90**(14): p. 18.
4. Abadias, G., P. Djemia, and L. Belliard, *Alloying effects on the structure and elastic properties of hard coatings based on ternary transition metal (M = Ti, Zr or Ta) nitrides.* Surface & Coatings Technology, 2014. **257**: p. 129-137.
5. Braeckman, B.R., et al., *High entropy alloy thin films deposited by magnetron sputtering of powder targets.* Thin Solid Films, 2015. **580**: p. 71-76.
6. Braeckman, B.R. and D. Depla, *Structure formation and properties of sputter deposited Nb-x-CoCrCuFeNi high entropy alloy thin films.* Journal of Alloys and Compounds, 2015. **646**: p. 810-815.
7. Braeckman, B. *Sputter deposition of complex alloy thin films*. 2016, Universiteit Gent. p. 256.
8. Braeckman, B.R., et al., *Impurity-controlled film growth and elastic properties of CoCrCuFeNi thin films.* Surface & Coatings Technology, 2017. **315**: p. 475-483.
9. Braeckman, B.R., et al., *The nanostructure and mechanical properties of nanocomposite Nb-x-CoCrCuFeNi thin films.* Scripta Materialia, 2017. **139**: p. 155-158.
10. Dedoncker, R., et al., *Reactive sputter deposition of CoCrCuFeNi in nitrogen/argon mixtures.* Journal of Alloys and Compounds, 2018. **769**: p. 881-888.
11. Dedoncker, R., et al., *Reactive sputter deposition of CoCrCuFeNi in oxygen/argon mixtures.* Surface and Coatings Technology, 2019: p. 124362.
12. Kresse, G. and J. Furthmüller, *Efficiency of ab-initio total energy calculations for metals and semiconductors using a plane-wave basis set.* Computational Materials Science, 1996. **6**(1): p. 15-50.

13. Kresse, G. and J. Furthmuller, *Efficient iterative schemes for ab initio total-energy calculations using a plane-wave basis set.* Physical Review B, 1996. **54**(16): p. 11169-11186.

14. Vitos, L., *Total-energy method based on the exact muffin-tin orbitals theory.* Physical Review B, 2001. **64**(1): p. 11.

15. **Vitos** , L., *Computational Quantum Mechanics for Materials Engineers*

The EMTO Method and Applications. Engineering Materials and Processes. 2007: Springer-Verlag London. XII, 237.

16. Van de Walle, A., et al., *Efficient stochastic generation of special quasirandom structures.* Calphad-Computer Coupling of Phase Diagrams and Thermochemistry, 2013. **42**: p. 13-18.

17. Soven, P., *Coherent-potential model of substitutional disordered alloys.* Physical Review, 1967. **156**(3): p. 809-&.

18. Gyorffy, B.L., *Coherent-potential approximation for a "nonoverlapping-muffin-tin-potential model of random substitutional alloys.* Physical Review B, 1972. **5**(6): p. 2382-&.

19. Kao, S.W., et al., *A preliminary molecular dynamics simulation on equiatomic alloys with up to six elements.* Annales De Chimie-Science Des Materiaux, 2006. **31**(6): p. 657-668.

20. Music, D., R.W. Geyer, and J.M. Schneider, *Recent progress and new directions in density functional theory based design of hard coatings.* Surface & Coatings Technology, 2016. **286**: p. 178-190.

21. Shodja, H.M., M. Tabatabaei, and K. Esfarjani, *First principles molecular dynamics studies of elastic constants, ideal tensile strength, chemistry of crack initiation, and surface and cohesive energies in amorphous silicon.* Philosophical Magazine, 2014. **94**(25): p. 2913-2936.

22. Huhn, W.P., et al., *First-principles calculation of elastic moduli of early-late transition metal alloys.* Physical Review B, 2014. **89**(10).

23. Chen, X.-Q., et al., *Modeling hardness of polycrystalline materials and bulk metallic glasses.* Intermetallics, 2011. **19**(9): p. 1275-1281.

24. Pugh, S.F., *Relations between the elastic moduli and the plastic properties of polycrystalline pure metals.* Philosophical Magazine, 1954. **45**(367): p. 823-843.

25. Pettifor, D.G., *Theoretical predictions of structure and related properties of intermetallics.* Materials Science and Technology, 1992. **8**(4): p. 345-349.

26. Hill, R., *The Elastic Behaviour of a Crystalline Aggregate.* Proceedings of the Physical Society. Section A, 1952. **65**(5): p. 349-354.

27. Li, J.Y., *On micromechanics approximation for the effective thermoelastic moduli of multi-phase composite materials.* Mechanics of Materials, 1999. **31**(2): p. 149-159.

28. Lind, H., et al., *Improving thermal stability of hard coating films via a concept of multicomponent alloying.* Applied Physics Letters, 2011. **99**(9): p. 3.

29. Daniel, R., et al., *Size effect of thermal expansion and thermal/intrinsic stresses in nanostructured thin films: Experiment and model.* Acta Materialia, 2011. **59**(17): p. 6631-6645.

30. Holec, D., et al., *Phase stability and alloy-related trends in Ti-Al-N, Zr-Al-N and Hf-Al-N systems from first principles.* Surface & Coatings Technology, 2011. **206**(7): p. 1698-1704.

31. Kindlund, H., et al., *A review of the intrinsic ductility and toughness of hard transition-metal nitride alloy thin films.* Thin Solid Films, 2019. **688**: p. 11.

32. Abrikosov, I.A., et al., *Phase Stability and Elasticity of TiAlN.* Materials, 2011. **4**(9): p. 1599-1618.

33. Horling, A., et al., *Mechanical properties and machining performance of Ti1-xAlxN-coated cutting tools.* Surface & Coatings Technology, 2005. **191**(2-3): p. 384-392.

34. Knutsson, A., et al., *Machining performance and decomposition of TiAlN/TiN multilayer coated metal cutting inserts.* Surface & Coatings Technology, 2011. **205**(16): p. 4005-4010.

35. Holec, D., et al., *Trends in the elastic response of binary early transition metal nitrides.* Physical Review B, 2012. **85**(6).

36. Sangiovanni, D.G., L. Hultman, and V. Chirita, *Supertoughening in B1 transition metal nitride alloys by increased valence electron concentration.* Acta Materialia, 2011. **59**(5): p. 2121-2134.

37. Kindlund, H., et al., *Effect of WN content on toughness enhancement in V1-xWxN/MgO(001) thin films.* Journal of Vacuum Science & Technology A, 2014. **32**(3).

38. Kindlund, H., et al., *V0.5Mo0.5Nx/MgO(001): Composition, nanostructure, and mechanical properties as a function of film growth temperature.* Acta Materialia, 2017. **126**: p. 194-201.

39. Sangiovanni, D.G., *Inherent toughness and fracture mechanisms of refractory transition-metal nitrides via density-functional molecular dynamics.* Acta Materialia, 2018. **151**: p. 11-20.

40. Sangiovanni, D.G., et al., *Effects of phase stability, lattice ordering, and electron density on plastic deformation in cubic TiWN pseudobinary transition-metal nitride alloys.* Acta Materialia, 2016. **103**: p. 823-835.

41. Kindlund, H., et al., *Vacancy-induced toughening in hard single-crystal V0.5Mo0.5Nx/MgO(001) thin films.* Acta Materialia, 2014. **77**: p. 394-400.

42. Zhou, L., D. Holec, and P.H. Mayrhofer, *Ab initio study of the alloying effect of transition metals on structure, stability and ductility of CrN.* Journal of Physics D-Applied Physics, 2013. **46**(36).

43. Holec, D., et al., *Alloying-related trends from first principles: An application to the Ti-Al-X-N system.* Journal of Applied Physics, 2013. **113**(11).

44. Petrman, V. and J. Houska, *Trends in formation energies and elastic moduli of ternary and quaternary transition metal nitrides.* Journal of Materials Science, 2013. **48**(21): p. 7642-7651.

45. Abadias, G., et al., *Electronic structure and mechanical properties of ternary ZrTaN alloys studied by ab initio calculations and thin-film growth experiments.* Physical Review B, 2014. **90**(14).

46. Wang, F., et al., *Systematic ab initio investigation of the elastic modulus in quaternary transition metal nitride alloys and their coherent multilayers.* Acta Materialia, 2017. **127**: p. 124-132.

47. Klimashin, F.F. and P.H. Mayrhofer, *Ab initio-guided development of super-hard Mo-Al-Cr-N coatings.* Scripta Materialia, 2017. **140**: p. 27-30.

48. Zhou, L., et al., *Structural and mechanical properties of nitrogen-deficient cubic Cr-Mo-N and Cr-W-N systems.* Scripta Materialia, 2016. **123**: p. 34-37.

49. Buchinger, J., et al., *Toughness enhancement in TiN/WN superlattice thin films.* Acta Materialia, 2019. **172**: p. 18-29.

50. Rehak, P., M. Cerny, and D. Holec, *Interface-induced electronic structure toughening of nitride superlattices.* Surface & Coatings Technology, 2017. **325**: p. 410-416.

51. Balasubramanian, K., S.V. Khare, and D. Gall, *Valence electron concentration as an indicator for mechanical properties in rocksalt structure nitrides, carbides and carbonitrides.* Acta Materialia, 2018. **152**: p. 175-185.

52. Kindlund, H., et al., *Toughness enhancement in hard ceramic thin films by alloy design.* Apl Materials, 2013. **1**(4).

53. Shin, C.S., et al., *Epitaxial growth of metastable delta-TaN layers on MgO(001) using low-energy, high-flux ion irradiation during ultrahigh vacuum reactive magnetron sputtering.* Journal of Vacuum Science & Technology A, 2002. **20**(6): p. 2007-2017.

54. Mei, A.B., et al., *Physical properties of epitaxial ZrN/MgO(001) layers grown by reactive magnetron sputtering.* Journal of Vacuum Science & Technology A, 2013. **31**(6).

55. Mei, A.B., et al., *Elastic constants, Poisson ratios, and the elastic anisotropy of VN(001), (011), and (111) epitaxial layers grown by reactive magnetron sputter deposition.* Journal of Applied Physics, 2014. **115**(21): p. 8.

56. Weinberger, C.R., et al., *Ab initio investigations of the phase stability in group IVB and VB transition metal nitrides.* Computational Materials Science, 2017. **138**: p. 333-345.

57. Shin, C.S., et al., *Phase composition and microstructure of polycrystalline and epitaxial TaNx layers grown on oxidized Si(001) and MgO(001) by reactive magnetron sputter deposition.* Thin Solid Films, 2002. **402**(1–2): p. 172-182.

58. Hu, S., et al., *The stabilization of the rocksalt structured tantalum nitride.* Journal of Applied Physics, 2017. **122**(4): p. 6.

59. Kim, T.E., et al., *Phase stability and electronic structures of stoichiometric tantalum mononitrides.* Computational Materials Science, 2008. **44**(2): p. 577-580.

60. Christensen, A.N. and B. Lebech, *Reinvestigation of structure of epsilon-tantalum nitride.* Acta Crystallographica Section B-Structural Science, 1978. **34**(JAN): p. 261-263.

61. Tsvyashchenko, A.V., S.V. Popova, and E.S. Alekseev, *Band-structure of hexagonal tantalum nitride.* Physica Status Solidi B-Basic Research, 1980. **100**(1): p. 99-102.

62. Koutna, N., et al., *Point defects stabilise cubic Mo-N and Ta-N.* Journal of Physics D-Applied Physics, 2016. **49**(37): p. 8.

63. Koutna, N., et al., *Stability and elasticity of metastable solid solutions and superlattices in the MoN-TaN system: First-principles calculations.* Materials & Design, 2018. **144**: p. 310-322.

64. Balasubramanian, K., S.V. Khare, and D. Gall, *Energetics of point defects in rocksalt structure transition metal nitrides: Thermodynamic reasons for deviations from stoichiometry.* Acta Materialia, 2018. **159**: p. 77-88.

65. Freysoldt, C., et al., *First-principles calculations for point defects in solids.* Reviews of Modern Physics, 2014. **86**(1): p. 53.

66. Tasnadi, F., et al., *Non-equilibrium vacancy formation energies in metastable alloys - A case study of Ti0.5Al0.5N.* Materials & Design, 2017. **114**: p. 484-493.

67. Tasnadi, F., M. Oden, and I.A. Abrikosov, *Ab initio elastic tensor of cubic Ti0.5Al0.5N alloys: Dependence of elastic constants on size and shape of the supercell model and their convergence.* Physical Review B, 2012. **85**(14): p. 9.

68. Holec, D., et al., *Macroscopic elastic properties of textured ZrN-AlN polycrystalline aggregates: From ab initio calculations to grainscale interactions.* Physical Review B, 2014. **90**(18): p. 9.

69. Zhang, K., et al., *Growth and mechanical properties of epitaxial NbN(001) films on MgO(001).* Surface & Coatings Technology, 2016. **288**: p. 105-114.

70. Balasubramanian, K., S. Khare, and D. Gall, *Vacancy-induced mechanical stabilization of cubic tungsten nitride.* Physical Review B, 2016. **94**(17).

71. Ozsdolay, B.D., et al., *Elastic constants of epitaxial cubic MoNx (001) layers.* Surface & Coatings Technology, 2017. **325**: p. 572-578.

72. Abadias, G., et al., *Electronic structure and mechanical properties of ternary ZrTaN alloys studied by ab initio calculations and thin-film growth experiments.* Physical Review B, 2014. **90**(14): p. 144107.

73. Ozsdolay, B.D., et al., *Epitaxial growth and properties of cubic WN on MgO(001), MgO(111), and Al2O3(0001).* Thin Solid Films, 2015. **590**: p. 276-283.

74. Shin, C.S., et al., *Epitaxial NaCl structure delta-TaNx(001): Electronic transport properties, elastic modulus, and hardness versus N/Ta ratio.* Journal of Applied Physics, 2001. **90**(6): p. 2879-2885.

75. Gall, D., et al., *Growth of single-crystal CrN on MgO(001): Effects of low-energy ion-irradiation on surface morphological evolution and physical properties.* Journal of Applied Physics, 2002. **91**(6): p. 3589-3597.

76. Shin, C.S., et al., *Vacancy hardening in single-crystal TiNx(001) layers.* Journal of Applied Physics, 2003. **93**(10): p. 6025-6028.

77. Kim, J.O., et al., *Elastic-constants of single-crystal transition-metal nitride films measured by line-focus acoustic microscopy.* Journal of Applied Physics, 1992. **72**(5): p. 1805-1811.

78. Mayrhofer, P.H., et al., *Microstructural design of hard coatings.* Progress in Materials Science, 2006. **51**(8): p. 1032-1114.

79. Johnson, L.J.S., et al., *Spinodal decomposition of Ti0.33Al0.67N thin films studied by atom probe tomography.* Thin Solid Films, 2012. **520**(13): p. 4362-4368.

80. Rogstrom, L., et al., *Strain evolution during spinodal decomposition of TiAlN thin films.* Thin Solid Films, 2012. **520**(17): p. 5542-5549.

81. Gronhagen, K., J. Agren, and M. Oden, *Phase-field modelling of spinodal decomposition in TiAlN including the effect of metal vacancies.* Scripta Materialia, 2015. **95**: p. 42-45.

82. Tasnadi, F., et al., *Significant elastic anisotropy in Ti1-xAlxN alloys.* Applied Physics Letters, 2010. **97**(23): p. 3.

83. Steneteg, P., et al., *Temperature dependence of TiN elastic constants from ab initio molecular dynamics simulations.* Physical Review B, 2013. **87**(9): p. 7.

84. Shulumba, N., et al., *Temperature-dependent elastic properties of Ti1-xAlxN alloys.* Applied Physics Letters, 2015. **107**(23): p. 4.

85. Tang, Z., et al., *Aluminum Alloying Effects on Lattice Types, Microstructures, and Mechanical Behavior of High-Entropy Alloys Systems.* Jom, 2013. **65**(12): p. 1848-1858.

86. Churyumov, A.Y., A.V. Pozdniakov, and A.I.e.a. Bazlov, *Effect of Nb Addition on Microstructure and Thermal and Mechanical Properties of Fe-Co-Ni-Cu-Cr*

Multiprincipal-Element (High-Entropy) Alloys in As-Cast and Heat-Treated State. JOM, 2019: p. 1–9.

87. Moravcik, I., et al., *Nitrogen Interstitial Alloying of CoCrFeMnNi High Entropy Alloy through Reactive Powder Milling.* Entropy, 2019. **21**(4).

88. Cheng, C.Y., et al., *Physical metallurgy of concentrated solid solutions from low-entropy to high-entropy alloys.* Current Opinion in Solid State & Materials Science, 2017. **21**(6): p. 299-311.

89. Yeh, J.W., *Physical Metallurgy of High-Entropy Alloys.* Jom, 2015. **67**(10): p. 2254-2261.

90. Reed-Hill, R.E. and R. Abbaschian, *Physical Metallurgy Principles*. 1994, Boston, MA: PWS Publishing Company.

91. Cahn, R.W. and P. Haasen, *Physical Metallurgy*. 1983, New York: Elsevier Science Publishers.

92. Zhang, Y., et al., *Microstructures and properties of high-entropy alloys.* Progress in Materials Science, 2014. **61**: p. 1-93.

93. Yeh, J.W., *Recent progress in high-entropy alloys.* Annales De Chimie-Science Des Materiaux, 2006. **31**(6): p. 633-648.

94. Zhang, Y., et al., *Minor alloying behavior in bulk metallic glasses and high-entropy alloys.* Science in China Series G-Physics Mechanics & Astronomy, 2008. **51**(4): p. 427-437.

95. Zhang, Y., et al., *Solid-Solution Phase Formation Rules for Multi-component Alloys.* Advanced Engineering Materials, 2008. **10**(6): p. 534-538.

96. Yang, X. and Y. Zhang, *Prediction of high-entropy stabilized solid-solution in multi-component alloys.* Materials Chemistry and Physics, 2012. **132**(2–3): p. 233-238.

97. Gao, M.C., et al., *Thermodynamics of concentrated solid solution alloys.* Current Opinion in Solid State & Materials Science, 2017. **21**(5): p. 238-251.

98. Guo, S. and C.T. Liu, *Phase stability in high entropy alloys: Formation of solid-solution phase or amorphous phase.* Progress in Natural Science-Materials International, 2011. **21**(6): p. 433-446.

99. Yurchenko, N., N. Stepanov, and G. Salishchev, *Laves-phase formation criterion for high-entropy alloys.* Materials Science and Technology, 2017. **33**(1): p. 17-22.

100. Tsai, M.-H., et al., *Incorrect predictions of simple solid solution high entropy alloys: Cause and possible solution.* Scripta Materialia, 2017. **127**: p. 6-9.

101. Andreoli, A.F., et al., *The elastic-strain energy criterion of phase formation for complex concentrated alloys.* Materialia, 2019. **5**: p. 100222.

102. Kube, S.A., et al., *Phase selection motifs in High Entropy Alloys revealed through combinatorial methods: Large atomic size difference favors BCC over FCC.* Acta Materialia, 2019. **166**: p. 677-686.

103. Mizutani, U., *The hume-rothery rules for structurally complex alloy phases*, in *Surface Properties and Engineering of Complex Intermetallics*. 2010, WORLD SCIENTIFIC. p. 323-399.

104. Tsai, M.H., *Physical Properties of High Entropy Alloys.* Entropy, 2013. **15**(12): p. 5338-5345.

105. Zaddach, A.J., et al., *Structure and magnetic properties of a multi-principal element Ni-Fe-Cr-Co-Zn-Mn alloy.* Intermetallics, 2016. **68**: p. 107-112.

106. *John Mary S.*, et al., *high entropy alloys and*

corrosion resistance –a bird's eye view. Eur. Chem. Bull, 2014. **3**(12): p. 1031-1035.

107. Qiu, Z.K., et al., *Tribological behavior of CrCoNiAlTiY coating synthesized by double-glow plasma surface alloying technique.* Tribology International, 2015. **92**: p. 512-518.

108. Senkov, O.N., et al., *Refractory high-entropy alloys.* Intermetallics, 2010. **18**(9): p. 1758-1765.

109. Hsu, C.Y., et al., *On the superior hot hardness and softening resistance of AlCoCrxFeMo0.5Ni high-entropy alloys.* Materials Science and Engineering a-Structural Materials Properties Microstructure and Processing, 2011. **528**(10-11): p. 3581-3588.

110. Senkov, O.N., et al., *Microstructure and room temperature properties of a high-entropy TaNbHfZrTi alloy.* Journal of Alloys and Compounds, 2011. **509**(20): p. 6043-6048.

111. Dirras, G., et al., *Elastic and plastic properties of as-cast equimolar TiHfZrTaNb high-entropy alloy.* Materials Science and Engineering a-Structural Materials Properties Microstructure and Processing, 2016. **654**: p. 30-38.

112. Yao, L. and J.H. He, *Recent progress in antireflection and self-cleaning technology - From surface engineering to functional surfaces.* Progress in Materials Science, 2014. **61**: p. 94-143.

113. Gludovatz, B., et al., *A fracture-resistant high-entropy alloy for cryogenic applications.* Science, 2014. **345**(6201): p. 1153-1158.

114. Laplanche, G., et al., *Temperature dependencies of the elastic moduli and thermal expansion coefficient of an equiatomic, single-phase CoCrFeMnNi high-entropy alloy.* Journal of Alloys and Compounds, 2015. **623**: p. 348-353.

115. Niu, C., et al., *First principles exploration of near-equiatomic NiFeCrCo high entropy alloys.* Journal of Alloys and Compounds, 2016. **672**: p. 510-520.

116. Kresse, G. and J. Hafner, *Abinitio hellmann-feynman molecular-dynamics for liquid-metals.* Journal of Non-Crystalline Solids, 1993. **156**: p. 956-960.

117. Tian, F.Y., et al., *Calculating elastic constants in high-entropy alloys using the coherent potential approximation: Current issues and errors.* Computational Materials Science, 2016. **111**: p. 350-358.

118. Tian, F.Y., et al., *Ab initio investigation of high-entropy alloys of 3d elements.* Physical Review B, 2013. **87**(7): p. 8.

119. Wang, X.F., et al., *Novel microstructure and properties of multicomponent CoCrCuFeNiTix alloys.* Intermetallics, 2007. **15**(3): p. 357-362.

120. Wang, F.J., et al., *Tensile and compressive mechanical behavior of a CoCrCuFeNiAl0.5 high entropy alloy.* International Journal of Modern Physics B, 2009. **23**(6-7): p. 1254-1259.

121. Liao, M., et al., *Modeling of alloying effect on elastic properties in BCC Nb-Ti-V-Zr solid solution: From unary to quaternary.* Computational Materials Science, 2020. **172**: p. 109289.

122. Liu, Z.K., et al., *Computational modeling of effects of alloying elements on elastic coefficients.* Scripta Materialia, 2010. **63**(7): p. 686-691.

123. Song, S.X., et al., *Flow serration in a Zr-based bulk metallic glass in compression at low strain rates.* Intermetallics, 2008. **16**(6): p. 813-818.

124. Bulatov, V.V. and E. Kaxiras, *Semidiscrete variational Peierls framework for dislocation core properties.* Physical Review Letters, 1997. **78**(22): p. 4221-4224.

125. Lu, G., et al., *Hydrogen-enhanced local plasticity in aluminum: An ab initio study.* Physical Review Letters, 2001. **87**(9): p. art. no.-095501.

126. Huang, S., et al., *Temperature dependent stacking fault energy of FeCrCoNiMn high entropy alloy.* Scripta Materialia, 2015. **108**: p. 44-47.

127. Zaddach, A.J., et al., *Mechanical Properties and Stacking Fault Energies of NiFeCrCoMn High-Entropy Alloy.* Jom, 2013. **65**(12): p. 1780-1789.

128. Takeuchi, A., et al., *Entropies in Alloy Design for High-Entropy and Bulk Glassy Alloys.* Entropy, 2013. **15**(9): p. 3810-3821.

129. Ma, D.C., et al., *Ab initio thermodynamics of the CoCrFeMnNi high entropy alloy: Importance of entropy contributions beyond the configurational one.* Acta Materialia, 2015. **100**: p. 90-97.

130. Senkov, O., et al., *Refractory high-entropy alloys.* Intermetallics, 2010. **18**(9): p. 1758-1765.

131. Otto, F., et al., *The influences of temperature and microstructure on the tensile properties of a CoCrFeMnNi high-entropy alloy.* Acta Materialia, 2013. **61**(15): p. 5743-5755.

132. Nagase, T., et al., *In-situ TEM observation of structural changes in nano-crystalline CoCrCuFeNi multicomponent high-entropy alloy (HEA) under fast electron irradiation by high voltage electron microscopy (HVEM).* Intermetallics, 2015. **59**: p. 32-42.

133. Okamoto, N.L., et al., *Size effect, critical resolved shear stress, stacking fault energy, and solid solution strengthening in the CrMnFeCoNi high-entropy alloy.* Scientific Reports, 2016. **6**: p. 35863.

134. Yao, J., et al., *Microstructure and hardness of FeCrNiCoMn high-entropy alloy coating prepared by laser cladding with pre-alloyed gas atomized powder*. 2013. 480-486.

135. Nishimoto, A., T. Fukube, and T. Maruyama, *Microstructural, mechanical, and corrosion properties of plasma-nitrided CoCrFeMnNi high-entropy alloys.* Surface and Coatings Technology, 2018.

136. Reed, R.P., *Nitrogen in austenitic stainless steels.* Jom, 1989. **41**(3): p. 16-21.

137. Moravcik, I., et al., *Nitrogen Interstitial Alloying of CoCrFeMnNi High Entropy Alloy through Reactive Powder Milling.* Entropy, 2019. **21**(4): p. 363.

138. Lei, Z., et al., *Enhanced strength and ductility in a high-entropy alloy via ordered oxygen complexes.* Nature, 2018. **563**(7732): p. 546-550.

139. Seol, J.B., et al., *Boron doped ultrastrong and ductile high-entropy alloys.* Acta Materialia, 2018. **151**: p. 366-376.

140. Wang, Z., et al., *The effect of interstitial carbon on the mechanical properties and dislocation substructure evolution in Fe40.4Ni11.3Mn34.8Al7.5Cr6 high entropy alloys.* Acta Materialia, 2016. **120**: p. 228-239.

141. Li, Z., *Interstitial equiatomic CoCrFeMnNi high-entropy alloys: carbon content, microstructure, and compositional homogeneity effects on deformation behavior.* Acta Materialia, 2019. **164**: p. 400-412.

142. Park, J.M., et al., *Superior tensile properties of 1%C-CoCrFeMnNi high-entropy alloy additively manufactured by selective laser melting.* Materials Research Letters, 2019: p. 1-7.

143. Dedoncker, R., et al., *Reactive sputter deposition of CoCrCuFeNi in oxygen/argon mixtures.* Surface and Coatings Technology, 2019.

144. Rost, C.M., et al., *Entropy-stabilized oxides.* Nature Communications, 2015. **6**(1): p. 8485.

145. Huang, P.-K. and J.-W. Yeh, *Effects of substrate temperature and post-annealing on microstructure and properties of (AlCrNbSiTiV) N coatings.* Thin Solid Films, 2009. **518**(1): p. 180-184.

146. Lai, C.-H., et al., *Preparation and characterization of AlCrTaTiZr multi-element nitride coatings.* Surface and Coatings Technology, 2006. **201**(6): p. 3275-3280.

147. Tsai, M.-H., et al., *Effects of nitrogen flow ratio on the structure and properties of reactively sputtered (AlMoNbSiTaTiVZr) Nx coatings.* Journal of Physics D: Applied Physics, 2008. **41**(23): p. 235402.

148. Hsieh, M.-H., et al., *Structure and properties of two Al–Cr–Nb–Si–Ti high-entropy nitride coatings.* Surface and Coatings Technology, 2013. **221**: p. 118-123.

149. Chen, T.K., et al., *Nanostructured nitride films of multi-element high-entropy alloys by reactive DC sputtering.* Surface and Coatings Technology, 2004. **188-189**: p. 193-200.

150. Ren, B., et al., *Structure and properties of (AlCrMnMoNiZrB0.1)Nx coatings prepared by reactive DC sputtering.* Applied Surface Science, 2011. **257**(16): p. 7172-7178.

151. Yalamanchili, K., et al., *Exploring the high entropy alloy concept in (AlTiVNbCr)N.* Thin Solid Films, 2017. **636**: p. 346-352.

152. Braic, V., et al., *Nanostructured multi-element (TiZrNbHfTa)N and (TiZrNbHfTa)C hard coatings.* Surface and Coatings Technology, 2012. **211**: p. 117-121.

153. Pogrebnjak, A., et al., *Microstructure, physical and chemical properties of nanostructured (Ti–Hf–Zr–V–Nb) N coatings under different deposition conditions.* Materials Chemistry and Physics, 2014. **147**(3): p. 1079-1091.

154. Firstov, S.A., et al., *Thermal Stability of Superhard Nitride Coatings from High-Entropy Multicomponent Ti–V–Zr–Nb–Hf Alloy.* Powder Metallurgy and Metal Ceramics, 2014. **52**(9): p. 560-566.

155. Lin, C.H., J.G. Duh, and J.W. Yeh, *Multi-component nitride coatings derived from Ti–Al–Cr–Si–V target in RF magnetron sputter.* Surface and Coatings Technology, 2007. **201**(14): p. 6304-6308.

156. Chang, H.-W., et al., *Influence of substrate bias, deposition temperature and post-deposition annealing on the structure and properties of multi-principal-component (AlCrMoSiTi)N coatings.* Surface and Coatings Technology, 2008. **202**(14): p. 3360-3366.

157. Huang, P.-K. and J.-W. Yeh, *Effects of nitrogen content on structure and mechanical properties of multi-element (AlCrNbSiTiV)N coating.* Surface and Coatings Technology, 2009. **203**(13): p. 1891-1896.

158. Chang, Z.-C., D.-C. Tsai, and E.-C. Chen, *Effect of N2 flow on the structure and mechanical properties of (CrTaTiVZr)Nx coatings processed by reactive magnetron sputtering.* Journal of Materials Research, 2015. **30**(7): p. 924-934.

159. Liang, S.-C., et al., *Effects of substrate temperature on the structure and mechanical properties of (TiVCrZrHf)N coatings.* Applied Surface Science, 2011. **257**(17): p. 7709-7713.

160. Zhang, Y., et al., *Effects of nitrogen content on the structure and mechanical properties of (Al0. 5CrFeNiTi0. 25) Nx high-entropy films by reactive sputtering.* Entropy, 2018. **20**(9): p. 624.

161. Li, W., P. Liu, and P.K. Liaw, *Microstructures and properties of high-entropy alloy films and coatings: a review.* Materials Research Letters, 2018. **6**(4): p. 199-229.

162. Pei, H.J., et al., *Tensile behavior of amorphous/nanocrystalline ZrCu/Cu multilayered films with graded interfaces.* Intermetallics, 2012. **31**: p. 191-195.

163. Hui, L.C., et al., *Magnetic and magnetoelastic properties or CoCrCuFeNi thin films probed by ferromagnetic resonance* Journal of Magnetism and Magnetic Materials, 2019.

164. Kirchlechner, C., et al., *Expected and unexpected plastic behavior at the micron scale: An in situ mu Laue tensile study.* Acta Materialia, 2012. **60**(3): p. 1252-1258.

165. Ghidelli, M., et al., *Homogeneous flow and size dependent mechanical behavior in highly ductile Zr65Ni35 metallic glass films.* Acta Materialia, 2017. **131**: p. 246-259.

166. Born, M. and R. Oppenheimer, *Zur Quantentheorie der Molekeln.* Annalen der Physik, 1927. **389**(20): p. 457-484.

167. Hohenberg, P. and W. Kohn, *Inhomogeneous electron gas.* Physical review, 1964. **136**(3B): p. B864.

168. Kohn, W. and L.J. Sham, *Self-consistent equations including exchange and correlation effects.* Physical review, 1965. **140**(4A): p. A1133.

169. Vitos, L., *Computational quantum mechanics for materials engineers: the EMTO method and applications*. 2007: Springer Science & Business Media.

170. Vitos, L., *Total-energy method based on the exact muffin-tin orbitals theory.* Physical Review B, 2001. **64**(1): p. 014107.

171. Gyorffy, B.L., *Coherent-Potential Approximation for a Nonoverlapping-Muffin-Tin-Potential Model of Random Substitutional Alloys.* Physical Review B, 1972. **5**(6): p. 2382-2384.

172. Soven, P., *Coherent-Potential Model of Substitutional Disordered Alloys.* Physical Review, 1967. **156**(3): p. 809-813.

173. Wołoszyn, M. and A.Z. Maksymowicz, *Coherent potential approximation technique in a simple example of resistivity calculations for binary alloys.* Task Quarterly, 2002. **6**(4): p. 669-680.

174. Pinski, F.J., et al., *Ferromagnetism versus Antiferromagnetism in Face-Centered-Cubic Iron.* Physical Review Letters, 1986. **56**(19): p. 2096-2099.

175. Kresse, G. and J. Furthmüller, *Efficient iterative schemes for ab initio total-energy calculations using a plane-wave basis set.* Physical review B, 1996. **54**(16): p. 11169.

176. Kresse, G. and J. Hafner, *Ab initio molecular dynamics for liquid metals.* Physical Review B, 1993. **47**(1): p. 558-561.

177. Kresse, G. and J. Hafner, *Norm-conserving and ultrasoft pseudopotentials for first-row and transition elements.* Journal of Physics: Condensed Matter, 1994. **6**(40): p. 8245.

178. Kresse, G. and D. Joubert, *From ultrasoft pseudopotentials to the projector augmented-wave method.* Physical Review B, 1999. **59**(3): p. 1758.

179. Zunger, A., et al., *Special quasirandom structures.* Physical Review Letters, 1990. **65**(3): p. 353-356.

180. Wei, S.H., et al., *Electronic properties of random alloys: Special quasirandom structures.* Physical Review B, 1990. **42**(15): p. 9622-9649.

181. van de Walle, A., et al., *Efficient stochastic generation of special quasirandom structures.* Calphad, 2013. **42**: p. 13-18.

182. van de Walle, A., *Multicomponent multisublattice alloys, nonconfigurational entropy and other additions to the Alloy Theoretic Automated Toolkit.* Calphad, 2009. **33**(2): p. 266-278.

183. van de Walle, A., M. Asta, and G. Ceder, *The alloy theoretic automated toolkit: A user guide.* Calphad, 2002. **26**(4): p. 539-553.

184. Tian, L.Y., et al., *CPA descriptions of random Cu-Au alloys in comparison with SQS approach.* Computational Materials Science, 2017. **128**: p. 302-309.

185. Song, H.Q., et al., *Local lattice distortion in high-entropy alloys.* Physical Review Materials, 2017. **1**(2): p. 8.

186. Niu, C. *First Principles Studies of NiFeCrCoMn High Entropy Alloys*. 2015, North Carolina State University. p. 56-57.

187. Ehrenfest, P., *On interference phenomena to be expected whem Rontgen rays pass through a di-atomic gas.* Proceedings of the Koninklijke Akademie Van Wetenschappen Te Amsterdam, 1915. **17**: p. 1184-1190.

188. Shin, C.S., et al., *Vacancy hardening in single-crystal TiNx (001) layers.* Journal of applied physics, 2003. **93**(10): p. 6025-6028.

189. Jhi, S.-H., et al., *Vacancy Hardening and Softening in Transition Metal Carbides and Nitrides.* Physical Review Letters, 2001. **86**(15): p. 3348-3351.

190. Man, C.-S. and M. Huang, *A Simple Explicit Formula for the Voigt-Reuss-Hill Average of Elastic Polycrystals with Arbitrary Crystal and Texture Symmetries.* Journal of Elasticity, 2011. **105**(1): p. 29-48.

191. Li, J-Y., et al., *On micromechanics approximation for the effective thermoelastic moduli of multi-phase composite materials.* Mechanics of Materials, 1999. **31**: p. 149-159.

192. Abadias, G., et al., *Reactive magnetron cosputtering of hard and conductive ternary nitride thin films: Ti-Zr-N and Ti-Ta-N.* Journal of Vacuum Science & Technology A, 2010. **28**(4): p. 541-551.

193. Parratt, L.G., *Surface studies of solids by total reflection of x-rays.* Physical Review, 1954. **95**(2): p. 359-369.

194. Egami, T. and Y. Waseda, *Atomic size effect on the formability of metallic glasses.* Journal of Non-Crystalline Solids, 1984. **64**(1-2): p. 113-134.

195. Ye, Y.F., et al., *The general effect of atomic size misfit on glass formation in conventional and high-entropy alloys.* Intermetallics, 2016. **78**: p. 30-41.

196. Tong, C.J., et al., *Microstructure characterization of AlxCoCrCuFeNi high-entropy alloy system with multiprincipal elements.* Metallurgical and Materials Transactions a-Physical Metallurgy and Materials Science, 2005. **36A**(4): p. 881-893.

197. Thangaraju, S., E. Bouzy, and A. Hazotte, *Phase Stability of a Mechanically Alloyed CoCrCuFeNi High Entropy Alloy.* Advanced Engineering Materials, 2017. **19**(8): p. 6.

198. Ingerle, D., et al., *JGIXA — A software package for the calculation and fitting of grazing incidence X-ray fluorescence and X-ray reflectivity data for the characterization of nanometer-layers and ultra-shallow-implants.* Spectrochimica Acta Part B: Atomic Spectroscopy, 2016. **118**: p. 20-28.

199. Henke, B.L., E.M. Gullikson, and J.C. Davis, *X-Ray Interactions: Photoabsorption, Scattering, Transmission, and Reflection at E = 50-30,000 eV, Z = 1-92.* Atomic Data and Nuclear Data Tables, 1993. **54**(2): p. 181-342.

200. Bragg, W.H. and W.L. Bragg, *The reflection of X-rays by crystals.* Proceedings of the Royal Society of London. Series A, Containing Papers of a Mathematical and Physical Character, 1913. **88**(605): p. 428-438.

201. 15305, E., *Nondestructive Testing—Test Method for Residual Stress Analysis by X-Ray Diffraction*. 2008.

202. Oliver, W.C. and G.M. Pharr, *Measurement of hardness and elastic modulus by instrumented indentation: Advances in understanding and refinements to methodology.* Journal of Materials Research, 2004. **19**(1): p. 3-20.

203. Thomsen, C., et al., *Coherent phonon generation and detection by picosecond light-pulses.* Physical Review Letters, 1984. **53**(10): p. 989-992.

204. Thomsen, C., et al., *Surface generation and detection of phonons by picosecond light-pulses.* Physical Review B, 1986. **34**(6): p. 4129-4138.

205. Sugawara, Y., et al., *Spatiotemporal mapping of surface acoustic waves in isotropic and anisotropic materials.* Ultrasonics, 2002. **40**(1-8): p. 55-59.

206. Xu, F., et al., *Complete elastic characterization of lithium phosphorous oxynitride films using picosecond ultrasonics.* Thin Solid Films, 2013. **548**: p. 366-370.

207. Fillon, A., et al., *Lattice instability and elastic response of metastable Mo1-xSix thin films.* Physical Review B, 2013. **88**(17).

208. Rossignol, C., et al., *Elastic properties of ultrathin permalloy/alumina multilayer films using picosecond ultrasonics and Brillouin light scattering.* Physical Review B, 2004. **70**(9).

209. Belliard, L., et al., *Elastic properties and phonon generation in Mo/Si superlattices.* Physical Review B, 2009. **80**(15).

210. van Dijk, M.A., M. Lippitz, and M. Orrit, *Detection of acoustic oscillations of single gold nanospheres by time-resolved interferometry.* Physical Review Letters, 2005. **95**(26).

211. Bonello, B., et al., *Negative refraction of surface acoustic waves in the subgigahertz range.* Physical Review B, 2010. **82**(10).

212. Maznev, A.A., O.B. Wright, and O. Matsuda, *Mapping the band structure of a surface phononic crystal.* New Journal of Physics, 2011. **13**.

213. Moch, P., P. Djemia, and F. Ganot, *Tool for studying the elastic properties of thin layers and multilayers: Brillouin spectroscopy.* Vide-Science Technique Et Applications, 2001. **56**(301): p. 565-+.

214. Djemia, P., et al., *Brillouin scattering from the icosahedral quasicrystal Al70.4Mn8.4Pd21.2.* Solid State Communications, 1998. **106**(7): p. 459-461.

215. Philippe, D. *Diffusion Brillouin dans des couches et multicouches ultraminces : influences de la microstructure et des interfaces dans quelques systèmes représentatifs ($Cux_{M}o1_{-x,}$ Mo/Ni, Permalloy/Alumine, Co/Cu)*. 1998, Université Paris 13. p.

216. Djemia, P., et al., *Brillouin scattering investigation of elastic properties of Cu-Mo solid solution thin films.* Journal of Applied Physics, 2001. **90**(2): p. 756-762.

217. Kueny, A. and M. Grimsditch, *Surface-waves in a layered material.* Physical Review B, 1982. **26**(8): p. 4699-4702.

218. Djemia, P., et al., *Elastic properties of beta-SiC films by Brillouin light scattering.* Journal of Applied Physics, 2004. **95**(5): p. 2324-2330.

219. Perdew, J.P., K. Burke, and M. Ernzerhof, *Generalized gradient approximation made simple.* Physical review letters, 1996. **77**(18): p. 3865.

220. Abadias, G., P. Djemia, and L. Belliard, *Alloying effects on the structure and elastic properties of hard coatings based on ternary transition metal (M= Ti, Zr or Ta) nitrides.* Surface and Coatings Technology, 2014. **257**: p. 129-137.

221. Loudon, R., *Theory of surface-ripple Brillouin scattering by solids.* Physical Review Letters, 1978. **40**(9): p. 581.

222. Tasnadi, F., et al., *Non-equilibrium vacancy formation energies in metastable alloys—A case study of Ti0. 5Al0. 5N.* Materials & Design, 2017. **114**: p. 484-493.

223. Wang, F., et al., *Systematic ab initio investigation of the elastic modulus in quaternary transition metal nitride alloys and their coherent multilayers.* Acta Materialia, 2017. **127**: p. 124-132.

224. Lerch, D., et al., *UNCLE: a code for constructing cluster expansions for arbitrary lattices with minimal user-input.* Modelling and Simulation in Materials Science and Engineering, 2009. **17**(5): p. 055003.

225. Le Page, Y. and P. Saxe, *Symmetry-general least-squares extraction of elastic data for strained materials from ab initio calculations of stress.* Physical Review B, 2002. **65**(10): p. 104104.

226. Le Page, Y. and P. Saxe, *Symmetry-general least-squares extraction of elastic coefficients from ab initio total energy calculations.* Physical Review B, 2001. **63**(17): p. 174103.

227. Moakher, M. and A.N. Norris, *The Closest Elastic Tensor of Arbitrary Symmetry to an Elasticity Tensor of Lower Symmetry.* Journal of Elasticity, 2006. **85**(3): p. 215-263.

228. Thomas Browaeys, J. and S. Chevrot, *Decomposition of the elastic tensor and geophysical applications*. Vol. 159. 2004. 667-678.

229. Holec, D., et al., *Trends in the elastic response of binary early transition metal nitrides.* Physical Review B, 2012. **85**(6): p. 064101.

230. Hu, S., et al., *The stabilization of the rocksalt structured tantalum nitride.* Journal of Applied Physics, 2017. **122**(4): p. 045109.

231. Weinberger, C.R., et al., *Ab initio investigations of the phase stability in group IVB and VB transition metal nitrides.* Computational Materials Science, 2017. **138**: p. 333-345.

232. Koutna, N., et al., *Stability and elasticity of metastable solid solutions and superlattices in the MoN–TaN system: First-principles calculations.* Materials & Design, 2018. **144**: p. 310-322.

233. Klimashin, F.F., et al., *The impact of nitrogen content and vacancies on structure and mechanical properties of Mo–N thin films.* Journal of Applied Physics, 2016. **120**(18): p. 185301.

234. Stampfl, C. and A.J. Freeman, *Metallic to insulating nature of TaN x: Role of Ta and N vacancies.* Physical Review B, 2003. **67**(6): p. 064108.

235. Grumski, M., P.P. Dholabhai, and J.B. Adams, *Ab initio study of the stable phases of 1: 1 tantalum nitride.* Acta Materialia, 2013. **61**(10): p. 3799-3807.

236. Gu, Z., et al., *On the nature of point defect and its effect on electronic structure of rocksalt hafnium nitride films.* Acta Materialia, 2014. **81**: p. 315-325.

237. Lee, T., et al., *Elastic constants of single-crystal TiNx (001)(0.67≤x≤1.0) determined as a function of x by picosecond ultrasonic measurements.* Physical Review B, 2005. **71**(14): p. 144106.

238. Kim, J., et al., *Elastic constants of single-crystal transition-metal nitride films measured by line-focus acoustic microscopy.* Journal of Applied Physics, 1992. **72**(5): p. 1805-1811.

239. Mirkarimi, P.B., et al., *Elastic properties of TiN/(VxNb1−x)N superlattices measured by Brillouin scattering.* Journal of Applied Physics, 1992. **71**(10): p. 4955-4958.

240. Abadias, G., et al., *Structure, phase stability and elastic properties in the Ti1–xZrxN thin-film system: Experimental and computational studies.* Acta Materialia, 2012. **60**(15): p. 5601-5614.

241. Gaillac, R., P. Pullumbi, and F.-X. Coudert, *ELATE: an open-source online application for analysis and visualization of elastic tensors.* Journal of Physics: Condensed Matter, 2016. **28**(27): p. 275201.

242. Ljungcrantz, H., et al., *Nanoindentation studies of single-crystal (001)-, (011)-, and (111)-oriented TiN layers on MgO.* Journal of Applied Physics, 1996. **80**(12): p. 6725-6733.

243. Sangiovanni, D., *Inherent toughness and fracture mechanisms of refractory transition-metal nitrides via density-functional molecular dynamics.* Acta Materialia, 2018. **151**: p. 11-20.

244. Mouhat, F. and F.-X. Coudert, *Necessary and sufficient elastic stability conditions in various crystal systems.* Physical review B, 2014. **90**(22): p. 224104.

245. Togo, A. and I. Tanaka, *First principles phonon calculations in materials science.* Scripta Materialia, 2015. **108**: p. 1-5.

246. Huang, S., et al., *Thermal Expansion, Elastic and Magnetic Properties of FeCoNiCu-Based High-Entropy Alloys Using First-Principle Theory.* JOM, 2017. **69**(11): p. 2107-2112.

247. Tian, F., et al., *Ab initio investigation of high-entropy alloys of 3d elements.* Physical Review B, 2013. **87**(7): p. 075144.

248. Levämäki, H., et al., *An automated algorithm for reliable equation of state fitting of magnetic systems.* Computational Materials Science, 2019. **156**: p. 121-128.

249. Tian, L.-Y., et al., *CPA descriptions of random Cu-Au alloys in comparison with SQS approach.* Computational Materials Science, 2017. **128**: p. 302-309.

250. Tian, L.-Y., et al., *Elastic constants of random solid solutions by SQS and CPA approaches: the case of fcc Ti-Al.* Journal of Physics: Condensed Matter, 2015. **27**(31): p. 315702.

251. Marmier, A., et al., *ElAM: A computer program for the analysis and representation of anisotropic elastic properties.* Computer Physics Communications, 2010. **181**(12): p. 2102-2115.

252. Zhang, H., et al., *In situmechanical characterization of CoCrCuFeNi high-entropy alloy micro/nano-pillars for their size-dependent mechanical behavior.* Materials Research Express, 2016. **3**(9): p. 094002.

253. Salvadori, M., et al., *Measurement of the elastic modulus of nanostructured gold and platinum thin Films.* Phys. Rev. B, 2003. **67**.

254. Braeckman, B., et al., *Impurity-controlled film growth and elastic properties of CoCrCuFeNi thin films*. Vol. 315. 2017.

255. Zhang, L.J., et al., *Microstructure and mechanical behaviors of GdxCoCrCuFeNi high-entropy alloys.* Materials Science and Engineering: A, 2017. **707**: p. 708-716.

256. Bescond, C. and M. Deschamps, *Dynamical surface response of a semi-infinite anisotropic elastic media to an impulsive force (vol 103, pg 114, 1998).* Journal of the Acoustical Society of America, 1998. **104**(1): p. 599-599.

257. Bescond, C. and M. Deschamps, *Dynamical surface response of a semi-infinite anisotropic elastic medium to an impulsive force.* Journal of the Acoustical Society of America, 1998. **103**(1): p. 114-124.

258. Stoneley, R., *The propagation of surface elastic waves in a cubic crystal.* Proceedings of the Royal Society of London Series a-Mathematical and Physical Sciences, 1955. **232**(1191): p. 447-458.

259. Laplanche, G., et al., *Processing of a single-crystalline CrCoNi medium-entropy alloy and evolution of its thermal expansion and elastic stiffness coefficients with temperature.* Scripta Materialia, 2020. **177**: p. 44-48.

260. Kresse, G. and J. Hafner, *Abinitio molecular-dynamics for liquid-metals.* Physical Review B, 1993. **47**(1): p. 558-561.

261. Kresse, G. and D. Joubert, *From ultrasoft pseudopotentials to the projector augmented-wave method.* Physical Review B, 1999. **59**(3): p. 1758-1775.

262. Wei, S.H., et al., *Electronic-properties of random alloys - special quasirandom structures.* Physical Review B, 1990. **42**(15): p. 9622-9649.

263. Perdew, J.P., K. Burke, and M. Ernzerhof, *Generalized gradient approximation made simple.* Physical Review Letters, 1996. **77**(18): p. 3865-3868.

264. Monkhorst, H.J. and J.D. Pack, *Special points for brillouin-zone integrations.* Physical Review B, 1976. **13**(12): p. 5188-5192.

265. Melnick, A.B. and V.K. Soolshenko, *Thermodynamic design of high-entropy refractory alloys.* Journal of Alloys and Compounds, 2017. **694**: p. 223-227.

266. Vitos, L., I.A. Abrikosov, and B. Johansson, *Anisotropic lattice distortions in random alloys from first-principles theory.* Physical Review Letters, 2001. **87**(15): p. 4.

267. Owen, L.R., et al., *An assessment of the lattice strain in the CrMnFeCoNi high-entropy alloy.* Acta Materialia, 2017. **122**: p. 11-18.

268. Korzhavyi, P.A., et al., *Madelung energy for random metallic alloys in the coherent-potential approximation.* Physical Review B, 1995. **51**(9): p. 5773-5780.

269. Tian, L.Y., et al., *Alloying effect on the elastic properties of refractory high-entropy alloys.* Materials & Design, 2017. **114**: p. 243-252.

270. Tian, F.Y., et al., *Structural stability of NiCoFeCrAlx high-entropy alloy from ab initio theory.* Physical Review B, 2013. **88**(8): p. 5.

271. Tian, F., et al., *Ab initio design of elastically isotropic TiZrNbMoVx high-entropy alloys.* Journal of Alloys and Compounds, 2014. **599**: p. 19-25.

272. Huang, S., et al., *Mechanism of magnetic transition in FeCrCoNi-based high entropy alloys.* Materials & Design, 2016. **103**: p. 71-74.

273. Sun, X., et al., *Phase selection rule for Al-doped CrMnFeCoNi high-entropy alloys from first-principles.* Acta Materialia, 2017. **140**: p. 366-374.

274. Pindor, A.J., et al., *Disordered local moment state of magnetic transition-metals - a self-consistent kkr cpa calculation.* Journal of Physics F-Metal Physics, 1983. **13**(5): p. 979-989.

275. Staunton, J., et al., *The disordered local moment picture of itinerant magnetism at finite temperatures.* Journal of Magnetism and Magnetic Materials, 1984. **45**(1): p. 15-22.

276. Gyorffy, B.L., et al., *A 1ST-PRINCIPLES THEORY OF FERROMAGNETIC PHASE-TRANSITIONS IN METALS.* Journal of Physics F-Metal Physics, 1985. **15**(6): p. 1337-1386.

277. Mouhat, F. and F.-X. Coudert, *Necessary and sufficient elastic stability conditions in various crystal systems.* Physical Review B, 2014. **90**(22).

278. Moruzzi, V.L., J.F. Janak, and K. Schwarz, *Calculated thermal-properties of metals.* Physical Review B, 1988. **37**(2): p. 790-799.

279. Nose, S., *A unified formulation of the constant temperature molecular-dynamics methods.* Journal of Chemical Physics, 1984. **81**(1): p. 511-519.

280. Zhang, H., et al., *Elastic parameters of paramagnetic iron-based alloys from first-principles calculations.* Physical Review B, 2012. **85**(5).

281. Ramakrishnan, N. and V.S. Arunachalam, *Effective elastic-moduli of porous solids.* Journal of Materials Science, 1990. **25**(9): p. 3930-3937.

282. Senkov, O.N. and D.B. Miracle, *A topological model for metallic glass formation.* Journal of Non-Crystalline Solids, 2003. **317**(1-2): p. 34-39.

283. Gao, M.C., et al., *Thermodynamics of concentrated solid solution alloys.* Current Opinion in Solid State and Materials Science, 2017. **21**(5): p. 238-251.

284. David, M., *Alloy software for high-entropy alloys*. 2019.

285. Gao, M.C. and D.E. Alman, *Searching for Next Single-Phase High-Entropy Alloy Compositions.* Entropy, 2013. **15**(10): p. 4504-4519.

286. Albano, C. and D.H.J.T. M., *Nanostructured Coatings*. Nanostructure Science and Technology. Springer, New York, NY.

287. Haas, P., F. Tran, and P. Blaha, *Calculation of the lattice constant of solids with semilocal functionals.* Physical Review B, 2009. **79**(8): p. 085104.

288. Takahashi, T., et al., *Elastic properties of γ'-Fe4N probed by nanoindentation and ab initio calculation.* Acta Materialia, 2012. **60**(5): p. 2054-2060.

289. Leineweber, A., H. Jacobs, and S. Hull, *Ordering of Nitrogen in Nickel Nitride Ni3N Determined by Neutron Diffraction.* Inorganic Chemistry, 2001. **40**(23): p. 5818-5822.

290. Leineweber, A., et al., *ε-Fe3N: magnetic structure, magnetization and temperature dependent disorder of nitrogen.* Journal of Alloys and Compounds, 1999. **288**(1): p. 79-87.

291. Kim, K.J., J.H. Kim, and J.H. Kang, *Structural and optical characterization of Cu3N films prepared by reactive RF magnetron sputtering.* Journal of Crystal Growth, 2001. **222**(4): p. 767-772.

292. Xing, W., et al., *Structure stabilization effect of configuration entropy in cubic WN.* Physical Chemistry Chemical Physics, 2018. **20**(46): p. 29243-29248.

293. Liu, Z.T.Y., et al., *First-principles investigation of the structural, mechanical and electronic properties of the NbO-structured 3d, 4d and 5d transition metal nitrides.* Computational Materials Science, 2014. **84**: p. 365-373.

294. Schuh, C.A., T.C. Hufnagel, and U. Ramamurty, *Mechanical behavior of amorphous alloys.* Acta Materialia, 2007. **55**(12): p. 4067-4109.

295. Marx, V.M., et al., *The influence of a brittle Cr interlayer on the deformation behavior of thin Cu films on flexible substrates: Experiment and model.* Acta Materialia, 2015. **89**: p. 278-289.

296. Putz, B., et al., *Two-stage cracking of metallic bi-layers on polymer substrates under tension.* Scripta Materialia, 2018. **145**: p. 5-8.

297. Faurie, D., et al., *In situ x-ray diffraction analysis of 2D crack patterning in thin films.* Acta Materialia, 2019. **165**: p. 177-182.

298. Merabtine, S., et al., *Multicracking and Magnetic Behavior of Ni80Fe20 Nanowires Deposited onto a Polymer Substrate.* Nano Letters, 2018. **18**(5): p. 3199-3202.

299. Wu, K., et al., *Cohesive and adhesive properties of nanocrystalline Ti thin films on polyimide substrates.* Materials Science and Engineering: A, 2019. **744**: p. 746-753.

300. Kreiml, P., et al., *Electro-mechanical behavior of Al/Mo bilayers studied with in situ straining methods.* Thin Solid Films, 2018. **665**: p. 131-136.

301. Leterrier, Y., et al., *Adhesion of silicon oxide layers on poly(ethylene terephthalate). I: Effect of substrate properties on coating's fragmentation process.* Journal of Polymer Science Part B: Polymer Physics, 1997. **35**(9): p. 1449-1461.

302. Xia, Z.C. and J.W. Hutchinson, *Crack patterns in thin films.* Journal of the Mechanics and Physics of Solids, 2000. **48**(6): p. 1107-1131.

303. Beuth, J.L., *Cracking of thin bonded films in residual tension.* International Journal of Solids and Structures, 1992. **29**(13): p. 1657-1675.

304. Frank, S., et al., *The relationship between thin film fragmentation and buckle formation: Synchrotron-based in situ studies and two-dimensional stress analysis.* Acta Materialia, 2009. **57**(5): p. 1442-1453.

305. Ben Cheikh, I., et al., *Analysis of the multi-cracking mechanism of brittle thin films on elastic-plastic substrates.* International Journal of Solids and Structures, 2019. **180-181**: p. 176-188.

306. Frank, S., et al., *In situ studies on the cohesive properties of α- and β-Ta layers on polyimide substrates.* Acta Materialia, 2011. **59**(15): p. 5881-5892.

307. Schlich, F.F., et al., *Cohesive and adhesive properties of ultrathin amorphous and crystalline Ge2Sb2Te5 films on polyimide substrates.* Acta Materialia, 2017. **126**: p. 264-271.

308. Schlich, F.F. and R. Spolenak, *Size- and phase-dependent mechanical properties of ultrathin Si films on polyimide substrates.* Acta Materialia, 2016. **110**: p. 122-130.

309. Rochat, G., et al., *Mechanical analysis of ultrathin oxide coatings on polymer substrates in situ in a scanning electron microscope.* Thin Solid Films, 2003. **437**(1): p. 204-210.

310. Faurie, D., et al., *Fragmentation and adhesion properties of CoFeB thin films on polyimide substrate.* Applied Physics Letters, 2017. **110**(9): p. 091904.

311. Wu, K., et al., *Fragmentation and adhesion properties of Cu-Zr amorphous thin films on polyimide substrates.* Philosophical Magazine Letters, 2018. **98**(10): p. 464-472.

312. Chason, E. and P.R. Guduru, *Tutorial: Understanding residual stress in polycrystalline thin films through real-time measurements and physical models.* Journal of Applied Physics, 2016. **119**(19): p. 191101.

313. Yu, H.Z. and C.V. Thompson, *Correlation of shape changes of grain surfaces and reversible stress evolution during interruptions of polycrystalline film growth.* Applied Physics Letters, 2014. **104**(14): p. 141913.

314. Li, W., P.K. Liaw, and Y. Gao, *Fracture resistance of high entropy alloys: A review.* Intermetallics, 2018. **99**: p. 69-83.

315. Xia, A., et al., *Electromechanical properties of cathodic arc deposited high entropy alloy thin films on polymer substrates.* Journal of Vacuum Science & Technology A, 2018. **37**(1): p. 010601.

316. Xiao, Y., et al., *Nanostructured NbMoTaW high entropy alloy thin films: High strength and enhanced fracture toughness.* Scripta Materialia, 2019. **168**: p. 51-55.

317. Coupeau, C., et al., *Atomic force microscopy of in situ deformed nickel thin films.* Thin Solid Films, 1999. **353**(1): p. 194-200.

318. Pundt, A., et al., *Adhesion-energy measurements by means of white-light interferometry and controlled-buckling technique.* Scripta Materialia, 2007. **57**(9): p. 889-892.

319. Pundt, A., et al., *Adhesion energy between metal films and polymers obtained by studying buckling induced by hydrogen.* Acta Materialia, 2004. **52**(6): p. 1579-1587.

320. Cordill, M.J., et al., *Adhesion energies of Cr thin films on polyimide determined from buckling: Experiment and model.* Acta Materialia, 2010. **58**(16): p. 5520-5531.

321. Yeager, J.D., et al., *Characterization of flexible ECoG electrode arrays for chronic recording in awake rats.* Journal of neuroscience methods, 2008. **173**(2): p. 279-285.

322. Taylor, A.A., et al., *An elevated temperature study of a Ti adhesion layer on polyimide.* Thin solid films, 2013. **531**(C): p. 354-361.

323. Wu, K., et al., *Fracture behavior and adhesion energy of nanostructured Cu/Mo multilayer films.* Materials Science and Engineering: A, 2014. **613**: p. 130-135.

324. Wu, K., et al., *Buckling behaviors and adhesion energy of nanostructured Cu/X (X=Nb, Zr) multilayer films on a compliant substrate.* Acta Materialia, 2013. **61**(20): p. 7889-7903.

325. Wu, K., et al., *An Easy Way to Quantify the Adhesion Energy of Nanostructured Cu/X (X = Cr, Ta, Mo, Nb, Zr) Multilayer Films Adherent to Polyimide Substrates.* Acta Metallurgica Sinica (English Letters), 2016. **29**(2): p. 181-187.

326. Lerch, D., et al., *UNCLE: a code for constructing cluster expansions for arbitrary lattices with minimal user-input.* Modelling and Simulation in Materials Science and Engineering, 2009. **17**(5): p. 19.

327. Mota, O.U.O., et al., *Mechanical Properties of Metal Nitrides for Radiation Resistant Coating Applications: A DFT Study.* 23rd International Conference on the Application of Accelerators in Research and Industry - CAARI 2014, 2015. **66**: p. 576-585.

328. Zhao, E.J., et al., *First Principles Investigation on the Ultra-Incompressible and Hard TaN.* Journal of Computational Chemistry, 2009. **30**(14): p. 2358-2363.